FLORIDA INTERNATIONAL UNIVERSITY

Miami, Florida

INVESTIGATION OF CARBON-BASED LABEL-FREE ELECTROCHEMICAL APTASENSORS FOR POINT-OF-CARE CANCER BIOMARKER DETECTION

A dissertation submitted in partial fulfillment of the

requirement for the degree of

DOCTOR OF PHILOSOPHY

in

ELECTRICAL AND COMPUTER ENGINEERING

By

Shahrzad Forouzanfar

2021

To: Dean John L. Volakis
College of Engineering and Computing

This dissertation, written by Shahrzad Forouzanfar, and entitled Investigation of Carbon-Based Label-Free Electrochemical Aptasensors for Point-of-Care Cancer Biomarker Detection, having been approved in respect to style and intellectual content, is referred to you for judgment.

We have read this dissertation and recommend that it be approved.

_____
Shekhar Bhansali

_____
Pulugurtha Markondeya Raj

_____
Lidia Kos

_____
Chunlei (Peggy) Wang, Co-Major Professor

_____
Nezih Pala, Co-Major Professor

Date of Defense: June 4, 2021

The dissertation of Shahrzad Forouzanfar is approved.

_____
Dean John L. Volakis
College of Engineering and Computing

_____
Andrés G. Gil
Vice President for Research and Economic Development
and Dean of the University Graduate School

Florida International University, 2021

DEDICATION

I dedicate my dissertation to my mum, Fariba, and my husband, Thomas, who loved me unconditionally and supported me in every step of my Ph.D. career.

ACKNOWLEDGMENTS

First and foremost, I would like to express my deepest appreciation to my advisors Dr. Nezih Pala and Dr. Chunlei Wang for their guidance, vision, and support throughout my doctoral program. I also appreciate their efforts on reviewing and critiquing my research and writing, which helped me in improving the quality of my work.

I would like to extend my gratitude to the members of my dissertation committee – Dr. Shekhar Bhansali, Dr. Lidia Kos, and Dr. P. M. Raj for their willingness to serve on my committee and for providing unwavering support, professionally and personally, along the way.

I am very thankful to the University Graduate School (UGS) at Florida International University for supporting me through Dissertation Evidence Acquisition (DEA), and Dissertation Year Fellowship (DYF) awards. I am also thankful to the National Science Foundation (NSF) to support my PhD program.

This work would not have been possible without the technical facilities provided at Advanced Materials Engineering Research Institute (AMERI) at FIU. I am very grateful to Dr. Patrick Roman, Dr. Alexander Franco Hernandez, Dr. Meer Safa, Jonathan Comparan, and Steward Schwarz for their patience and help with my experimentation.

I am thankful to our previous and present members of my research group – Dr. Amin Rabeie, Dr. Richa Agrawal, Dr. Ebenezer Dotun Adelowo, Fahmida Alam, Iman Khakpour, Naznin Akter, Omena Okpowe, Azmal Chowdhury, Borzooye Jafarizadeh, and Ana Claus for their company and help during my PhD.

Last but not the least; I would also like to express my appreciations to my mum, my parents in-low, and my husband and my close friends at FIU. Also, I would like to

acknowledge the teachers, professors, and other professionals who either directly trained me, or inspired me in some way.

ABSTRACT OF THE DISSERTATION

INVESTIGATION OF CARBON-BASED LABEL-FREE ELECTROCHEMICAL APTASENSORS FOR POINT-OF-CARE CANCER BIOMARKER DETECTION

by

Shahrzad Forouzanfar

Florida International University, 2021

Miami, Florida

Professor Nezih Pala, Co-Major Professor

Professor Chunlei Wang, Co-Major Professor

Cancer is the second cause of death, with millions of fatalities every year. The early detection of cancer can tremendously increase the survival chances of the patients. An effective approach for early detection of cancer is developing reliable and relatively cheap biosensors that can quantify the cancer biomarkers from blood samples. These classes of the biosensor are commonly referred to as point-of-care (POC) cancer biomarker biosensors. The label-free electrochemical biosensors based on carbon dravite materials can be feasible for POC cancer biomarker biosensors. The present dissertation aims to design, develop, and optimize carbon-based biosensors for label-free detection of lactic acid and platelet-derived growth factor-BB (PDGF-BB) cancer biomarkers. Two carbon-based materials are used for developing the biosensor: carbon-micro electrotechnical systems (aka. C-MEMS) and bipolar exfoliated graphene. In the first phase of this dissertation, enzymatic biosensors based on interdigitated C-MEMS microelectrodes were investigated. The achieved results confirmed that the C-MEMS-based sensing platform functionalized with oxygen-plasma treatment could provide a stable sensing system with

low background noise, which can be used for label-free detection. In the next phase of the dissertation, for the first time, the C-MEMS electrode functionalized with oxygen-plasma was adopted for ssDNA aptamer-based biosensors (aka. aptasensors). The attained results confirmed that the developed aptasensors are highly sensitive, selective, and robust, and the developed system is adaptable for turn-on and turn-off sensing strategies. In the following phase of the dissertation, the adaptability of the bipolar exfoliated graphene for aptasensors was investigated. The achieved results revealed that the graphene deposited on a negative feeding electrode (i.e., reduced graphene oxide) is more suitable for label-free electrochemical aptasensing. Hence, POC PDGF-BB aptasensors based on bipolar reduced graphene oxide were developed and investigated for the first time. The achieved results were highly promising for feasible POC cancer aptasensors. The last phase of this dissertation explores the in-situ integration of bipolar exfoliated graphene on C-MEMS microelectrodes. The biosensor developed based on this integration showed enhanced sensitivity. In the present dissertation, novel carbon-based biosensors were developed and optimized. The achieved results show the high potential of C-MEMS and bipolar exfoliated graphene-based biosensors for label-free POC cancer biomarker biosensing.

TABLE OF CONTENTS

CHAPTER PAGE

LIST OF TABES

TABLE PAGE

LIST OF FIGURES

FIGURE PAGE

1. Introduction

1.1 Overview

Cancer is one of the major causes of death and kills millions of people every year. Many cancer patients have no apparent physical symptoms in the early stages of their diseases. An effective way to diagnose cancer early and increase the patients' survival chances is quantifying cancer biomarkers' levels in the human body. Thus far, many cancer biomarkers (aka. tumor makers) have been discovered, indicating cancer in the human body at the very early stages of the disease. Among the discovered cancer biomarkers, platelet-derived growth factor-BB (PDGF-BB) is an important biomarker since it plays a crucial role in developing and spreading cancerous cells in the human body. It has been reported that the changes in the levels of PDGF-BB have a strong correlation with the progress and metastasis of solid malignant tumors in vital organs such as the brain, liver, prostate, lung, and pancreas. A feasible way for early detection of cancer is quantifying cancer biomarkers using precise and affordable point-of-care (POC) biosensors. Label-free electrochemical biosensors can be a potent candidate for POC biosensors due to their unique features, such as eliminating laborious labeling or tagging, compatibility with available lab-on-chip technologies, and integration with CMOS circuits the output can be digitized, and they are applicable for continuous monitoring. However, label-free electrochemical biosensors suffer from several drawbacks compared to labeled optical and electrochemical biosensors, such as having higher background noise, which reduces the sensitivity and signal-to-noise ratio of the biosensor's lower selectivity, and the sensing unit is more prone to degrade. The importance of early detection of cancer and exiting

limitations in electrochemical biosensors enlightens the necessity of developing POC biosensors that possess the advantages of label-free electrochemical biosensors while having improved sensitivity, selectivity, and higher stability.

Carbon allotropes have dominated materials science and engineering for several decades due to their unique features, making them suitable for a wide variety of applications. The feasibility of carbon-based devices for various biotechnology applications and various fabrication techniques has been studied and demonstrated extensively. One effective way to synthesize carbon is a top-down manufacturing approach via an organic polymer precursor and pyrolyzing patterning. One of the carbon fabrication techniques that this dissertation focuses on is photoresist-derived glass-like carbon. The microstructures derived from SU-8 photoresist were the first to be commonly referred to as carbon microelectromechanical systems (C-MEMS) [1, 2]. C-MEMS platforms have distinguishing features such as low background capacitance and high stability when exposed to different physical/chemical treatments, biocompatibility, and good electrical conductivity [3].

Furthermore, the surface of C-MEMS can be modified effectively, both via electrochemical processes and by depositing nanomaterials [3]. Various studies have investigated the integration of nanomaterials on the surface of C-MEMS platforms for various applications such as graphene/carbon nanotubes [4] and graphene nanoplatelets [5] for supercapacitors, and graphene/enzymes for biofuel cells [6]. Carbon nanomaterials, in particular graphene, offer high surface area, tunable depositing, and high specific capacitance, which could noticeably benefit label-free electrochemical aptasensors by enlarging the accessible surface area and enhancing the signal-to-noise ratio [5]. The

feasibility of C-MEMS for mass-production and integration with lab-on-chips technology and desirable features of graphene for biosensing applications is highly promising for label-free POC cancer biosensors. This dissertation, for the first time, investigates the application of C-MEMS platforms for label-free detection.

1.2 Research Problems

This dissertation's ultimate goal is to design, fabricate, and access highly sensitive and stable label-free electrochemical biosensors to detect cancer biomarkers quantitatively. However, several issues can challenge the feasibility and reliability of the prospect biosensors. The *research problems* encountered in this dissertation and their possible solutions are discussed as follows:

a) What are the factors that affect the stability of the biosensors?

The stability of the biosensors can be divided into two major types of stability issues related to the physical stability of the biosensor and stability issues related to the shelf life or activity of the bio-recognizer (i.e., bio/chemical compounds used for detecting biomolecules) agents.

i. The biosensors' physical stability mainly depends on the fabrication process: The platforms used for the developed biosensors for this dissertation include C-MEMS thin films, interdigitated finger microelectrodes, and 3D arrays micropillar and PET/Au electrodes. The low physical stability of C-MEMS-based devices can be the result of the weak adhesion of the SU-8 photoresist to the supporting substrate. The adhesion of SU-8 photoresist to silicon wafers can be improved via wafer cleaning and dehydration bake of the wafer at 150-200°C for 5-15 minutes to evaporate the remaining solvent and moisture [7-9]. Furthermore, the peeling of the

SU-8 structures, especially structures with high thickness, can result from the underdevelopment of the photoresist's bottom layers. Such issues can result from insufficient UV dose, inadequate post-exposure bake, or non-uniform coating of the SU-8 photoresist. Several approaches have been adopted to resolve this issue, such as conducting the post-exposure bake on hot plates instead of the convection oven, increasing the post-bake time, and an extra step of hard baking at 190°C [10, 11].

ii. The stability of bio-agents mostly depends on the sensor development stage and storage conditions:

Several factors can jeopardize the stability of the bio-recognizer agents, including storage under fluctuating temperatures, multiple frosts and defrosting of bio-recognizer, contamination of the bio-recognizer, and variation in pH of the solution. In order to minimize the effect of temperature fluctuation, the main stocks of bio-recognizers (i.e., enzyme and single-stranded DNA aptamers) were stored at a deep-freezing temperature of -70°C, and the only portion of them was stored at normal freezer at -20°C. Furthermore, to prevent multiple frost and defrost and reduce the contamination, several diluted portions with desired concentrations and amounts were prepared and stored. For stabilizing the pH of bio-recognizer solutions, 0.1 M Phosphate-buffered saline (PBS) buffer was used for lactate oxidase enzyme, and platelet-derived growth factor-BB (PDGF-BB) aptamer.

b) What are the factors that affect the repeatability of the fabrication process?

The repeatability of biosensors fabrication can be categorized into two groups: repeatability of the device fabrication process and repeatability of the sensor development.

i. *The device fabrication process repeatability:* The repeatability of the device fabrication process was enhanced by considering several factors in designing the fabrication process, such as changes in ambient conditions, the amount of dispensed photoresist, the waiting times between each fabrication steps, and the changes in viscosity of photoresist because of storage time.

ii. *The sensor development repeatability:* The repeatability of the sensor development process was enhanced by considering several factors in designing the process, such as thorough washing of the device before and after each step, controlling the contamination by using fresh tubes and plastic containers, precise control of time between each step, and controlling the temperature of incubation. Furthermore, the repeatability of the sensors depends on the amount of immobilized bio-recognizer agents on the surface of the sensors. In this dissertation, the covalent immobilization of bio-recognizers was used as the primary immobilization mechanism to enhance the repeatability of the developed biosensors.

c) What are the factors that affect the sensitivity of the biosensors?

The sensitivity of the biosensors can be enhanced by optimizing the parameters that affect the measurements. Several factors, including the reaction time, pH of the electrolyte, the concentration of supporting salt, incubation temperature, and concentration of bio-recognizers, are optimized for the developed sensors in this dissertation. Furthermore, the

sensitivity of the biosensor depends on the measurement technique used for quantifying the target amounts. Three techniques of cyclic voltammetry (CV), electrochemical impedance spectroscopy (EIS), and differential pulse voltammetry (DPV) are applied for analytical purposes.

1.3 Research Hypotheses

In this dissertation, several hypotheses were considered for developing the biosensors and analyzing the sensing performance of the biosensors.

a) *The bio-recognizers agents can be directly immobilized on the surface of oxygen-plasma treated CMEMS electrodes:*

   Penmatsa et al. showed that the oxygen-plasma treatment increases the carboxyl group percentage on the surface of C-MEMS electrodes [12]. It is assumed that the carboxyl functional group can be used to covalently immobilize the enzymes and amino group-terminated ssDNA aptamers, which can provide a stable and repetitive immobilization of bio-recognizer agents. This hypothesis is studied in chapters 4 and 5 for enzyme immobilization and ssDNA aptamer immobilization, respectively.

b) *The interaction of biosensors with target molecules on the surface of the electrodes affects the properties of the double layer and reduces the double layer capacitance:*

The interaction of the bio-recognizer can affect the default double-layer capacitance. The changes can result from changes in ion concentration in the electrolyte-electrode medium or changes in the biosensors' surface. This hypothesis is studied in chapters 4, 5, and 7.

c) *Trapping the target molecules can be traced by increased charge transfer rate:*

Capturing the target molecules and forming the aptamer-target complex can affect the electrons' exchange rate between the electrolyte and sensor electrodes, and it is expected to increase the charge transfer rate. This hypothesis is studied in chapters 5 and 6.

d) *The bipolar exfoliated graphene deposited on negative feeding electrode provides more suitable properties for biosensing application than exfoliated graphene deposited on positive feeding electrode:*

The previous study on bipolar exfoliated graphene has shown that the graphene deposited on the negative feeding electrode has porous morphology with vertically aligned nanosheets and possesses better electrochemical properties than graphene deposited on the positive feeding electrode. It is assumed that the porous morphology and the graphene's better electrochemical properties deposited on the negative feeding electrode can provide better material for biosensing applications. This hypothesis is studied in chapter 6.

e) *Integration of bipolar exfoliated graphene on the surface of CMEMS can increase the capacitance of the biosensors and enhance its sensitivity:*

The bipolar exfoliated graphene has porous morphology and is vertically aligned. The vertically aligned morphology of the bipolar exfoliated graphene provides a large surface and eliminates the necessity of using spacers such as carbon nanotubes to stop stacking the graphene nanosheets. Therefore, it is expected that the deposition of

graphene on the surface of C-MEMS microelectrodes will increase the electrode's active area, resulting in increased capacitance and, subsequently, the sensitivity of the biosensor. This hypothesis is studied in chapter 7.

1.4 Research Plan

The research plan adopted for this dissertation is presented in Figure 1.1; the specific goals that were worked toward are as follows:

a) Developing enzymatic biosensors based on C-MEMS microelectrodes:

In order to investigate the first and second hypotheses mentioned in section 1.3, enzymatic biosensors based on lactate oxidase enzymes immobilized on interdigitated C-MEMS microelectrodes were developed.

b) Developing label-free aptasensors for detection of PDGF-BB cancer biomarkers:

After confirming the feasibility of the oxygen-plasma treatment for functionalization of C-MEMS electrodes and the covalent immobilization of bio-recognizers, the oxygen-plasma treated electrodes were used as active electrodes for developing label-free electrochemical aptasensor. For developing label-free aptasensors, DNA aptamers with the oligonucleotide sequence of amino linker-C_6-CAG GCT ACG GCA CGT AGA GCA TCA CCA TGA TCC TG were used as the bio-recognizer agent for detection of PDGF-BB cancer biomarker. In addition, the turn-off and turn-on detection strategies based on capacitance and resistance measurement were deployed.

c) *Investigating the application of bipolar exfoliated graphene for label-free cancer biomarker aptasensor:*

In order to define whether bipolar exfoliated graphene is suitable for biosensing development, a comparative study was deployed. After confirming that the bipolar exfoliated graphene deposited on negative feeding provides a more suitable material than graphene deposited on the positive electrode, a disposable, flexible aptasensor was developed, and the amperometric response was investigated.

d) *Investigating the integration of bipolar exfoliated graphene with C-MEMS microelectrodes:*

The bipolar graphene was deposited on 3D C-MEMS microelectrodes to study the fifth hypothesis mentioned in section 1.3. The C-MEMS microelectrodes were used as the negative feeding electrode, and the capacitive response was investigated.

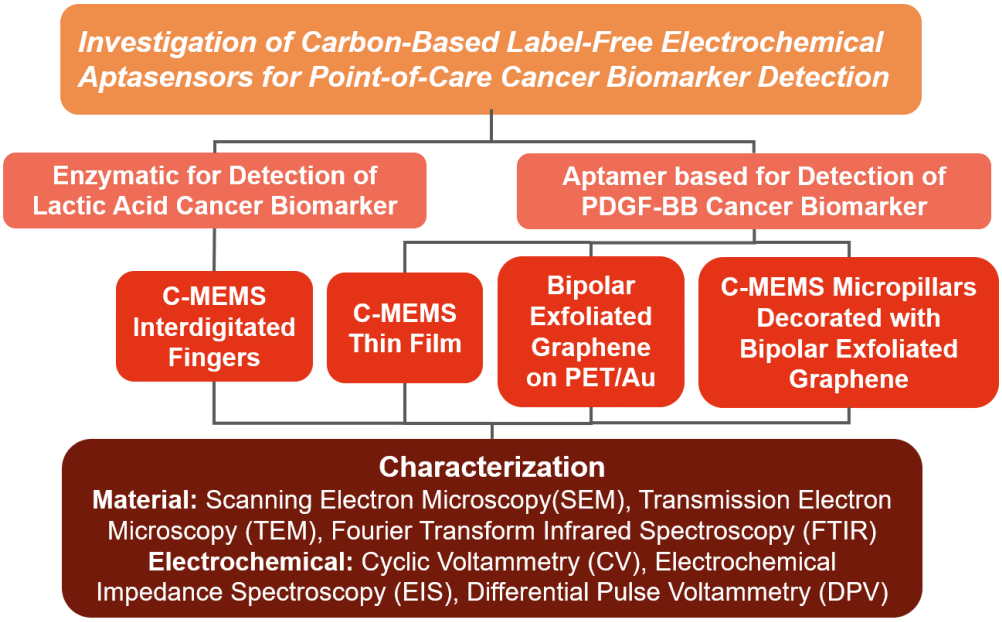

Figure 1.1 Flow chart of the research plan

1.5 Scope of the Dissertation

The first part of chapter 2 presents a thorough review of label-free aptasensors for cancer biomarker detection. Two major types of aptasensors, optical and electrochemical, are discussed, and relevant information is presented. The second part of chapter 2 presents a comprehensive review of biotech devices based on C-MEMS technology. Chapter 3 provides the detailed methodology of this dissertation's experimental techniques, including photolithography, sensor development, and analytical techniques adopted for this dissertation. Chapter 4 investigates the lactic acid enzymatic biosensors based on C-MEMS interdigitated microelectrodes. The sensing platform of the biosensor was synthesized by pyrolysis of photo-patterned photoresist polymer in oxygen-free and high-temperature conditions. The surfaces of the microelectrodes were functionalized by the oxygen-plasma pretreatment technique to form –COOH functional groups. In addition, the lactate oxidase enzyme was immobilized on the carboxylic group-covered surfaces of the microelectrodes. Chapter 5 investigates the label-free electrochemical aptasensors based on C-MEMS for the detection of PDGF-BB. The oxygen-plasma oxidation treatment was used to functionalize the C-MEMS electrodes, which provided efficient covalent immobilization of amino terminated affinity aptamers. The turn-off and turn-on detection strategies based on capacitance and resistance measurement were deployed, respectively. In chapter 6, a comparative study on the bipolar exfoliated graphene deposited on the negative and feeding electrode is presented. After confirming that the bipolar exfoliated graphene deposited on the negative feeding electrode (i.e., reduced graphene oxide) possesses better electrochemical properties for aptasensing than the bipolar exfoliated graphene deposited on the negative feeding electrode (i.e., graphene oxide), electrochemical aptasensors were

based on gold-covered polyethylene terephthalate electrodes (PET/Au) as a possible contender for disposable label-free aptasensor applications is studied. Chapter 7 explores the in-situ integration of bipolar exfoliated graphene and 3D C-MEMS microelectrodes for label-free PDGF-BB aptasensors. Chapter 8 provides a summary and future works in the direction of this dissertation.

1.6 References

[1] C. Wang and M. Madou, "From MEMS to NEMS with carbon," Biosensors and bioelectronics, vol. 20, pp. 2181-2187, 2005.

[2] S. Ranganathan, R. Mccreery, S. M. Majji, and M. Madou, "Photoresist-derived carbon for microelectromechanical systems and electrochemical applications," Journal of the Electrochemical Society, vol. 147, p. 277, 2000.

[3] V. Penmatsa, A. R. Ruslinda, M. Beidaghi, H. Kawarada, and C. Wang, "Platelet-derived growth factor oncoprotein detection using three-dimensional carbon microarrays," Biosensors and bioelectronics, vol. 39, pp. 118-123, 2013.

[4] M. Beidaghi and C. Wang, "Micro-supercapacitors based on interdigital electrodes of reduced graphene oxide and carbon nanotube composites with ultrahigh power handling performance," Advanced Functional Materials, vol. 22, pp. 4501-4510, 2012.

[5] M. Beidaghi, Z. Wang, L. Gu, and C. Wang, "Electrostatic spray deposition of graphene nanoplatelets for high-power thin-film supercapacitor electrodes," Journal of Solid State Electrochemistry, vol. 16, pp. 3341-3348, 2012.

[6] Y. Song, C. Chen, and C. Wang, "Graphene/enzyme-encrusted three-dimensional carbon micropillar arrays for mediatorless micro-biofuel cells," Nanoscale, vol. 7, pp. 7084-7090, 2015.

[7] Y. Li, "Challenges and issues of using polymers as structural materials in MEMS: A review," Journal of Microelectromechanical Systems, vol. 27, pp. 581-598, 2018.

[8] S. Forouzanfar, F. Alam, N. Pala, and C. Wang, "Highly sensitive label-free electrochemical aptasensors based on photoresist derived carbon for cancer biomarker detection," Biosensors and Bioelectronics, vol. 170, p. 112598, 2020.

[9] R. Mishra, B. Pramanick, A. Chatterjee, T. Maiti, and T. Bhattacharyya, "Fabrication of C-MEMS Derived 3-Dimensional Glassy Carbon Microelectrodes for Neural Sensing and Stimulation," in 2018 IEEE SENSORS, 2018, pp. 1-4.

[10] M. V. Piñón, B. C. Benítez, B. Pramanick, V. H. Perez-Gonzalez, M. J. Madou, S. O. Martinez-Chapa, et al., "Direct current-induced breakdown to enhance reproducibility and performance of carbon-based interdigitated electrode arrays for AC electroosmotic micropumps," Sensors and Actuators A: Physical, vol. 262, pp. 10-17, 2017.

[11] M. Vazquez-Pinon, B. Pramanick, F. G. Ortega-Gama, V. H. Perez-Gonzalez, L. Kulinsky, M. J. Madou, et al., "Hydrodynamic channeling as a controlled flow reversal mechanism for bidirectional AC electroosmotic pumping using glassy carbon microelectrode arrays," Journal of Micromechanics and Microengineering, vol. 29, p. 075007, 2019.

[12] V. Penmatsa, H. Kawarada, Y. Song, and C. Wang, "Comparison of different oxidation techniques for biofunctionalization of pyrolyzed carbon," Material Science Research India, vol. 11, pp. 01-08, 2014.

2. Background and Literature Review

2.1 Electrochemical Aptasensors for Label-Free Cancer Diagnosis

2.1.1 Introduction

Aptamers exhibit similar levels of target-binding affinities in comparison with monoclonal antibodies [1, 2]. Aptamers have considerable advantages over antibodies for clinical applications, including less batch variation, roughly no immunogenicity, cost-effectiveness, more straightforward modification, and short production times [1, 3]. Over the past two decades, substantial improvement has been made in applying aptamers, mainly RNA-based aptamers, as diagnosis and investigative tools, in micro-agents for intra-corpus drug delivery, as therapeutic mediators biosensors, and even genetically controllable devices [4]. For example, 'Macugen' is the first therapeutic aptamer approved by the Food and Drug Administration (FDA) to treat age-related macular degradation of the retina [5]. DNA aptamers comprise the largest share of the global pharmaceutical and biotechnology market, with 'research and development' and diagnostics constituting the two major areas of expenditure in the aptamer market [6]. As of 2019, the North America aptamer market was valued at USD 66.9M, and it is expected to increase to USD 143.6M by the end of 2024[7], illustrating both the size of the market and the rapid rate at which the utilization of DNA aptamers is increasing.

Biosensors, as the International Union of Pure and Applied Chemistry (IUPAC), has defined, are integrated recognition-transduction devices, which can provide quantitative data utilizing biochemical recognition component [8]. The recognition part is composed of biological or synthetic receptors like aptamers, enzymes, and antibodies,

which utilize a specific biochemical or chemical reaction mechanism. A group of biosensors in which the recognition part is based on aptamers is referred to as ‘aptasensors’. Aptasensors can be used for specified detection of numerous analyte targets varying from small ions to large biomolecules as well as malignant cells [9], tissues [10], and cancer biomarker proteins [11]. In the transducer part of a biosensor, an output signal is obtained and converted into a measurable parameter. The method used in the transducer part has a significant impact on the sensitivity of the biosensor, whereas the bio-recognizing component determines the degree of specificity or selectivity of the biosensor. The classical methods for clinical tests such as high-performance liquid chromatography or spectrophotometry are costly and require trained operators to perform additional sample pretreatments. Hence advanced techniques based on various mechanisms such as piezoelectric [12], optical (e.g., plasmonics [13] and colorimetric [14]), and electrochemical (e.g., impedance [15] and amperometric [16]) are used for developing biosensors for cancer diagnosis. Among them, electrochemical biosensors have attracted many interests in recent years because they are highly favorable for portable and point-of-care measurements due to their potential to be miniaturized and integrated with MEMS devices and circuits [17]. Rapidly growing attention to electrochemical cancer aptasensors has recently led an explosive increase in scientific publications in the past decade. Despite the vast potential implementations and applications of cancer aptasensors, these sensors are not commercially available yet. Here, by focusing specifically on label-free electrochemical cancer aptasensors, this chapter aims to present the current state of the art, challenges, and possible opportunities for cancer aptasensors’ commercialization.

2.1.2 Aptamers and Aptamer-based Sensors

In the early 1990s, Ellington et al. introduced the "SELEX" procedure (systematic evolution of ligands by exponential enrichment) for aptamer preparation, which excludes the sophisticated design for receptor units [18]. The process, which is schematically described in Figure 2.1.1 starts with creating an oligonucleotide library of vast numbers of random sequences (usually 10^{15}-10^{16}), that contains a constant region (primary transcription) at both ends and an intermediate random region. The selection process of desired RNA-aptamers starts with passing the primary DNA library through an isolation matrix to which the target molecules adhere. The nucleic acids attached to the desired target remain in the isolation matrix while the rest is removed. Replicating the searched nucleic acids via polymerase chain reaction (PCR) produces a combination of nucleic acid sequences with an affinity for the target molecules. Thus, the selection and amplification need to be repeated until the oligonucleotide sequences with the highest affinity for the desired target dominate the population. This repetition is necessary because the library contains a vast array of oligonucleotide arrangements, making it impossible to develop the sequence with the highest affinity in one single selection-amplification cycle [18].

The application of aptamers for biosensors is particularly attractive because aptamers are reliable substitutes for antibodies and enzymes in bioanalytical studies and exhibit several advantages over immunosensors, including but not limited to the following aspects: 1) The aptamers' structures are highly-reproducible, whereas antibodies undergo alterations and structural perturbations during their production process; 2) The process of chemically modifying aptamers with functional groups (i.e., by attaching optical (e.g., fluorescent), magnetic, or redox-active labels) is more accessible than that of modifying

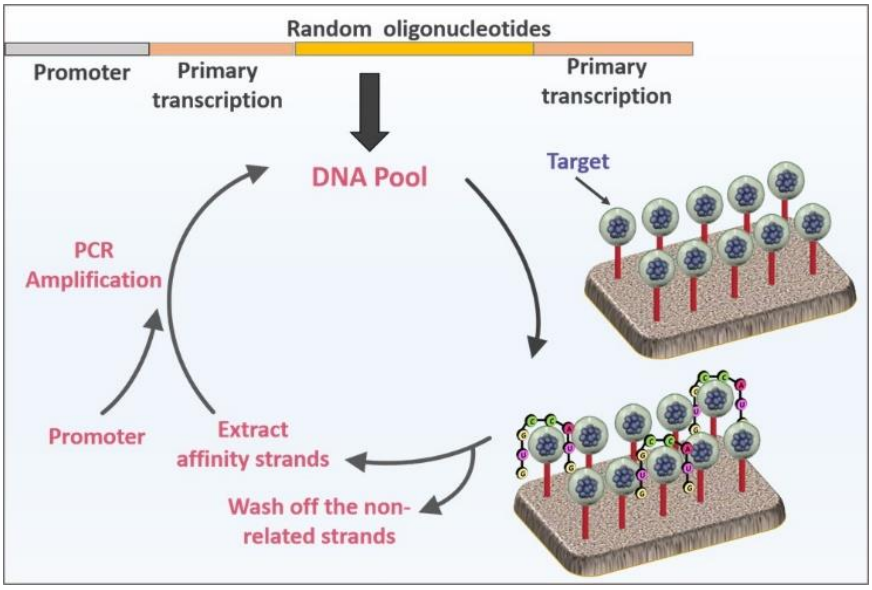

Figure 2.1 Synthesizing of aptamers by the systematic evolution of ligands by exponential enrichment (SELEX) protocol (PCR: polymerase chain reaction.).

antibodies; 3) Direct signal transducing from the aptamer-substrate complex is easily achievable by applying labeled aptamers, whereas the antigen-antibody approach requires complex sandwich structures for readout; 4) Aptamers exhibit fewer non-specific adsorption phenomena than protein interfaces (e.g., antibodies)[19]. In the last decade, DNA aptamers have been synthesized for various cancer biomarkers, antigens, and cells such as Mucin 1 (MUC-1), human epidermal growth factor receptor 2 (HER-2), vascular endothelial growth factor-165 (VEGF), and platelet-derived growth factor-BB (PDGF-BB). The affinity sequences of aptamers utilized in recent studies and their modification tag/functional groups are summarized in Table 2.1, wherein they are organized by the target type. As can be seen, the same affinity sequence synthesized for a target can be applied to both optical and electrochemical aptasensors. For example, both optical and electrochemical aptasensors for the HER-2 cancer biomarker are developed utilizing the same affinity sequence but with a different tag/functional group [20, 21]. It is worth

mentioning that comprehensive information on synthesized aptamers and related information such as target type, aptamer category (RNA or DNA), and affinity sequence can be found at the online library of the National Institutes of Health (NIH) [22].

Table 2.1 The synthesized affinity sequences and embedded tag/functional groups of aptamers utilized in recent cancer aptasensors

Target	**Affinity Sequences**	**Terminus**	**Tag/Functional Group**	**Sensor type**	**Ref.**
MUC1	-GGG AGA CAA GAA TAA ACG CTC AAG CAG TTG ATC CTT TGG ATA CCC TGG TTC GA	5’	biotin	optical	[20]
	GCA GTT GAT CCT TTG GAT ACC CTG G	5’	methylene blue	electrochemical	[23]
	GCA GTT GAT CCT TTG GAT ACC CTG G	5’	HS-$(CH_2)_6$	electrochemical	[24]
HER-2	AAC CGC CCA AAT CCC TAA GAG TCT GCA CTT GTC ATT TTG TAT ATG TAT TTG GTT TTT GGC TCT CAC AGA CAC ACT ACA CAC GCA CA	5’	biotin	optical	[20]
	GGG CCG TCG AAC ACG AGC ATG GTG CGT GGA CCT AGG ATG ACC TGA GTA CTG TCC	5’	NH_2-$(CH_2)_6$	electrochemical	[25]
	AAC CGC CCA AAT CCC TAA GAG TCT GCA CTT GTC ATT TTG TAT ATG TAT TTG GTT TTT GGC TCT CAC AGA CAC ACT ACA CAC GCA CA	5’	SH-$(CH2)_6$	electrochemical	[21]
VEGF	ACG CAG UUU GAG AAG UCG CGC GU	3’	Cyanine 3B	optical	[26]
	CCG TCT TCC AGA CAA GAG TGC AGG G	5’	6-carboxyfluorescein	optical	[27]
	TTG TCC CGT CTT CCA GAC AAG AGT GCA GGG A	5’	NH_2-$(CH_2)_6$	optical	[28]
	TTT TTT TTT TTT TTT TTT TTC AAT TGG GCC CGT CCG TAT GGT GGG T	5’	H_2N	optical	[29]
	TTT TTT TGT GGG GGT GGA CTG GGT GGG TAC C	5’	SH	optical	[30]
	TTT TTT TTT TTG TGG GGG TGG ACG GGC CGG GTA GA	5’	OH–$(CH_2)_6$–S–S–$(CH_2)_6$	optical	[31]
	CAG GCT ACG GCA CGT AGA GCA TCA CCA TGA TCC TG	3’	biotin	optical	[32]
	TTT CCC GTC TTC CAG ACA AGA GTG CAG GG	5’	SH	electrochemical	[33]
PDGF-BB	CAT AGC GAG ATC CAG ACC TAG CAG	N/A	No-Tag	optical	[34]
	AAA AAA AAT ACT CAG GGC ACT GCA AGC AAT TGT GGT CCC AAT GGG CTG AGT A	5’	Biotin and SH	optical	[34]

	T_{30} CAG GCT ACG GCA CGT AGA GCA TCA CCA TGA TCC	5’	SH	optical	[35]
	TCT AGA CAT TCA TCC TCA GCC AGG CTA CGG CAC GTA GAG CAT CAC CAT GAT CCTG	5’	SH	optical	[36]
	CAG GAT CAT GGT GAT GCT CTA CGT GCC GTA GCC TG	5’	NH_2-$(CH_2)_6$	optical	[37]
prostate-specific antigen	TTT TTA ATT AAA GCT CGC CAT CAA ATA GCT TT	5’ 3’	HS-$(CH_2)_6$ NH_2-$(CH2)_6$	electrochemical	[38]
	TTT TTA ATT AAA GCT CGC CAT CAA ATA GCT TT	5’	NH_2-$(CH2)_6$	electrochemical	[39]
	TTT TTA ATT AAA GCT CGC CAT CAA ATA GCT TT	5’	HS–$(CH_2)_6$	electrochemical	[40]
	TTT AAT TAA AGC TCG CCA TCA AAT AGC TTT	5’	NH_2-$(CH2)_6$	electrochemical	[41]
	TTT TTA ATT AAA GCT CGC CAT CAA ATA GCT TT	5’	$(CH_2)_6$	electrochemical	[42]
K562 human chronic myelogenous leukemia	TTT TTT TTT TAC AGC AGA TCA GTC TAT CTT CTC CTG ATG GGT TCC TAT TTA TAG GTG AAG CTG T	5’	NH_2	optical	[43]
	ATC CAG AG TGA CGC AGC AGA TCA GTC TAT CTT CTC CTG ATG GGT TCC TAT TTA TAG GTG AAG CTG GAC ACG GTG GCT TAG T	3’	$(CH2)_6$-NH_2	electrochemical	[44]
	TTT TTT TTT TAC AGC AGA TCA GTC TAT CTT CTC CTG ATG GGT TCC TAT TTA TAG GTG AAG CTG T	5’	SH	electrochemical	[45]
anterior gradient homolog 2	CGG GTG GGA GTT GTG GGG GGG GGT GGG AGG GTT	5’	biotin	optical	[46]
HER	GGC GCU CCG ACC UUA GUC UCU GUG CCG CUA UAA UGC ACG GAU UUA AUC GCC GUA GAA AAG CAU GUC AAA GCC GGA ACC GUG UAG CAC AGC AGA	5’	$(CH_2)_6$	electrochemical	[47]
angiogenin	CGG ACG AAT GCT TTG ATG TTG TGC TGG ATC CAG CGT TCA TTC TCA	3’	$(CH_2)_6$-(SH)	electrochemical	[48]
carcinoembryonic antigen	ATA CCA GCT TAT TCA ATT	5’	SH-$(CH_2)_6$	electrochemical	[49]
	TTA ACT TAT TCG ACC ATA TTT TTT TTT T	3’	SH	electrochemical	[50]
	ATA CCA GCT TAT TCA ATT	5’	SH-$(CH_2)_6$	electrochemical	[51]
	ATA CCA GCT TAT TCA ATT	5’	SH	electrochemical	[52]
	ATA CCA GCT TAT TCA ATT	5’	SH-$(CH_2)_6$	electrochemical	[53]
α-methylacyl-CoA racemase	TTT TTT CCC TAC GGC GCT AAC CCA TGC TAC GAA TTC GTT GTT AAA CAA TAG GCC ACC GTG CTA CAA	5’	histidine	electrochemical	[54]

protein tyrosine kinase-7	ATC TAA CTG CTG CGC CGC CGG GAA AAT ACT GTA CGG TTA GA	3’	$(CH_2)_3$-SH	electrochemical	[55]
3,3′4,4′-polychlorinated biphenyl	GGC GGG GCT ACG AAG TAG TGA TTT TTT CCG ATG GCC CGT G	5’ 3’	SH-$(CH_2)_6$ Fc	electrochemical	[56]
	GGC GGG GCT ACG AAG TAG TGA TTT TTT CCG ATG GCC CGT G	5’ 3’	SH-$(CH_2)_6$ Fc	electrochemical	[57]
cytochrome c	CCG TGT CTG GGG CCG ACC GGC GCA TTG GGT ACG TTG TTG C	5’	NH_2	electrochemical	[58]
cancerous exosomes	ATC CAG AGT GAC GCA GCA TAT TAG TAC GGC TTA ACC CPC ATG GTG GAC ACG GTG GCT TAG T	5’	SH	electrochemical	[59]
	GCG TTT TCG CTT TTG CGT TTT GGG TCA TCT GCT TAC GAT AGC AAT GCT	3’	NH_2	electrochemical	[60]
hepatocellular carcinoma	ACA GCA TCC CCA TGT GAA CAA TCG CAT TGT GAT TGT TAC GGT TTC CGC CTC ATG GAC GTG CTG	5’	$(CH_2)_6$–NH_2	electrochemical	[61]
	ACA GCA TCC CCA TGT GAA CAA TCG CAT TGT GAT TGT TAC GGT TTC CGC CTC ATG GAC GTG CTG	5’	SH-$(CH_2)_6$	electrochemical	[62]
	ACA GCA TCC CCA TGT GAA CAA TCG CAT TGT GAT TGT TAC GGT TTC CGC CTC ATG GAC GTG CTG	5’	SH-$(CH_2)_6$	electrochemical	[63]
	ACA GCA TCC CCA TGT GAA CAA TCG CAT TGT GAT TGT TAC GGT TTC CGC CTC ATG GAC GTG CTG	5’	SH-$(CH_2)_6$	electrochemical	[64]

Although they have tremendous advantages, both RNA and DNA aptamers can be strongly affected by nucleases through hydrolytic digestion (this is particularly true for RNA aptamers) and thus require a clean application environment [65]. Applications and features of the two major types of aptasensor are summarized in the following section.

2.1.2.1 Optical Cancer Aptasensors

The first application of aptamers as bio-detection agents in biosensors was reported in 1996, with an optical biosensor utilizing fluorescently labeled aptamers [66]. Due to the high sensitivity and automation capabilities of optical-based sensing, this method has been vastly applied in food/environmental monitoring and medical diagnosis. Fluorescent labels are the most commonly utilized transduction agents in optical aptasensors due to their

sensitivity and the existence of accurate measuring techniques. Optical aptasensor studies mainly focus on relating the changes in fluorescence intensity to the target-aptamer interactions and increasing the sensitivity of the sensing platform [67]. The fluorescent intensity and fluorescent anisotropy measurements are the most commonly employed methods in optical aptasensors [68]. In the former, a biochemical reaction or binding event can be quantified by using either fluorogenic assays or fluorescence quench assays. In fluorogenic assays, the reaction products are fluorescent, while in fluorescence quench assays, a fluorescent label is covalently linked to the substrate, and the reaction quenches the label [69]. The cancer biosensors based on optical measurement techniques exhibit noticeable features such as low limit of detection (LoD), high quality factors (high signal to noise ratio) in extremely low target concentrations, and versatility to be used for various targets. However, many of them have some drawbacks including 1) narrow dynamic ranges compared to clinical application requirements, 2) need for complicated optical analysis tools for the output signals, 3) complicated labeling process, and 4) endpoint signal reading which makes the optical aptasensors insufficient for point-of-care applications and studying the kinetics of bio-reactions. Table 2.2 lists the recently reported optical cancer aptasensors along with the cutoff points of the target biomarkers. It should be noted that some of the cancer biomarkers (e.g. prostate specific antigen (PSA)) are FDA-approved and that the clinical data regarding healthy ranges are available to the public [70].

Table 2.2 Different cancer optical aptasensors and their performance characteristics

Target	Healthy Range	Method	Sensing Enhancement	Linear Range	Limit of Detection	Ref.
MUC-1	<500 U/mL	fluorescence	sandwich assay	10 - 10^6 cells/mL	10 cells/mL	[71]
MUC-1		fluorescence	dye-Si nanoparticles	N/A	10 cells/mL	[20]

VEGF	<200 pg/mL	fluorescence	AuNPs/localized surface plasmon resonance	1.25 pM - 1.25 nM	N/A	[26]
PDGF-BB	<1127.5 pg/mL	fluorescence	homogeneous aptamer proximity binding assay, split aptamer	10 - 200 nM	3.2 nM	[34]
PDGF-BB		fluorescence	silver NPs	N/A	625 pM	[76]
PDGF-BB		fluorescence	aptamers-based sandwich assay for silver-enhanced fluorescence multiplex detection	0.25 – 8 nM	16 pM	[77]
PDGF-BB		fluorescence	single-walled carbon nanotubes	0.1 − 10 nM	N/A	[78]
VEGF	<200 pg/mL	fluorescence polarization	N/A	0.32 - 5.0 nM	0.32 nM	[27]
VEGF		fluorescence resonance energy transfer (FRET)	quantum dots (QD)	N/A	1 nM	[28]
VEGF		FRET	QD+Dye	N/A	12 nm	[28]
T-cell acute lymphoblastic leukemia cells	N/A	colorimetric	AuNPs/cell triggered cyclic enzymatic	10^2 - 10^4 cells/mL	40 cells/mL	[79]
CCRF-CEM	N/A	colorimetric	AuNPs	102 - 10^5 cells/mL	90 cells/mL	[80]
tumor necrosis factor-alpha	<11.00 pg/mL	colorimetric	AuNPs	0 to 22.3 nM	97.2 pM	[81]
VEGF	<200 pg/ml	surface plasmon resonance	horse radish peroxidase	N/A	10 nM	[83]
VEGF		surface plasmon resonance	rolling circle amplification (isothermal enzymatic DNA replication process)	3 pM - 10 µM	3 pM	[29]
VEGF		surface plasmon resonance	N/A	3 nM - 60 nM	1 fM	[84]
VEGF		surface enhanced Raman scattering	silver NPs ornamented/AuNPs pyramids	0.01 - 1.0 fM	22.6 aM	[30]
VEGF		surface enhanced Raman scattering	silica encapsulated hollow Au nano-spheres/VEGF antigen	3 fM - 10 nM	3 aM	[31]
PDGF-BB	<1127.5 pg/mL	surface enhanced Raman scattering	AuNPs	1 – 50 pM	0.5 pM	[35]
PDGF-BB		surface enhanced	one- two- three-cascaded amplification	1 pM − 10 nM	420 fM	[36]

		Raman scattering				
PSA	0.5 – 2 ng/ml	surface enhanced Raman scattering	magnetic nanoparticles core- AuNPs satellite	5 – 500 pg/mL	5.0 pg/mL	[85]
K562 human chronic myeloge nous leukemia	N/A	electro chemilumine scence	carbon QDs/ZnO nanoshpere electro chemiluminescence label	10^2 - 10^7 cells/mL	46 cells/mL	[43]
PDGF-BB	<1127.5 pg/mL	electro-chemilumine scence	beta-cyclodextrine/graphitic carbon nitride composite	0.02 pM – 20 nM	0.01 pM	[37]
VEGF	<200 pg/ml	chemilumine scence resonance energy transfer	QD/hemin/H_2O_2+lumin ol	N/A	180 nM	[28]
VEGF		tunable resistive pulse sensing	aptamer immobilized on 120 nm bead	mass measurement 0 -10 nM	N/A	[32]

2.1.2.2 Electrochemical Cancer Aptasensors

An electrochemical sensor transforms chemical reaction information into analytically useful information via electrochemical measurement methods. Electrochemical measurement methods have been widely utilized as fast, low-cost, and easy-operation tools for highly sensitive biochemical analysis of complex samples. In a typical electrochemical aptamer-based sensing platform, aptamers are immobilized on a sensing electrode (also referred to as the working electrode or sensing probes). In labeled-type electrochemical biosensors, labels are used to increase the signal produced per event. Typically, the electrochemical labeling process involves the covalent binding of labels through chemical processes, whereas some probe labeling requires only temporary (physical-binding) attachment of labels [87]. As it is schematically illustrated in Figure 2.2 (A & B), the developed aptamers for labeled type electrochemical aptasensors could have dynamic distances to the transducer's surface. Capturing the targets can ignite electron

transfer (Figure 2.2A) or quench the electron transfer (Figure 2.2B) [68]. In the case of label-free aptasensors, the attachment of targets to aptamers changes the electrical properties of aptamers and sensing platforms by having different steric hindrances or electrochemical isolation properties, which is especially true for cancer cell diagnosis (Figure 2.2C) [68]. In other words, the formation of a target-aptamer complex in label-free electrochemical aptasensors would affect the electrochemical properties of the sensing electrode, which can be detected via redox-species or impedance variations.

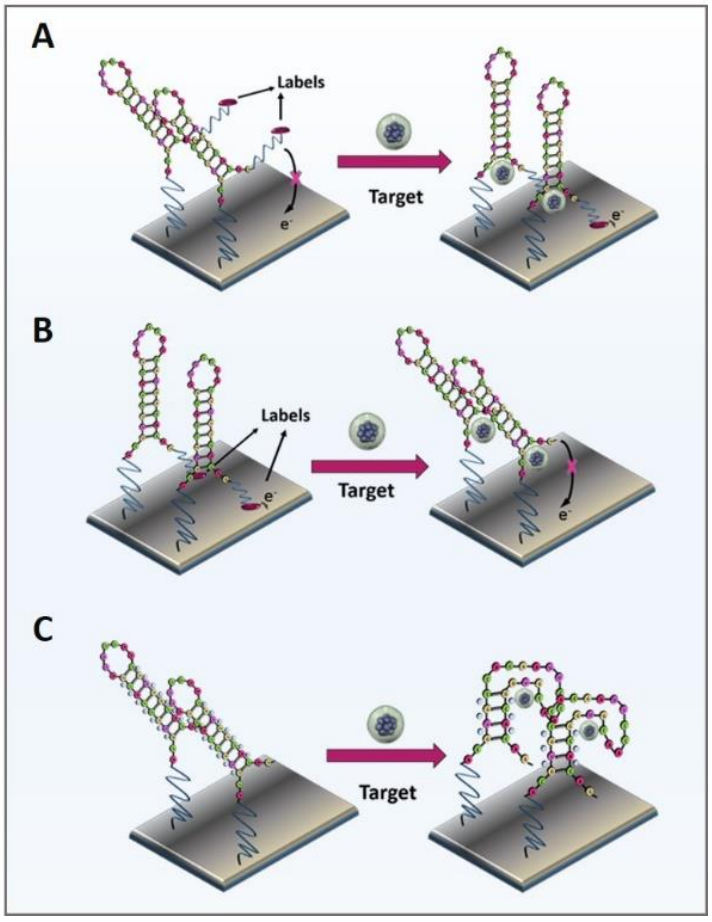

Figure 2.2 Schematic illustration of A) labeled type aptasensors in which aptamer-target binding induces the electron transferring, B) labeled type aptasensors in which aptamer-target binding quenches or reduces the electron transferring, and C) label-free type apt

Both label-free and labeled electrochemical aptasensors reveal the presence of targets by changes either in current or in capacitance. Accordingly, various electrochemical aptasensors based on different measurement techniques such as field-effect transistors (FET) [88], differential pulse voltammetry (DPV) [89], cyclic voltammetry (CV) [90], electrochemical impedance spectroscopy (EIS) [91] and tunable resistive pulse sensing (TRPS) [32] have been developed. In the FET technique, bio-recognition agents are immobilized on the gate surface and binding of targets leads to an increase or decrease of conductance which can be detected in a real-time manner via measuring the drain current [88]. DPV is a voltammetry technique in which a linear or staircase sweep of potential

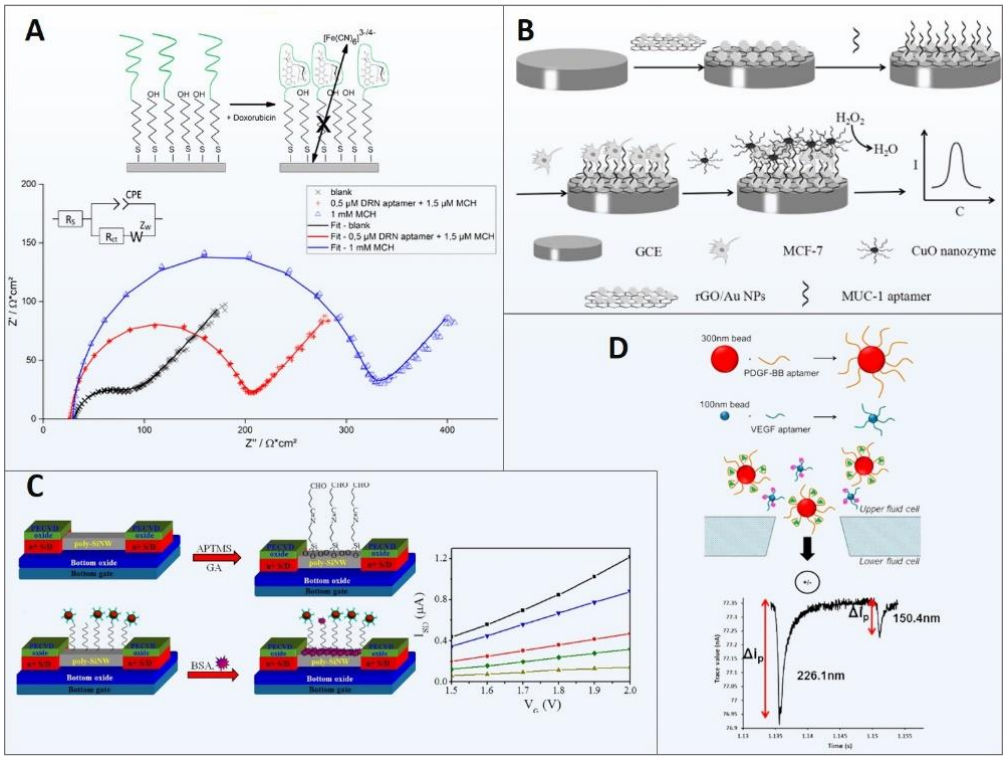

Figure 2.3 Examples of electrochemical cancer aptasensors. A) Charge transfer resistance (RCT) measured via EIS technique for detecting doxorubicin (one type of anthracyclines used in cancer treatment)[91], B) Current measured via DVP method for detecting circulating tumor cells (MCF-7)[97], C) Current measured at drain of a FET for identifying VEGF [88], and D) Analyzed average rate of triplicate for detecting VEGF and PDGF through TRPS technique [32].

pulses is applied to the sensing probe and the current is measured before each potential change. This technique has been vastly utilized for cancer electrochemical aptasensors because of two main reasons: 1) it is highly sensitive to the change of bio/electrochemical species because the effect of current variations is minimized and 2) only faradaic current is extracted which minimizes the effect of background capacitance [92]. CV measurement is another voltammetry technique extensively used in cancer electrochemical aptasensors' studies. In this technique, the current of sensing probe is measured while the potential of sensing probe is ramped linearly over time until it reaches the set potential and ramps in the opposite direction to return to its starting potential. This technique can be used in two-electrodes and three-electrodes cell configurations, depending on the desired analytical characterization [93]. EIS technique measures the variation of impedance in two modes of faradaic and non-faradaic. The faradaic mode studies the change of electron transfer rate caused by aptamer-target interactions, while the non-faradaic mode mainly measures the variations of surface capacitance resulted from aptamer-target bindings [94]. TRPS technique utilizes tunable nanopores to measure various characteristics of the sample, such as size, charge, and concentration [95]. The capture-probe of TRPS cancer aptasensors is consist of chosen nanoparticles modified with the proper affinity aptamers. The information of aptamer-target interactions is measured by analyzing the pulse observed as the capture-probe traverses the nanopore [96]. In Figure 2.3, some examples of sensing mechanisms and output sensing signals are illustrated.

Besides the importance of choosing appropriate electrochemical sensing technique based on the electrochemical nature of the sensing platform and different targets, following factors can affect the performance of an electrochemical biosensor: 1) fabrication

procedure of the working electrodes, 2) pretreatment of the electrode surface, and 3) bio-functionality of the electrodes. Of these factors, pretreatment and bio-functionality of the working electrode surfaces are particularly significant in terms of their impact on diagnosis performance. For instance, proper treatment of the working electrodes with protein-repellants and functional group quenchers (e.g., bovine serum albumin and Tween-20) can prevent the binding of undesired similar molecules and effectively enhance the selectivity of the sensors. Furthermore, detecting several targets in the same sample serum is possible by locally functionalizing different surface areas of one working electrode, which is referred to as 'multiplexing' [98]. Multiplexing is particularly desirable since it reduces both the required sample volume and the cost of each test. Moreover, surface modifications can significantly affect the surface capacitance. Surface capacitance is often modeled as a 'constant phase element' in EIS measurements and depends on the thickness and dielectric properties of the sensing electrode [99].

Label-free electrochemical cancer aptasensors have remarkable advantages over optical and labeled electrochemical cancer biosensors such as the capability of continuously monitoring the kinetics of biochemical reactions, wider dynamic range, relatively fast reaction time, eliminating the complicated labeling process, and capability of compact lab-on-chip integration which make them highly suitable and desirable for practical applications and commercialization. It is worth mentioning that besides the noticeable advantages of label-free electrochemical cancer aptasensors, they also suffer from some drawbacks such as lower selectivity than similar optical and labeled electrochemical aptasensors, low signal-to-noise ratio in low-target concentrations which

requires complicated mediator composites to enhance the output signal, and complicated reaction pathways and kinetics.

The following sections focus on reviewing label-free electrochemical cancer aptasensors to address their key features, performances, challenges, and potential for further enhancement.

2.1.3 Label-Free Electrochemical Cancer Aptasensors

Designing accurate, fast, and reliable biosensors—especially for early cancer diagnosis—requires a deep understanding of the sensing mechanisms and behavior of the sensing materials. Gold, glassy carbon, and screen-printed carbon have been used extensively as electrode materials for label-free electrochemical cancer aptasensors. The enhancement methods used to improve the performance of an aptasensor can be vastly different, depending on the bio-reception strategy and the physiochemical characteristics of the targets. The surface functionalization process is typically used to bind aptamers covalently on the sensor surface, increase the electron transfer to the electrode, and reduce non-specific bindings. In the case of biomarker-based electrochemical cancer detection, the aptamer-target bindings can be detected via voltammetry measurements, including DPV, CV, and square wave voltammetry (SWV), while measuring impedance variation is more useful for whole-cell detection. Label-free electrochemical cancer aptasensors can be divided into two major groups based on the nature of their targets, and this division is helpful for more in-depth understanding of developed sensing mechanisms and suitable methods for functionalizing their sensing platforms: 1) aptasensors based on biomarkers

and related proteins, and 2) aptasensors based on whole-cell detection. The electrochemical measuring strategies and functionalization methods for both groups are discussed below.

2.1.3.1 Label-free Electrochemical Cancer Aptasensors Based on Biomarkers and Related Proteins

One of the effective cancer diagnosis methods includes detecting cancer via antigens produced in the body in the presence of cancer cells or using established biomarkers for indirect cancer detection. Different types of biomarkers such as HER [47], HER-2 [25], VEGF [100], MUC-1[23], and PSA [90] have been studied for label-free electrochemical aptasensors. Both current and capacitance measurements can be used for this purpose. Measuring current requires an assay containing redox/oxidation couples (e.g. $[Fe(CN)_6]^{-3/-4}$), while capacitive measurement could be done in situ without requiring further electrochemical agents (e.g., EIS measurements in non-faradaic mode) [101, 102]. Furthermore, turn-off and turn-on signal transduction strategies can be likewise applied to label-free aptasensors. Turn-off strategies are often based on lessened available sites for passing electrons resulted from aptamer-target assemblies. These types of probes require a redox/oxidation couple to produce appropriate signals. As an example, M. Shamsipur et al. developed a VGEF aptasensor utilizing gold nanocluster based nanocomposites as the immobilization platform for aptamers and $[Fe(CN)_6]^{3-/-4}$ as a signal probe [103]. In their sensor, the interaction of the aptamer and the target led to DVP results with linear decaying response to the VGEF molecules in the range of 1 – 120 pM. Turn-on strategy can be applied for label-free cancer biomarker aptasensors by using EIS technique and measuring charge transfer resistance (often modeled as R_{ct}) and surface capacitances. R_{ct} can be

measured directly from radius of semicircle in EIS spectra or can be calculated from

Table 2.3 Comparison of performance of recent biomarker-based label-free electrochemical cancer aptasensors

Target	Sensing Platform	Sensing Enhancement	Utilized Method	Detection Linear Range	Limit of Detection	Stability (Stored at 4°C)	Ref.
HER-2	Au with streptavidin-coated magnetic beads	AuNPs and aptamer/antibody	DPV	1 - 40 ng/ml	50pg/ml	95% after 7 days	[47]
HER-2	Au	micro-electrode capacitors	EIS	0.2 - 2 ng/ml	200 pg/ml	N/A	[25]
HER-2	Au	interdigitated gold electrodes	CV/EIS	1 pM -100 nM	1 pM.	N/A	[21]
MUC-1	Au	N/A	SWV	10 pM – 1 µM	4 pM	93.75 after 4 weeks	[23]
MUC-1	Au	AuNPs	EIS	0.5 - 10 nM	0.1 nM	N/A	[24]
PSA	glassy carbon	quinone-based conducting polymer	SWV	1 - 10 ng/ml	1 ng/ml	93% after 7 days	[113]
PSA	Au	Thiol-modified sulfo-betaine	EIS	1 - 10 ng/ml	1 ng/ml	N/A	[38]
PSA	Au	rolling circle amplification reaction with poly (thymine) - templated copper nanoparticles and AuNPs	CV	0.05 - 500 fg/mL	0.020 ± 0.001 fg/mL	N/A	[90]
PSA	Au	imprinted polymer	CV/EIS	100 pg/ml - 100 ng/ml	1 pg/ml	N/A	[39]
PSA	glassy carbon	AuNPs / rGO / multi-walled carbon nanotubes	DPV	0.005 – 20 ng/mL	1.0 pg/mL	95%-92% after 30 days	[40]
PSA	glassy carbon	Au / Pt-polymethylene blue and magnetic particles	CV/EIS	10 fg/mL - 100 ng/mL	2.3 fg/mL	91.4% after 7 days and 97.9% after 14 days	[41]
PSA	Au	mesoporous silica thin film	DPV	1 - 300 ng/mL	280 pg/mL	98% after 30 days	[42]
PSA	glassy carbon	titanium oxide nanoparticles / silk fibroin nanofiber	CV/EIS	2.5 fg/mL - 25 pg/mL and 25 pg/mL - 25 ng/mL	0.8 fg/mL	94% after 7 days	[104]
PSA	Au interdigitated fingers	self-assembled monolayer	EIS	0.5 – 5000 ng/mL	0.51 ng/mL	90 % after 6 days	[114]
Angiogenin	glassy carbon	poly(diallyldimethyl ammonium chloride) / graphene / AuNPs	SWV	0.1 pM - 5 nM	0.064 pM	N/A	[48]

carcinoembryonic antigen	glassy carbon	nanocomposite of AuNPs/hemin/graphene nanosheets	CV / amperometry	0.0001 - 10 ng/mL	40 fg/ml	97% after 7 days	[49]
carcinoembryonic antigen	Au	enzymatic polymerization (aptamer-OTEP)	CV / amperometry	5 fM - 500 nM	5 fM	N/A	[50]
carcinoembryonic antigen	Au	glucose oxidase and ferrocene dually functionalized nanoporous gold	CV/EIS	1.0 pg/mL - 100 ng/mL	0.45 pg/mL	93% after 14 days	[51]
carcinoembryonic antigen	glassy carbon	Molybdate	CV	10 pg/mL - 10 ng/mL	0.05 pg/mL	NR	[52]
carcinoembryonic antigen	Au	horse radish peroxidase/concanavalin A	DPV/ CV	5 - 40 ng/mL	3.4 ng/mL	N/A	[53]
carcinoembryonic antigen	Plastic tubes	TiO2Pt/ reduced graphene oxide (rGO)	Chronoamperometry	6.4×10^{-5}-1.0×10^{0} µg/mL	6.4×10^{-5} µg/mL	98.8% after 30 days	[116]
carcinoembryonic antigen	glassy carbon	AuNPs/ amino-functionalized MCM–41	EIS	1.0×10^{-3} − 100.0 ng/mL	9.8×10^{-4} ng/mL^{-1}	93.5% after 3 days	[117]
α-methyl acyl-CoA racemase	Au	polypyrrole (PPy)−polyethylene glycol (PEG)	SWV	1 fM – 1 nM	5 fM	N/A	[54]
lung cancer-related protein	Au	silica-coated iron oxide magnetic beads grafted with hydrophobic C8 and C4 alkyl groups	SWV	0.023 - 230 ng/mL	0.023 ng/ml	N/A	[118]
3,3′4,4′-polychlorinated biphenyls	Au	N/A	CV/EIS	0.2 - 200 µg/L	0.01 µg/L	80% after 14 days	[56]
3,3′4,4′-polychlorinated biphenyls	Au	AuNPs dotted rGO	CV	1 pg/L and 10 µg/L	0.1 pg/L	85% after 14 days	[57]
cytochrome c	glassy carbon	electro-polymerized neutral red and decacarboxylated pillar	CV/EIS	80 pM - 80 nM	varied from 0.02 to1.0 nM	85% after 14 days	[58]
interleukin 6	screen printed carbon	Polypyrrole/AuNPs	CV/EIS	1 pg/mL - 15 µg/mL	0.33 pg/mL	93% after 10 days	[121]
cancerous exosomes	Au	DNA nanotetrahedra	CV/ SWV	10^{5} - 10^{12} exosomes/mL	10^{4} exosomes/mL	N/A	[59]
cancerous exosomes	Au	N/A	DPV	1000 − 120 000 particles/µL	70 particles/µL	N/A	[60]
VEGF	screen printed carbon	ordered mesoporous carbon–Au	CV/EIS	10.0 – 300.0 pg/mL	1.0 pg/mL	N/A	[100]
VEGF	graphite screen printed	AuNPs / spacer thiol/6-mercapto-1-hexanol	DPV/EIS	0 - 250 nmol/L	30 nmol/L	N/A	[123]

equivalent EIS circuits [98]. For instance, A. Benvidi and his coworkers developed a turn-on PSA label-free aptasensor based on silk fibroin nanofibers modified with titanium oxide

nanoparticles deposited on glassy carbon electrode in which they measured R_{ct} as the sensing indicator [104].

For voltammetry and EIS methods, various composites have been introduced to enhance the performance of aptasensors by improving applicable features of sensing probes such as aptamer immobilization efficiency [105], target binding affinities [106], and response kinetics [107]. AuNPs, as promising enhancement mediators, have been widely used either directly on the surfaces of electrodes [9, 47], or in compound with other materials such as graphene [57], poly(diallyl dimethyl ammonium chloride) [48], and poly (thymine) templated copper nanoparticles [90]. For capacitive methods, different factors including but not limited to geometry, material, the design of the electrodes, the variation of charge propagation upon aptamer-target binding, and frequency of the applied AC electrical signal in addition to the ones mentioned above contribute the response of a cancer aptasensor [21, 25]. The reported capacitive electrochemical cancer aptasensors usually have simple sensing probes without having complicated surface functionalization and labeling processes. However, interpretation and calibration of the capacitive output signals could be challenging due to the complexity of the capacitive response itself (e.g., memory effects and charge leakage of capacitors [108]) and bio-electrochemical processes.

Reaction time is one of the crucial parameters for portable and point-of-care biosensors. In the case of aptasensors, reaction time is the minimum time required for aptamer-target integration. Reaction time reported in the literature varies from 5 minutes [56] to several hours [104], with an average of 60 minutes. For label-free electrochemical aptasensors, reaction time is independent of applied measurement techniques and mainly depends on the features of aptamers (e.g., length of the affinity oligonucleotide) and pH of

the reaction medium [109]. LoD is another critical parameter for portable and point-of-care biosensors and represents the lowest quantity of the target molecules that the sensor can distinguish from blank response [110]. The reported limits of detection in label-free electrochemical aptasensors are considerably higher compared to optical aptasensors for the same targets. As an example, the label-free electrochemical aptasensor for VGEF developed by Han et al. has the LoD of 30 nmol/L [111], while optical VGEF aptasensors have an extremely low LoD such as 3 aM achieved by surface-enhanced Raman scattering based immunoassays [31]. Stability, as another critical performance parameter, is acceptably high for sufficiently long storage times in the reviewed label-free electrochemical cancer aptasensors studies. For instance, Wen et al. reported stability of 93.75% for MUC-1 aptasensor in 4 weeks period of time [23], and Argoubi et al. reported stability of 98% for PSA aptasensor after 30 days storage [42]. Last but not least, the majority of the reviewed.

Label-free electrochemical cancer aptasensors exhibited wider linear response ranges compared to optical cancer aptasensors for the same targets, which makes them practically useful for clinical and point-of-care applications. Table 2.3 presents the recent studies in label-free electrochemical cancer aptasensors.

2.1.3.2 Label-free Electrochemical Cancer Aptasensors Based on Cell Detection

The establishment of a technique free from complicated purification and sample preparation procedures would represent a significant breakthrough in the development of aptasensors for whole-cell cancer detection. Different types of cancer cells such as hepatocellular (liver cancer cells) [61], HCT 116, HT 29 and HEP-2 cell lines (colon cancer) carcinoma [124], K562 leukemia cancer cells, and SW620 colorectal carcinoma

cells [111] have been detected by using label-free electrochemical aptasensors. The most commonly-used detecting strategy in cell-based label-free electrochemical cancer aptasensors is the successful specific capture of the cells on the surface of electrodes. Depending on the selected measurement method, the captured cell would either block the direct access of the redox species or would change the surface capacitance, resulting in a change in the impedance of the sensing probe. Hence, EIS has been extensively exploited as a noninvasive measurement technique for the investigation of living cells; since living cells exhibit exceptional dielectric characteristics at different frequencies [61]. Surface functionalization is an effective way to create a suitable and stable linkage between aptamers and cells. Different configurations, such as covalent binding based on the last segment of the designed aptamer and compositing with nanomaterials or polymers, are reported in recent works. For example, label-free impedance cytosensor measures the correlations of the impedance and biological status of the cancer cells at the sensor-cell interface [17]. Recently, highly specific and sensitive peptide-fused phage cytosensors with low LoD and relatively wide linear detection range has been demonstrated [111]. Effectively blocking nonspecific binding is one of the keys to developing high-performance sensing platforms. For example, the excess area on the surfaces of the probes can be blocked by bovine serum albumin to prevent nonspecific bindings [45].

Advanced label-free aptasensors for whole-cell cancer diagnosis exhibit fast reaction/detection time with extremely low LoDs such as 2 cells/mL for K562 leukemia cancer cells [45], 2 cells/mL for CT26 cancer cells [125], and 7 cells/mL for HCT 116, HT 29 and HEP-2 cell lines (colon cancer) [124]. Besides, these advanced aptasensors showed wide dynamic ranges such as $30 – 1 \times 10^6$ cells/mL for circulating tumor cells [126], 1×10^2

– 1×10^7 cells/mL for human liver hepatocellular carcinoma cells [62], and $0 – 5.0 \times 10^4$ cells/mL for K562 leukemia cancer cells [45]. Furthermore, some of the reported label-free electrochemical whole-cell cancer aptasensors are stable for a long period of time. As an example, the label-free electrochemical aptasensor developed by T. A. Mir et al. for detecting lung cancer cells showed 90% stability after 60 days, which is highly promising for clinical applications [127]. Table 2.4 presents a comparison of the recently reported label-free electrochemical aptasensors for direct cancer cell diagnosis.

Table 2.4 Comparison of performance of recent whole cell based label-free electrochemical cancer aptasensors

Target (Cells)	**Sensing Platform**	**Sensing Enhancement**	**Utilized method**	**Detection Linear Range (cells/mL)**	**Limit of Detection (cells/mL)**	**Stability (Stored at 4°C)**	**Ref.**
hepatocellular carcinoma	Au	N/A	EIS	$1 \times 10^2 – 1 \times 10^6$	2	96.3% after 7 days	[61]
Human non-small-cell lung cancer	glassy carbon	self-assembled of 4-([2,2':5',2''- terthiophen]-3'-yl) benzoic acid (TTBA) on AuNPs.	Chronoamperometric	$15 – 1 \times 10^6$	8	90% after 60 days	[127]
HCT 116, HT 29 and HEp-2 (colon cancer)	Au	11-mercaptoundecanoic acid (11-MUA)/modified KCHA10a aptamer.	CV	N/A	7	N/A	[124]
hepatocellular carcinoma	Au	G-quadruplex/hemin/aptamer/horseradish peroxidase/AuNPs	CV / EIS	$1 \times 1\ 0^2 – 1 \times 10^7$	30	N/A	[62]
K562 leukemia cancer	Au	G-quadruplex/DNAzyme	DPV	$14 - 1.4 \times 10^6$	14		[44]
circulating tumor	Au	epithelial cell adhesion molecule (EpCAM)/6-mercapto-1-hexanol interspaces	EIS	$30 – 1 \times 10^6$	10	91.9% after 15 days	[126]
K562 leukemia cancer	Au	graphene–Hemin/Au nano-flowers	CV	$0 – 5.0 \times 10^4$	2	NR	[45]
SW620 colorectal carcinoma	Au	specific peptide-fused phage	CV / EIS	$2.0 \times 10^2 – 2.0 \times 10^8$	79	92.4% after 30 days	[111]
hepatocellular carcinoma	glassy carbon	hybrid nano-electrocatalysts / enzyme / AuNPs	CV / EIS/ DPV	$1 \times 10^2 – 1 \times 10^7$	15	N/A	[63]
MCF-7	Au	AuNPs/graphene oxide hybrid	CV /EIS	$10 – 10^5$	8	N/A	[128]
CT26	graphite screen printed	3-aminopropyltriethoxysilane/ (AuNPs)	CV / EIS	$10 – 1.0 \times 10^5$ (CV) and $1.0 \times 10^5 – 6.0 \times 10^6$ (EIS)	2	98% after 7 days	[125]
Leukemia	carbon screen printed	AuNPs-coated magnetic Fe_3O_4 nanoparticles coated on nitrogen-doped graphene nanosheets	DPV	$10 - 1 \times 10^6$	10	N/A	[129]

hepatocellular carcinoma	PDMS	platinum nanoparticles / AuNPs/indium tin oxide glass	CV / EIS / DPV	$50 – 1 \times 10^6$	15	N/A	[64]
MCF-7	glassy carbon	rGO / AuNPs	CV / EIS / DPV	$50 – 7 \times 10^3$	27	N/A	[130]

2.1.4 Challenges and Future Perspectives

The conducted studies on both biomarker and whole-cell label-free electrochemical cancer aptasensor exhibited promising performances for early and point-of-care cancer diagnosis. However, there is room for improving these types of sensors and make them more feasible for clinical applications. Performance of label-free electrochemical cancer aptasensors can be further enhanced by 1) decreasing LoD of cancer biomarker aptasensors to be in the levels comparable to benchtop methods and optical aptasensors, 2) enhancing the accuracy of the diagnosis by eliminating false negative or positive responses, 3) developing disposable sensing probes, and 4) integrating these aptasensors with MEMS devices and circuits such as microfluidics and lab-on-chips. One of the highly promising approaches for further enhancements of LoD of biomarker-based aptasensor could be the use of carbon-based materials, e.g., single- and multiple-walled carbon nanotubes, doped graphene (nano) sheets, on transduction surfaces. This enhancement can widen the dynamic range and increase sensitivity by enlarging the accessible surface area [131]. Moreover, carbon-based materials have unique electrochemical properties such as excellent conductivity and high stability window during hybridization processes, at elevated temperatures, and during prolonged incubation in aqueous solutions [132]. The recent progress in the carbon-based nanomaterials synthesis methods has improved the electrochemical properties of these materials. For example, the improved synthesizing methods have increased the electron-transfer rate between electrode and recognition

molecules, which can make the carbon-based materials even more suitable for biological applications [133].

Another potential technique to improve label-free biomarker-based cancer aptasensors is subsiding the false-positive responses and misdiagnosis. The established cancer biomarkers and antigens are commonly used to detect several cancer types. For instance, carcinoembryonic antigen has been associated with colorectal, lung, pancreas, liver, breast, and gastric cancers [134]. Hence, multiplexed detection of more specific cancer antigens and biomarkers along with carcinoembryonic antigen can help highly reliable diagnosis. Developing disposable and reliable sensing electrodes is another crucial aspect of label-free electrochemical cancer aptasensor studies. Besides the gold and carbon nanomaterials, other nanomaterials can be used to construct disposable sensitive and selective aptasensors. Various disposable nano-composites have already been developed for cancer immunosensor, which can be adapted for cancer aptasensors. For example, Hong et al. developed a cancer immunosensor for detecting breast cancer antigen (CA 15-3) utilizing using silica nanoparticles doped with ferrocene-carboxylic acid (Fc-COOH) [135]. Likewise, Li et al. developed a thin film composed of cobalt hexacyanoferrate nanoparticles and graphene sheets [136]. Li's studies showed that the presence of the graphene sheet greatly improves the electroactivity of cobalt nanoparticles and the stability of the sensors.

The first attempt to incorporate label-free aptasensors into a standalone compact system, including a signal processing unit, potentiostat, microfluidic channel, and an electrochemical cell, has been reported by A. Tashtoush [137]. This integrated label-free aptasensor is capable of performing precise potentiometry and voltammetry. Furthermore,

Sung-Chi Tsai et al. has recently introduced an “integrated microfluidic system” with magnetic beads for the separation and diagnosis of ovarian circulating cancer cells [138]. Their “integrated microfluidic system” is capable of direct depletion of the white blood cells (WBC) through a reverse selection procedure, the lysis of red blood cells (RBC), and isolation of cancerous target cells from blood samples via aptamer-based sensing probes. The developed lab-on-chip device presents a promising application of the portable system for early diagnosis of different cancers’ cells if the adequate and appropriate aptamers have been used.

By virtue of the well-known advantages of aptamers over antibodies for diagnosis proposes, successful commercialization of the label-free electrochemical cancer aptasensors could be possible by optimizing several factors typically overlooked in the research stage, such as ease of production; cost of manufacturing; stability under mechanical and environmental stress; fabrication failure rate; integration and packaging flexibility; as well as storage requirements. Furthermore, biosensor tests are usually conducted in highly-controlled and contamination-free conditions, and this is particularly true for aptasensors. In light of the potentials and challenges, it is clear that more research needs to be devoted before commercial aptasensors become readily available.

2.1.5 Conclusion

This chapter provided an extensive review of cancer aptasensors presenting their principles of operation for different types, the current state of the art, challenges, and future perspectives. The advantages that label-free cancer aptasensors offer over optical and labeled electrochemical cancer aptasensors make them highly favorable for lab-on-chip

and portable clinical applications. Label-free electrochemical cancer aptasensors are discussed in two major groups based on the nature of their targets. For biomarker-based label-free electrochemical cancer aptasensors, voltammetry techniques are mainly utilized, while EIS methods are more useful for the whole-cell label-free electrochemical cancer aptasensors. The majority of the label-free electrochemical cancer aptasensors are acceptably sensitive, fast, and adequately stable for many clinical applications. Addressing the discussed challenges would allow label-free electrochemical cancer aptasensors to be widely adopted for clinical use and contribute to the early detection of cancer.

2.1.6 References

[1] A. D. Keefe, S. Pai, and A. Ellington, "Aptamers as therapeutics," Nature reviews Drug discovery, vol. 9, pp. 537-550, 2010.

[2] K. L. Hong and L. J. Sooter, "Single-stranded DNA aptamers against pathogens and toxins: identification and biosensing applications," BioMed research international, vol. 2015, pp. 31-62, 2015.

[3] H. Sun and Y. Zu, "A highlight of recent advances in aptamer technology and its application," Molecules, vol. 20, pp. 11959-11980, 2015.

[4] P. K Tsae and M. C DeRosa, "Outlook for aptamers after twenty five years," Current topics in medicinal chemistry, vol. 15, pp. 1153-1159, 2015.

[5] C. A. Stein and D. Castanotto, "FDA-approved oligonucleotide therapies in 2017," Molecular Therapy, vol. 25, pp. 1069-1075, 2017.

[6] E. Walz, V. Gräf, and R. Greiner, "Potential Economic Impact of Engineered Nanomaterials in Agriculture and the Food Sector," Nanotechnology in Agriculture and Food Science, 2017.

[7] M. D. Forecast. (2019). North America Aptamers Market Research Report. Available: https://www.marketdataforecast.com/market-reports/north-america-aptamers-market

[8] C. Tsé, A.-S. Gauchez, W. Jacot, and P.-J. Lamy, "HER2 shedding and serum HER2 extracellular domain: biology and clinical utility in breast cancer," Cancer treatment reviews, vol. 38, pp. 133-142, 2012.

[9] L. Cao, L. Cheng, Z. Zhang, Y. Wang, X. Zhang, H. Chen, et al., "Visual and high-throughput detection of cancer cells using a graphene oxide-based FRET aptasensing microfluidic chip," Lab on a Chip, vol. 12, pp. 4864-4869, 2012.

[10] G. S. Zamay, T. I. Ivanchenko, T. N. Zamay, V. L. Grigorieva, Y. E. Glazyrin, O. S. Kolovskaya, et al., "DNA aptamers for the characterization of histological structure of lung adenocarcinoma," Molecular Therapy-Nucleic Acids, vol. 6, pp. 150-162, 2017.

[11] S.-C. Chiang, C.-L. Han, K.-H. Yu, Y.-J. Chen, and K.-P. Wu, "Prioritization of cancer marker candidates based on the immunohistochemistry staining images deposited in the human protein atlas," PloS one, vol. 8, p. e81079, 2013.

[12] L. Su, C.-C. Fong, P.-Y. Cheung, and M. Yang, "Development of novel piezoelectric biosensor using pzt ceramic resonator for detection of cancer markers," in Biosensors and biodetection, ed: Springer, 2017, pp. 277-291.

[13] S. Sugumaran, M. F. Jamlos, M. N. Ahmad, C. S. Bellan, and D. Schreurs, "Nanostructured materials with plasmonic nanobiosensors for early cancer detection: a past and future prospect," Biosensors and Bioelectronics, vol. 100, pp. 361-373, 2018.

[14] L. Xiao, A. Zhu, Q. Xu, Y. Chen, J. Xu, and J. Weng, "Colorimetric biosensor for detection of cancer biomarker by au nanoparticle-decorated Bi2Se3 nanosheets," ACS applied materials & interfaces, vol. 9, pp. 6931-6940, 2017.

[15] J. C. Soares, A. C. Soares, V. C. Rodrigues, M. E. Melendez, A. C. Santos, E. F. Faria, et al., "Detection of the prostate cancer biomarker PCA3 with electrochemical and impedance-based biosensors," ACS applied materials & interfaces, vol. 11, pp. 46645-46650, 2019.

[16] P. Kumar, V. Narwal, R. Jaiwal, and C. Pundir, "Construction and application of amperometric sarcosine biosensor based on SOxNPs/AuE for determination of prostate cancer," Biosensors and bioelectronics, vol. 122, pp. 140-146, 2018.

[17] M. Oguzhan Caglayan, "Electrochemical Aptasensors for Early Cancer Diagnosis: A Review," Current Analytical Chemistry, vol. 13, pp. 18-30, 2017.

[18] A. D. Ellington and J. W. Szostak, "In vitro selection of RNA molecules that bind specific ligands," nature, vol. 346, p. 818, 1990.

[19] I. Willner and M. Zayats, "Electronic aptamer-based sensors," Angewandte Chemie International Edition, vol. 46, pp. 6408-6418, 2007.

[20] H. Jo, J. Her, and C. Ban, "Dual aptamer-functionalized silica nanoparticles for the highly sensitive detection of breast cancer," Biosensors and Bioelectronics, vol. 71, pp. 129-136, 2015.

[21] S. K. Arya, P. Zhurauski, P. Jolly, M. R. Batistuti, M. Mulato, and P. Estrela, "Capacitive aptasensor based on interdigitated electrode for breast cancer detection in undiluted human serum," Biosensors and Bioelectronics, vol. 102, pp. 106-112, 2018.

[22] J. F. Lee, J. R. Hesselberth, L. A. Meyers, and A. D. Ellington, "Aptamer database," Nucleic acids research, vol. 32, pp. D95-D100, 2004.

[23] W. Wen, R. Hu, T. Bao, X. Zhang, and S. Wang, "An insertion approach electrochemical aptasensor for mucin 1 detection based on exonuclease-assisted target recycling," Biosensors and Bioelectronics, vol. 71, pp. 13-17, 2015.

[24] X. Liu, Y. Qin, C. Deng, J. Xiang, and Y. Li, "A simple and sensitive impedimetric aptasensor for the detection of tumor markers based on gold nanoparticles signal amplification," Talanta, vol. 132, pp. 150-154, 2015.

[25] A. Qureshi, Y. Gurbuz, and J. H. Niazi, "Label-free capacitance based aptasensor platform for the detection of HER2/ErbB2 cancer biomarker in serum," Sensors and Actuators B: Chemical, vol. 220, pp. 1145-1151, 2015.

[26] H. Cho, E.-C. Yeh, R. Sinha, T. A. Laurence, J. P. Bearinger, and L. P. Lee, "Single-step nanoplasmonic VEGF165 aptasensor for early cancer diagnosis," ACS nano, vol. 6, pp. 7607-7614, 2012.

[27] S.-E. Wang, Y. Huang, K. Hu, J. Tian, and S. Zhao, "A highly sensitive and selective aptasensor based on fluorescence polarization for the rapid determination of oncoprotein vascular endothelial growth factor (VEGF)," Analytical Methods, vol. 6, pp. 62-66, 2014.

[28] R. Freeman, J. Girsh, A. Fang-ju Jou, J.-a. A. Ho, T. Hug, J. Dernedde, et al., "Optical aptasensors for the analysis of the vascular endothelial growth factor (VEGF)," Analytical chemistry, vol. 84, pp. 6192-6198, 2012.

[29] H. Chen, Y. Hou, F. Qi, J. Zhang, K. Koh, Z. Shen, et al., "Detection of vascular endothelial growth factor based on rolling circle amplification as a means of signal enhancement in surface plasmon resonance," Biosensors and Bioelectronics, vol. 61, pp. 83-87, 2014.

[30] S. Zhao, W. Ma, L. Xu, X. Wu, H. Kuang, L. Wang, et al., "Ultrasensitive SERS detection of VEGF based on a self-assembled Ag ornamented–AU pyramid superstructure," Biosensors and Bioelectronics, vol. 68, pp. 593-597, 2015.

[31] J. Ko, S. Lee, E. K. Lee, S.-I. Chang, L. Chen, S.-Y. Yoon, et al., "SERS-based immunoassay of tumor marker VEGF using DNA aptamers and silica-encapsulated hollow gold nanospheres," Physical Chemistry Chemical Physics, vol. 15, pp. 5379-5385, 2013.

[32] E. R. Billinge and M. Platt, "Multiplexed, label-free detection of biomarkers using aptamers and Tunable Resistive Pulse Sensing (AptaTRPS)," Biosensors and Bioelectronics, vol. 68, pp. 741-748, 2015.

[33] M. A. Tabrizi, M. Shamsipur, and L. Farzin, "A high sensitive electrochemical aptasensor for the determination of VEGF165 in serum of lung cancer patient," Biosensors and Bioelectronics, vol. 74, pp. 764-769, 2015.

[34] Y. Wei, W. Zhou, J. Liu, Y. Chai, Y. Xiang, and R. Yuan, "Label-free and homogeneous aptamer proximity binding assay for fluorescent detection of protein biomarkers in human serum," Talanta, vol. 141, pp. 230-234, 2015.

[35] C.-W. Wang and H.-T. Chang, "Sensitive detection of platelet-derived growth factor through surface-enhanced Raman scattering," Analytical chemistry, vol. 86, pp. 7606-7611, 2014.

[36] S. Ye, X. Zhai, Y. Wu, and S. Kuang, "Dual-primer self-generation SERS signal amplification assay for PDGF-BB using label-free aptamer," Biosensors and Bioelectronics, vol. 79, pp. 130-135, 2016.

[37] J. Gao, H. Xiong, W. Zhang, Y. Wang, H. Wang, W. Wen, et al., "Electrochemiluminescent aptasensor based on β-cyclodextrin/graphitic carbon nitride composite for highly selective and ultrasensitive assay of platelet derived growth factor BB," Carbon, 2018.

[38] P. Jolly, N. Formisano, J. Tkáč, P. Kasák, C. G. Frost, and P. Estrela, "Label-free impedimetric aptasensor with antifouling surface chemistry: A prostate specific antigen case study," Sensors and Actuators B: Chemical, vol. 209, pp. 306-312, 2015.

[39] P. Jolly, V. Tamboli, R. L. Harniman, P. Estrela, C. J. Allender, and J. L. Bowen, "Aptamer–MIP hybrid receptor for highly sensitive electrochemical detection of prostate specific antigen," Biosensors and Bioelectronics, vol. 75, pp. 188-195, 2016.

[40] E. Heydari-Bafrooei and N. S. Shamszadeh, "Electrochemical bioassay development for ultrasensitive aptasensing of prostate specific antigen," Biosensors and Bioelectronics, vol. 91, pp. 284-292, 2017.

[41] J. Zhao and Z. Ma, "Ultrasensitive detection of prostate specific antigen by electrochemical aptasensor using enzyme-free recycling amplification via target-induced catalytic hairpin assembly," Biosensors and Bioelectronics, vol. 102, pp. 316-320, 2018.

[42] W. Argoubi, A. Sánchez, C. Parrado, N. Raouafi, and R. Villalonga, "Label-free electrochemical aptasensing platform based on mesoporous silica thin film for the detection of prostate specific antigen," Sensors and Actuators B: Chemical, vol. 255, pp. 309-315, 2018.

[43] M. Zhang, H. Liu, L. Chen, M. Yan, L. Ge, S. Ge, et al., "A disposable electrochemiluminescence device for ultrasensitive monitoring of K562 leukemia cells based on aptamers and ZnO@ carbon quantum dots," Biosensors and Bioelectronics, vol. 49, pp. 79-85, 2013.

[44] C.-Y. Lu, J.-J. Xu, Z.-H. Wang, and H.-Y. Chen, "A novel signal-amplified electrochemical aptasensor based on supersandwich G-quadruplex DNAzyme for highly sensitive cancer cell detection," Electrochemistry Communications, vol. 52, pp. 49-52, 2015.

[45] J. Liu, M. Cui, L. Niu, H. Zhou, and S. Zhang, "Enhanced Peroxidase-Like Properties of Graphene–Hemin-Composite Decorated with Au Nanoflowers as Electrochemical Aptamer Biosensor for the Detection of K562 Leukemia Cancer Cells," Chemistry-A European Journal, vol. 22, pp. 18001-18008, 2016.

[46] Y. Hu, L. Li, and L. Guo, "The sandwich-type aptasensor based on gold nanoparticles/DNA/magnetic beads for detection of cancer biomarker protein AGR2," Sensors and Actuators B: Chemical, vol. 209, pp. 846-852, 2015.

[47] H. Ilkhani, M. Sarparast, A. Noori, S. Z. Bathaie, and M. F. Mousavi, "Electrochemical aptamer/antibody based sandwich immunosensor for the detection of EGFR, a cancer biomarker, using gold nanoparticles as a signaling probe," Biosensors and Bioelectronics, vol. 74, pp. 491-497, 2015.

[48] Z. Chen, C. Zhang, X. Li, H. Ma, C. Wan, K. Li, et al., "Aptasensor for electrochemical sensing of angiogenin based on electrode modified by cationic polyelectrolyte-functionalized graphene/gold nanoparticles composites," Biosensors and Bioelectronics, vol. 65, pp. 232-237, 2015.

[49] Z. Liu, Y. Wang, Y. Guo, and C. Dong, "Label-free Electrochemical Aptasensor for Carcino-embryonic Antigen Based on Ternary Nanocomposite of Gold

Nanoparticles, Hemin and Graphene," Electroanalysis, vol. 28, pp. 1023-1028, 2016.

[50] P. Wang, Y. Wan, S. Deng, S. Yang, Y. Su, C. Fan, et al., "Aptamer-initiated on-particle template-independent enzymatic polymerization (aptamer-OTEP) for electrochemical analysis of tumor biomarkers," Biosensors and Bioelectronics, vol. 86, pp. 536-541, 2016.

[51] H. Cheng, L. Xu, H. Zhang, A. Yu, and G. Lai, "Enzymatically catalytic signal tracing by a glucose oxidase and ferrocene dually functionalized nanoporous gold nanoprobe for ultrasensitive electrochemical measurement of a tumor biomarker," Analyst, vol. 141, pp. 4381-4387, 2016.

[52] Z. Si, B. Xie, Z. Chen, C. Tang, T. Li, and M. Yang, "Electrochemical aptasensor for the cancer biomarker CEA based on aptamer induced current due to formation of molybdophosphate," Microchimica Acta, vol. 184, pp. 3215-3221, 2017.

[53] Q.-L. Wang, H.-F. Cui, X. Song, S.-F. Fan, L.-L. Chen, M.-M. Li, et al., "A label-free and lectin-based sandwich aptasensor for detection of carcinoembryonic antigen," Sensors and Actuators B: Chemical, vol. 260, pp. 48-54, 2018.

[54] P. Jolly, A. Miodek, D.-K. Yang, L.-C. Chen, M. D. Lloyd, and P. Estrela, "Electro-engineered polymeric films for the development of sensitive aptasensors for prostate cancer marker detection," ACS Sensors, vol. 1, pp. 1308-1314, 2016.

[55] X. Miao, Z. Li, A. Zhu, Z. Feng, J. Tian, and X. Peng, "Ultrasensitive electrochemical detection of protein tyrosine kinase-7 by gold nanoparticles and methylene blue assisted signal amplification," Biosensors and Bioelectronics, vol. 83, pp. 39-44, 2016.

[56] L. Wu, P. Qi, X. Fu, H. Liu, J. Li, Q. Wang, et al., "A novel electrochemical PCB77-binding DNA aptamer biosensor for selective detection of PCB77," Journal of Electroanalytical Chemistry, vol. 771, pp. 45-49, 2016.

[57] L. Wu, X. Lu, X. Fu, L. Wu, and H. Liu, "Gold Nanoparticles dotted Reduction Graphene Oxide Nanocomposite Based Electrochemical Aptasensor for Selective, Rapid, Sensitive and Congener-Specific PCB77 Detection," Scientific reports, vol. 7, p. 5191, 2017.

[58] V. Stepanova, D. Shurpik, V. Evtugyn, I. Stoikov, G. Evtugyn, Y. N. Osin, et al., "Label-free electrochemical aptasensor for cytochrome c detection using pillar [5] arene bearing neutral red," Sensors and Actuators B: Chemical, vol. 225, pp. 57-65, 2016.

[59] S. Wang, L. Zhang, S. Wan, S. Cansiz, C. Cui, Y. Liu, et al., "Aptasensor with expanded nucleotide using DNA nanotetrahedra for electrochemical detection of cancerous exosomes," ACS nano, vol. 11, pp. 3943-3949, 2017.

[60] H. Dong, H. Chen, J. Jiang, H. Zhang, C. Cai, and Q. Shen, "Highly Sensitive Electrochemical Detection of Tumor Exosomes Based on Aptamer Recognition-Induced Multi-DNA Release and Cyclic Enzymatic Amplification," Analytical chemistry, vol. 90, pp. 4507-4513, 2018.

[61] L. Kashefi-Kheyrabadi, M. A. Mehrgardi, E. Wiechec, A. P. Turner, and A. Tiwari, "Ultrasensitive detection of human liver hepatocellular carcinoma cells using a label-free aptasensor," Analytical chemistry, vol. 86, pp. 4956-4960, 2014.

[62] D. Sun, J. Lu, Z. Chen, Y. Yu, and M. Mo, "A repeatable assembling and disassembling electrochemical aptamer cytosensor for ultrasensitive and highly selective detection of human liver cancer cells," Analytica chimica acta, vol. 885, pp. 166-173, 2015.

[63] D. Sun, J. Lu, Y. Zhong, Y. Yu, Y. Wang, B. Zhang, et al., "Sensitive electrochemical aptamer cytosensor for highly specific detection of cancer cells based on the hybrid nanoelectrocatalysts and enzyme for signal amplification," Biosensors and Bioelectronics, vol. 75, pp. 301-307, 2016.

[64] Y. Jiang, D. Sun, Z. Liang, L. Chen, Y. Zhang, and Z. Chen, "Label-free and competitive aptamer cytosensor based on layer-by-layer assembly of DNA-platinum nanoparticles for ultrasensitive determination of tumor cells," Sensors and Actuators B: Chemical, vol. 262, pp. 35-43, 2018.

[65] W. A. Pieken, D. B. Olsen, F. Benseler, H. Aurup, and F. Eckstein, "Kinetic characterization of ribonuclease-resistant 2'-modified hammerhead ribozymes," Science, vol. 253, pp. 314-317, 1991.

[66] K. A. Davis, B. Abrams, Y. Lin, and S. D. Jayasena, "Use of a high affinity DNA ligand in flow cytometry," Nucleic acids research, vol. 24, pp. 702-706, 1996.

[67] R. E Wang, Y. Zhang, J. Cai, W. Cai, and T. Gao, "Aptamer-based fluorescent biosensors," Current medicinal chemistry, vol. 18, pp. 4175-4184, 2011.

[68] J. Ping, Y. Zhou, Y. Wu, V. Papper, S. Boujday, R. S. Marks, et al., "Recent advances in aptasensors based on graphene and graphene-like nanomaterials," Biosensors and Bioelectronics, vol. 64, pp. 373-385, 2015.

[69] R. G. Hill, Drug Discovery and Development-E-Book: Technology in Transition: Elsevier Health Sciences, 2012.

[70] G. De Angelis, H. G. Rittenhouse, S. D. Mikolajczyk, L. B. Shamel, and A. Semjonow, "Twenty years of PSA: from prostate antigen to tumor marker," Reviews in urology, vol. 9, p. 113, 2007.

[71] B. Zhao, P. Wu, H. Zhang, and C. Cai, "Designing activatable aptamer probes for simultaneous detection of multiple tumor-related proteins in living cancer cells," Biosensors and Bioelectronics, vol. 68, pp. 763-770, 2015.

[72] J. De Bono, S. Y. Rha, J. Stephenson, B. Schultes, P. Monroe, G. Eckhardt, et al., "Phase I trial of a murine antibody to MUC1 in patients with metastatic cancer: evidence for the activation of humoral and cellular antitumor immunity," Annals of oncology, vol. 15, pp. 1825-1833, 2004.

[73] T. B. Wang, Z. G. Chen, X. Q. Wei, B. Wei, and W. G. Dong, "Serum vascular endothelial growth factor-C and lymphoangiogenesis are associated with the lymph node metastasis and prognosis of patients with colorectal cancer," ANZ journal of surgery, vol. 81, pp. 694-699, 2011.

[74] Y. Ma, B. Liu, B. Yuan, J. Wang, H. Yu, Y. Zhang, et al., "Sustained high level of serum VEGF at convalescent stage contributes to the renal recovery after HTNV infection in patients with hemorrhagic fever with renal syndrome," Clinical and Developmental Immunology, vol. 2012, 2012.

[75] S. Kondo, H. Ueno, J. Hashimoto, C. Morizane, F. Koizumi, T. Okusaka, et al., "Circulating endothelial cells and other angiogenesis factors in pancreatic carcinoma patients receiving gemcitabine chemotherapy," BMC cancer, vol. 12, p. 268, 2012.

[76] Y. Wang, H. Li, and D. Xu, "Aptamers-based sandwich assay for silver-enhanced fluorescence multiplex detection," Analytica chimica acta, vol. 905, pp. 149-155, 2016.

[77] L. Guo and Q. Zhao, "Thrombin-linked aptamer assay for detection of platelet derived growth factor BB on magnetic beads in a sandwich format," Talanta, vol. 158, pp. 159-164, 2016.

[78] K. Lee, A. Nojoomi, J. Jeon, C. Y. Lee, and K. Yum, "Near-Infrared Fluorescence Modulation of Refolded DNA Aptamer-Functionalized Single-Walled Carbon Nanotubes for Optical Sensing," ACS Applied Nano Materials, vol. 1, pp. 5327-5336, 2018.

[79] X. Zhang, K. Xiao, L. Cheng, H. Chen, B. Liu, S. Zhang, et al., "Visual and highly sensitive detection of cancer cells by a colorimetric aptasensor based on cell-triggered cyclic enzymatic signal amplification," Analytical chemistry, vol. 86, pp. 5567-5572, 2014.

[80] C. D. Medley, J. E. Smith, Z. Tang, Y. Wu, S. Bamrungsap, and W. Tan, "Gold nanoparticle-based colorimetric assay for the direct detection of cancerous cells," Analytical chemistry, vol. 80, pp. 1067-1072, 2008.

[81] S. Ghosh, D. Datta, S. Chaudhry, M. Dutta, and M. A. Stroscio, "Rapid Detection of Tumor Necrosis Factor-Alpha Using Quantum Dot-Based Optical Aptasensor," IEEE transactions on nanobioscience, vol. 17, pp. 417-423, 2018.

[82] E. Papadopoulou, G. Tripsianis, K. Anagnostopoulos, I. Tentes, S. Kakolyris, G. Galazios, et al., "Significance of serum tumor necrosis factor-alpha and its combination with HER-2 codon 655 polymorphism in the diagnosis and prognosis of breast cancer," The International journal of biological markers, vol. 25, pp. 126-135, 2010.

[83] Y. Li, H. J. Lee, and R. M. Corn, "Detection of protein biomarkers using RNA aptamer microarrays and enzymatically amplified surface plasmon resonance imaging," Analytical chemistry, vol. 79, pp. 1082-1088, 2007.

[84] C. Liu, T. Lei, K. Ino, T. Matsue, N. Tao, and C.-Z. Li, "Real-time monitoring biomarker expression of carcinoma cells by surface plasmon resonance biosensors," Chemical Communications, vol. 48, pp. 10389-10391, 2012.

[85] K. Yang, Y. Hu, N. Dong, G. Zhu, T. Zhu, and N. Jiang, "A novel SERS-based magnetic aptasensor for prostate specific antigen assay with high sensitivity," Biosensors and Bioelectronics, vol. 94, pp. 286-291, 2017.

[86] V. Kulasingam and E. P. Diamandis, "Strategies for discovering novel cancer biomarkers through utilization of emerging technologies," Nature clinical practice Oncology, vol. 5, pp. 588-599, 2008.

[87] A. Syahir, K. Usui, K.-y. Tomizaki, K. Kajikawa, and H. Mihara, "Label and label-free detection techniques for protein microarrays," Microarrays, vol. 4, pp. 228-244, 2015.

[88] H.-C. Chen, J.-T. Qiu, F.-L. Yang, Y.-C. Liu, M.-C. Chen, R.-Y. Tsai, et al., "Magnetic-composite-modified polycrystalline silicon nanowire field-effect transistor for vascular endothelial growth factor detection and cancer diagnosis," Analytical chemistry, vol. 86, pp. 9443-9450, 2014.

[89] Z. Lv, K. Wang, and X. Zhang, "A new electrochemical aptasensor for the analysis of the vascular endothelial growth factor," Journal of Immunoassay and Immunochemistry, vol. 35, pp. 233-240, 2014.

[90] Y. Zhu, H. Wang, L. Wang, J. Zhu, and W. Jiang, "Cascade signal amplification based on copper nanoparticle-reported rolling circle amplification for ultrasensitive electrochemical detection of the prostate cancer biomarker," ACS applied materials & interfaces, vol. 8, pp. 2573-2581, 2016.

[91] N. Bahner, P. Reich, D. Frense, M. Menger, K. Schieke, and D. Beckmann, "An aptamer-based biosensor for detection of doxorubicin by electrochemical impedance spectroscopy," Analytical and bioanalytical chemistry, vol. 410, pp. 1453-1462, 2018.

[92] E. Laborda, J. González, and Á. Molina, "Recent advances on the theory of pulse techniques: A mini review," Electrochemistry communications, vol. 43, pp. 25-30, 2014.

[93] A. J. Bard, L. R. Faulkner, J. Leddy, and C. G. Zoski, Electrochemical methods: fundamentals and applications vol. 2: wiley New York, 1980.

[94] E. Barsoukov and J. R. Macdonald, Impedance spectroscopy: theory, experiment, and applications: John Wiley & Sons, 2018.

[95] D. Kozak, W. Anderson, R. Vogel, and M. Trau, "Advances in resistive pulse sensors: devices bridging the void between molecular and microscopic detection," Nano Today, vol. 6, pp. 531-545, 2011.

[96] E. R. Billinge, M. Broom, and M. Platt, "Monitoring aptamer–protein interactions using tunable resistive pulse sensing," Analytical chemistry, vol. 86, pp. 1030-1037, 2014.

[97] L. Tian, J. Qi, K. Qian, O. Oderinde, Q. Liu, C. Yao, et al., "Copper (II) oxide nanozyme based electrochemical cytosensor for high sensitive detection of circulating tumor cells in breast cancer," Journal of Electroanalytical Chemistry, vol. 812, pp. 1-9, 2018.

[98] J. S. Daniels and N. Pourmand, "Label-free impedance biosensors: Opportunities and challenges," Electroanalysis: An International Journal Devoted to Fundamental and Practical Aspects of Electroanalysis, vol. 19, pp. 1239-1257, 2007.

[99] J.-G. Guan, Y.-Q. Miao, and Q.-J. Zhang, "Impedimetric biosensors," Journal of bioscience and bioengineering, vol. 97, pp. 219-226, 2004.

[100] M. A. Tabrizi, M. Shamsipur, and L. Farzin, "A high sensitive electrochemical aptasensor for the determination of VEGF 165 in serum of lung cancer patient," Biosensors and Bioelectronics, vol. 74, pp. 764-769, 2015.

[101] S. Vogt, Q. Su, C. Gutiérrez-Sánchez, and G. Nöll, "Critical view on electrochemical impedance spectroscopy using the ferri/ferrocyanide redox couple at gold electrodes," Analytical chemistry, vol. 88, pp. 4383-4390, 2016.

[102] J.-Y. Park and S.-M. Park, "DNA hybridization sensors based on electrochemical impedance spectroscopy as a detection tool," Sensors, vol. 9, pp. 9513-9532, 2009.

[103] M. Shamsipur, L. Farzin, M. A. Tabrizi, and F. Molaabasi, "Highly sensitive label free electrochemical detection of VGEF165 tumor marker based on “signal off” and “signal on” strategies using an anti-VEGF165 aptamer immobilized BSA-gold nanoclusters/ionic liquid/glassy carbon electrode," Biosensors and Bioelectronics, vol. 74, pp. 369-375, 2015.

[104] A. Benvidi, M. Banaei, M. D. Tezerjani, H. Molahosseini, and S. Jahanbani, "Impedimetric PSA aptasensor based on the use of a glassy carbon electrode modified with titanium oxide nanoparticles and silk fibroin nanofibers," Microchimica Acta, vol. 185, p. 50, 2018.

[105] Z. Zhang, C. Guo, S. Zhang, L. He, M. Wang, D. Peng, et al., "Carbon-based nanocomposites with aptamer-templated silver nanoclusters for the highly sensitive and selective detection of platelet-derived growth factor," Biosensors and Bioelectronics, vol. 89, pp. 735-742, 2017.

[106] M. Hasanzadeh, N. Razmi, A. Mokhtarzadeh, N. Shadjou, and S. Mahboob, "Aptamer based assay of plated-derived grow factor in unprocessed human plasma sample and MCF-7 breast cancer cell lysates using gold nanoparticle supported α-cyclodextrin," International journal of biological macromolecules, vol. 108, pp. 69-80, 2018.

[107] Y. Chang, M. Li, Z. Wu, Y. Zhuo, Y. Chai, Q. Xiao, et al., "Homogeneous Entropy Catalytic-Driven DNA Hydrogel as Strong Signal Blocker for Highly Sensitive Electrochemical Detection of Platelet-Derived Growth Factor," Analytical chemistry, vol. 90, pp. 8241-8247, 2018.

[108] A. Lewandowski, P. Jakobczyk, M. Galinski, and M. Biegun, "Self-discharge of electrochemical double layer capacitors," Physical Chemistry Chemical Physics, vol. 15, pp. 8692-8699, 2013.

[109] M. R. Battig and Y. Wang, "Nucleic acid aptamers for biomaterials development," in Natural and Synthetic Biomedical Polymers, ed: Elsevier, 2014, pp. 287-299.

[110] A. D. McNaught and A. D. McNaught, Compendium of chemical terminology vol. 1669: Blackwell Science Oxford, 1997.

[111] L. Han, P. Liu, V. A. Petrenko, and A. Liu, "A label-free electrochemical impedance cytosensor based on specific peptide-fused phage selected from landscape phage library," Scientific reports, vol. 6, p. 22199, 2016.

[112] K. S. Asgeirsson, A. Agrawal, C. Allen, A. Hitch, I. O. Ellis, C. Chapman, et al., "Serum epidermal growth factor receptor and HER2 expression in primary and metastatic breast cancer patients," Breast Cancer Research, vol. 9, p. R75, 2007.

[113] M. Souada, B. Piro, S. Reisberg, G. Anquetin, V. Noël, and M. Pham, "Label-free electrochemical detection of prostate-specific antigen based on nucleic acid aptamer," Biosensors and Bioelectronics, vol. 68, pp. 49-54, 2015.

[114] C. Ibau, M. M. Arshad, S. C. Gopinath, M. Nuzaihan, M. Fathil, and P. Estrela, "Gold interdigitated triple-microelectrodes for label-free prognosticative aptasensing of prostate cancer biomarker in serum," Biosensors and Bioelectronics, vol. 136, pp. 118-127, 2019.

[115] R. H. Fletcher, "Carcinoembryonic antigen," Annals of internal medicine, vol. 104, pp. 66-73, 1986.

[116] L. A. Gugoasa, R.-I. Stefan-van Staden, A. J. M. Al-Ogaidi, C. Stanciu-Gavan, J. F. van Staden, M.-C. Rosu, et al., "Molecular recognition of colon cancer biomarkers: P53, KRAS and CEA in whole blood samples," Journal of The Electrochemical Society, vol. 164, p. B443, 2017.

[117] Z. Shekari, H. R. Zare, and A. Falahati, "Developing an impedimetric aptasensor for selective label–free detection of CEA as a cancer biomarker based on gold nanoparticles loaded in functionalized mesoporous silica films," Journal of The Electrochemical Society, vol. 164, pp. B739-B745, 2017.

[118] G. S. Zamay, T. N. Zamay, V. A. Kolovskii, A. V. Shabanov, Y. E. Glazyrin, D. V. Veprintsev, et al., "Electrochemical aptasensor for lung cancer-related protein detection in crude blood plasma samples," Scientific reports, vol. 6, p. 34350, 2016.

[119] B. Lauby-Secretan, D. Loomis, Y. Grosse, F. El Ghissassi, V. Bouvard, L. Benbrahim-Tallaa, et al., "Carcinogenicity of polychlorinated biphenyls and polybrominated biphenyls," The Lancet. Oncology, vol. 14, p. 287, 2013.

[120] T. Eleftheriadis, G. Pissas, V. Liakopoulos, and I. Stefanidis, "Cytochrome c as a potentially clinical useful marker of mitochondrial and cellular damage," Frontiers in immunology, vol. 7, p. 279, 2016.

[121] M. Tertiş, B. Ciui, M. Suciu, R. Săndulescu, and C. Cristea, "Label-free electrochemical aptasensor based on gold and polypyrrole nanoparticles for interleukin 6 detection," Electrochimica Acta, vol. 258, pp. 1208-1218, 2017.

[122] A. Khan and Z. Ali, "Normal Ranges for Acute Phase Reactants (Interleukin-6, Tumour Necrosis Factor-alpha and C-reactive Protein) in Umbilical Cord Blood of Healthy Term Neonates at the Mount Hope Women's Hospital, Trinidad," The West Indian Medical Journal, vol. 63, p. 465, 2014.

[123] A. Ravalli, L. Rivas, A. De La Escosura-Muñiz, J. Pons, A. Merkoçi, and G. Marrazza, "A DNA aptasensor for electrochemical detection of vascular endothelial growth factor," Journal of nanoscience and nanotechnology, vol. 15, pp. 3411-3416, 2015.

[124] M. A. Raji, G. Amoabediny, P. Tajik, M. Hosseini, and E. Ghafar-Zadeh, "An Apta-Biosensor for Colon Cancer Diagnostics," Sensors, vol. 15, pp. 22291-22303, 2015.

[125] A. B. Hashkavayi, J. B. Raoof, R. Ojani, and S. Kavoosian, "Ultrasensitive electrochemical aptasensor based on sandwich architecture for selective label-free detection of colorectal cancer (CT26) cells," Biosensors and Bioelectronics, vol. 92, pp. 630-637, 2017.

[126] H. Shen, J. Yang, Z. Chen, X. Chen, L. Wang, J. Hu, et al., "A novel label-free and reusable electrochemical cytosensor for highly sensitive detection and specific collection of CTCs," Biosensors and Bioelectronics, vol. 81, pp. 495-502, 2016.

[127] T. A. Mir, J.-H. Yoon, N. Gurudatt, M.-S. Won, and Y.-B. Shim, "Ultrasensitive cytosensing based on an aptamer modified nanobiosensor with a bioconjugate: Detection of human non-small-cell lung cancer cells," Biosensors and Bioelectronics, vol. 74, pp. 594-600, 2015.

[128] K. Wang, M.-Q. He, F.-H. Zhai, R.-H. He, and Y.-L. Yu, "A novel electrochemical biosensor based on polyadenine modified aptamer for label-free and ultrasensitive detection of human breast cancer cells," Talanta, vol. 166, pp. 87-92, 2017.

[129] S. M. Khoshfetrat and M. A. Mehrgardi, "Amplified detection of leukemia cancer cells using an aptamer-conjugated gold-coated magnetic nanoparticles on a nitrogen-doped graphene modified electrode," Bioelectrochemistry, vol. 114, pp. 24-32, 2017.

[130] L. Tian, J. Qi, K. Qian, O. Oderinde, Q. Liu, C. Yao, et al., "Copper (II) oxide nanozyme based electrochemical cytosensor for high sensitive detection of circulating tumor cells in breast cancer," Journal of Electroanalytical Chemistry, vol. 63, pp. 3680, 2017.

[131] C. Wang and M. Madou, "From MEMS to NEMS with carbon," Biosensors and bioelectronics, vol. 20, pp. 2181-2187, 2005.

[132] J.-H. Yang, V. Penmatsa, S. Tajima, H. Kawarada, and C. Wang, "Direct amination on 3-dimensional pyrolyzed carbon micropattern surface for DNA detection," Materials Letters, vol. 63, pp. 2680-2683, 2009.

[133] A. Thiha, F. Ibrahim, S. Muniandy, I. J. Dinshaw, S. J. Teh, K. L. Thong, et al., "All-carbon suspended nanowire sensors as a rapid highly-sensitive label-free chemiresistive biosensing platform," Biosensors and Bioelectronics, vol. 107, pp. 145-152, 2018.

[134] M. Freitas, H. P. Nouws, and C. Delerue-Matos, "Electrochemical Biosensing in Cancer Diagnostics and Follow-up," Electroanalysis, vol. 633, pp. 244, 2009.

[135] C. Hong, R. Yuan, Y. Chai, and Y. Zhuo, "Ferrocenyl-doped silica nanoparticles as an immobilized affinity support for electrochemical immunoassay of cancer antigen 15-3," Analytica chimica acta, vol. 633, pp. 244-249, 2009.

[136] T. Li, M. Yang, and H. Li, "Label-free electrochemical detection of cancer marker based on graphene–cobalt hexacyanoferrate nanocomposite," Journal of electroanalytical chemistry, vol. 655, pp. 50-55, 2011.

[137] A. Tashtoush, "Fully IC Label-Free Aptasensor with Interdigitated Microelectrodes in Microfluidic Channel," in Modelling Symposium (AMS), 2014 8th Asia, 2014, pp. 124-127.

[138] S.-C. Tsai, L.-Y. Hung, and G.-B. Lee, "An integrated microfluidic system for the isolation and detection of ovarian circulating tumor cells using cell selection and enrichment methods," Biomicrofluidics, vol. 11, p. 034122, 2017.

2.2 Prospect of C-MEMS and C-NEMS technology for Biotech

2.2.1 Introduction

Carbon allotropes have dominated materials science and engineering for several decades due to their unique features making them suitable for a wide variety of applications. The feasibility of carbon-based devices for various biotechnology applications along with various fabrication techniques have been studied and demonstrated extensively. One effective way to synthesize carbon is a top-down manufacturing approach via an organic polymer precursor and pyrolyzing patterning. In the past two decades, a variety of radiation-induced micropatterning techniques have been adopted for polymer-derived carbon patterning. Notable examples include photolithography [6], electron-beam lithography (EBL) [1], nanoimprint lithography [7], and X-ray lithography [20]. These techniques usually include coating a suitable substrate (e.g., silicon wafer), pre- and post-pattering bakes at temperatures below the glass-transition temperatures (T_g), and radiation exposure.

One of the carbon fabrication techniques this chapter focuses on is photoresist derived glass-like carbon (designated here as GC). The micro and nanostructures derived from SU-8 photoresist were the first ones to be commonly referred to as carbon microelectromechanical systems (C-MEMS) and carbon nanoelectromechanical systems (C-NEMS)[25, 26]. SU-8 photoresist has several desirable features: low shrinkage, high adhesion to different substrates, ease of curing and processing, making it a suitable precursor for the top-down fabrication of GC devices[30]. Micro and nanopatterned SU-8 devices are converted to GC using thermochemical decomposition (also known as

pyrolysis). During pyrolysis, the patterned SU-8 devices are heated up to high temperatures above 600°C in an inert atmosphere. The pyrolysis step defines the physico-chemical properties of C-MEMS/C-NEMS, such as microstructure, shrinkage, electrical and thermal conductivity, mechanical stiffness, and chemical reactivity. Therefore, it is crucial to adjust the pyrolysis procedure to achieve the desired intracorporeal for the intended application [33].

Besides the pyrolysis details, the surface of C-MEMS and C-NEMS devices can also be functionalized and activated for different applications, including for electrochemical biosensors, biofuel cells, and micro-supercapacitors. For example, the surface of C-MEMS devices can be directly functionalized with oxidation techniques such as vacuum ultraviolet (VUV) treatment, electrochemical activation (EA), UV/Ozone (UV/O_3), and oxygen reactive ion etching (RIE). Also, surface reduction treatment techniques are available, including direct amination and diazonium grafting [35, 36]. Integration of various nanomaterials such as reduced graphene oxide (rGO)[36, 37], carbon nanotubes (CNTs)[38], zinc oxide (ZnO)[9], and gold nanoparticles (AuNPs)[4] in C-MEMS and C-NEMS devices have been demonstrated to be feasible for developing new types of microdevices with novel properties and applications. Despite the vast potential for C-MEMS/C-NMES based devices, there are only a few commercially available applications. Notably, those are non-biotech applications such as Enevate's lithium-ion batteries (US patent no. US20140170498A1) and capacitive pressure sensors [39]. Here, by focusing specifically on C-MEMS/C-NEMS biotechnology devices, this chapter aims to present the current state of the art for C-MEMS/C-NEMS technology, challenges, and

possible opportunities for further development and commercialization of this class of biotechnology devices.

2.2.2 Fundamentals and Fabrication of C-MEMS and C-NEMS

2.2.2.1 Fundamentals of SU-8 Derived Glassy Carbon

The name glassy-carbon comes from the fact that this material features a smooth, shiny glass-like appearance and a conchoidal fracture. Although the GC structure is amorphous, it cannot be referred to as amorphous carbon since this term is restricted by the International Union of Pure and Applied Physics (IUPAC) to describe carbon materials with localized Π-electrons [40]. The microstructure of GC is yet to be completely understood, but the widely accepted GC microstructural models are consist of either of these two models (1) interconnected graphene ribbons with voids or (2) cage-like graphene structures similar to fullerenes [41, 42]. These models can explain the most experimentally determined characteristics of commercial GC, such as thermal and electrical conductivity, impermeability, and brittleness, but they are inadequate in addressing the microstructural variations in miniaturized GC [41-44]. In terms of GC micro and nanodevices derived from SU-8 precursor, the exact microstructure is known to be affected by pyrolysis parameters, the chemical composition of the precursor, and the forces applied during polymer-patterning [45-47]

GC is highly inert and impermeable to gases and comes with high resilience against corrosive agents such as bromine and strong acids like sulfuric and hydrofluoric[48]. The oxidation rate of GC in carbon dioxide, oxygen, or water vapor is lower than those of any other carbon material, but it can be etched at high temperatures in an oxygen atmosphere.

With a wider electrochemical stability window than platinum and gold, GC is ideal for many electrochemistry experiments [49-52]. The density value of GC is between 1.4 and 1.5 g cm^{-3} [53], compared to 2.3 g cm^{-3} for graphite, suggesting a noticeable degree of porosity. Regarding the GC mechanical properties, its Young's modulus ranges between 10 and 50 GPa and features a hardness of 6 to 7 on Mohs' scale, a value comparable to that of quartz [54]. X-ray diffraction studies have shown that GC presents an extremely small pore size, around 50 Å, of a closed nature [55, 56]. Similar to some borosilicate glasses, GC has a thermal expansion coefficient of $2.2–3.2\times10^{-6}$ K^{-1}. The electric and electronic properties of GC have been extensively reported in the literature [26, 41, 57-59].

The values mentioned above could be considered as an initial reference for most GC materials. However, the material properties of C-MEMS and C-NEMS devices can vary depending on various factors, including but not limited to (1) the pyrolysis parameters, (2) the fabrication type, and (3) geometry and structure of the intended device (e.g., suspended structure vs. thin layer structure)[33, 52, 60]. The effect of some of the general factors such as pyrolysis parameters relevant to biotechnology application is discussed in this chapter.

SU-8 was originally developed in the 1980s by the IBM research center (US patent no. 4882245, 1989). SU-8 is an epoxy resin mainly composed of eight benzene rings and eight epoxy groups having a molecular weight (monomer) of around 7 kDa[61]. SU-8 is a highly sensitive negative tone photoresist that can be patterned via various micro and nanopatterning methods, including conventional photolithography[19, 62], photo nanoimprint lithography[7], EBL[1], X-ray lithography[63], and two-photon polymerization [60].

Furthermore, SU-8 photoresist exists in various viscosities, enabling its deposition with an extraordinary range of thicknesses from hundreds of micrometers to submicron levels. This flexibility of deposition thickness is highly suitable for fabricating high aspect ratio structures using the proper lithography parameters. For instance, Wang et al. reported high aspect ratio C-MEMS devices with a ratio of 100:1[64], and since then, various C-MEMS and C-NEMS devices made this way have been reported. The fabrication of dense 3-dimensional (3D) carbon pillars[62, 65], nano-electrodes [4, 66], nano string resonators [67], suspended nanowires [1, 68], and the integration of carbon electrodes on flexible substrates [2] are some of the milestones achieved. In the following, fabrication of C-MEMS/C-NEMS devices and related technical points are discussed in two major categories based on photolithography or non-photolithography techniques (e.g., X-ray lithography, EBL).

2.2.2.2 Photolithography Based Fabrication

Photolithography of SU-8 photoresist provides a reliable patterning means to fabricate various shapes with an extensive range of dimensions on both hard (i.e., silicon wafer) and flexible substrates (i.e., polyimide). Thus far, various innovative structures such as dense 3D GC micropillars [14, 65], suspended GC structures [13, 68], and nanogap GC [18] devices have been developed based on conventional photolithography. Next, some state-of-art examples of GC structures for biotechnology applications are presented.

2.2.2.2.1 *Fabrication of 3D C-MEMS Structures*

As a deep UV photoresist, SU-8 is a perfect choice to fabricate high aspect ratio structures for various applications, in which it can be used as a mold for pattering (i.e., nanoimprint lithography) or as the primary precursor of GC electrodes. For example, 3D

carbon micropillars mounted on thin-film or interdigitated arrays (IDA) can be modified to act as an active electrode for biosensing and biofuel cells (detailed in section 3.1), as neural probes (detailed in section 3.2), or as lateral flow arrays for cell trapping (detailed

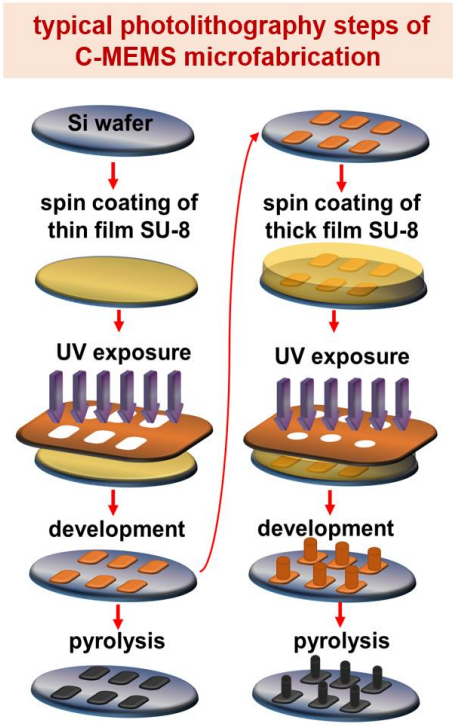

Figure 2.4 Schematic illustration of typical photolithography process for fabrication of 2D and 3D C-MEMS electrodes.

in section 3.3). The schematic illustration of the photolithography process of 2-dimensional (2D) and 3D C-MEMS microelectrodes is represented in Figure 2.4. The fabrication process of high aspect ratio C-MEMS structures typically starts with photopatterning of the base layer (e.g., an IDA electrode) with a thickness between 5-25 µm, followed by the patterning of a second layer on top of the first layer. The developed structure is pyrolyzed under an inert atmosphere at high temperatures above 600°C [27, 64, 69].

2.2.2.2.2 *Effect of Pyrolysis Parameters*

The SU-8 pyrolysis process is a sensitive and essential step in the C-MEMS and C-NEMS fabrication process, and several pyrolysis parameters can directly or indirectly affect the final GC structures. Parameters such as maximum pyrolysis temperature, temperature ramp rate, and type of inert gas (e.g., nitrogen), and flow rate can directly affect the final carbon structures. To achieve high-quality carbon—such as a higher percentage of carbon and a lower percentage of oxygen—the maximum pyrolysis temperature is the most critical parameter. For instance, Pramanick et al. have concluded that 900°C is the optimized temperature for electrochemical sensing applications [33]. Furthermore, the maximum pyrolysis temperature can affect the pore size of GC, in which the increase of maximum pyrolysis temperature decreases the pore size of the material.

Heating ramp or temperature ramp rates affect the quality of carbon by directly affecting the chemical reaction rate at which the bi-products generation and their removal from the structure surface should be optimized. The temperature ramp can also affect the pore size of GC in which in lower temperature rates (i.e., below 10°C min^{-1}), increasing the temperature ramp decreases the pore size while for higher temperature ramps (i.e., above 10°C min^{-1}), increasing the temperature ramp increases the pore size [33]. A ramp rate of 10°C min^{-1} is typically considered as an optimum temperature ramp for electrochemical performances [33, 64].

The inert gas flow rate (e.g., nitrogen gas) should be high enough to keep the furnace atmosphere inert since even a small amount of oxygen can destroy the intended C-MEMS device. The flow rate affects the pore size, percentages of carbon, and electrochemical performance of the pyrolyzed carbon and should be adjusted accordingly

depending on the tube furnace volume. Pramanick et al. reported the gas flow rate of furnace tube volume in liters per minute (volume/min) as an optimum gas flow rate for pyrolysis in which the highest percentage of carbon and optimized electrochemical performance were achieved [6, 33, 48].

Shrinkage of SU-8 devices during pyrolysis is another critical factor that indirectly affects the GC structure, and therefore, should be factored into the process design. The shrinkage of SU-8 structures during pyrolysis strongly depends on pyrolysis parameters and the geometry of the SU-8 precursor. The three controlling parameters for shrinkage are surface area ratio (lateral surface area divided by the top surface area), pyrolysis temperature, and pyrolysis atmosphere [70-72]. However, the specific geometry does not affect the shrinkage of the SU-8 during pyrolysis. For instance, Natu et al. reported that different 3D geometries (cylinder, triangle, and square) with similar surface area ratios had similar shrinkage percentages [70].

2.2.2.2.3 *Fabrication of Flexible C-MEMS*

Critical parameters for intracorporeal neural probes include biocompatibility, high physico-chemical stability, and small footprint area —all can be satisfied by employing C-MEMS technology[73]. Several studies have demonstrated that polyimide-based C-MEMS provide electrochemically stable and biocompatible neural probes with long-term reliability [73-75]. The fabrication process can be summarized into three main steps: (1) standard C-MEMS fabrication process including photolithography and pyrolysis, (2) spin-coating the GC with photosensitive polyimide, and (3) customized steps for adding extra layers of metal traces and bump pads [2, 76].

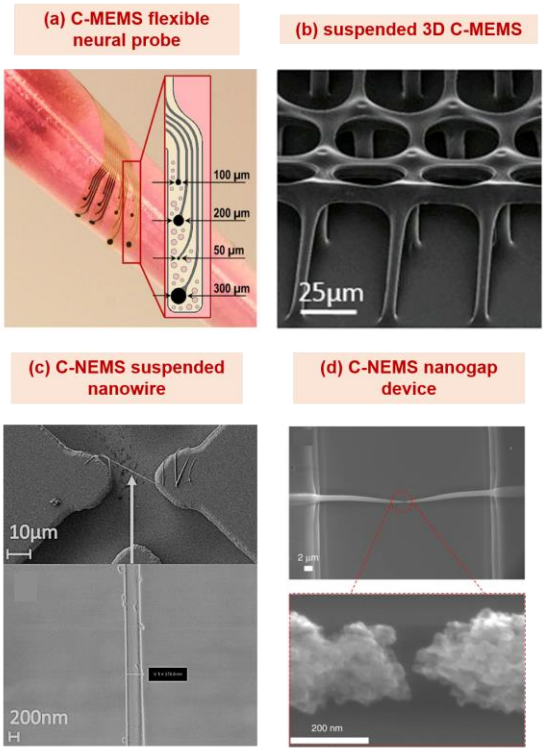

Figure 2.5 (a) A digital image of C-MEMS flexible neural probes mounted on a pipette[2]. (b) SEM cross-section image of suspended 3D C-MEMS microelectrode [8]. (c) SEM images of suspended C-NEMS nanowires [13]. (d) SEM image of C-NEMS nanogap device with nanogap of 20 nm [18]

An example of a flexible C-MEMS neural probe is shown in Figure 2.5a. The low adhesion of gold or platinum on polyimide is one of the more significant challenges for the fabrication of durable implants. An innovation implemented here was replacing the chromium adhesion layer—a standard adhesion layer for gold deposition—with noncytotoxic alternatives such as silicon carbide and diamond-like carbon adhesion promoters. These adhesion promoters enhanced the durability of the electrodes and increased the flexibility of the electrode while also making them less toxic and thus more biocompatible [2].

2.2.2.2.4 *Fabrication of Suspended C-MEMS and C-NEMS*

Suspended carbon structures are another fascinating application of C-MEMS and C-NEMS technology and can be fabricated by photolithography only or photolithography combined with electrospinning of the SU-8 precursor on a 3D C-MEMS supporting structure. Suspended C-MEMS and C-NEMS structures such as nanowires [13, 68, 77], nanoresonators [67], suspended meshes [8, 31], and carbon nanofibers [78] have been demonstrated. These structures with their unique features such as excellent mechanical, electrochemical, and electronic properties, as well as large surface to volume ratio, are of interest for numerous applications, including nanoresonators, nanoelectronics, and micro and nano-biosensors [18, 46, 78].

The fabrication of suspended C-MEMS devices via photolithography starts with the fabrication of 3D high aspect ratio structures with an extra step of ultraviolet (UV) exposure for crosslinking the suspended sections (Figure 2.5b). One of the significant challenges associated with this process is the shrinkage during the pyrolysis. High shrinkage can result in higher residual stress, leading to deformation, delamination, and collapse of the 3D microstructures. Careful design of suspended mesh window size and the radius of the supporting carbon pillars can considerably improve the quality and reproducibility of the intended devices [8].

Another innovative method for the fabrication of suspended structures is combining electrospinning with C-MEMS technology. This technique minimizes production costs while maximizing throughput. Unfortunately, traditional electrospinning in far-field mode is less controllable for precise positioning and controlling the numbers of nanofibers or nanowires deposited on the electrodes compared to synthesizing carbon nanofibers and

nanowires with techniques such as EBL and dip-pen lithography. To overcome this drawback, Bisht et al. adopted electro-mechanical spinning—also known as low-voltage near-field electrospinning—to enhance the positioning accuracy and number control of SU-8 precursor nanofiber deposition [78, 79]. Electro-mechanical spinning provides a more stable and controllable fiber deposition method by: (1) lowering the electrospinning deposition voltage, (2) requiring a smaller distance between the needle and the substrate electrodes, and (3) the use of highly visco-elastic polymer solutions [78, 80]. The fabrication of nanowires is efficiently integrated with the 3D C-MEMS photolithography process. The SU-8 precursor nanofibers can be deposited on C-MEMS micropillars utilizing near field electrospinning and subsequent pyrolysis. An example of suspended C-NEMS nanowires with a width of 200 nm is given in Figure 2.5c. This class of carbon nanofibers and nanowires comes with improved thermal and electrical conductivities[81]. The study by Ferrer-Argemi et al. on carbon nanofibers and nanowires reveals that the thermal and electrical conductivities are higher for shorter and thinner GC wires [47].

2.2.2.2.5 Fabrication of C-NEMS Nanogap Devices

Electrospinning for C-NEMS fabrication has also been used for fabricating carbon-based nanogap devices. Developing carbon-based nanogap devices have been the subject of great interest for researchers in the field of molecular-scale devices because of their numerous advantages over gold or platinum electrodes in terms of resistance to electromigration, better stability at or above room temperature, and easier binding for a greater variety of molecules for biosensing applications.

Initially, carbon-based nanogap electrodes were fabricated using carbon nanotubes (CNTs) [82]. Nanogap devices based on CNTs exhibit high electrical and thermal

conductivities. However, this technique fails to provide a desirable level of control on the position and orientation of CNTs on the contacting electrodes, making it challenging to obtain reproducible ohmic contacts [83-85]. Another issue with more traditional carbon-based nanogap electrodes is the high contact resistance at the carbon and metal contact pads [45].

Fabrication of carbon nanogap electrodes based on the process explained earlier for the fabrication of suspended carbon nanofibers on C-MEMS electrodes can overcome both drawbacks. The current process provides a highly controllable deposition process while eliminating the contact resistance since the nanofiber is deposited on carbon posts. The studies on the correlation between gap size and the length of fiber have demonstrated that the shorter fibers produced smaller nanogaps, which implies the necessity of fibers shorter than 2 μm for attaining nanogaps with separation of 10 nm or less [86]. Fabrication of fibers that are less than 2 μm with conventional photolithography is very challenging. The electrospinning of SU-8 precursor fibers can eliminate the need for using fibers with lengths on the order of 2 μm or less and successfully overcome the problem associated with the limited resolution of photolithography [18]

2.2.2.3 Non-photolithography Methods

Conventional photolithography is a powerful means for the fabrication of C-MEMS and C-NEMS devices. However, several factors limit the achievable resolution for conventional photolithography tools, including but not limited to projection conditions, mask characteristics, properties and thickness of the photoresist, and depth of focus [87]. The resolution limitation of conventional photolithography has encouraged scientists to deploy alternative nanopatterning techniques such as EBL, nanoimprint, and X-ray

lithography to fabricate C-NEMS devices. For instance, EBL—as a direct writing method—offers high resolution for nanoscale patterning. Because of the small beam size, the minimum feature size can be reduced to 20–50 nm, and the scanned area is highly localized. This technique can be directly used to pattern the C-NEMS structure or fabricate a nanoscale mold for soft-lithography or nanoimprint processes. In 2006, Wang et al. reported utilizing EBL for the fabrication of GC nanowires mounted on C-MEMS micropillars (Figure 2.6a**)** [1].

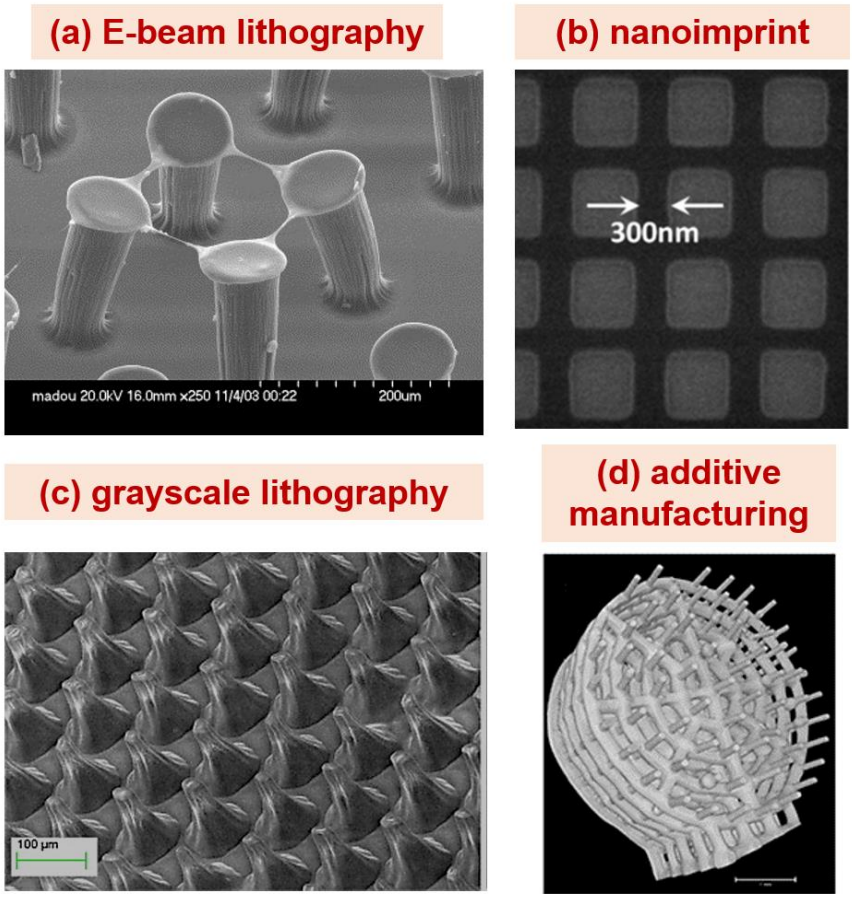

Figure 2.6 Examples of C-MEMS and C-NEMS devices fabricated via non-photolithography techniques. (a) A SEM image of suspended C-NEMS nanowires fabricated via E-beam lithography [1]. (b) A SEM image of C-NEMS pattern fabricated via nanoimprint method [7]. (c) A SEM image of needle like C-MEMS structures fabricated using grayscale lithography [12]. (d) An X-ray micro-computed tomography image reconstruction of C-MEMS 3D structure fabricated using additive manufacturing [17].

The EBL is a highly precise technique with high resolution; however, it is impractical for mass-production because of the cost and complexity of the procedure. An effective way to make EBL more feasible is to fabricate nanomold and use the nanomold for patterning the intended photoresist. In 2012, the application of this technique was reported by Penmatsa for the fabrication of C-NEMS with sub-micron resolution in which they used a UV transparent nanoimprint mold followed by ion reactive etching [7]. As the SEM image presented in Figure 2.6b shows, the nanoimprint has provided a high resolution. Since the emergence of this technology, devices for various applications have been developed, including cell culture [88], optical resonators[89], flexible electronics [90], magnetic devices [91]. However, a limited number of studies have reported the nanoimprint method for the fabrication of C-MEMS and C-NEMS, which indicates the high potential of this technique for further investigations.

The application of conventional photolithography and EBL for complex 3D structures fabrication is laborious and time-consuming; thus, making them impracticable for mass production purposes. Two techniques of grayscale lithography and additive manufacturing can efficiently resolve this problem. Photolithography and EBL are binary patterning techniques in which only two areas of crosslinked and non-crosslinked could exist. Such binary feature dictates the fabrication of 3D structures in several steps. In contrast, in grayscale patterning, the gray tone masks allow different amounts of light to be shined to the photoresist resin. The variation in light exposure dose enables mass production of complicated 3D morphologies with a single exposure step and eliminates the need for different masks and laborious alignment procedures[48]. For instance, the needle-like C-MEMS microstructure presented in Figure 2.6c was fabricated using one mask and

a single setup[12]. The grayscale lithography has been developed based on UV light[12, 92], X-ray lithography[93, 94], and holographic lithography [95, 96]. Various applications such as C-MEMS microcantilever, bridges, and micromixers have been demonstrated using grayscale lithography [12, 48].

Another feasible technique for the fabrication of complex 3D structures is additive manufacturing based on stereolithography printing. This novel technique can fabricate complex freestanding 3D C-MEMS structures with high accuracy that are impossible to pattern via traditional methods. Rezaei et al. have investigated the application of this method for patterning the complex SU-8 precursors (Figure 2.6d). Their studies showed that this technique could provide sub-100 μm resolution, which can be used for fabricating devices for a broad spectrum of applications [17].

2.2.2.4 Common Fabrication Challenges

Several issues, including adhesion, uniformity, and repeatability, challenge the fabrication of C-MEMS and C-NEMS devices [48, 60, 63]. Weak adhesion of the SU-8 photoresist to the wafer could result from trapped air bubbles in the photoresist, contamination on the wafer, moisture on the wafer before coating it, and intrinsic stress in SU-8 layers. The adhesion can be improved by thorough wafer cleaning and dehydration bake of the wafer at 150-200°C for 5-15 minutes to evaporate the remaining solvent and moisture [29, 97, 98]. Furthermore, the peeling of the SU-8 structures, especially structures with high thickness, can result from the underdevelopment of the photoresist's bottom layers. Such issues can result from insufficient UV dose, inadequate post-exposure bake, or non-uniform coating of the SU-8 photoresist. Several approaches are proposed to resolve this issue, such as conducting the post-exposure bake on hot plates instead of the

convection oven, increasing the post bake time, and an extra step of hard baking at 190°C [52, 69].

Applying proper pyrolysis parameters, including but not limited to (1) factoring-in the anticipated shrinkage, (2) optimizing the temperature ramp, and (3) applying multistep heating steps [19, 38, 99] are known to improve the durability and adhesion of the final C-MEMS and C-NEMS devices. Along with the inappropriate pyrolysis parameters, the high intrinsic stress in SU-8 layers can lead to cracks, deformity, and low adhesion of SU-8 and consequently C-MEMS and C-NEMS devices. The intrinsic stress can be related to soft and post-exposure bakes (e.g., mismatch of coefficients of thermal expansions) and UV exposure [100-102]. Several measures can be considered to reduce the intrinsic stress, such as lowering soft and post-exposure bakes temperatures, ramping the soft bake temperature, and factoring-in the type of substrate in calculating the UV dose (e.g., 1.5 times higher for glass substrates). Application of different materials with SU-8 and the incompatibility of design with intended thickness SU-8 can also cause stress. However, systematic studies on the effect of design on intrinsic stress have not been found. Such study can enlighten the roots of intrinsic stress in SU-8 derived C-MEMS and C-NEMS devices.

Uniformity and repeatability of the C-MEMS and C-NEMS process could be challenging, especially for the fabrication of 3D dense structures. The problems of uniformity and low repeatability can be managed by considering several factors in designing the fabrication process, such as changes in ambient conditions, inadequate amount of dispensed photoresist, different waiting times between each lithography steps, changes in viscosity of photoresist because of long storage time, and T-topping of tall pillar-like structures [48, 97]. T topping is a well-known phenomenon, which leads to

joining the tall structures at their top. These phenomena result from the diffraction of light at the photoresist-mask interface because of existing air gaps [103]. One solution could be using hard contact mode in which the photoresist is pushed against the mask can eliminate the air gaps between mask and photoresist. Another way is to do the coating process in several steps for layers above 100 µm thickness. Furthermore, Martinez-Duarte has proposed using a lower UV dose than the recommended dose in the fabrication datasheet for the specific thickness. For instance, Martinez-Duarte has proposed 180 mJ cm^2 for thick layers up to 200 µm followed by increased post-exposure bake time of 60 minutes at 90°C [48].

2.2.3 Application of C-MEMS and C-NEMS in Biotechnology

C-MEMS and C-NEMS devices possess the unique features of carbon such as wide electrochemical window, high physico-chemical stability, higher tolerance against biofouling, and highly accessible surface functionalization[36, 62]. Such features combined with a wide accessible range of resolution and geometry—as discussed in the previous section—make C-MEMS and C-NEMS structures exceptionally versatile for numerous biotechnology-based applications. Thus far, various biotechnology-based applications such as biosensors [19, 29], biofuel cell [10, 27], neural probes[104], and cell trapping [105] have been developed using C-MEMS and C-NEMS technology.

In Figure 2.7, examples of the recent C-MEMS and C-NEMS based biotechnology devices for the various applications are presented. Figure 2.7a shows SEM image, schematics, and the amperometric response of a C-NEMS enzymatic biosensor for cholesterol detection based on IDA electrodes decorated with AuNPs[4]. The AuNPs were

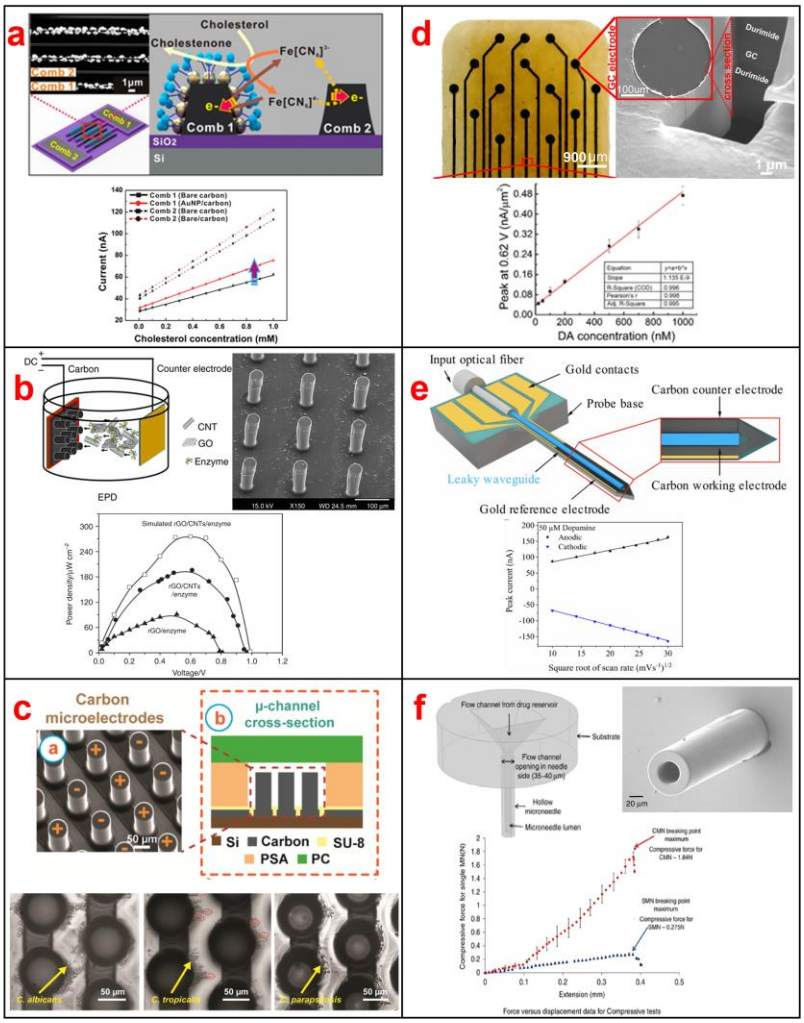

Figure 2.7 Example of C-MEMS Biotechnology devices and the output signals. (a) SEM image and illustration of electrochemical enzymatic cholesterol biosensor based on nano-size IDA decorated with AuNPs and amperometric response of the biosensor to cholesterol [4]. (b) Schematic illustration of enzymatic biofuel cell, SEM image the bioanode of glucose enzymatic biofuel based on rGO/CNT/GOx-decorated 3D C-MEMS micropillars, and the power density performance of the rGO/CNTs/GOx biofuel cell [10]. (c) SEM image and cross section illustration of the microchannel based on 3D C-MEMS IDA; Optical-microscope image of trapping different candida strains using positive dielectrophoresis on 3D C-MEMS microfluidic electrodes [15]. (d) Image 15-channel C-MEMS electrocorticography probe, SEM image of a single microelectrode, and the amperometric response of electrocorticography probe to dopamine [22]. (e) Schematic of the proposed opto-electrical C-MEMS neural probe for stimulation and electrochemical detection of dopamine exocytosis; and correlation of CV peak-current with square root of scan rate in 50 µM dopamine [24]. (f) Illustration of proposed C-MEMS microneedle for drug delivery and SEM image of C-MEMS microneedles; force vs. displacement results of the C-MEMS microneedles [28].

selectivity electrodeposited on IDA C-NEMS electrodes in which AuNPs facilitated cholesterol oxidase enzyme covalent immobilization via diazonium moiety functionalization. The example calibration curve shows the superb performance of the enzymatic biosensor.

Figure 2.7b shows a schematic illustration and an SEM image of the enzymatic biofuel cell and the power density of the biofuel cell fabricated with and without CNT, as well as simulated values. The proposed biofuel cell was developed based on decorating C-MEMS micropillars with CNT+rGO nanocomposite. This nanocomposite, along with the high surface area of 3D carbon micropillars, provided large accessible surfaces for enzyme immobilization, which considerably enhanced the biofuel cell's performance[10].

In Figure 2.7c, an SEM image and cross-section illustration of the microchannel for analyzing the dielectrophoretic behavior of three salmonella strains proposed in reference[15] are presented. As the opto-microscopic image illustrates, the C-MEMS based microchannel was successfully trapped the salmonella strains.

Figure 2.7d shows a digital and SEM image of C-MEMS based flexible and implantable neural probe for simultaneous electrical stimulations and recording. In this study, Nimbalkar et al. successfully implanted the proposed neural probe in a mouse's brain. The amperometric calibration plot confirms the high accuracy of the developed neural probe [22].

Another interesting biotechnology application of C-MEMS is its integration with optical fibers. Figure 2.7e illustrates a leaky opto-electrical neural probe for stimulation and electrochemical detection of dopamine exocytosis. The provided curve represents a good electrochemical sensitivity of this probe to dopamine concentration[24].

Biocompatibility and good stiffness of C-MEMS micropillars have been successfully harnessed to fabricate microneedle applicable for drug delivery. Figure 2.7f shows the illustration and the SEM image of a C-MEMS microneedle developed in [28]. The graph in Figure 2.7f shows force vs. displacement of microneedles tests, which confirms the capability of microneedles to stand enough force for skin penetration without breaking.

Thus far, significant progress has been made in developing C-MEMS and C-NEMS based biotechnology devices; however, the authors believe that the true potential of this technology is yet to be reached and that there is room for further development of C-MEMS and C-NEMS based biotechnology applications. Hence, a deep understanding of recent accomplishments in this field would be a good starting point for further studies. This section summarizes the C-MEMS and C-NEMS based biotechnology devices in five major groups of (1) biosensors, (2) biofuel cells, (3) intracorporeal neural probes, (4) microfluidics-based cell trapping devices, and (5) cell culture platforms. Such distinguishing would help demonstrate the specific appropriate functionalization and modifications for each application, existing drawback, and possible enhancements associated with each group of devices.

2.2.3.1 C-MEMS-Based Biosensors

The novel application of C-MEMS for biosensing was reported in 2008 for glucose enzymatic biosensors in which glucose oxidase enzymes were immobilized on 3D C-MEMS micropillars [106]. Since then, various types of biosensors, including enzymatic [3, 19, 37], optical and electrochemical aptasensors [13, 29, 36, 107], and immunosensors [31, 32] were developed using C-MEMS and C-NEMS technology. The examples of recently developed biosensors are given in Table 2.5. As shown, the C-MEMS and C-NEMS

technology are adaptable for all three types of biorecognizers (i.e., enzymes, antibodies, and aptamers). The developed biosensors exhibited low limits of detection (LoD) and wide linear ranges. Having low background noise and easily accessible functionalization is

Table 2.5 Examples of recent C-MEMS based biosensors (selected studies from 2015-2020)

Sensor type	**Target**	**Structure**	**Modification**	**LoD**	**Special Features**	**Ref**
enzymatic	glucose	IDA	N/A	0.4 µM	reproducible and selective enzyme immobilization	[3]
		micropillars	sol-gel $Al(OH)_3$	0.12 mM	test in human blood	[9]
		micropillars	rGO	1.2 µM	high selectivity and repeatability	[14]
	lactic acid	IDA	oxygen plasma	1.45 µM	covalent immobilization of enzymes	[19]
	cholesterol	IDA	AuNPs	1.28 µM	nano-sized; wide linear range	[4]
aptasensor	salmonella	suspended nanowire	oxygen plasma	10 CFU mL^{-1}	rapid, sensitive and selective whole cell detection	[13]
	PDGF-BB*	thin film	oxygen plasma	1.9 pM	label-free detection; wide linear range	[29]
immunosensor	cardiac myoglobin	suspended mesh and IDA	EDC/NHS	0.4 pg mL^{-1}	efficient redox cycling; selective detection in human serum	[31]
	Hep-B**	thin film	N/A	1 pM	direct immobilization of antibodies	[32]
non-enzymatic	glucose	thin film	O_2 microwave plasma etch/ AuNPs	36 µM	direct detection without enzyme	[34]

*platelet-derived growth factor-BB
**hepatitis-B

perhaps the main reason for excellent biosensing performances of C-MEMS and C-NEMS based biosensors. Herein, the demonstrated functionalizations for C-MEMS and C-MEMS platforms are discussed.

The surface C-MEMS and C-NEMS can be used directly or with modifications to accommodate the biorecognition agents. The surface of GC has local oxidations, which can be used to directly immobilize the biorecognition agents such as enzymes [3] and antibodies[32]. As mentioned above, the surface of C-MEMS can be functionalized with carboxyl groups via four techniques of VUV, EA, UV/Ozone, and RIE. Penmatsa et al. have reported that carboxyl group concentration was highest in the case of VUV pretreatment (15%) followed by oxygen RIE (12.5%) and EA pretreatments (12.5%), and UV/O3 pretreatment showed a significantly lower carboxyl group percentage of 6% [35]. The carboxyl modified C-MEMS electrodes can be used for covalent immobilization of amino-group modified biorecognizers. Similarly, the surface of C-MEMS electrodes can be functionalized with amino groups using direct amination and diazonium grafting, which can be used to immobilize carboxyl-terminated bioreceptors. The easily attainable functionalization of C-MEMS and C-NEMS's surfaces is highly feasible for developing biosensing and biofuel cells for two reasons: first, they eliminate the need for using self-assembled monolayers, and second, the biorecognizers can be covalently immobilized.

Several examples of the recently developed C-MEMS based biosensors using RIE (i.e., oxygen-plasma) for carboxyl group functionalization are given in Table 2.5. The RIE technique was used for both enzymatic and aptamer-based biosensors (aptasensors), which implies that this functionalization technique is a simple yet efficient means for stable covalent immobilization of different biorecognizers.

Integration of nanomaterial onto the surface of C-MEMS electrodes is another powerful and efficient functionalization method. Deposition of CNT, CNT based nanocomposites, and metal-based nanoparticles (e.g., AuNPs or ZnO) can simultaneously functionalize and increase the active surface area of C-MEMS microelectrodes. These nanomaterials can be deposited using electrostatic spray deposition (ESD) [10], drop-casting [14], and electrodeposition [4].

In the ESD technique, the nanocomposite is dispersed in a proper solvent and sprayed under high voltage acceleration on a heated substrate. Achieving various and uniform morphologies is the main advantage of this technique, while requiring high voltage and nonselective deposition are the downsides. ESD has been employed to deposit CNT and CNT+rGO nanocomposites on C-MEM devices envisioned for biosensor and biofuel cell applications [10, 27]. Drop-casting is a simple and effective way for depositing thin-films on flat substrates. This technique is widely used for developing biosensors and biofuel cells because of its simplicity; however, this method lacks the selective deposition and the coverage of 3D structures (i.e., the side of micropillars). Electrodepositing is a versatile technique for depositing charged nanomaterials. This technique is developed based on the effect of electric fields on charged particles. Electrodepositing is most useful for selective deposition on IDA arrays since the voltage can be selectively applied onto the desired arrays. This technique's main challenge is preventing the deposition between the arrays since this unintended deposition can shortcut the connections. This problem can be solved by increasing the solution's conductivity or using a sacrificial photoresist to cover the gap between arrays and remove it after the deposition.

The C-MEMS technology has been successfully deployed to develop enzymatic biosensors for detecting various biomolecules, including glucose, lactic acid, and cholesterol. The developed C-MEMS enzymatic biosensors show highly promising performances, including low limits of detections and high stability. For instance, the glucose enzymatic biosensors based on 3D C-MEMS micropillars decorated with rGO showed a wide linear range of 0-10 mM and a low LoD of 1.2 µM. The biosensor exhibit high accuracy for glucose measurements from blood samples [14]. The recently developed cholesterol enzymatic biosensors based on C-NMES IDA decorated with AuNPs demonstrated highly promising performance with a low LoD of 1.28 µM and a wide linear range of 1-10 mM [4]. Besides the third generation enzymatic biosensors (i.e., biosensors coupled with immobilized enzymes), C-MEMS platforms are highly promising for non-enzymatic bioanayltes detection such as glucose. Sharma et al. demonstrated non-enzymatic glucose biosensors based on nanoporous C-MEMS structures decorated with AuNPs in which the C-MEMS structure was etched with O_2 microwave plasma to form the nano-pores. The proposed non-enzymatic glucose biosensor exhibited a low LoD of 36 µM and a wide leaner range of 0.05–10 mM[34]. By proving a stable covalent immobilization of enzymes and low background noises, the developed C-MEMS biosensors are highly promising for wearable or implantable enzymatic point-of-care (POC) biosensors.

The accessible functionalization of C-MEMS and C-NEMS structures make these platforms an excellent choice for aptasensor and immunosensors. The direct functionalization enables covalent immobilization of various aptamers and antibodies without using self-assembled monolayers (SAM layer). Elimination of the SAM layer

simplifies the fabrication process while immensely improving the stability of the C-MEMS based aptasensor and immunosensors.

Furthermore, the unique properties of GC, such as low background noise, resistance toward biofouling, and good conductivity, make GC a potent candidate for label-free detection. Label-free detection is significant for POC application because it simplifies the sample preparations and reduces operation costs. For instance, Forouzanfar et al. have proposed label-free PDGF-BB aptasensors in which the affinity aptamers were covalently immobilized on RIE-treated C-MEMS thin film. The proposed aptasensor exhibited a low LoD of 1.9 pM and a wide linear range of 0.005-50 nM, as well as a robust and stable performance in the presence of external interference agents [29]. The application of suspended C-MEMS and C-NEMS structures for biosensing has been demonstrated to improve the performance of the biosensors by providing better access to the redox species and easier sandwich formations (e.g., the sandwich formations in immunosensing). For instance, salmonella aptasensors were developed based on the suspended GC nanowires that demonstrated excellent label-free detection in which a low LoD of 10^1 CFU mL^{-1} and a fast reaction time of 5 minutes was achieved. The affinity aptamers were immobilized on RIE-treated GC nanowires [13]. Sharma et al. have proposed the application of C-NEMS suspended mesh structure for immunosensing. In the demonstrated immunosensor, affinity antibodies were immobilized on a suspended mesh structure, and the IDA below the mesh provided vast access of redox species to the formed antibody-target sandwich formation. The proposed immunosensor was highly sensitive and selective toward cardiac myoglobin in mouse serum [31].

In addition to the prominent properties of C-MEMS and C-NEMS biotechnology devices mentioned in the previous section, the exceptional performance of the electrochemical C-MEMS biosensors can be addressed C-MEMS and C-NEMS features such as low background noise, low ohmic drop at the surface, and tunable active surface area. Furthermore, C-MEMS and C-NEMS biosensing platforms in comparison to gold—as a common contender for biosensors—offer several advantages, including (1) higher stability of immobilized bio-recognizer (e.g., the covalent bond between bio-recognizer and GC) which can immensely improve the stability and robustness of the biosensors, (2) higher tolerance of GC toward biofouling which is highly crucial for selectivity of the biosensors, (3) higher compatibility of the GC with carbon-based and other organic nanomaterial and elimination SAM layers, and (4) lower fabrication costs [76, 108]. These features are most probably due to the homogeneity of GC in which lack of crystalline structure eliminates granular surfaces that could act as points of initiation of side chemical reactions or attachment of non-intended (i.e., biofouling) molecules [109-111]. Although more evidence is required to compare the electrochemical C-MEMS biosensors with optical C-MEMS biosensors, some general facts about electrochemical biosensors could be applied for electrochemical C-MEMS biosensors. Electrochemical biosensors, including C-MEMS and C-NEMS biosensors in which GC is used as the active electrode, suffer from some drawbacks such as (1) lower selectivity than similar optical biosensors, (2) low signal-to-noise ratio in low-target concentrations which can result in lower sensitivity and necessity of complicated mediator composites to enhance the output signal, and (3) complicated reaction pathways and kinetics which could lead to misinterpretation of existing electrochemical processes in the system [112, 113]. In the light of mentioned

facts about C-MEMS and C-NEMS-based biosensors, a systematic comparative study of electrochemical versus optical C-MEMS and C-NEMS biosensors can be an interesting topic for future studies. In general, the good biosensing performance of C-MEMS and C-NEMS-based biosensors and the feasibility of the C-MEMS and C-NEMS fabrication processes illustrate the high potential of this technology for developing various POC biosensors.

Table 2.6 Performance of glucose driven EBFC mediator free systems using carbon-based materials

Electrode	**Bioanode**	**Biocathode**	**P_{max} (μ W cm^{-2})**	**OCV[l] (v)**	**Stability**	**Ref.**
bioelectrode made of pellet	GOX[a]/catalase-compressed MWCNT[b] disk	laccase-compressed MWCNT[b] disk	190	0.57	N/A	[5]
gold electrode	[PQQ-GDH][c]-PAN[d]/MWCNT[b]	BOD[e]-MWCNT[b]	70	0.68	N/A	[11]
glassy carbon	DTNB[f]-Pyr[g]/MWCNT /[h]GDH	DTNB[f]-Pyr[g]/MWCNT / BOD[e]	500	0.36	42% after 6 days	[16]
cogel	GOX-graphene/SWCNT[i]	BOD[e]-graphene/SWCNT[i]	190	0.61	N/A	[21]
glassy carbon	[FAD-GDH][j]/Os(DMB)PVI[k]/MWCNTs	laccase/Os(BPY)PVI[k]/MWCNTs	430	0.59	56% after 7 days	[23]
3D C-MEMS	GOX/rGO	laccase/ rGO	136.3	0.59	N/A	[27]
3D C-MEMS	GOX/rGO/CNT	BOD[e]/ rGO/CNT	196	0.61	64.5%	[10]

[a]glucose oxidase; [b]multi-walled carbon nanotube; [c] pyrroloquinolinequinone-dependent glucose dehydrogenase; [d] polyaniline; [e]bilirubin oxidase; [f]5,5′-dithio-bis(2-nitrobenzoic acid); [g]1-pyrenebutyric acid; [h]NAD-dependent glucose dehydrogenase; [i]signle wall carbon nanotube; [j]flavin adenine dinucleotide-dependent glucose dehydrogenase; [k]Os(4,4′-dimethyl-2,2′-bipyridine)$_2$(poly-vinylimidazole)$_{10}$Cl]; [l]open circuit voltage

2.2.3.2 C-MEMS-Based Biofuel Cells

Driven by developed implantable devices and the increasing number of patients with chronic diseases, the demand for implantable medical devices has drastically increased [10]. One of the concerns for implantable medical devices is a reliable and biocompatible power source. Enzymatic biofuel cells (EBFCs)—a class of biofuel cells that employ enzymes to convert biological energy sources to electrical power—have been demonstrated as potent candidates for replacing commercially available lithium-ion batteries. EBFCs provide several advantages over conventional batteries such as application of nontoxic renewable biocomponets (e.g., glucose), high abundance of the biofuels in the human body, high reactivity and reaction selectivity of the biocatalysts (e.g., glucose oxidase), and compatibility of the EBFCs performance conditions with human physiological conditions (e.g., body temperature and pH) [114-116]. Since the first demonstration of micro EBFCs In 2001, in which Katz et al. proposed self-powered enzymatic biosensors, a noticeable attention has been devoted to improving the micro EBFCs [10, 117].

In choosing a suitable contender for developing high-powered micro EBFCs, various parameters should be considered, including having a large surface area, availability of a suitable confined area for enzyme immobilization, the biocompatibility of the EBFCs electrodes, and high-efficiency of electron transfer. The majority of the required parameters can be efficiently fulfilled via functionalizing a suitable C-MEMS or C-NEMS structure with the CNT-based nanocomposites using methods mentioned in subsection 3.1. Such integration has been investigated by Song and Wang in which CNT+rGO nanocomposites were co-deposited with enzymes on 3D C-MEMS micropillars. The experimental

performance of the developed EBFCc reached 71.1% of the theoretical value, with a maximum power density of 196.04 μW cm^{-2} at 0.61 V and 64.5% power remaining after 7 days [10].

The performance of recently developed glucose-based EBFC systems in which carbon-based material is used as a promoter is given in Table 2.6. The performance of the C-MEMS EBFC in comparison with other EBFS systems with CNT shows higher open-circuit voltage and better stability while providing high power density. The excellent performance of the proposed C-MEMS EBFCs can be explained with several facts, including (1) the 3D geometry of the C-MEMS provided more sites for co-deposition of the enzymes+rGO/CNT nanocomposite, (2) the application of CNT prohibited the stacking of graphene and improved the accessible surface area, and (3) GC facilitated the better charge transport which yielded high power density. The achieved power density of the proposed EBFC is sufficient to support wearable and intracorporeal implant devices. Hence, the C-MEMS based EBFCs are highly promising for future wearable POC biosensor and C-MEMS based intracorporeal implants and probes.

2.2.3.3 C-MEMS-Based Intracorporeal Neural Probes

Several parameters, including architecture, mechanical and electrochemical properties, and durability, should be considered in developing micro and nanoelectrodes for intracorporeal neural probes. C-MEMS technology can satisfy the majority of required features for viable neural probes. As discussed in the previous section, the C-MEMS and C-MEMS devices can be fabricated in various sizes and geometries by deploying proper fabrication techniques. Thus far, thin-film[118, 119], IDA [22, 75, 104], micropillars on thin-film[98], and microneedles [24] have been envisioned for neural probes applications.

The application of C-MEMS for intracorporeal neural probes is a relatively novel concept, and the reported studies have revealed the superior performance of GC electrodes over traditional gold or platinum-based probes. The performance of GC intracorporeal neural probes is highly dependent on pyrolysis parameters. Their different properties, such as mechanical properties (e.g., stiffness and hardness), electrical property, and electrochemical property (e.g., double-layer capacitance), can be tuned to be more compatible with the target tissue. Kassegne et al. studied the effect of pyrolysis parameters on electrical, mechanical, and electrochemical properties of GC neural probes and intracorporeal implants in which they were measured at *in vitro* conditions. Their study showed that the electrical properties of GC (i.e., impedance (Ω) at 1 kHz) is tailorable between 10-100 kΩ, in which for the same geometry, maximum impedance was recorded for GC pyrolyzed at 600°C. In contrast, the minimum was recorded for GC pyrolyzed at 1000°C. The maximum pyrolysis temperature and temperature ramp both had affected the electrochemical property. For instance, to have high double-layer capacitance and low charge transfer resistance, high-temperature ramps (e.g., >8°C min^{-1}) and a maximum temperature of 1000°C were suggested. Furthermore, their research showed that the highest hardness could be achieved at middle-range pyrolysis temperatures (800-900°C) and fast temperature ramps decrease GC's hardness [73].

The integration of C-MEMS on polyimide substrate for long-term electrocorticography is one of GC microelectrodes' unique applications. GC has a wider electrochemical window compare to gold and platinum as it can tolerate the larger voltage excursions without producing irreversible faradaic reactions[22, 74, 104, 120]. The larger electrochemical window can induce the physico-chemical stability of the

electrocorticography electrode. For instance, the comparative case study by Vomero et al. on platinum and GC electrocorticography electrodes showed visible corrosion on platinum electrodes after 5 million stimulation pulses while GC electrodes remained almost intact[104]. This side reaction could result from the adhesion layer's oxidation (i.e., chromium) that it is typically used for the deposition of platinum. The corrosion resistivity of GC probes can be explained by two facts (1) GC is a homogeneous material with no crystalline structure; hence it lacks the granular surfaces that could act as points of initiation of corrosive chemical reactions, and (2) the absence of metal adhesion layers in GC neural probes [26, 121].

The comparative case studies on the biocompatibility of GC electrocorticography microelectrodes showed a minimum difference in cell viability on the GC devices compared to the control cells. Furthermore, GC had lower background noise (due to its higher capacitance), enhancing the probe's signal-to-noise ratio and improving the sensitivity, spatial selectivity, and spatial resolution of GC electrocorticography microelectrodes [22, 74, 104, 120]. For instance, the C-MEMS based neural probes developed by Nimbalkar et al. have shown high performance, including (1) high signal-to-noise (>16) recordings, (2) exceptionally high charge storage capacity for the non-coated neural probe with a value of 61.4 ± 6.9 mC cm^{-2}, (3) highly sensitive dopamine detection (10 nM level), (4) dual recording of both electrical and electrochemical signals, and (5) no failure after 3.5 billion cycles of pulses [22]. The achieved high signal-to-noise ratio and high charge storage capacity can result from several factors such as fast electrode polarization, low ohmic drop on the surface of the GC probe, and higher surface charge density [26, 121]. The high sensitivity of the developed GC neural probe can be explained

by the fact that GC has high intrinsic hydroxyl groups on its surfaces. The hydroxyl groups are favorable for the adsorption of cationic species such as dopamine, whose amine side chain gets protonated at physiological pH[109, 110]. Moreover, Vomero et al. have investigated the *in vitro* stability of GC-based intracorporeal neural probes in which the GC neural probes implanted in rat brains for several weeks showed no significant change in morphology and performances [120].

Penetrating neural probes based on 3D C-MEMS is another noteworthy application of this technology. The envisioned penetrating neural probes were developed based on 3D GC micropillars [98], 3D origami-styled GC [75], 3D GC microcones fabricated by additive manufacturing [122], and leaky opto-electrical probes [24]. The 3D structure of the GC neural probes allows simultaneous electrophysiological signals recoding from both the brain surface (electrocorticography) and depth (single neuron). Furthermore, the neural probe can be factionalized to measure the neurotransmitters such as dopamine beside the double signal recoding. The multiplexing of the probe's function can be tremendously important since it can reduce operating costs and minimize tissue damage (due to lessened penetration sites). To the best of our knowledge, such integration for C-MEMS-based penetrating neural probes has only been investigated by S. Vasudevan et al. They have investigated the proposed neural probe's electrochemical performance in the presence of various dopamine concentrations [24].

2.2.3.4 C-MEMS Microfluidics Based Cell Trapping

Dielectrophoresis (DEP) is an electrical field-based technique enabling selective manipulation of target particles and cells, using an asymmetrical (non-uniform) electrical field with a sufficient dipole moment of the targeted particles or cells. The main advantage

of DEP over other techniques (e.g., magnetic-activated cell sorting) is conducting the separation solely based on the target's intrinsic physical properties (e.g., surface structure and internal compartmentalization). Tag-free target separation is essential for various applications, especially POC biosensors, since it eliminates the expensive and time-consuming labeling process and enables fast and real-time operations. DEP has been established for various applications ranging from separation of molecules and proteins to manipulating cells and bacteria [48, 123, 124].

C-MEMS based DEP electrode—also known as carbon-electrode DEP—provides several advantages over more traditional DEP devices. Perhaps feasible fabrication of high aspect ratio structures is the main advantage of carbon-electrode DEP. The high aspect ratio structures can improve the efficiency of the DEP devices in two ways of (1) increasing the effective surface area, which can improve the flow rate, and (2) covering the entire height of a flow channel, which reduces the mean distance of any particle to the closest electrode surface. The electrochemical stability and wider electrochemical window of GC compared to other commonly used metal films (e.g., gold or platinum) are other significant advantages of carbon-electrode DEP, allowing higher applied voltage in a given electrolyte without electrolyzing it [48, 123, 124].

It is worth noting that the photolithography of 3D C-MEMS DEP structures is very similar to the process mentioned in section 2.1, with a minor extra step of hard baking at 190°C after developing the SU-8 structures. The hard bake is crucial to improve the adhesion of SU-8 to the silicon wafer and prevent the peeling off during the extended time of operations. Several applications have been established using 3D carbon-electrode DEP, including separation of target cells[15, 125, 126], separation of live and dead

monocytes[105], decontamination of persisting bacteria from an antibiotic-treated sample[127], lambda-DNA trapping [128], and live-cell lysis [129]. The proposed applications suggest the high potential of 3D C-MEMS DEP technology for developing lab-on-chip sample preparation platforms for POC diagnosis devices.

2.2.3.5 C-MEMS-Based Cell Culture Platform

The development of engineered microenvironments that can provide proper chemical growth factors and mechanical properties (e.g., morphology and texture) is vital to have a more realistic *in vitro* cell culture model [130]. C-MEMS technology can provide the proper microenvironment for cell growth. For instance, Ferraro et al. investigated the effect of geometry on interaction and orientation on human iPSCs-derived neural stem cells[131]. Their study showed that the biocompatibility of C-MEMS structures provides a sustainable substrate for the adhesion and proliferation of cells. Moreover, their studies demonstrated that human iPSCs-derived neural stem cells recognize the differences in two configurations and orient their growth according to the structure [131]. This interesting behavior can be the topic of future studies by designing a complex 3D C-MEMS structure (e.g., using additive manufacturing mentioned in section 2.2) to mimic a biological morphology and investigate the human iPSCs-derived neural stem cells' response to various therapeutic stimulations.

Alongside the geometry manipulations, the integration of nanomaterials on C-MEMS microelectrodes allows controlling cell behavior on sub-micron levels. Sub-micron cell growth patterning presents fascinating opportunities in the field of bioelectronics and organ-on-chip technologies. Chauhan et al. have investigated this novel approach by integrating AuNPs within the synthesizing process of GC microelectrodes. Their proposed

fabrication approach provided various AuNPs size distributions and interparticle separations on fibronectin functionalized surfaces. The proposed AuNPs/fibronectin-modified GC substrates were highly biocompatible with a cytocompatibility of ≈80% after 3 and 8 days [132]. The compatibility of the metal-salt precursor (i.e., $NaAuCl_4$) with SU-8 photoresist had better control of fabrication parameters, including the size, distribution, and spacing of AuNPs without disturbing micropatterning and pyrolysis process on metal-loaded SU-8 microstructures. The control over AuNPs properties and the aforementioned unique features of C-MEMS technology make this metal-C-MEMS microfabrication process a promising approach for future organ-on-a-chip systems, bioelectronics, and biosensing applications.

2.2.4 Conclusion

C-MEMS and C-NEMS technologies are feasible techniques for manufacturing glass-like carbon devices in a wide range of structures and sizes. A vast variety of structures can be made by choosing the proper lithography technique and optimizing the pyrolysis parameters. The mechanical and material properties of C-MEMS and C-NEMS devices can be tuned by careful structure design and adjusting the pyrolysis properties to match the envisioned application better. The prominent features of glass-like carbon, such as wide electrochemical window and high physico-chemical stability, and biocompatibility, have made C-MEMS and C-NEMS devices highly versatile for various biotechnology-related applications. Highly accessible functionalization, the possibility of covalent immobilizing different biorecognizers, and resistance toward biofouling are unique advantages of C-MEMS and C-NEMS biosensing and biofuel cell over more traditional MEMS devices.

Low toxicity, elimination of metal adhesion layers, and lower degradation rate are significant benefits of these devices over traditional metallic-MEMS intracorporeal neural implants. The developed C-MEMS and C-NEMS biotechnology devices have demonstrated that these devices are highly promising for various biotechnology applications. Nevertheless, it should be noted that challenges and issues need to be addressed before C-MEMS and C-NEMS biotechnology devices are commercially available.

2.2.5 References

[1] K. Malladi, C. Wang, and M. Madou, "Fabrication of suspended carbon microstructures by e-beam writer and pyrolysis," Carbon, vol. 44, pp. 2602-2607, 2006.

[2] M. Vomero, E. Zucchini, E. Delfino, C. Gueli, N. C. Mondragon, S. Carli, et al., "Glassy carbon electrocorticography electrodes on ultra-thin and finger-like polyimide substrate: Performance evaluation based on different electrode diameters," Materials, vol. 11, p. 2486, 2018.

[3] D. Sharma, Y. Lim, Y. Lee, and H. Shin, "Glucose sensor based on redox-cycling between selectively modified and unmodified combs of carbon interdigitated array nanoelectrodes," Analytica chimica acta, vol. 889, pp. 194-202, 2015.

[4] D. Sharma, J. Lee, J. Seo, and H. Shin, "Development of a sensitive electrochemical enzymatic reaction-based cholesterol biosensor using nano-sized carbon interdigitated electrodes decorated with gold nanoparticles," Sensors, vol. 17, p. 2128, 2017.

[5] A. Zebda, S. Cosnier, J.-P. Alcaraz, M. Holzinger, A. Le Goff, C. Gondran, et al., "Single glucose biofuel cells implanted in rats power electronic devices," Scientific reports, vol. 3, pp. 1-5, 2013.

[6] C. Wang, L. Taherabadi, G. Jia, S. Kassegne, J. V. Zoval, and M. J. Madou, "Carbon-MEMS architectures for 3D microbatteries," in MEMS, MOEMS, and Micromachining, 2004, pp. 295-302.

[7] V. Penmatsa, H. Kawarada, and C. Wang, "Fabrication of carbon nanostructures using photo-nanoimprint lithography and pyrolysis," Journal of Micromechanics and Microengineering, vol. 22, p. 045024, 2012.

[8] S. Hemanth, C. Caviglia, and S. S. Keller, "Suspended 3D pyrolytic carbon microelectrodes for electrochemistry," Carbon, vol. 121, pp. 226-234, 2017.

[9] B. Hai, Y.-Q. Zou, G.-B. Guo, Z.-D. Wang, Y.-Y. Liu, X.-X. Wang, et al., "A novel strategy to prepare LDH networks loaded carbon structure by C-MEMS techniques for glucose detection," Chinese Chemical Letters, vol. 28, pp. 149-152, 2017.

[10] Y. Song and C. Wang, "High-power biofuel cells based on three-dimensional reduced graphene oxide/carbon nanotube micro-arrays," Microsystems & nanoengineering, vol. 5, pp. 1-11, 2019.

[11] I. W. Schubart, G. Göbel, and F. Lisdat, "A pyrroloquinolinequinone-dependent glucose dehydrogenase (PQQ-GDH)-electrode with direct electron transfer based on polyaniline modified carbon nanotubes for biofuel cell application," Electrochimica Acta, vol. 82, pp. 224-232, 2012.

[12] A. Rammohan, P. K. Dwivedi, R. Martinez-Duarte, H. Katepalli, M. J. Madou, and A. Sharma, "One-step maskless grayscale lithography for the fabrication of 3-dimensional structures in SU-8," Sensors and Actuators B: Chemical, vol. 153, pp. 125-134, 2011.

[13] A. Thiha, F. Ibrahim, S. Muniandy, I. J. Dinshaw, S. J. Teh, K. L. Thong, et al., "All-carbon suspended nanowire sensors as a rapid highly-sensitive label-free chemiresistive biosensing platform," Biosensors and Bioelectronics, vol. 107, pp. 145-152, 2018.

[14] S. Hemanth, A. Halder, C. Caviglia, Q. Chi, and S. S. Keller, "3D Carbon microelectrodes with bio-functionalized graphene for electrochemical biosensing," Biosensors, vol. 8, p. 70, 2018.

[15] M. Islam, D. Keck, J. Gilmore, and R. Martinez-Duarte, "Characterization of the dielectrophoretic response of different candida strains using 3d carbon microelectrodes," Micromachines, vol. 11, p. 255, 2020.

[16] F. Giroud, K. Sawada, M. Taya, and S. Cosnier, "5, 5-Dithiobis (2-nitrobenzoic acid) pyrene derivative-carbon nanotube electrodes for NADH electrooxidation and oriented immobilization of multicopper oxidases for the development of glucose/O2 biofuel cells," Biosensors and Bioelectronics, vol. 87, pp. 957-963, 2017.

[17] B. Rezaei, J. Y. Pan, C. Gundlach, and S. S. Keller, "Highly structured 3D pyrolytic carbon electrodes derived from additive manufacturing technology," Materials & Design, p. 108834, 2020.

[18] A. Salazar, S. Hosseini, M. Sanchez-Domínguez, M. J. Madou, A. Montesinos-Castellanos, and S. O. Martinez-Chapa, "Sub-10 nm nanogap fabrication on suspended glassy carbon nanofibers," Microsystems & Nanoengineering, vol. 6, pp. 1-10, 2020.

[19] S. Forouzanfar, F. Alam, I. Khakpour, A. R. Baboukani, N. Pala, and C. Wang, "Highly Sensitive Lactic Acid Biosensors Based on Photoresist Derived Carbon," IEEE Sensors Journal, 2020.

[20] J. R. Maldonado and M. Peckerar, "X-ray lithography: Some history, current status and future prospects," Microelectronic Engineering, vol. 161, pp. 87-93, 2016.

[21] A. S. Campbell, Y. J. Jeong, S. M. Geier, R. R. Koepsel, A. J. Russell, and M. F. Islam, "Membrane/mediator-free rechargeable enzymatic biofuel cell utilizing graphene/single-wall carbon nanotube cogel electrodes," ACS Applied Materials & Interfaces, vol. 7, pp. 4056-4065, 2015.

[22] S. Nimbalkar, E. Castagnola, A. Balasubramani, A. Scarpellini, S. Samejima, A. Khorasani, et al., "Ultra-capacitive carbon neural probe allows simultaneous long-term electrical stimulations and high-resolution neurotransmitter detection," Scientific reports, vol. 8, pp. 1-14, 2018.

[23] Z. Zhong, L. Qian, Y. Tan, G. Wang, L. Yang, C. Hou, et al., "A high-performance glucose/oxygen biofuel cell based on multi-walled carbon nanotube films with electrophoretic deposition," Journal of Electroanalytical Chemistry, vol. 823, pp. 723-729, 2018.

[24] S. Vasudevan, J. Kajtez, A. Heiskanen, J. Emnéus, and S. S. Keller, "Leaky Opto-Electrical Neural Probe for Optical Stimulation and Electrochemical Detection of Dopamine Exocytosis," in 2020 IEEE 33rd International Conference on Micro Electro Mechanical Systems (MEMS), 2020, pp. 388-391.

[25] C. Wang and M. Madou, "From MEMS to NEMS with carbon," Biosensors and bioelectronics, vol. 20, pp. 2181-2187, 2005.

[26] S. Ranganathan, R. Mccreery, S. M. Majji, and M. Madou, "Photoresist-derived carbon for microelectromechanical systems and electrochemical applications," Journal of the Electrochemical Society, vol. 147, p. 277, 2000.

[27] Y. Song, C. Chen, and C. Wang, "Graphene/enzyme-encrusted three-dimensional carbon micropillar arrays for mediatorless micro-biofuel cells," Nanoscale, vol. 7, pp. 7084-7090, 2015.

[28] R. Mishra, B. Pramanick, T. K. Maiti, and T. K. Bhattacharyya, "Glassy carbon microneedles—new transdermal drug delivery device derived from a scalable C-MEMS process," Microsystems & Nanoengineering, vol. 4, p. 38, 2018.

[29] S. Forouzanfar, F. Alam, N. Pala, and C. Wang, "Highly sensitive label-free electrochemical aptasensors based on photoresist derived carbon for cancer biomarker detection," Biosensors and Bioelectronics, vol. 170, p. 112598, 2020.

[30] J. Vilcakova, L. Kutejova, M. Jurca, R. Moucka, R. Vıcha, M. Sedlacık, et al., "Enhanced Charpy impact strength of epoxy resin modified with vinyl-terminated polydimethylsiloxane," J. Appl. Polym. Sci, vol. 135, pp. 45720, 2017.

[31] D. Sharma, J. Lee, and H. Shin, "An electrochemical immunosensor based on a 3D carbon system consisting of a suspended mesh and substrate-bound interdigitated array nanoelectrodes for sensitive cardiac biomarker detection," Biosensors and Bioelectronics, vol. 107, pp. 10-16, 2018.

[32] B. Pramanick, N. Mandal, D. Mondal, C. Royfhaudhuri, and S. Chakraborty, "C-MEMS Derived Glassy Carbon Electrodes as Sensitive Electrochemical Biosensors," in 2018 IEEE SENSORS, 2018, pp. 1-4.

[33] B. Pramanick, M. Vazquez-Pinon, A. Torres-Castro, S. O. Martinez-Chapaa, and M. Madou, "Effect of pyrolysis process parameters on electrical, physical, chemical and electro-chemical properties of SU-8-derived carbon structures fabricated using the C-MEMS process," Materials Today: Proceedings, vol. 5, pp. 9669-9682, 2018.

[34] D. Sharma, J. Lee, and H. Shin, "Gold Nanostructure Decorated 3D Porous Carbon Architectures as a Non-Enzymatic Glucose Sensor," in 2019 IEEE 32nd International Conference on Micro Electro Mechanical Systems (MEMS), 2019, pp. 580-583.

[35] V. Penmatsa, H. Kawarada, Y. Song, and C. Wang, "Comparison of different oxidation techniques for biofunctionalization of pyrolyzed carbon," Material Science Research India, vol. 11, pp. 01-08, 2014.

[36] J.-H. Yang, V. Penmatsa, S. Tajima, H. Kawarada, and C. Wang, "Direct amination on 3-dimensional pyrolyzed carbon micropattern surface for DNA detection," Materials Letters, vol. 63, pp. 2680-2683, 2009.

[37] V. Penmatsa, T. Kim, M. Beidaghi, H. Kawarada, L. Gu, Z. Wang, et al., "Three-dimensional graphene nanosheet encrusted carbon micropillar arrays for electrochemical sensing," Nanoscale, vol. 4, pp. 3673-3678, 2012.

[38] M. Beidaghi and C. Wang, "Micro-supercapacitors based on interdigital electrodes of reduced graphene oxide and carbon nanotube composites with ultrahigh power handling performance," Advanced Functional Materials, vol. 22, pp. 4501-4510, 2012.

[39] A. Stange, M. Imboden, J. Javor, L. K. Barrett, and D. J. Bishop, "Building a Casimir metrology platform with a commercial MEMS sensor," Microsystems & nanoengineering, vol. 5, pp. 1-9, 2019.

[40] E. Fitzer, K.-H. Kochling, H. Boehm, and H. Marsh, "Recommended terminology for the description of carbon as a solid (IUPAC Recommendations 1995)," Pure and applied chemistry, vol. 67, pp. 473-506, 1995.

[41] L. Pesin, "Review Structure and properties of glass-like carbon," Journal of Materials Science, vol. 37, pp. 1-28, 2002.

[42] S. Sharma, C. S. Kumar, J. G. Korvink, and C. Kübel, "Evolution of glassy carbon microstructure: in situ transmission electron microscopy of the pyrolysis process," Scientific reports, vol. 8, p. 16282, 2018.

[43] G. M. Jenkins, K. Kawamura, and L. Ban, "Formation and structure of polymeric carbons," Proceedings of the Royal Society of London. A. Mathematical and Physical Sciences, vol. 327, pp. 501-517, 1972.

[44] J. Kakinoki, "A model for the structure ofglassy carbon'," Acta Crystallographica, vol. 18, pp. 578-578, 1965.

[45] S. Sharma, A. Sharma, Y.-K. Cho, and M. Madou, "Increased graphitization in electrospun single suspended carbon nanowires integrated with carbon-MEMS and carbon-NEMS platforms," ACS applied materials & interfaces, vol. 4, pp. 34-39, 2012.

[46] C. S. Sharma, H. Katepalli, A. Sharma, and M. Madou, "Fabrication and electrical conductivity of suspended carbon nanofiber arrays," Carbon, vol. 49, pp. 1727-1732, 2011.

[47] L. Ferrer-Argemi, E. S. Aliabadi, A. Cisquella-Serra, A. Salazar, M. Madou, and J. Lee, "Size-dependent electrical and thermal conductivities of electro-mechanically-spun glassy carbon wires," Carbon, vol. 130, pp. 87-93, 2018.

[48] R. Martinez-Duarte, "SU-8 Photolithography as a Toolbox for Carbon MEMS," Micromachines, vol. 5, pp. 766-782, 2014.

[49] H. Zittel and F. Miller, "A Glassy-Carbon Electrode for Voltammetry," Analytical Chemistry, vol. 37, pp. 200-203, 1965.

[50] W. Van der Linden and J. W. Dieker, "Glassy carbon as electrode material in electro-analytical chemistry," Analytica Chimica Acta, vol. 119, pp. 1-24, 1980.

[51] S. Sharma, "Glassy carbon: A promising material for micro-and nanomanufacturing," Materials, vol. 11, p. 1857, 2018.

[52] M. V. Piñón, B. C. Benítez, B. Pramanick, V. H. Perez-Gonzalez, M. J. Madou, S. O. Martinez-Chapa, et al., "Direct current-induced breakdown to enhance reproducibility and performance of carbon-based interdigitated electrode arrays for AC electroosmotic micropumps," Sensors and Actuators A: Physical, vol. 262, pp. 10-17, 2017.

[53] S. Yamada and H. Sato, "Some physical properties of glassy carbon," Nature, vol. 193, pp. 261-262, 1962.

[54] Y. Peng, F. Zhong, L. Qian, and S. Jiang, "Effects of ultraviolet/ozone irradiation on glassy-like carbon film for the bioMEMS applications," Applied Surface Science, vol. 533, p. 147443, 2020.

[55] W. Rothwell, "Small-Angle X-Ray Scattering from Glassy Carbon," Journal of Applied Physics, vol. 39, pp. 1840-1845, 1968.

[56] F. McFeely, S. Kowalczyk, L. Ley, R. Cavell, R. Pollak, and D. Shirley, "X-ray photoemission studies of diamond, graphite, and glassy carbon valence bands," Physical Review B, vol. 9, p. 5268, 1974.

[57] L. Pesin and E. Baitinger, "A new structural model of glass-like carbon," Carbon, vol. 40, pp. 295-306, 2002.

[58] A. Yoshida, Y. Kaburagi, and Y. Hishiyama, "Microtexture and magnetoresistance of glass-like carbons," Carbon, vol. 29, pp. 1107-1111, 1991.

[59] I. L. Spain, "Electronic Transport-Properties Of Graphite, Carbons, And Related Materials," Chemistry and physics of carbon, vol. 16, pp. 119-304, 1981.

[60] B. Cardenas-Benitez, C. Eschenbaum, D. Mager, J. G. Korvink, M. J. Madou, U. Lemmer, et al., "Pyrolysis-induced shrinking of three-dimensional structures fabricated by two-photon polymerization: experiment and theoretical model," Microsystems & nanoengineering, vol. 5, pp. 1-13, 2019.

[61] J. M. Shaw, J. D. Gelorme, N. C. LaBianca, W. E. Conley, and S. J. Holmes, "Negative photoresists for optical lithography," IBM journal of Research and Development, vol. 41, pp. 81-94, 1997.

[62] M. Beidaghi, W. Chen, and C. Wang, "Electrochemically activated carbon micro-electrode arrays for electrochemical micro-capacitors," Journal of power sources, vol. 196, pp. 2403-2409, 2011.

[63] C. Wang, L. Taherabadi, G. Jia, M. Madou, Y. Yeh, and B. Dunn, "C-MEMS for the manufacture of 3D microbatteries," Electrochemical and Solid-State Letters, vol. 7, pp. A435-A438, 2004.

[64] C. Wang, G. Jia, L. H. Taherabadi, and M. J. Madou, "A novel method for the fabrication of high-aspect ratio C-MEMS structures," Journal of microelectromechanical systems, vol. 14, pp. 348-358, 2005.

[65] L. Amato, A. Heiskanen, R. Hansen, L. Gammelgaard, T. Rindzevicius, M. Tenje, et al., "Dense high-aspect ratio 3D carbon pillars on interdigitated microelectrode arrays," Carbon, vol. 94, pp. 792-803, 2015.

[66] J. Heo, D. Shim, G. T. Teixidor, S. Oh, M. Madou, and H. Shin, "Carbon interdigitated array nanoelectrodes for electrochemical applications," Journal of the Electrochemical Society, vol. 158, p. J76, 2011.

[67] L. N. Quang, P. E. Larsen, A. Boisen, and S. S. Keller, "Tailoring stress in pyrolytic carbon for fabrication of nanomechanical string resonators," Carbon, vol. 133, pp. 358-368, 2018.

[68] B. Pramanick, A. Salazar, S. O. Martinez-Chapa, and M. J. Madou, "Carbon TEM grids fabricated using C-MEMS as the platform for suspended carbon nanowire characterization," Carbon, vol. 113, pp. 252-259, 2017.

[69] M. Vazquez-Pinon, B. Pramanick, F. G. Ortega-Gama, V. H. Perez-Gonzalez, L. Kulinsky, M. J. Madou, et al., "Hydrodynamic channeling as a controlled flow reversal mechanism for bidirectional AC electroosmotic pumping using glassy carbon microelectrode arrays," Journal of Micromechanics and Microengineering, vol. 29, p. 075007, 2019.

[70] R. Natu, M. Islam, J. Gilmore, and R. Martinez-Duarte, "Shrinkage of SU-8 microstructures during carbonization," Journal of analytical and applied pyrolysis, vol. 131, pp. 17-27, 2018.

[71] R. Natu, M. Islam, and R. Martinez-Duarte, "Shrinkage analysis of carbon micro structures derived from SU-8 photoresist," ECS Transactions, vol. 72, p. 27, 2016.

[72] J. J. Heikkinen, J. Košir, V. Jokinen, and S. Franssila, "Fabrication and design rules of three dimensional pyrolytic carbon suspended microstructures," Journal of Micromechanics and Microengineering, vol. 30, p. 115003, 2020.

[73] S. Kassegne, M. Vomero, R. Gavuglio, M. Hirabayashi, E. Özyilmaz, S. Nguyen, et al., "Electrical impedance, electrochemistry, mechanical stiffness, and hardness tunability in glassy carbon MEMS μECoG electrodes," Microelectronic Engineering, vol. 133, pp. 36-44, 2015.

[74] M. Vomero, P. Van Niekerk, V. Nguyen, N. Gong, M. Hirabayashi, A. Cinopri, et al., "A novel pattern transfer technique for mounting glassy carbon microelectrodes on polymeric flexible substrates," Journal of Micromechanics and Microengineering, vol. 26, p. 025018, 2016.

[75] N. Goshi, E. Castagnola, M. Vomero, C. Gueli, C. Cea, E. Zucchini, et al., "Glassy carbon MEMS for novel origami-styled 3D integrated intracortical and epicortical neural probes," Journal of Micromechanics and Microengineering, vol. 28, p. 065009, 2018.

[76] S. Kassegne, M. Vomero, P. van Niekerk, M. Hirabayashi, V. Perez-Gonzalez, B. Pramanick, et al., "Glassy Carbon Microelectrodes for Neural Signal Sensing and Stimulation," in Book 2 Carbon-The next Silicon?-Applications, ed: Momentum Press, 2016, pp. 101-122.

[77] Y. Lim, S. Kim, Y. M. Kwon, J. M. Baik, and H. Shin, "A highly sensitive gas-sensing platform based on a metal-oxide nanowire forest grown on a suspended carbon nanowire fabricated at a wafer level," Sensors and Actuators B: Chemical, vol. 260, pp. 55-62, 2018.

[78] G. Canton, T. Do, L. Kulinsky, and M. Madou, "Improved conductivity of suspended carbon fibers through integration of C-MEMS and electro-mechanical spinning technologies," Carbon, vol. 71, pp. 338-342, 2014.

[79] G. S. Bisht, G. Canton, A. Mirsepassi, L. Kulinsky, S. Oh, D. Dunn-Rankin, et al., "Controlled continuous patterning of polymeric nanofibers on three-dimensional substrates using low-voltage near-field electrospinning," Nano letters, vol. 11, pp. 1831-1837, 2011.

[80] D. George, A. Garcia, Q. Pham, M. R. Perez, J. Deng, M. T. Nguyen, et al., "Fabrication of patterned graphitized carbon wires using low voltage near-field electrospinning, pyrolysis, electrodeposition, and chemical vapor deposition," Microsystems & Nanoengineering, vol. 6, pp. 1-12, 2020.

[81] A. Salazar and V. H. Perez-Gonzalez, "Reduction of electrical resistance on suspended glassy carbon nanofibers by localized thermal annealing," Materials Today: Proceedings, 2020.

[82] C. W. Marquardt, S. Grunder, A. Błaszczyk, S. Dehm, F. Hennrich, H. v. Löhneysen, et al., "Electroluminescence from a single nanotube–molecule–nanotube junction," Nature nanotechnology, vol. 5, pp. 863-867, 2010.

[83] A. Vijayaraghavan, S. Blatt, D. Weissenberger, M. Oron-Carl, F. Hennrich, D. Gerthsen, et al., "Ultra-large-scale directed assembly of single-walled carbon nanotube devices," Nano letters, vol. 7, pp. 1556-1560, 2007.

[84] F. Prins, A. Barreiro, J. W. Ruitenberg, J. S. Seldenthuis, N. Aliaga-Alcalde, L. M. Vandersypen, et al., "Room-temperature gating of molecular junctions using few-layer graphene nanogap electrodes," Nano letters, vol. 11, pp. 4607-4611, 2011.

[85] K. Otsuka, T. Inoue, Y. Shimomura, S. Chiashi, and S. Maruyama, "Field emission and anode etching during formation of length-controlled nanogaps in electrical breakdown of horizontally aligned single-walled carbon nanotubes," Nanoscale, vol. 8, pp. 16363-16370, 2016.

[86] A. Salazar, B. Cardenas-Benitez, B. Pramanick, M. J. Madou, and S. O. Martinez-Chapa, "Nanogap fabrication by Joule heating of electromechanically spun suspended carbon nanofibers," Carbon, vol. 115, pp. 811-818, 2017.

[87] D. Andrews, T. Nann, and R. H. Lipson, Comprehensive nanoscience and nanotechnology: Academic press, 2019.

[88] K. S. Beckwith, S. P. Cooil, J. W. Wells, and P. Sikorski, "Tunable high aspect ratio polymer nanostructures for cell interfaces," Nanoscale, vol. 7, pp. 8438-8450, 2015.

[89] A. V. Shneidman, K. P. Becker, M. A. Lukas, N. Torgerson, C. Wang, O. Reshef, et al., "All-polymer integrated optical resonators by roll-to-roll nanoimprint lithography," Acs Photonics, vol. 5, pp. 1839-1845, 2018.

[90] J. Shao, X. Chen, X. Li, H. Tian, C. Wang, and B. Lu, "Nanoimprint lithography for the manufacturing of flexible electronics," Science China Technological Sciences, vol. 62, pp. 175-198, 2019.

[91] T. Asari, R. Shibata, and H. Awano, "Novel magnetic wire fabrication process by way of nanoimprint lithography for current induced magnetization switching," AIP Advances, vol. 7, p. 055930, 2017.

[92] R. Fallica, R. Kirchner, H. Schift, and Y. Ekinci, "High-resolution grayscale patterning using extreme ultraviolet interference lithography," Microelectronic Engineering, vol. 177, pp. 1-5, 2017.

[93] P. Mouroulis, F. T. Hartley, D. W. Wilson, V. E. White, A. Shori, S. Nguyen, et al., "Blazed grating fabrication through gray-scale X-ray lithography," Optics express, vol. 11, pp. 270-281, 2003.

[94] H. Mekaru, "Performance of SU-8 membrane suitable for deep x-ray grayscale lithography," Micromachines, vol. 6, pp. 252-265, 2015.

[95] V. Shrauger, L. Erwin, J. Ahn, and C. Warde, "Computer-generated multiple-phase-level holograms by use of color-printer techniques," Applied optics, vol. 33, pp. 5318-5327, 1994.

[96] B. Liang, Y. Liu, J. Li, L. Song, Y. Li, J. Zhou, et al., "Fabrication of large-size photonic crystals by holographic lithography using a lens array," Journal of micromechanics and microengineering, vol. 22, p. 035013, 2012.

[97] Y. Li, "Challenges and issues of using polymers as structural materials in MEMS: A review," Journal of Microelectromechanical Systems, vol. 27, pp. 581-598, 2018.

[98] R. Mishra, B. Pramanick, A. Chatterjee, T. Maiti, and T. Bhattacharyya, "Fabrication of C-MEMS Derived 3-Dimensional Glassy Carbon Microelectrodes for Neural Sensing and Stimulation," in 2018 IEEE SENSORS, 2018, pp. 1-4.

[99] Z. Tang, T. Shi, J. Gong, L. Nie, and S. Liu, "An optimized process for fabrication of high-aspect-ratio photoresist-derived carbon microelectrode array on silicon substrate," Thin Solid Films, vol. 518, pp. 2701-2706, 2010.

[100] S. Keller, G. Blagoi, M. Lillemose, D. Haefliger, and A. Boisen, "Processing of thin SU-8 films," Journal of micromechanics and microengineering, vol. 18, p. 125020, 2008.

[101] T. A. Anhoj, A. M. Jorgensen, D. A. Zauner, and J. Hübner, "The effect of soft bake temperature on the polymerization of SU-8 photoresist," Journal of Micromechanics and Microengineering, vol. 16, p. 1819, 2006.

[102] J. Zhang, M. B. Chan-Park, and S. R. Conner, "Effect of exposure dose on the replication fidelity and profile of very high aspect ratio microchannels in SU-8," Lab on a Chip, vol. 4, pp. 646-653, 2004.

[103] R. Yang and W. Wang, "A numerical and experimental study on gap compensation and wavelength selection in UV-lithography of ultra-high aspect ratio SU-8 microstructures," Sensors and Actuators B: Chemical, vol. 110, pp. 279-288, 2005.

[104] M. Vomero, E. Castagnola, F. Ciarpella, E. Maggiolini, N. Goshi, E. Zucchini, et al., "Highly stable glassy carbon interfaces for long-term neural stimulation and low-noise recording of brain activity," Scientific reports, vol. 7, pp. 1-14, 2017.

[105] Y. Yildizhan, N. Erdem, M. Islam, R. Martinez-Duarte, and M. Elitas, "Dielectrophoretic separation of live and dead monocytes using 3D carbon-electrodes," Sensors, vol. 17, p. 2691, 2017.

[106] H. Xu, K. Malladi, C. Wang, L. Kulinsky, M. Song, and M. Madou, "Carbon post-microarrays for glucose sensors," Biosensors and Bioelectronics, vol. 23, pp. 1637-1644, 2008.

[107] V. Penmatsa, A. R. Ruslinda, M. Beidaghi, H. Kawarada, and C. Wang, "Platelet-derived growth factor oncoprotein detection using three-dimensional carbon microarrays," Biosensors and bioelectronics, vol. 39, pp. 118-123, 2013.

[108] B. Pramanick, S. O. Martinez-Chapa, and M. J. Madou, "Fabrication of biocompatible hollow microneedles using the C-MEMS process for transdermal drug delivery," ECS Transactions, vol. 72, p. 45, 2016.

[109] M. Hirabayashi, B. Mehta, N. W. Vahidi, A. Khosla, and S. Kassegne, "Functionalization and characterization of pyrolyzed polymer based carbon microstructures for bionanoelectronics platforms," Journal of Micromechanics and Microengineering, vol. 23, p. 115001, 2013.

[110] B. D. Bath, D. J. Michael, B. J. Trafton, J. D. Joseph, P. L. Runnels, and R. M. Wightman, "Subsecond adsorption and desorption of dopamine at carbon-fiber microelectrodes," Analytical chemistry, vol. 72, pp. 5994-6002, 2000.

[111] S. Forouzanfar, F. Alam, N. Pala, and C. Wang, "A Review of Electrochemical Aptasensors for Label-Free Cancer Diagnosis," Journal of The Electrochemical Society, vol. 167, p. 067511, 2020.

[112] M. Labib, E. H. Sargent, and S. O. Kelley, "Electrochemical methods for the analysis of clinically relevant biomolecules," Chemical reviews, vol. 116, pp. 9001-9090, 2016.

[113] Y. Dai and C. C. Liu, "Recent Advances on Electrochemical Biosensing Strategies toward Universal Point-of-Care Systems," Angewandte Chemie, vol. 131, pp. 12483-12496, 2019.

[114] W. Vielstich, A. Lamm, and H. A. Gasteiger, Handbook of fuel cells: fundamentals technology and applications vol. 2: Wiley New York, 2003.

[115] G. T. R. Palmore and G. M. Whitesides, "Microbial and enzymatic biofuel cells," ed: ACS Publications, 1994.

[116] A. Heller, "Miniature biofuel cells," Physical Chemistry Chemical Physics, vol. 6, pp. 209-216, 2004.

[117] E. Katz, A. F. Bückmann, and I. Willner, "Self-powered enzyme-based biosensors," Journal of the American Chemical Society, vol. 123, pp. 10752-10753, 2001.

[118] M. Vomero, E. Castagnola, J. S. Ordonez, S. Carli, E. Zucchini, E. Maggiolini, et al., "Incorporation of Silicon Carbide and Diamond-Like Carbon as Adhesion Promoters Improves In Vitro and In Vivo Stability of Thin-Film Glassy Carbon Electrocorticography Arrays," Advanced Biosystems, vol. 2, p. 1700081, 2018.

[119] J. Grossenbacher, M. Gullo, S. Lecaudé, H. T. Stahel, and J. Brugger, "SU-8 C-MEMS as candidate for long-term implantable pacemaker micro electrodes," in 2015 Transducers-2015 18th International Conference on Solid-State Sensors, Actuators and Microsystems (TRANSDUCERS), 2015, pp. 867-870.

[120] M. Vomero, E. Castagnola, J. S. Ordonez, S. Carli, E. Zucchini, E. Maggiolini, et al., "Improved long-term stability of thin-film glassy carbon electrodes through the use of silicon carbide and amorphous carbon," in 2017 8th International IEEE/EMBS Conference on Neural Engineering (NER), 2017, pp. 288-291.

[121] O. J. Schueller, S. T. Brittain, C. Marzolin, and G. Whitesides, "Fabrication and characterization of glassy carbon MEMS," Chemistry of Materials, vol. 9, pp. 1399-1406, 1997.

[122] B. Chen, B. Zhang, C. Chen, J. Hu, J. Qi, T. He, et al., "Penetrating glassy carbon neural electrode arrays for brain-machine interfaces," Biomedical Microdevices, vol. 22, pp. 43-43, 2020.

[123] D. Kim, M. Sonker, and A. Ros, "Dielectrophoresis: From molecular to micrometer-scale analytes," Analytical chemistry, vol. 91, pp. 277-295, 2018.

[124] S. S. Seyedi and D. V. Matyushov, "Protein dielectrophoresis in solution," The Journal of Physical Chemistry B, vol. 122, pp. 9119-9127, 2018.

[125] M. d. C. Jaramillo, E. Torrents, R. Martínez-Duarte, M. J. Madou, and A. Juárez, "On-line separation of bacterial cells by carbon-electrode dielectrophoresis," Electrophoresis, vol. 31, pp. 2921-2928, 2010.

[126] P. Puri, V. Kumar, S. Belgamwar, and N. Sharma, "Microfluidic device for cell trapping with carbon electrodes using dielectrophoresis," Biomedical Microdevices, vol. 20, p. 102, 2018.

[127] M. Elitas, R. Martinez-Duarte, N. Dhar, J. D. McKinney, and P. Renaud, "Dielectrophoresis-based purification of antibiotic-treated bacterial subpopulations," Lab on a Chip, vol. 14, pp. 1850-1857, 2014.

[128] R. Martinez-Duarte, F. Camacho-Alanis, P. Renaud, and A. Ros, "Dielectrophoresis of lambda-DNA using 3D carbon electrodes," Electrophoresis, vol. 34, pp. 1113-1122, 2013.

[129] G. Mernier, R. Martinez-Duarte, R. Lehal, F. Radtke, and P. Renaud, "Very high throughput electrical cell lysis and extraction of intracellular compounds using 3D carbon electrodes in lab-on-a-chip devices," Micromachines, vol. 3, pp. 574-581, 2012.

[130] P. Benzoni, P. Ginestra, L. Altomare, A. Fiorentino, L. De Nardo, E. Ceretti, et al., "Biomanufacturing of a chitosan/collagen scaffold to drive adhesion and alignment of human cardiomyocyte derived from stem cells," Procedia CIRP, vol. 49, pp. 113-120, 2016.

[131] R. Ferraro, P. Ginestra, G. Lanzi, S. Giliani, and E. Ceretti, "Production of micro-patterned substrates to direct human iPSCs-derived neural stem cells orientation and interaction," Procedia Cirp, vol. 65, pp. 225-230, 2017.

[132] G. Chauhan, A. L. Ángeles, E. Gonzalez-González, M. M. Kulkarni, B. Cardenas-Benitez, M. F. Jiménez, et al., "Nano-spaced Gold on Glassy Carbon Substrate for Controlling Cell Behavior," Advanced Materials Interfaces, p. 2000238, 2020.

3. Methodology

3.1 Introduction

This section presents the details of methodology adopted for this dissertation—for both fabricating the sensing electrodes and synthesis of nanomaterials (i.e., graphene nanosheets). For fabrication of miniaturized sensing electrodes *carbon-microelectromechanical system (C-MEMS*) technology was used to fabricate three designs of (i) thin-film electrodes, (ii) interdigitated electrodes, and (iii) 3D C-MEMS micro pillar arrays. For synthesis and deposition of nanomaterials, novel electrochemical bipolar exfoliation technique was used to exfoliate, reduce and deposit of graphene oxide (GO) and reduced graphene oxide (rGO) on intended electrodes.

3.2 Carbon Microelectromechanical Systems (C-MEMS)

As a deep UV photoresist, SU-8 is a perfect choice to fabricate high aspect ratio structures for various applications. For example, 3D carbon micropillars mounted on thin-film or interdigitated arrays (IDA) can be modified to act as an active electrode for biosensing. The schematic illustration of the photolithography process of 2-dimensional (2D) and 3D C-MEMS microelectrodes is represented in Figure 3.1a. The fabrication process of high aspect ratio C-MEMS structures typically starts with photopatterning of the base layer (e.g., an IDA electrode) with a thickness between 5-25 μm, followed by the patterning of a second layer on top of the first layer. The developed structure is pyrolyzed under an inert atmosphere at high temperatures above 600°C [1-3]. The detailed experimental procedure can be found in chapters 4, 5 and 7. Figures 3.2b and 3.2c illustrate typical SEM image of the C-MEMS based micro-pillar arrays and a digital image of the micro-device, respectively.

3.3 Electrochemical Bipolar Exfoliation of Graphene Nanosheets

The bipolar exfoliation method used in this dissertation is a direct single-step of exfoliation, deposition, and reduction of graphene utilizing a graphite rod in deionized water (DIW) (see Figure 3.2a). The process of bipolar exfoliation includes applying a constant electric field between two conductive feeder electrodes, which aggregates in opposite polarizations of the graphite rods. Consequently, if the apparent potential difference between opposite ends of the rod is sufficient (i.e., >1.5 V), simultaneous faradaic reactions of reduction at the cathodic pole and oxidation at the anodic pole would

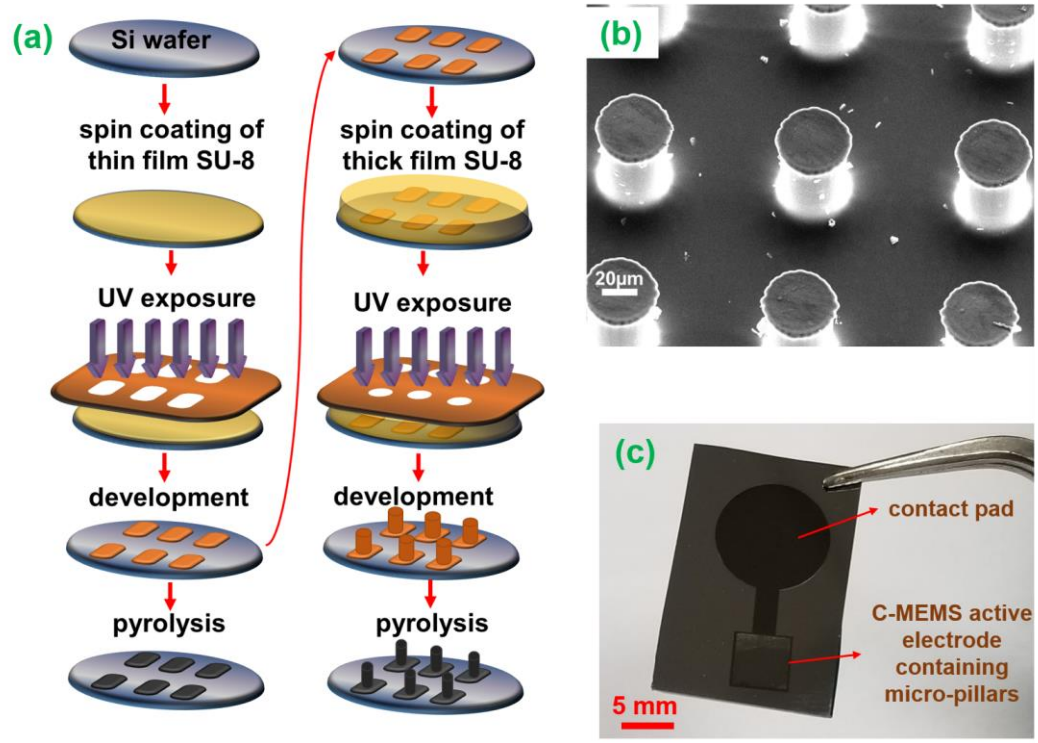

Figure 3.1 a) Schematic illustration of typical photolithography process for fabrication of 2D and 3D C-MEMS electrodes. (b) SEM micrograph of carbon micro-pillar arrays; (c) Photograph of a device containing micro-pillars on carbon current collectors and contact pad

occur[4]. A SEM image of rGO deposited on stainless steel negative feeding electrodes in presented in Figure 3.2b.

3.4 Sensor Development

In this dissertation two type of sensor were developed (i) enzymatic biosensors for detection of lactic acid and (ii) aptamer-based biosensors (aptasensors) for detection of platelet-derived growth factor-bb (PDGF-bb) cancer biomarkers. Herein, the sensor development processes for both types are briefly presented. The detailed process can be found in chapter 4 and chapters 5-7 for enzymatic biosensors and aptasensors, receptively.

3.4.1 Enzymatic Biosensor Development

Lactate oxidase (LOx) enzymes were immobilized on the surfaces of functionalized C-MEMS microelectrodes on the 0.25 cm^2 working area, which followed by drying at 4°C in the refrigerator overnight. The devices were washed thoroughly with phosphate-buffered saline for 10 minutes to wash away the unbounded enzymes. The prepared electrodes were stored in the refrigerator at 4°C when they were not used.

3.4.2 Aptasensor Development

The aptamer stock solutions were prepared based on the suggested procedure in the datasheet released by ThermoFisher Scientific for oligonucleotide preparation and storage. The diluted stocks were prepared in 0.1 M TE buffer with a final volume of 10 µL. Before immobilizing aptamers, 5 µL of 20 mg mL^{-1} EDC and 10 µL of 20 mg mL^{-1} NHS were added to the aptamer solution with the desired concentration. The aptamer solution was incubated for 30 minutes at room temperature. This step is recommended for activating the amino linker tags of the aptamers. The prepared aptamer solution was deposited on the electrode surfaces and followed by incubation for 2 hours at room temperature. After

incubation, electrodes were washed thoroughly in DI water to wash any unattached aptamers. In order to quench blank areas of the ThL electrodes, 50 µL of the aqueous solution of 0.1 M PBS + 1% (v:v) Tween-20 was deposited on the electrodes and followed by incubation for 10 minutes. The aptamer immobilized electrodes were washed with DI water for 5 minutes and stored in 0.1 M TE buffer in the refrigerator (4°C) when not in use.

3.5 Material Characterization

The techniques used for material characterization of developed biosensors are described in this section.

3.5.1 Scanning Electron Microscopy (SEM)

In order to investigate the microstructure of the materials synthesized, a field emission-scanning electron microscope (JEOL 7000FE-SEM, Peabody, MA, USA) was used; the accelerating voltages for imaging were generally kept between 10-20 kV for typical working distances between 6-10 mm.

3.5.2 Transmission Electron Microscopy (TEM)

The TEM images were taken by using a Philips CM-200 FEG TEM operating at 200 kV. Selected area electron diffraction (SAED) analyses were performed in order to study the sample crystallinity.

3.5.3 Fourier Transform Infrared (FT-IR) Spectroscopy

Spectroscopic studies on the samples were carried out using a JASCO FTIR-4100 equipped with an attenuated total reflectance (ATR) accessory between wavenumbers of 4000 and 500 cm^{-1} at room temperature.

3.6 Electrochemical Characterization

3.6.1 Cyclic Voltammetry (CV)

Cyclic voltammetry is a type potentiodynamic electrochemical technique which is used to investigate the reversibility of different electrochemical reactions. In a typical CV experiment, the working electrode potential is ramped linearly vs. time at a certain scan rate ($mV\ s^{-1}$). The data are plotted as current vs. voltage. For this dissertation, the CV tests were performed using a Bio-logic versatile multichannel potentiostat (VMP3, Bio logic). Detailed experimental details can be found in the respective research chapter.

3.6.2 Electrochemical Impedance Spectroscopy (EIS)

Electrochemical impedance spectroscopy (EIS) is a perturbative characterization of the dynamics of an electrochemical reaction, which records the response of an electrochemical cell to an applied potential or current. For this dissertation, EIS studies were performed using a Bio-logic versatile multichannel potentiostat (VMP3, Bio logic). Typically an AC oscillation of 10 mV amplitude was applied over the frequencies from 250 kHz to 10 Hz; the data were fitted using Z-fit function in EC-Lab (V10.40) software using relevant Randles circuits.

3.6.3 Differential Pulse Voltammetry (DPV)

Differential Pulse Voltammetry (DPV) is a voltammetry method used to make electrochemical measurements and a derivative of linear sweep voltammetry or staircase voltammetry, with a series of regular voltage pulses superimposed on the potential linear sweep or stair steps. The current is measured immediately before each potential change, and the current difference is plotted as a function of potential. By sampling the current just before the potential is changed, the effect of the charging current can be decreased. For this dissertation, DPV studies were performed using a Bio-logic versatile multichannel potentiostat (VMP3, Bio logic).

3.7 References

[1] M. Vazquez-Pinon, B. Pramanick, F. G. Ortega-Gama, V. H. Perez-Gonzalez, L. Kulinsky, M. J. Madou, et al., "Hydrodynamic channeling as a controlled flow reversal mechanism for bidirectional AC electroosmotic pumping using glassy carbon microelectrode arrays," Journal of Micromechanics and Microengineering, vol. 29, p. 075007, 2019.

[2] Y. Song, C. Chen, and C. Wang, "Graphene/enzyme-encrusted three-dimensional carbon micropillar arrays for mediatorless micro-biofuel cells," Nanoscale, vol. 7, pp. 7084-7090, 2015.

[3] C. Wang, G. Jia, L. H. Taherabadi, and M. J. Madou, "A novel method for the fabrication of high-aspect ratio C-MEMS structures," Journal of microelectromechanical systems, vol. 14, pp. 348-358, 2005.

[4] A. Allagui, M. A. Abdelkareem, H. Alawadhi, and A. S. Elwakil, "Reduced graphene oxide thin film on conductive substrates by bipolar electrochemistry," Scientific reports, vol. 6, p. 21282, 2016.

4. C-MEMS based Lactic Acid Biosensors

4.1 Introduction

Lactic acid with the chemical formula of $C_3H_6O_3$ is a product of anaerobic glycolysis generated in muscles and liver due to insufficient supply of O_2 in blood [1]. The level of LA in human blood can change from 0.5 – 1 mM for healthy persons up to >4 mM [2, 3] under the influence of different diseases and conditions, such as cancer in the metastatic spread of cancer cells in stage II or stage III [4, 5], antitumor treatments. [6], cardiovascular diseases (ischemia, hypoxemia, and anemia) [7], and head trauma [8]. This feature can be employed as an essential complementary indicator for different cancer types and metastatic levels [4, 9]. In the cases of brain stroke and head trauma, increasing LA concentration from the cut off level of 2.35 mM in mildly injured to >4mM in severely injured conditions, can be used to determine the severity of the case [8, 10]. Considering its significance in various diseases and conditions, fast and accurate detection of the LA level can be useful for their early diagnosis as well as monitoring their progress and severity.

Carbon-microelectromechanical systems (C-MEMS) are composed of well-defined carbon micropatterns in which carbon (such as glassy carbon) is synthesized through pyrolysis of micropatterned photoresist polymer in an oxygen-free environment at high temperatures [11, 12]. Photoresist-derived carbon (PDC) possesses various remarkable properties of carbon-based materials such as high biocompatibility, wide electrochemical window, low absorption of non-specific biomolecules, and scalability [13]. Additionally, PDC exhibits excellent electrical conductivity, as well as low background capacitance, better tolerance toward bio-fouling than gold, glass, and silicon substrates, and higher stability when exposed to different physical/chemical treatments [14]. The surface of PDC

can be functionalized efficiently via various chemical, physical, or electrochemical procedures [15, 16]. Moreover, utilizing high surface area C-MEMS in miniaturized electrochemical devices circumvents the significant drawbacks associated with commercialized screen-printed carbon electrodes such as low resolution, low aspect ratio, and limitations for further miniaturization [13, 17]

Various studies have been conducted to develop non-invasive electrochemical biosensors based on carbon materials for real-time measuring of LA concentration. For example, Luo et al. developed a wearable cotton fabric biosensor for amperometric monitoring of LA concentration in sweat with a detection range of 0.5-1.5 mM [18]. The electrochemical sensor developed by Lamas-Ardisana et al. for measuring LA in human sweat based on screen-printed carbon electrodes functionalized with platinum nanoparticle has presented a linear range of 25–1500 μM [19]. However, these non-invasive electrochemical sensors have narrow dynamic ranges compared to the actual LA concentrations in sweat and saliva. Therefore, developing highly feasible LA sensors with high sensitivity and sufficiently broad dynamic range to meet the demands for medicine and personal health monitoring is highly significant.

In this work, we developed an electrochemical enzymatic LA sensing platform based on interdigitated PDC microelectrode arrays and using the lactic oxidase (LOx) enzyme as a catalyst for the oxidation of LA. The PDC microelectrodes were pre-treated with oxygen-plasma to form –COOH functional groups on their surfaces, through which LOx enzymes were immobilized directly on them. The scanning electron microscope (SEM) and Fourier-transform infrared spectroscopy (FTIR) were used to study the morphology and surface characteristics of the fabricated electrodes. Cyclic voltammetry (CV) was used to analyze

the performance of the sensor. The results showed that the developed PDC-based LA sensors are highly sensitive, selective, and stable, and have a sufficiently broad dynamic range compared to previously reported carbon-based LA sensors. Furthermore, the C-MEMS technique is both feasible and amenable to mass production, thus making PDC-based LA sensors highly promising for point-of-care health monitoring applications.

4.2 Materials and Methodology

4.2.1 Fabrication of Photoresist Derived Carbon Microelectrode

The PDC microelectrodes were fabricated by a standard C-MEMS process [11, 20]. They consist of fingers with 100µm width and 100 µm distance between each finger (total of 25 fingers in 0.25cm^2 area). The C-MEMS process is schematically illustrated in Figure 4.1A (1-3). A 4-inch silicon dioxide covered silicon wafer was cleaned by acetone and methanol followed by a 20 min bake in the oven at 200°C to evaporate any solvent and moisture. NANO^{TM} SU-8 25 negative photoresist (Microchem., USA) was spin-coated using photoresist spinner (Headway Research^{TM}) at 500 rpm for 12 s and then 3000 rpm for the 30 s to get a uniform photoresist layer with a thickness of approximately 25 µm. The photoresist was baked at 65°C for 3 min and 95°C for 8 min to evaporate any solvents. The photoresist was optically patterned using the OAI model 800 contact aligner (light intensity, 13.2 mW.cm^{-2}) for 22 s to crosslink polymer chains in the photoresist. Post-expose bake was conducted at temperatures of 65°C for 1 min and 95°C for 3 min. The photo-patterned sample was developed using NANO^{TM} SU-8 25 negative photoresist developer (Microchem., USA). The carbonization process of the photo-patterned photoresist was performed in a Lindberg tube furnace via 200 mL.min^{-1} flow of forming

gas (95% N_2 + 5% H_2). The samples were heated from room temperature to 350°C with the ramp of 3°C.min^{-1} with a dwell time of 30 min continued by ramping to 900°C with the same rate and hold time of 60 min. The samples were cooled down to room temperature with the ramp of 5°C.min^{-1}.

4.2.2 Oxygen-Plasma Treatment

The PDC surface was treated with oxygen-plasma using the MARCH CS-1217 RIE system, which has a parallel-plate reactor equipped with 13.65 MHz RF source, as illustrated in Figure 4.1A(4). The gas line for oxygen was utterly evacuated before the

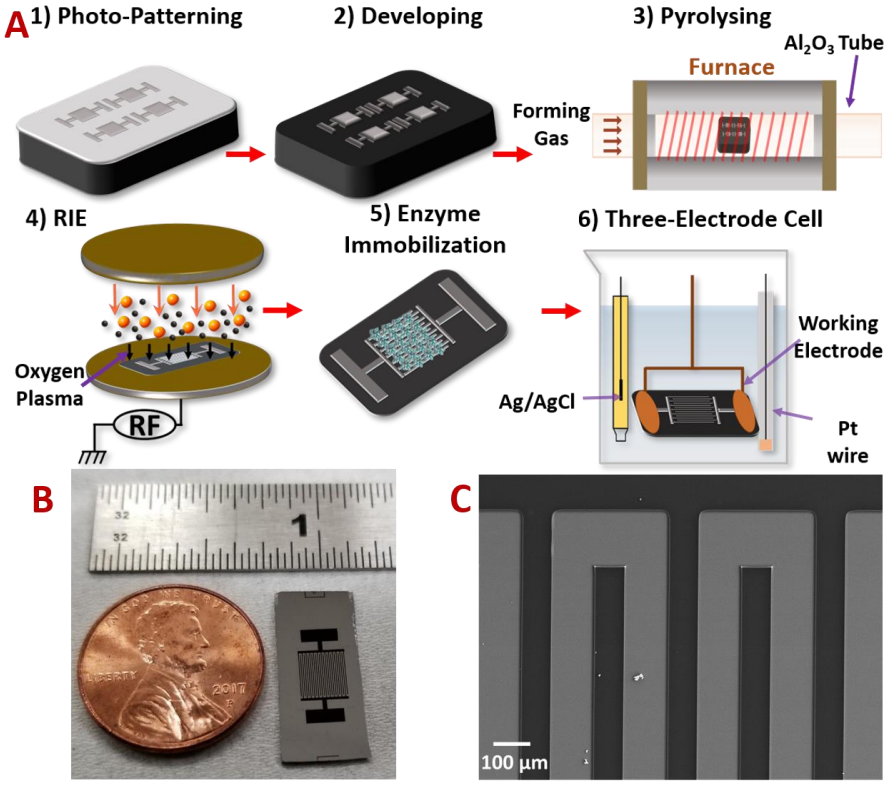

Figure 4.1 A) Schematic of the fabrication process of the C-MEMS based LA sensor and electrochemical test cell. B) Image of the PDC_{RIE} chip next to a one-cent coin. C) SEM picture of the PDC_{RIE}.

process. The etching parameters were: O_2 gas flow rate of 60 mL.min^{-1}, the RF power of

100 W, the chamber pressure of 400 mTorr, and the etching duration of 3 - 10 minutes. This process has no adverse effect on silicon dioxide underneath [21].

4.2.3 Enzyme Immobilization

As shown in Figure 4.1A (5), firstly, disodium phosphate salt (Na_2HPO_4, Sigma Aldrich, USA) was used to adjust the pH of the phosphate buffer solution (PBS, Sigma Aldrich, USA) to pH 6.6. The stock solution of 10 $mg.mL^{-1}$ LOx enzyme (Mybiosource, USA) was prepared in PBS (0.1 M, pH 7.4). LOx enzymes were immobilized on the surfaces of functionalized PDC microelectrodes with the amounts ranging from 5 µg to 40 µg confined on the 0.25 cm^2 working area, which followed by drying at 4°C in the refrigerator overnight. The devices were washed thoroughly with PBS for 10 minutes to wash away the unbounded enzymes. The prepared electrodes were stored in the refrigerator at 4°C when they were not used. The optimum amount of utilized enzymes was determined by measuring the responses of the functionalized PDC microelectrodes with various amounts of immobilized LOx enzyme to 500 µM LA. The response reached saturation at 25 µg of immobilized LOx enzymes; hence, 25 µg was chosen as the optimum amount.

4.2.4 Sensor Characterization

The electrochemical characterization was carried out using a Bio-Logic versatile multichannel potentiostat (VMP3) at room temperature. For CV studies, the three electrode cell shown in Figure 4.1A (6) with the PDC microelectrodes, platinum wire, and Ag/AgCl were used as the working electrodes, counter electrode, and reference electrode, respectively. The working electrodes were tested between potentials of -0.8 V and 0.8 V

(vs. Ag/AgCl) in which 3mL aqueous electrolytes of 0 - 15 mM LA in 0.1M PBS (0.1 M, pH 6.6) were used. The pH of the PBS was chosen as 6.6 based on the fact that the pH of human sweat is variable between 4.0 and 7.0, with the mean value of 6.3 [22, 23]. In order to define the optimum number of CV cycles, CV tests were conducted for 20 continuous cycles. The obtained curves after the cycle of n=4, repeated with a small deviation (STDEV= 7.3311 µA). Hence, n=4 was chosen for further measurements. A series of CV tests of the sensing electrodes were conducted with the scan rates of 10, 20, 40, 60, 80, and 100 $mV.s^{-1}$ in an aqueous electrolyte of 15 mM LA in 0.1M PBS (pH 6.6). Moreover, series of CV tests of the sensing electrodes were conducted in a 3 mL aqueous electrolyte of 500 µM LA with 9.92 $mg.mL^{-1}$ uric acid (Sigma Aldrich, USA) and 1.76 $mg.mL^{-1}$ ascorbic acid (Sigma Aldrich, USA). FTIR analysis was carried out using a JASCO FTIR 4100 equipped with an attenuated total reflectance (ATR) accessory to verify –COOH carboxylic group and other functional groups on the sensor surfaces. The morphology of the fabricated microelectrodes was studied using an SEM (JEOL SEM 6330F, Peabody, MA, USA) in the secondary electron imaging mode.

4.3 Results and Discussions

4.3.1 Surface Morphology and FTIR Characterization

A summary of PDC microelectrode fabrication and sensor development is illustrated in Figure 4.1A. The photolithography and carbonization parameters were optimized based on the well documented C-MEMS procedures in previous studies [12-16]. The optimum exposure time in oxygen-plasma treatment was found to be 7 minutes without breaking or detaching the PDC micro-fingers. LOx enzyme was directly immobilized on

the activated surfaces of the PDC microelectrodes without utilizing commonly applied crosslinks such as EDC [(1-ethyl-3-(3-dimethylamino) propyl carbodiimide, hydrochloride]. It is worth mentioning that in order to minimize the possible side reactions, all areas of the working electrode and connection wires were isolated utilizing bee wax, and only 5mm×5mm window was kept open. Figure 4.1B shows a picture of an oxygen-plasma treated PDC microelectrode chip (designated as PDC_{RIE}) and Figure 4.1C shows the SEM picture of PDC_{RIE}.

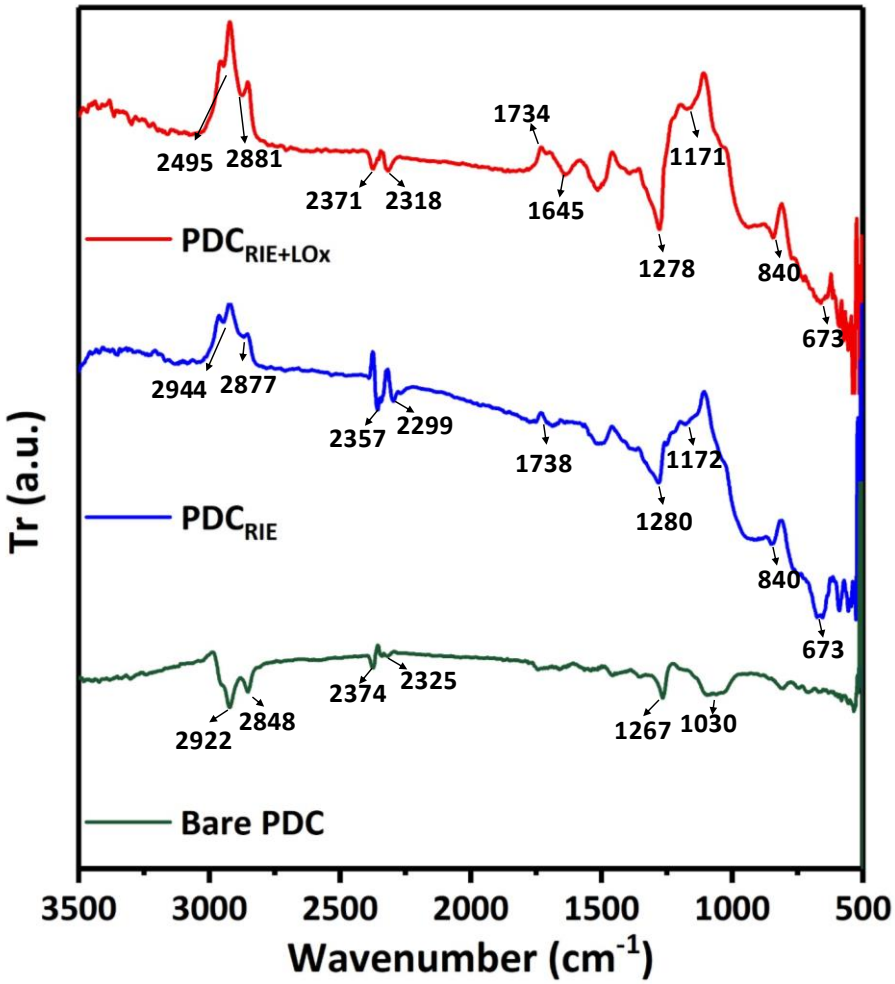

Figure 4.2 FTIR spectrum of PDC microelectrodes before modification (Bare PDC), after functionalization (PDC_{RIE}), and after enzyme immobilization ($PDC_{RIE+LOx}$)

The FTIR spectroscopy was used to track the formation of carboxylic groups and enzymes' immobilization on the surfaces of the working electrodes. As shown in Figure 4.2, the FTIR spectra of all three samples showed two peaks between 2800 - 3000 cm^{-1} and two peaks between 2290 - 2400 cm^{-1}, which are attributed to OH and sp C-H stretching, and sp C≡C bending, respectively [24]. Furthermore, PDC_{RIE} and PDC microelectrodes functionalized through oxygen-plasma treatment and having immobilized LOx enzyme (designated as $PDC_{RIE+LOx}$) show two peaks at 673 cm^{-1} and 840 cm^{-1} which are attributed to sp^2 C-H bending [24]. The spectrum of the bare PDC shows two peaks at 1030 and 1267 cm^{-1}, which are assigned to alkoxy C-O and acyl C-O, respectively [25]. These peaks are the result of native oxidation of carbon in contact with air. The FTIR of PDC_{RIE} and $PDC_{RIE+LOx}$ exhibited the same peaks around 1172 and 1287 cm^{-1}, respectively. The peak at 1738 cm^{-1} in the PDC_{RIE} spectrum and 1734 in the $PDC_{RIE+LOx}$ spectrum are attributed to C=O stretching vibrations, which indicate that the PDC microelectrodes were successfully functionalized with carboxylic groups. The FTIR spectrum for $PDC_{RIE+LOx}$ shows an apparent peak at 1645 cm^{-1} which is related to amide bond and represents covalent bonding of enzymes on the surfaces of the PDC microelectrodes [25]. The FTIR results suggest that the oxygen-plasma treatment was a simple yet effective means for generating reactive surfaces with the high possibility of covalent bonding of LOx enzymes on PDC surfaces.

4.3.2 CV Characterization of the PDC Microelectrodes

LOx is an FMN (Flavin mononucleotide)-dependent alpha hydroxyl acid oxidizing enzyme, which catalyzes the aerobic oxidation of LA to pyruvate and releases H_2O_2 [26].

Oxidation of LA is followed by releasing H_2O_2 (eq. 1). Although there are vast studies on LA reactions, the precise information of the H_2O_2 reduction reaction on the surface of carbon electrodes is absent [27, 28]. In this study, equation 4.2 is considered for H_2O_2 reduction [27, 28]. Figure 4.3A shows the CV responses with a scan rate of 20 $mV.s^{-1}$ (vs. Ag/AgCl) for the bare PDC, PDC_{LOx}, and $PDC_{RIE+LOx}$ in the 500 µM LA solutions. The CV response of the bare PDC shows no apparent oxidation peak, whereas the PDC_{LOx} has an oxidation peak at 0.05V/0.028 mA, and the $PDC_{RIE+LOx}$ exhibits an oxidation peak at

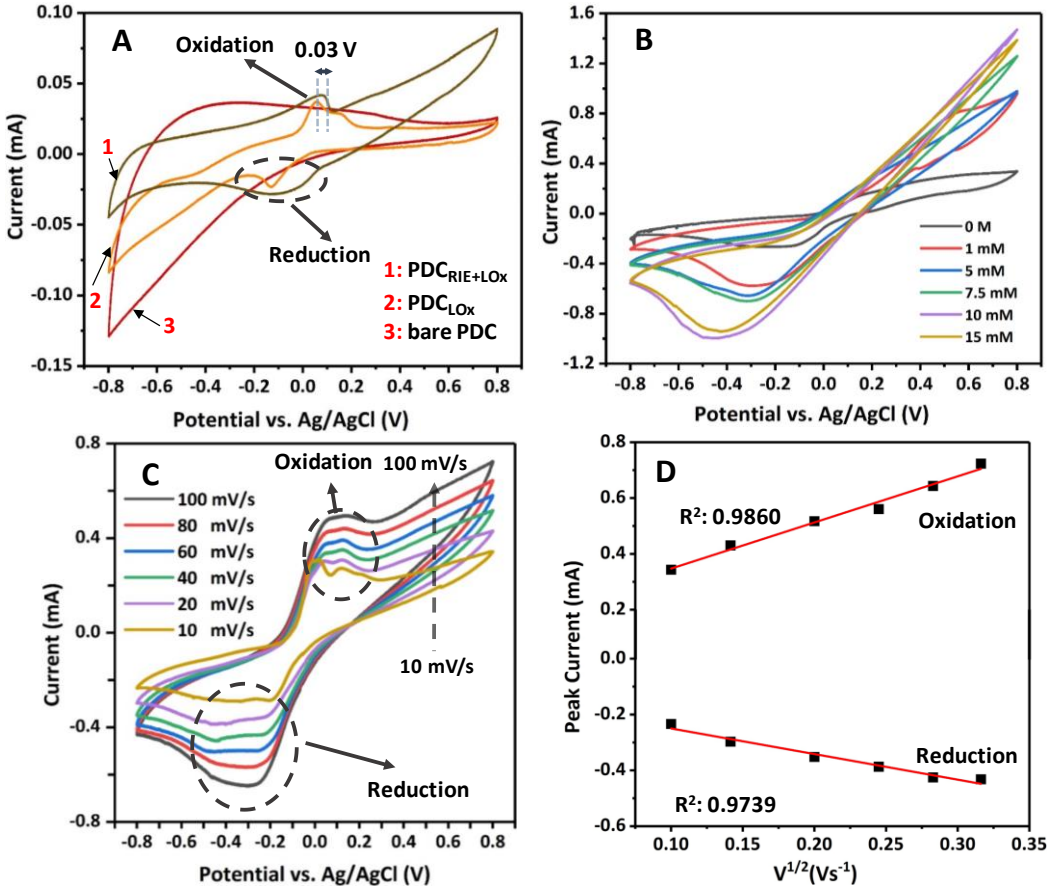

Figure 4.3 A) CV response of the bare PDC, PDCLOx, and PDCRIE+LOx in 500 µM LA solution. B) CV response of the bare PDC to different H2O2 concentrations. C) CV responses and D) correlation of peak currents to the square root of scan rate of PDCRIE+LOx in a 15 mM LA solution and different scan rates of 10 - 100 $mV.s^{-1}$ (vs Ag/AgCl).

0.08 V/0.042 mA. The appeared oxidation peaks are related to the oxidation reaction of LA molecules catalyzed by the LOx (eq. 1) and they are in good agreement with previous studies on electrochemical LA sensors [29, 30] while the reduction peaks are related to the reduction of H_2O_2 (equation 4.2).

$$\underset{\text{(Lactic Acid)}}{CH_3CH(OH)CO_2^- + O_2} \xrightarrow{LOx} \underset{\text{(Pyruvate)}}{CH_3COCOO^- + H_2O_2} \quad (4.1)$$

$$2H^+ + H_2O_2 + 2e^- \longrightarrow 2H_2O \quad (4.2)$$

The enhanced current response of $PDC_{RIE+LOx}$ to LA compared to PDC_{LOx} can be explained by the promoted immobilization of LOx enzymes onto the PDC microelectrodes surfaces by introducing carboxylic groups to the surface. In order to confirm the origin of observed peaks in CV results, the response of bare PDC microelectrode to H_2O_2 as a product of the LA oxidation reaction was studied. The results presented in Figure 4.3B shows that only the reduction reaction takes place in the presence of H_2O_2, and the reduction peak current increases by increasing the concentration of H_2O_2. The absence of oxidation peaks and a proportional increase in reduction current indicate that the observed oxidation and reduction peaks in Figure 4.3A are associated with LA oxidation (eq. 1) and H_2O_2 reduction (Eq. 2), respectively. The CV curves of $PDC_{RIE+LOx}$ in a 15 mM LA solution with various scan rates ranging from 10 - 100 $mV.s^{-1}$ (vs. Ag/AgCl) are presented in Figure 4.3C. The oxidation and reduction peak currents increase with the increasing scan rates. The relations between the square root of the scan rates and the oxidation/reduction peak currents are shown in Figure 4.3D. The peak currents are linearly proportional to the

square root of the scan rates up 100 mV.s^{-1} with the correlation coefficient (R^2) of 0.9860 and 0.9739 for oxidation and reduction, respectively. The linearity indicates that the process involves diffusion of LA, which is highly important for enzymatic electrochemical sensors [31].

4.3.3 Sensing Characterization of PDC Microelectrodes

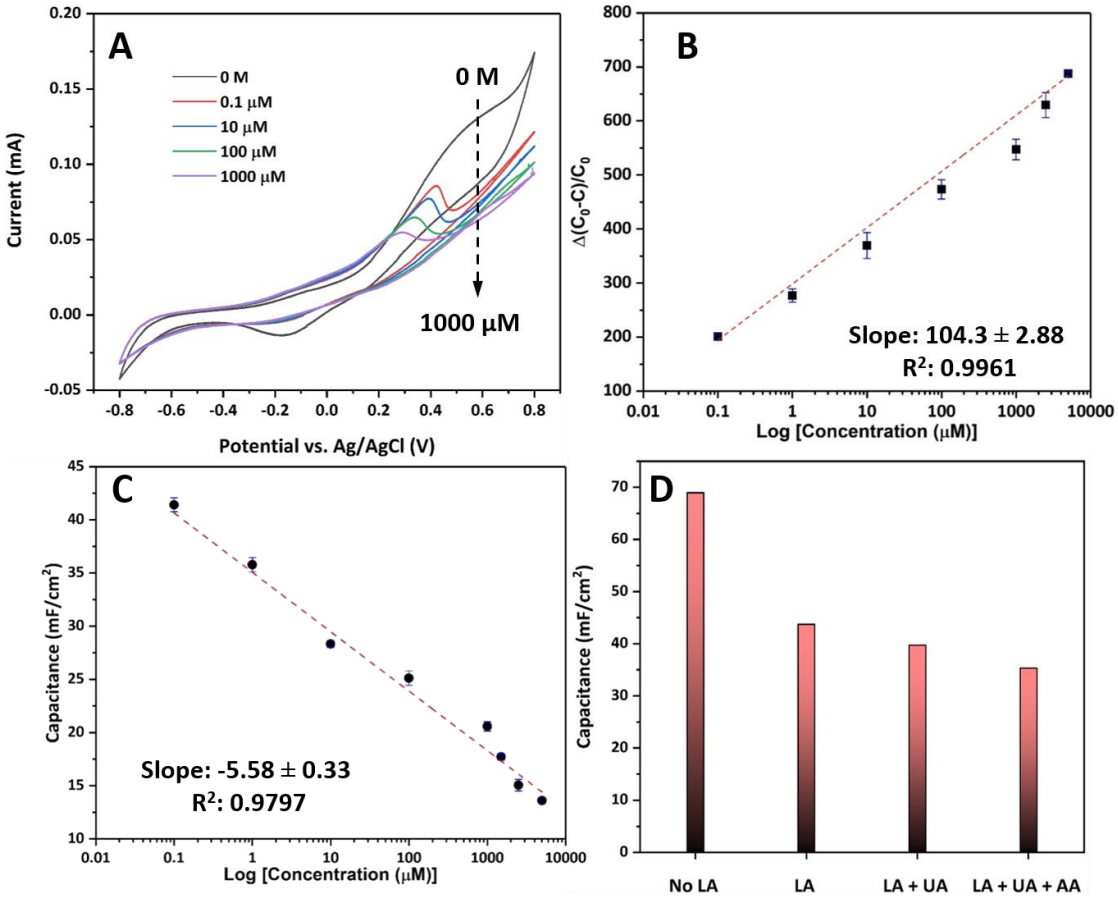

Figure 4.4 A) CV curves of PDCRIE+LOx in 0, 0.1, 10, 100, and 1000 µM LA solutions. B) Calibration plot of normalized areal capacitances calculated from CV curves in 0.1-5000 µM LA solutions. C) Calibration plot of absolute areal capacitances calculated from CV curves in 0.1-5000 µM LA solutions. D) The response of PDCRIE+LOx microelectrode to 500 µM LA and with 9.92 mg.mL-1 uric acid (UA) and 1.76 mg.mL-1 ascorbic acid (AA).

The CV results of the $PDC_{RIE+LOx}$ in the 0 - 1000 µM LA solutions are represented in Figure 4.4A. The oxidation peaks of 0.2 - 0.35 V (vs. Ag/AgCl) were observed by introducing the LA to the solution. The observed shift in the oxidation peaks by increasing LA concentration can be explained by the increased amount of oxygen uptake (equation 4.1) [34]. The areal capacitances were calculated from the CV curves to study the sensing performance of the $PDC_{RIE+LOx}$ using the equation 4.3 [35]:

$$C = \frac{1}{2AsΔV} \int IdV \qquad (4.3)$$

where *A* is the electrode area, *s* is the scan rate, ΔV is the voltage window, *I* is current, and *V* is the voltage. Figure 4.4B shows the calibration plot of normalized areal capacitances [$\Delta C_{normalized} = \Delta(C_0\text{-}C_i)/C_0$] for LA sensing in 0.1 - 5000 µM LA solutions, where each point is an average value of C (µF.cm^{-2}) from responses of optimized PDC sensor with repeated measurements of N=4. The area under the CV curves decreased substantially upon increasing the LA concentrations. The decrease in capacitance (charge density) suggests that the LA oxidation products are adsorbed to the PDC microelectrode surface and displace the double layer. The normalized areal capacitance showed a semi-logarithmic relationship with the LA concentrations ranging from 0.1 - 5000 µM. The linear dependence of the output capacitance on the logarithm of LA concentration has a slope of 104.3 ± 2.88 µF.cm^{-2}.(Log (µM))$^{-1}$ and the correlation coefficient (R^2) of 0.9961. The sensitivity of $PDC_{RIE+LOx}$ to LA can be estimated from the slope of the calibration curve of absolute capacitances (Figure 4.4C) as 18.94 mF.cm^{-2}.(Log (M))$^{-1}$. The dependence of capacitance to the logarithm of LA can be estimated as following (equation 4.4),

$$C=35.07 + 33.48\ Log\ (M)^{-1} \qquad (4.4)$$

where C is areal capacitance (mF.cm^{-2}) and M is the concentration (mol.L^{-1}) of LA.

The limit of detection (LoD) for PDC microelectrodes was calculated as 1.45 µM based on linear regression (equation 4.5) [36],

$$LoD = \frac{3S}{b} \quad (4.5)$$

where S is the standard deviation of the blank response (STDEV= 1.81 mF.cm^{-2}, N=8) and b is the slope of the calibration curve (b = -5.5815 mF.cm^{-2}.(Log (M))$^{-1}$) of absolute areal capacitance.

4.3.4 Selectivity and Stability of PDC Microelectrodes

The selectivity of the $PDC_{RIE+Lox}$ was studied by recording the response of the sensor to LA in the presence of uric acid (UA) and ascorbic acid (AA) in the system. The amounts of these interference agents were chosen to be 9.92 mg.mL^{-1} for UA and 1.76 mg.mL^{-1} for AA based on a suggested recipe for artificial human sweat [37]. Figure 4.4D shows the areal capacitance of $PDC_{RIE+Lox}$ before adding LA, in the presence of pure 500 µM LA,

Table 4.1 Comparison of recent electrochemical carbon-based enzymatic LA sensors

SUBSTRATE	ACTIVE ELECTRODE	MEASUREMENT TECHNIQUE	LINEAR RESPONSE RANGE	DETECTION LIMIT	STABILITY	REF
hydrophilic cloth	screen printed carbon electrode	electrochemiluminescence	0.05 - 2.5 mM	0.035 mM	96.4% after 18 days	[1]
cotton fabric	hand printed carbon graphite	amperometry	0.05 – 1.5 mM	5.0 µM	N/A	[2]
screen printed carbon	reduced graphene oxide with Au nanoparticles	amperometry	10 µM – 5 mM	0.13 µM	N/A	[5, 6]
pencil graphite electrode	multi walled carbon nanotubes/copper nanoparticles/polyaniline	amperometry	1.0 µM – 2.5 mM	0.25 µM	60% after 180 days	[7]
SiO2/Si	interdigitated PDC micro-fingers	capacitance measurement	100.0 nM - 5.0 mM	1.45 µM	97.65% after 20 days	current study

500 µM LA with uric acid, and 500 µM LA with uric acid and ascorbic respectively. The response of the sensor to LA in the presence of uric acid and ascorbic acid showed 80.07% of the initial signal, which indicates good selectivity. The operational stability of the $PDC_{RIE+LOx}$ was evaluated by recording the CV response to 500 µM LA every 2 days over 20 days. The results revealed a 2.35% decrease of the capacitance in 20 days, implying sufficiently well long lifetime and stability of the sensor. Table 4.1 compares the developed sensor in the current study with some of the recently reported carbon-based LA electrochemical sensors. The obtained detection limit in this work is sufficiently low in comparison to the results reported in the literature. Additionally, the developed sensor provided a wide linear response range, which adequately covers the target ranges of LA concentrations in healthy humans as well as most diseases and head trauma. The linear response range is wider than other carbon-based LA electrochemical sensors. Moreover, the sensor exhibited better stability and selectivity compared to most reports.

The developed PDC based enzymatic sensors can be further enhanced to be more feasible for clinical applications which could be an interesting topic for future studies. For instance, the performance of the purposed sensor can be improved by studying the effect of the ionic strength of LA and its oxidation products on the sensor's response and activity of LOx enzymes. Various optical-based techniques can be used for studying enzyme activity such as spectrophotometric assays, fluorometric, and chemiluminescent [38, 39]. Moreover, the developed enzymatic LA sensors can be integrated with other MEMS devices such as lab-on-disk designed by Dr. Madou group for point-of-care applications which is based on a compact disk (CD) centrifugal platform [40]. Furthermore, PDC microelectrodes can be adopted for detecting multiple targets in one sensing unit, which is commonly referred to

as multiplexing [41]. Multiplexing the C-MEMS based biosensors can be achieved by minor modifications of the PDC microelectrodes fabrication and functionalization process.

4.4 Conclusion

In this work, an electrochemical enzymatic lactic acid sensor based on photoresist-derived carbon microelectrode is successfully demonstrated. The oxygen-plasma treatment of photoresist derived carbon microelectrodes enhanced the immobilization of lactate oxidase enzymes on the surfaces of the electrodes through the covalent bonding of enzymes and -COOH groups. Furthermore, the oxygen-plasma treated photoresist derived carbon microelectrodes exhibited higher current generated during the oxidation of lactic acid in the electrolyte. The sensor yielded an extremely low detection limit of 1.45 µM, high sensitivity of 33.48 $mF.cm^{-2}.(Log\ (M))^{-1}$, and a relatively wide dynamic detection range of 0.1 - 5000 µM. The highly sensitive, selective, and stable LA sensor indicates that the C-MEMS platform is very promising for developing fast, precise, and biocompatible sensors for non-invasive detection of lactic acid.

4.5 References

[1] H. A. Favre and W. H. Powell, Nomenclature of organic chemistry: IUPAC recommendations and preferred names 2013: Royal Society of Chemistry, 2013.

[2] D. De Backer, "Lactic acidosis," Intensive care medicine, vol. 29, pp. 699-702, 2003.

[3] F. Alam, A. H. Jalal, S. Forouzanfar, M. Karabiyik, A. R. Baboukani, and N. Pala, "Flexible and Linker-Free Enzymatic Sensors Based on Zinc Oxide Nanoflakes for Noninvasive L-Lactate Sensing in Sweat," IEEE Sensors Journal, 2020.

[4] S. Walenta, M. Wetterling, M. Lehrke, G. Schwickert, K. Sundfør, E. K. Rofstad, et al., "High lactate levels predict likelihood of metastases, tumor recurrence, and restricted patient survival in human cervical cancers," Cancer research, vol. 60, pp. 916-921, 2000.

[5] S. Forouzanfar, F. Alam, N. Pala, and C. Wang, "A Review of Electrochemical Aptasensors for Label-Free Cancer Diagnosis," Journal of The Electrochemical Society, vol. 167, p. 067511, 2020.

[6] S. Azzouzi, L. Rotariu, A. M. Benito, W. K. Maser, M. B. Ali, and C. Bala, "A novel amperometric biosensor based on gold nanoparticles anchored on reduced graphene oxide for sensitive detection of l-lactate tumor biomarker," Biosensors and Bioelectronics, vol. 69, pp. 280-286, 2015.

[7] W. A. Neill, P. E. Jensen, G. B. Rich, and J. D. Werschkul, "Effect of decreased O 2 supply to tissue on the lactate: pyruvate ratio in blood," The Journal of clinical investigation, vol. 48, pp. 1862-1869, 1969.

[8] E. L. Cureton, R. O. Kwan, K. C. Dozier, J. Sadjadi, J. D. Pal, and G. P. Victorino, "A different view of lactate in trauma patients: protecting the injured brain," Journal of Surgical Research, vol. 159, pp. 468-473, 2010.

[9] R. A. Gatenby and R. J. Gillies, "Why do cancers have high aerobic glycolysis?," Nature Reviews Cancer, vol. 4, p. 891, 2004.

[10] H. Oliveros-Rodríguez, R. Estupiñán-López, and J. Rodríguez-Gómez, "Lactate serial measurements and predictive validity of early mortality in trauma patients admitted to the intensive care unit," Revista Colombiana de Anestesiología, vol. 45, pp. 166-172, 2017.

[11] C. Wang, G. Jia, L. H. Taherabadi, and M. J. Madou, "A novel method for the fabrication of high-aspect ratio C-MEMS structures," Journal of microelectromechanical systems, vol. 14, pp. 348-358, 2005.

[12] C. Wang and M. Madou, "From MEMS to NEMS with carbon," Biosensors and bioelectronics, vol. 20, pp. 2181-2187, 2005.

[13] H. Xu, K. Malladi, C. Wang, L. Kulinsky, M. Song, and M. Madou, "Carbon post-microarrays for glucose sensors," Biosensors and Bioelectronics, vol. 23, pp. 1637-1644, 2008.

[14] V. Penmatsa, A. R. Ruslinda, M. Beidaghi, H. Kawarada, and C. Wang, "Platelet-derived growth factor oncoprotein detection using three-dimensional carbon microarrays," Biosensors and bioelectronics, vol. 39, pp. 118-123, 2013.

[15] J.-H. Yang, V. Penmatsa, S. Tajima, H. Kawarada, and C. Wang, "Direct amination on 3-dimensional pyrolyzed carbon micropattern surface for DNA detection," Materials Letters, vol. 63, pp. 2680-2683, 2009.

[16] V. Penmatsa, H. Kawarada, Y. Song, and C. Wang, "Comparison of different oxidation techniques for biofunctionalization of pyrolyzed carbon," Material Science Research India, vol. 11, pp. 01-08, 2014.

[17] V. Penmatsa, T. Kim, M. Beidaghi, H. Kawarada, L. Gu, Z. Wang, et al., "Three-dimensional graphene nanosheet encrusted carbon micropillar arrays for electrochemical sensing," Nanoscale, vol. 4, pp. 3673-3678, 2012.

[18] X. Luo, H. Yu, and Y. Cui, "A Wearable Amperometric Biosensor on a Cotton Fabric for Lactate," IEEE Electron Device Letters, vol. 39, pp. 123-126, 2018.

[19] P. J. Lamas-Ardisana, O. A. Loaiza, L. Añorga, E. Jubete, M. Borghei, V. Ruiz, et al., "Disposable amperometric biosensor based on lactate oxidase immobilised on platinum nanoparticle-decorated carbon nanofiber and poly (diallyldimethylammonium chloride) films," Biosensors and Bioelectronics, vol. 56, pp. 345-351, 2014.

[20] C. Wang, L. Taherabadi, G. Jia, M. Madou, Y. Yeh, and B. Dunn, "C-MEMS for the manufacture of 3D microbatteries," Electrochemical and Solid-State Letters, vol. 7, pp. A435-A438, 2004.

[21] A. Alam, M. Howlader, and M. Deen, "The effects of oxygen plasma and humidity on surface roughness, water contact angle and hardness of silicon, silicon dioxide and glass," Journal of Micromechanics and Microengineering, vol. 24, p. 035010, 2014.

[22] S. Jadoon, S. Karim, M. R. Akram, A. Kalsoom Khan, M. A. Zia, A. R. Siddiqi, et al., "Recent developments in sweat analysis and its applications," International journal of analytical chemistry, vol. 2015, 2015.

[23] F. Alam, A. H. Jalal, S. Forouzanfar, C. Wang, and N. Pala, "ZnO Nanoflakes based Enzymatic Sensor for the determination of lactic acid in sweat," in 2019 IEEE SENSORS, 2019, pp. 1-3.

[24] E.-Y. Choi, T. H. Han, J. Hong, J. E. Kim, S. H. Lee, H. W. Kim, et al., "Noncovalent functionalization of graphene with end-functional polymers," Journal of Materials Chemistry, vol. 20, pp. 1907-1912, 2010.

[25] J. Coates, "Interpretation of infrared spectra, a practical approach," Encyclopedia of analytical chemistry, vol. 12, pp. 10815-10837, 2000.

[26] F. Alam, S. RoyChoudhury, A. H. Jalal, Y. Umasankar, S. Forouzanfar, N. Akter, et al., "Lactate Biosensing: The Emerging Point-of-Care and Personal Health Monitoring," Biosensors and Bioelectronics, 2018.

[27] M. M. Morrison, J. L. Roberts Jr, and D. T. Sawyer, "Oxidation-reduction chemistry of hydrogen peroxide in aprotic and aqueous solutions," Inorganic Chemistry, vol. 18, pp. 1971-1973, 1979.

[28] R. R. Adzic, F. C. Anson, and K. Kinoshita, "Proceedings of the Symposium on Oxygen Electrochemistry," Electrochem. Soc., Pennington, NJ,USA, Tech. Rep. ISBN: 1566771218, 1996..

[29] Y. Zhao, X. Fang, Y. Gu, X. Yan, Z. Kang, X. Zheng, et al., "Gold nanoparticles coated zinc oxide nanorods as the matrix for enhanced l-lactate sensing," Colloids and Surfaces B: Biointerfaces, vol. 126, pp. 476-480, 2015.

[30] Q. Chen, T. Sun, X. Song, Q. Ran, C. Yu, J. Yang, et al., "Flexible electrochemical biosensors based on graphene nanowalls for the real-time measurement of lactate," Nanotechnology, vol. 28, p. 315501, 2017.

[31] A. J. Bard, L. R. Faulkner, J. Leddy, and C. G. Zoski, Electrochemical Methods: Fundamentals and Applications. New York, NY, USA: Wiley, 1980.

5. PDGF-BB Aptasensors based on Thin-Film C-MEMS

5.1 Introduction

Cancer is the second major cause of death as responsible for an estimated 9.6 million death in 2019 [1]. Many cancer patients have a high chance of cure if they are diagnosed early [1]. An effective means to early diagnosis of cancer is quantifying the number of cancer biomarkers collected from biofluids like blood and urine [3]. Among the discovered cancer biomarkers detectable from blood, platelet-derived growth factor-BB (PDGF-BB) plays a crucial role in solid malignant tumors development and lymphatic metastasis [5]. Similarly, several studies have investigated the potential contribution of PDGF-BB in several benign tumors such as breast cancer [7], pancreatic cancer [9], prostate cancer [11], ovarian cancer [13], and liver cancer [14]. There is no food and drug administration (FDA) confirmation for the normal range of PDGF-BB in human plasma; however, the 0.1-1.5 ng mL^{-1} is widely considered as a normal range [15]. The concentration of this biomarker can vary vastly in different cancer diseases. For instance, PDGF-BB concentration above 42 ng mL^{-1} (the equivalent of 1.72 nM) is reported for patients with lung cancer [16]. The role of PDGF-BB in various cancerous tumors illustrates the importance of developing accurate and affordable point-of-care (POC) PDGF-BB cancer biomarkers sensors applicable to the diagnosis of cancerous tumors at early stages.

Synthetic affinity RNA and DNA based bio-recognizers, which are referred to as aptamers, have attracted considerable attention for developing cancer biosensors. Aptamers have various advantages that make them suitable for this purpose, such as the production of aptamers is highly repeatable, modifying aptamers (e.g., chemical modifications or attaching optical tags) is more accessible than that of modifying

antibodies, and aptamers show less non-specific detection phenomena compared to other bio-receptors [17]. Various mechanisms can be used for POC label-free aptamer-based biosensors (i.e., aptasensors), including optical, piezoelectric (i.e., mass-spectroscopy), and electrochemical detection strategies [18]. The optical aptasensors can offer an extremely low limit of detection and high signal to noise ratios. However, they have some critical drawbacks such as the need for complicated labeling processes and complicated optical analysis tools for obtaining output signals, and limitations in providing stable surface functionalization for aptamers immobilization [19]. The mass-spectroscopy (MS) can offer extremely accurate measurements. However, there are technical considerations in using MS, which makes this technique less feasible for on-site and POC applications. For instance, the MS machines require specific footprint area on each side of the MS machine, complicated analysis tools, and high sensitivity of this technique to surrounding conditions (e.g., requiring specific heat and ventilation system) are some of the complications related to MS measurements [20, 21]. The electrochemical aptasensors can be highly feasible for POC applications since they possess several advantages over other types of aptasensors. For instance, the electrochemical parameters can be measured without utilizing labels (i.e., label-free detection), in which label-free detection is referred to elimination of foreign molecule (e.g., fluorescents tags, chemiluminescent, and nanoparticle) that is temporarily or chemically attached to the target of interest to detect its presence or activity [22, 23]. They can be efficiently miniaturized and integrated with lab-on-chip devices and complementary metal–oxide–semiconductor (i.e., CMOS) circuits. The price of electrochemical sensing units can be considerably reduced. Besides, label-free electrochemical detection can reduce the cost of operation and blood sample consumption

by requiring relatively simple sample preparation [24-27]. However, the sensing performance of label-free electrochemical aptasensors such as sensitivity, selectivity, and dynamic range requires further enhancements to match the performance of the clinical test.

Recently, several studies have reported highly sensitive label-free electrochemical aptasensors for PDGF-BB detection. For example, Jiang et al. have developed an amperometric aptasensors based on hydroxyapatite nanoparticles deposited on a glassy carbon electrode with the amperometric signal linear in the range of 0.1 pg mL^{-1}-10 ng mL^{-1} PDGF-BB concentration [6]. Zhang et al. introduced a sensing probe based on graphene-enhanced with sliver nanoclusters that showed a linear range toward PDGF-BB from 32.3 fM–16.61 pM [2]. However, in most published studies, the linear range is narrower than the required linear range for cancer diagnosis purposes. For instance, the PDGF-BB concentrations higher than 42 ng mL^{-1} (the equivalent of 1.72 nM) has been discovered in serum samples of lung cancer patients [16]. Hence, further studies are required to improve the performance (especially detection range) of label-free electrochemical PDGF-BB aptasensors and make them more feasible for scale-up and mass production.

Carbon-based microelectromechanical devices (C-MEMS) are glassy-carbon devices derived from pyrolyzed epoxy-based photoresist (i.e., SU-8 photoresist) at high temperatures in oxygen-free environments. C-MEMS based electrodes have features that are highly suitable for biosensing applications such as good conductivity, high physiochemical stability, wide electrochemical window, higher tolerance against biofouling phenomenon, and highly accessible surface functionalization [28-31]. The surface of C-MEMS based electrodes can be functionalized with carboxyl functional

groups using vacuum ultraviolet, electrochemical activation, and oxygen reactive ion etching (RIE) [32, 33]. The C-MEMS's synthesis technique can offer electrodes with high resolution (i.e., tens of nanometer) and good yields of fabrication, which are highly favorable for POC applications [28]. The nano-enabled C-MEMS electrodes enhance aptamer immobilization efficiency (i.e., by providing larger accessible surface area), and highly accessible functionalization promotes the stability of the aptasensor by providing covalent immobilization of the aptamers.

In this work, we demonstrated a label-free electrochemical PDGF-BB aptasensors based on a thin layer (designated as ThL) electrodes fabricated via the C-MEMS synthesis procedure and PDGF-BB binding DNA aptamers. The designation of the "thin layer" refers to the single layer of photoresist derived carbon without additional 3-dimensional features such as micropillars. The ThL electrodes were pretreated with oxygen plasma oxidation treatment to form –COOH functional groups on their surfaces, in which amino-group modified affinity aptamers were immobilized directly on them. The Fourier-transform infrared spectroscopy (FTIR) was used to study the surface characteristics of the fabricated C-MEMS electrodes. Cyclic voltammetry (CV) and electrochemical impedance spectroscopy (EIS) were used to optimize the fabrication parameters and analyze the performance of the aptasensor. The results showed that the developed ThL-based PDGF-BB aptasensors are highly sensitive, selective, stable, and robust, and have a sufficiently broad dynamic range compared to previously reported label-free electrochemical PDGF-BB aptasensors. Furthermore, the C-MEMS technique is both feasible and amenable to mass production, thus making C-MEMS based PDGF-BB aptasensors promising for further enhanced cancer diagnosis and monitoring POC microdevices.

5.2 Materials and Methods

5.2.1 Materials and Reagents

The PDGF-BB binding aptamer (ssDNA, amino linker-5'-C_6-CAG GCT ACG GCA CGT AGA GCA TCA CCA TGA TCC TG-3' [18]) was purchased in HPLC purification from ThermoFisher Scientific, USA. Tris-ethylenediaminetetraacetic acid (TE) buffer, ethanol, acetone, phosphate-buffered saline (1M and pH 7.4) (PBS), 1-ethyl-3-(3-dimethylaminopropyl) carbodiimide hydrochloride linker (EDC), N-hydroxysuccinimide linker (NHS), hydrochloric acid (HCl), Polyoxyethylene (20) sorbitan monolaurate (Tween-20), KCl, and $k_3Fe(CN)_6$ were purchased from ThermoFisher Scientific, USA. Trehalose, bovine serum albumin (BSA), platelet-derived growth factor-AA, AB, and BB were purchased from Sigma Aldrich, USA. NANO^{TM} SU-8 25 negative photoresist was purchased from Microchem., USA. All the chemicals were analytical grade. Milli-Q (Sigma Aldrich, USA) deionized water (DI water) was used in this study.

5.2.2 Apparatus

The plasma-oxidation treatment was conducted via MARCH CS-1217 reactive ion etch (RIE) system. All electrochemical characterizations were carried out using a Bio-Logic versatile multichannel potentiostat (VMP3) at room temperature. The three-electrode cell, including ThL electrodes as the working electrode, a platinum wire as a counter electrode, and Ag/AgCl (KCl saturated) as a reference electrode, was used for all electrochemical measurements. The 713 Metrohm pH meter was used for measuring the pH of electrolytes. FTIR analysis was carried out using a JASCO FTIR 4100 equipped with

an attenuated total reflectance ATR accessory to verify –COOH carboxylic group and other functional groups on the sensor surfaces.

5.2.3 Fabrication of ThL Electrodes

The ThL electrodes were fabricated via the previously reported C-MEMS synthesis process [34, 35], which is schematically illustrated in Figure 5.1A and 5.1B. The fabrication process started with cleaning a 4-inch p-doped single-side polished silicon wafer by acetone and methanol. A layer of SU-8 25 photoresist was spin-coated on the wafer at 300 rpm for 10 seconds and then accelerated to 3000 rpm for 30 seconds to get a uniform photoresist layer with a thickness of approximately 15 µm. Soft bakes at 65°C for 3 minutes and 95°C for 7 minutes were conducted on hotplates which followed by UV light exposure with a dose of 300 mJ cm^{-2}. Post-exposure bakes were conducted at 65°C for 1 minute and 95°C for 5 minutes on hotplates. The electrodes were pyrolyzed in Lindenberg tube furnace with a temperature ramp of 10°C min^{-1} in two steps of 250°C with a dwell time of 30 minutes and 900°C with a dwell time of 60 minutes under 500 sccm flow of forming gas (5%H_2 + 95%N_2). The samples were left in the furnace to cool down to the room temperature overnight.

5.2.4 Preparation of PDGF-BB aptasensors

The ThL electrodes were functionalized using oxygen-plasma oxidation conducted in the RIE system illustrated in Figure 5.1C. The oxygen flow of 60 mL min^{-1} at 400 mTorr pressure and RF power of 100 W were used for functionalization. The optimum etching time was chosen as 7 minutes based on previous studies [32]. The oxygen plasma-treated

electrode (designated as ThL_{RIE}), was washed thoroughly in 1 M PBS for 5 minutes and DI water for 3 minutes before the next preparation steps.

The aptamer stock solutions were prepared based on the suggested procedure in the

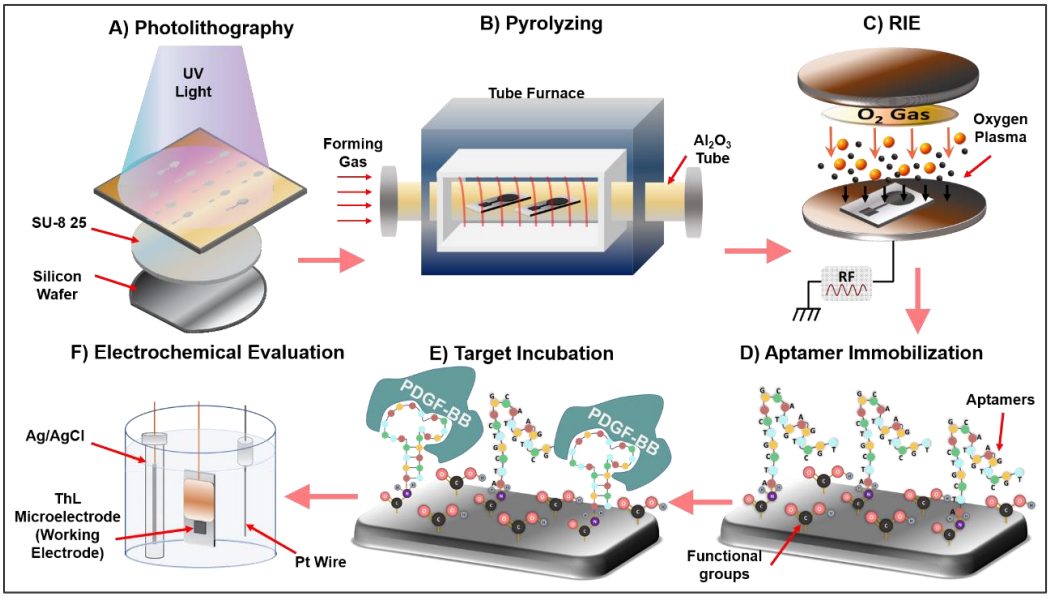

Figure 5.1 Schematic illustration of the fabrication process of the C-MEMS based PDGF-BB aptasensor and electrochemical test cell with 5 mL aqueous electrolytes based on a mixture of 5 mM k3Fe(CN)6 and 0.1 M PBS with various concentrations of KCl ranging from 50 m to 1M

datasheet released by ThermoFisher Scientific for oligonucleotides preparation and storage. The diluted stocks were prepared in 0.1 M TE buffer with a final volume of 10 µL. Before immobilizing aptamers, 5 µL of 20 mg mL^{-1} EDC and 10 µL of 20 mg mL^{-1} NHS were added to the solution of aptamer with desired concentration ranging from 50 nM to 15 µM. The aptamer solution was incubated for 30 minutes at room temperature. This step is recommended for activating the amino linker tag of the aptamers. The prepared aptamer solution was dropped on the ThL_{RIE} electrodes surfaces and followed by incubation for 2 hours at room temperature. After incubation, electrodes were washed thoroughly in DI water to wash any unattached aptamers. In order to quench blank areas of the ThL

electrodes, 50 µL of the aqueous solution of 0.1 M PBS + 1% (v:v) Tween-20 was dropped on the electrodes and followed by incubation for 10 minutes. The aptamer immobilized electrodes (designated as $ThL_{RIE+Apt}$) (Figure 5.1D) were washed by DI water for 5 minutes and stored in 0.1 M TE buffer in the refrigerator (4°C) when they were not in use.

5.2.5 Electrochemical Characterization of PDGF-BB Aptasensors

The stock solutions of PDGF-AA, AB, and BB were prepared based on the suggested procedure in the datasheet released by Sigma Aldrich. The samples were diluted in an aqueous solution of DI water and 5% (v:v) trehalose in the final volume of 15 µL. The desired target was added to the ThL electrodes and followed by incubation at room temperature (25°C) for various times ranging from 10 minutes to 150 minutes. The optimum time for reaction of target molecules with binding aptamers was found to be 40 minutes. Following target immobilization, which is schematically illustrated in Figure 5.1E, the ThL electrodes were washed in DI water before conducting electrochemical measurements. The electrodes incubated with the target were immediately tested via the three-electrode setup illustrated in Figure 5.1F for CV and EIS evaluations. The 5 mL aqueous electrolytes based on a mixture of 5 mM $k_3Fe(CN)_6$ and 0.1 M PBS with various concentrations of KCl ranging from 50 mM to 1 M were used for electrochemical measurements. In CV measurements, ThL electrodes were tested between -0.2 V to 0.6 V versus reference electrode with scan rates of 10–120 $mV.s^{-1}$. All CV data were typically taken after conducting 20 continuous cycles to make a reliable data recording. EIS measurements were recorded at frequencies range of 10-250,000 Hz and at various potentials including open-circuit potential (E_{OC}), 0.15, 0.2, and 0.35 V (vs. Ag/AgCl). The

pH of the electrolyte was adjusted using HCl to achieve electrolytes with a pH of 7.4-4.0. The optimum pH of 6.5 was used for sensing performance characterizations. After every electrochemical measurement, the C-MEMS aptasensors were regenerated by immersing the sensing electrodes in 1 M TE buffer with a gentle string for 30 minutes. It is worth mentioning that all the target incubations and electrochemical tests were conducted at room temperature (25°C).

5.3 Results and Discussion

In the PDGF-BB detection experiments, PDGF-BB binding aptamers modified with amino-linker tags were used as bio-recognizers. The FTIR and Electrochemical characterization were conducted on three types of C-MEMS thin layer (designated as ThL) electrodes samples referred to as ThL_{Bare}, ThL_{RIE}, and $ThL_{RIE+Apt,}$ which they describe the C-MEMS electrodes without any modifications, after RIE functionalization, and after immobilizing aptamers, respectively. The 2.5 µM aptamer concentration was used in the fabrication of $ThL_{RIE+Apt}$ studied in subsections 5.3.1, 5.3.2, and 5.3.3 with an exception for $ThL_{RIE+Apt}$ electrodes prepared to study the effect of aptamer concentration. The optimum aptamer concentration of 7.5 µM was used for the fabrication of $ThL_{RIE+Apt}$ electrodes studied in subsections 5.3.4 and 3.5. The active area of 5×5 mm^2 in all C-MEMS electrodes was confined using bee wax to minimize the side reactions. The 5 mM of $K_3Fe(CN)_6$ was used as a redox agent.

Two electrochemical measurement strategies of EIS and CV were used for analytical purposes. The faradaic mode of EIS was conducted at the oxidation potential of $Fe(CN)_6^{-3/-4}$ to measure the charge-transfer resistance. The CV measurements were conducted at a scan rate of 50 mV s^{-1} unless it is mentioned otherwise (i.e., in studies on the effect of scan

rates presented in section 3.2). The areal capacitances were calculated from CV curves using equation 5.1 [36]:

$$C = \frac{1}{2AS\Delta V} \int IdV \qquad (5.1)$$

where *A* is the electrode area, *s* is the scan rate, ΔV is the voltage window, *I* is current, and *V* is the voltage. It is worth mentioning that the sample size (i.e., n) in this article refers to the number of repeated tests on each measurement point, which varies between 3 to 20 throughout the measurements presented herein.

5.3.1 FTIR Characterization of ThL Electrodes

The FTIR characterization was used to confirm the formation of carboxylic groups during the functionalization and immobilization of affinity aptamers via amide binding on the surfaces of the C-MEMS electrodes. The FTIR spectra of ThL_{Bare}, ThL_{RIE}, and $ThL_{RIE+Apt}$ are represented in Figure 5.2. All three samples showed two peaks between 2800-3000 cm^{-1} and two peaks between 2300-2400 cm^{-1}, which are attributed to OH and sp C-H stretching, and sp C≡C bending, respectively[37]. Furthermore, ThL_{RIE} showed a peak at 823 cm^{-1}, and $ThL_{RIE+Apt}$ showed two peaks at 607 cm^{-1} and 819 cm^{-1}, which are attributed to sp^2 C-H bending [37].

The spectrum of the ThL_{Bare} showed a peak at 1110 cm^{-1}, which is assigned to alkoxy C-O [38]. This peak is the result of native oxidation of carbon in contact with air. The FTIR spectrum of ThL_{RIE} and $ThL_{RIE+Apt}$ exhibited the same peak around 1155 and 1105 cm^{-1}, respectively. The FTIR of ThL_{RIE} also showed a peak at 1251 cm^{-1}, which is attributed to acyl C-O[38]. The peak at 1730 cm^{-1} in the ThL_{RIE} and $ThL_{RIE+Apt}$ spectrum

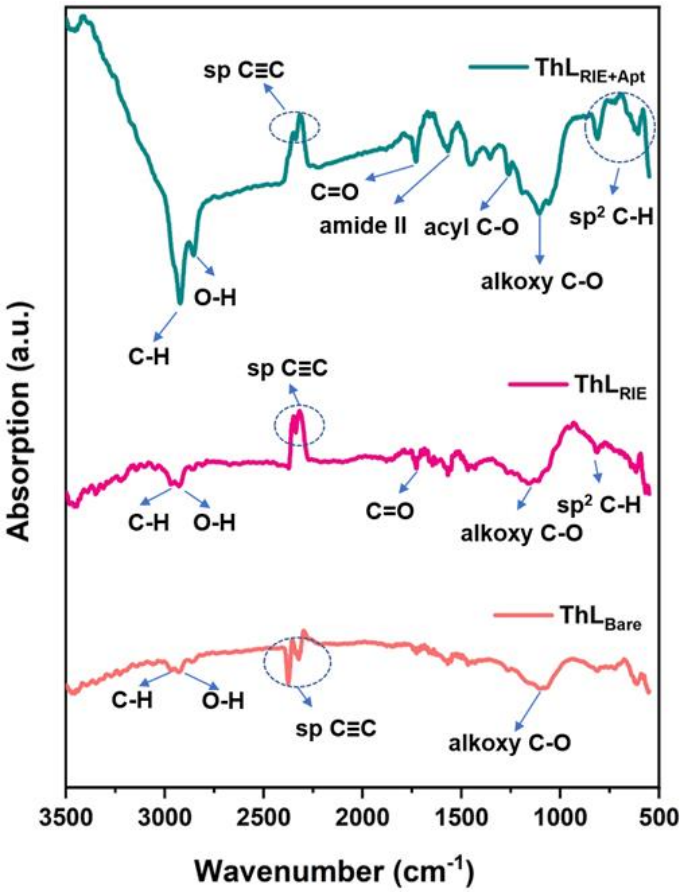

Figure 5.2 FTIR spectra of ThL electrodes before functionalization (ThL_{Bare}), after functionalization (ThL_{RIE}), and after aptamer immobilization ($ThL_{RIE+Apt}$).

is attributed to C=O stretching vibrations, which indicate that the ThL electrodes were successfully functionalized with carboxylic groups [38]. The FTIR spectrum for $ThL_{RIE+Apt}$ shows an apparent peak at 1571 cm^{-1}, which is related to the amide II bond and represents covalent bonding affinity aptamers on the surfaces of the ThL electrodes [37]. The FTIR results confirm that the oxygen plasma oxidation treatment was a simple yet effective means for generating reactive surfaces with the high possibility of covalent bonding of PDGF-BB binding aptamers on ThL electrode surfaces.

5.3.2 Electrochemical Analysis of ThL Electrodes

In this section, electrochemical analyses of C-MEMS electrodes after each stage of development are presented. These analyses aimed to confirm the successful immobilization of aptamer and binding of target molecules on surfaces of aptasensors. Two hypotheses for designing the aptasensors were considered; first, the formation of PDGF-BB oncoproteins-aptamer complex (i.e., capturing the target molecules) increases the charge-transfer resistance by hindering the access of redox species to the surface of the aptasensor. Second, the formation of this complex diminishes the double-layer capacitance (i.e., charge density), which can be traced by calculating the areal capacitance from CV measurements as well as evaluating the double layer capacitance from EIS measurements. The EIS measurements were conducted in the faradaic mode (E=0.35 V vs. Ag/AgCl) and non-faradaic mode ($E=E_{OC}$) to measure the charge-transfer resistance and the double-layer capacitance, respectively. The 500 pM PDGF-BB was used as the sample target (referred to as T). Randle's equivalent circuit (Fig. S1) was used to evaluate the charge-transfer resistance values from EIS measurements. This circuit was composed of Rs, C_{DL}, R_{CT}, and Z_W representing the solution resistivity, the double-layer capacitance, the charge-transfer resistance, and impedance of the cell in low frequencies (i.e., Warburg impedance), respectively. The faradaic path was modeled with R_{CT} and Z_W. Furthermore, the assumption on the reversibility of oxidation/reduction of $Fe(CN_6)^{-3/-4}$ redox couple was validated by measuring the CV responses with various scan rates.

The results of the EIS characterization of ThL_{Bare}, ThL_{RIE}, $ThL_{RIE+Apt}$, and responses of $ThL_{RIE+Apt}$ electrodes to 500 pM PDGF-BB are represented. in Figure 5.3A. The Nyquist

plot of ThL_{Bare} has a small semi-circle radius compared to the others, which indicates a small R_{CT} of 72.01 Ω and good conductivity of the ThL_{Bare} electrodes. ThL_{RIE} electrode has a higher R_{CT} of 152.18 Ω compared to the ThL_{bare}, which is due to the negatively charged carboxylate group covering the surface of ThL_{RIE}. The immobilization of aptamers slightly decreased the R_{CT} to a value of 114.9 Ω, which could be the result of the engagement of carboxylate groups of the surface in amide bonding (i.e., covalent immobilization of aptamers) and quenched remaining carboxyl groups by Tween-20 quencher. The $ThL_{RIE+Apt}$ electrode incubated with target molecules ($ThL_{RIE+Apt}$+T) has a considerably high R_{CT} of 1423.9 Ω, which is resulted by isolative properties of the target and reduced access of the charged species to the surface of the sensing electrodes [39].

The results of the CV measurements, which were designed to examine the second hypothesis and validate the efficiency of CV measurements, are shown in Figure 5.3B. The curves represent the CV characteristics of the ThL_{Bare}, ThL_{RIE}, $ThL_{RIE+Apt}$, and their response to 500 pM PDGF-BB. ThL_{Bare} and ThL_{RIE} electrodes showed no response to PDGF-BB in which the areal capacitance of ThL_{Bare} remained 6.05 mF cm^{-2} after target incubation and the areal capacitance of ThL_{RIE} showed a negligible change of 23.38 to 22.34 mF cm^{-2} after target incubation. The area of CV curve of the $ThL_{RIE+Apt}$ electrode after PDGF-BB incubation showed a noticeable decrease. The binding of PDGF-BB oncoproteins decreased the areal capacitance of the $ThL_{RIE+Apt}$ electrode from 14.14 to 7.24 mF cm^{-1}. This change indicates that the aptamers were able to capture the target molecules successfully, and CV measurement is sensitive to the captured PDGF-BB oncoproteins. Furthermore, the second hypothesis was investigated by studying the fitting value of C_{DL} measured at non-faradaic mode (i.e., at $E=E_{OC}$). The calibration curve of C_{DL} fitting values

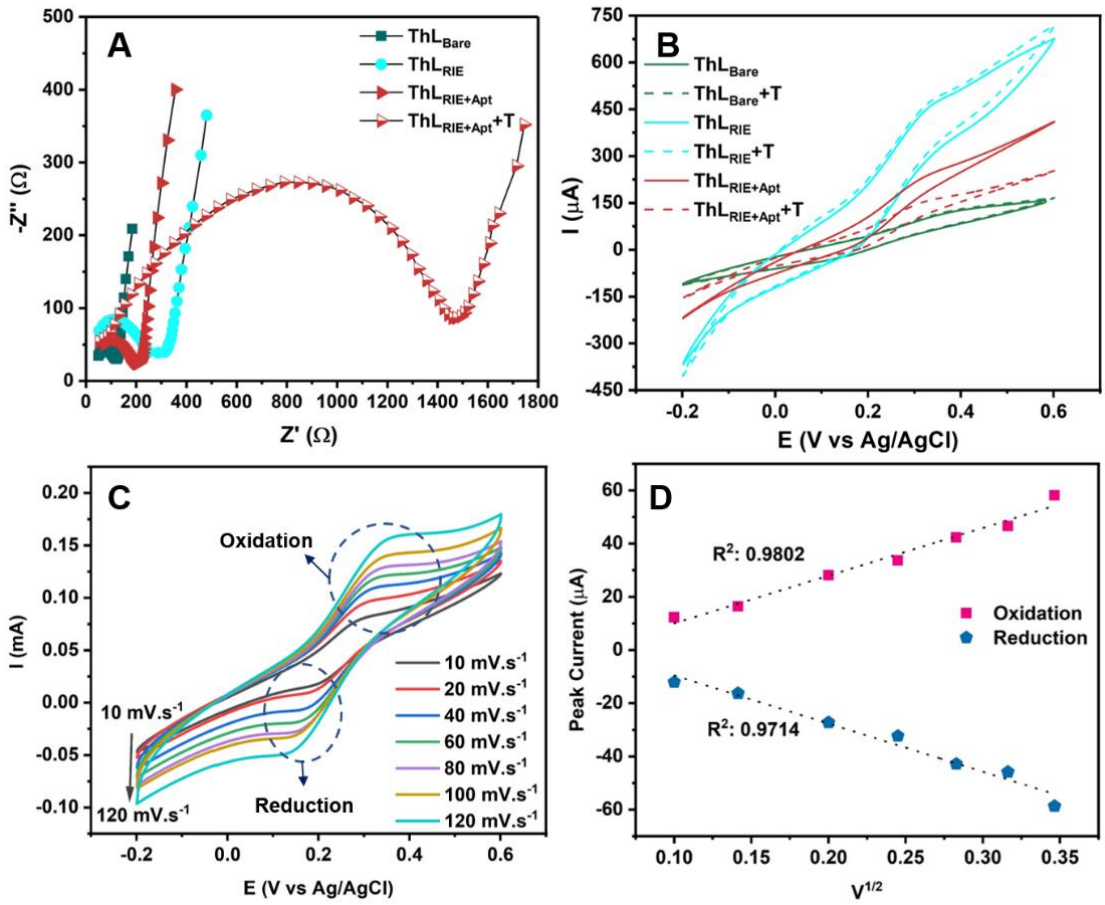

Figure 5.3 . A) The Nyquist plots of ThL electrodes at various stages of development and response of $ThL_{RIE+Apt}$ electrode to 500 pM PDGF-BB. B) The CV responses of ThL_{bare}, ThL_{RIE}, and $ThL_{RIE+Apt}$ electrodes to 500 pM PDGF-BB. C) The CV curves of the $ThL_{RIE+Apt}$ electrode at various scan rates ranging from 10–120 mV s^{-1}. D) The calibration curves of oxidation and reduction peak current versus the square root of scan rates.

reveals a declining linear response to the logarithm of PDGF-BB concentration with a slope of -5.02×10^{-7} Ω $Logc^{-1}$ (unit of c, nM) and correlation coefficient (R^2) of 0.8488. Both CV and EIS results validate the second hypothesis on responses of C-MEMS electrodes to target molecules.

In order to investigate the reversibility of the oxidation/reduction of $Fe(CN)_6^{-3/-4}$ and the ohmic drop, a set of CV measurements with different scan rates were conducted on $ThL_{RIE+Apt}$ electrodes. The CV curves of $ThL_{RIE+Apt}$ measured in different scan rates in the

range of 10–120 mV s^{-1} are shown in Figure 5.3C, indicating the oxidation and reduction peak currents found to be linearly proportional to the square root of the scan rates in the range of 10–120 mV s^{-1} with R^2 of 0.9802 and 0.9714 for oxidation peak currents and reduction peak currents, respectively (Figure 5.3D). This linear correlation indicates that a diffusion-controlled process accrued on the $ThL_{RIE+Apt}$ electrodes. Hence, the Randles-Sevcik equation (equation 5.2) was used to calculate the electrochemically active surface area of the $ThL_{RIE+Apt}$ electrodes at room temperature (T=295 K) [40].

$$I_P=(2.69\times10^5)n^{3\backslash2}ACD^{1/2}v^{1/2} \quad (5.2)$$

where n is electron transfer number (n=1), A is active surface area (cm^{-2}), C is the concentration of $Fe(CN)_6^{-3\backslash-4}$ (5 mol cm^{-3}), D is the diffusion coefficient of 5 mM $Fe(CN)_6^{-3/-4}$ (7.6×10^{-6} cm^2 s^{-1}), and v is the scan rate (V s^{-1}). The active surface area was calculated as 0.0313 cm^2 with a STDEV of 0.00193.

The charge transfer coefficient (α) for a similar system was assumed to be 0.5 [41]. The α was calculated experimentally using the equation 5.3[40].

$$E_P - E_{P/2}= 48/\alpha n \quad (5.3)$$

where E_P (mV) is the voltage of peak current and n is electron transfer number (n=1). The value of α for oxidation reactions was found to have an average of 0.41 with STDEV of 0.0172. The theoretical and experimental values are slightly different, but this difference is insignificant since the experimental value lies in the reversible zone [40]

The Nicholson method based on peak separation (equation 5.4) was used for evaluating the standard heterogeneous electron transfer rate constant (k^0) [42].

$$k^0=2.18\left[\frac{\alpha DnFv}{RT}\right]^{1/2} exp\left[\frac{-\alpha^2 nF(E_{P,O-E_{P,R}})}{RT}\right] \quad (5.4)$$

where α was calculated from Eq. 3, D is the diffusion coefficient of 5 mM $Fe(CN)_6^{-3/-4}$ (7.6×10^{-6} cm^2 s^{-1}), F is Faraday constant (96,485.34 C mol^{-1}), ν is scan rate (V s^{-1}), R is the universal gas constant (8.3145 J mol^{-1} K^{-1}), T is room temperature (295 K), $E_{P,O}$ and $E_{P,R}$ are oxidation and reduction peak current, respectively [40]. The calculated standard heterogeneous electron transfer rate constants (k^0) had an average of 0.00036 cm s^{-1} and STDEV of 0.00006 with the highest value at the scan rate of 50 mV s^{-1}.

Furthermore, the highest oxidation to the reduction peak currents had a ratio of 1.015, which indicates a reversible reaction [43]. The peak-to-peak separation values in each scan rate had a STDEV of 0.008 V, which indicates that the reaction was reversible and the adsorption of redux species on the surface of $ThL_{RIE+Apt}$ was negligible. Besides, the small variation in peak-to-peak separation indicated the small ohmic drop of solution [43, 44].

5.3.3 Optimization of Fabrication and Sensing Conditions

Several known factors can affect the performance of electrochemical aptasensors [18]. In this study, we have analyzed the effect of four parameters on responses of the C-MEMS aptasensors, including reaction-time, the binding aptamer concentration, the pH of the electrolyte, and concentration of supporting salt (i.e., KCl). It worth noting that the temperature of the target incubation bath can also affect the sensing performance of the aptasensors [45]. In designing the C-MEMS based aptasensors, it was envisioned that the aptasensing unit would be integrated with temperature control units to make sure the aptasensor performs at its optimized condition.

Reaction time in aptasensors is referred to as the minimum time required for the formation of the aptamer-target complex, and it mainly depends on the DNA features (e.g., the length of the DNA sequence) [18]. As expected, longer reaction times (i.e., incubation) would result in better detection efficiency. This optimization aimed to define the reaction times to be both sufficiently quick and efficient. For investigating the effect of reaction time, the $ThL_{RIE+Apt}$ electrodes were incubated with the target for various periods ranging from 10-150 minutes and tested by measuring the areal capacitance calculated from the CV curves using Eq. 1. The results are presented in Figure 5.4A with the error bars calculated for n=3 measurements. As shown, the areal capacitances decrease by increasing the reaction up to 40 minutes and saturate afterward. Hence, 40 minutes was chosen as the optimum reaction time.

In this study, we recorded the capacity values after the redox reaction fully completed, so the concentration of the aptamer stock solution was simply considered as the aptamer concentration. For each aptamer concentration ranging from 0.5-10 μM, a separate $ThL_{RIE+Apt}$ electrode was used. The areal capacitances were calculated from CV measurements conducted on $ThL_{RIE+Apt}$ electrodes using equation 5.1 for n=3 measurements. As it is represented in Figure 5.4B, the $ThL_{RIE+Apt}$ electrode has its peak capacitive response at the aptamer concentration of 7.5 μM. The likely reason for the observed bell-shaped plot on the effect of aptamer concentration can be the reduced amount of immobilized affinity aptamers after a certain concentration due to repealing of the DNA molecules by other DNA molecules; since DNA molecules are negatively charged because of their phosphate groups[46]. Consequently, the reduced amount of immobilized binding aptamers lessens the areal capacitance change in response to PDGF-BB, which can be seen

as an increased value of areal capacitance after 7.5 µM aptamer concentration. Based on the results, the optimum aptamer concentration of 7.5 µM was used for the fabrication of C-MEMS aptasensors.

The optimum pH for electrochemical measurement was studied by measuring CV responses of $ThL_{RIE+Apt}$ electrodes to 500 pM PDGF-BB measured in the electrolyte of 0.1 M PBS/ 0.2 M KCl/ 5 mM $K_3Fe(CN)_6$ at different pH ranging from 5 to 7.5. As shown in Figure 5.4C, the highest response was recorded at pH 6.5. Hence, pH 6.5 was used for sensing measurements. The effect of supporting salt in the electrolyte on electrochemical

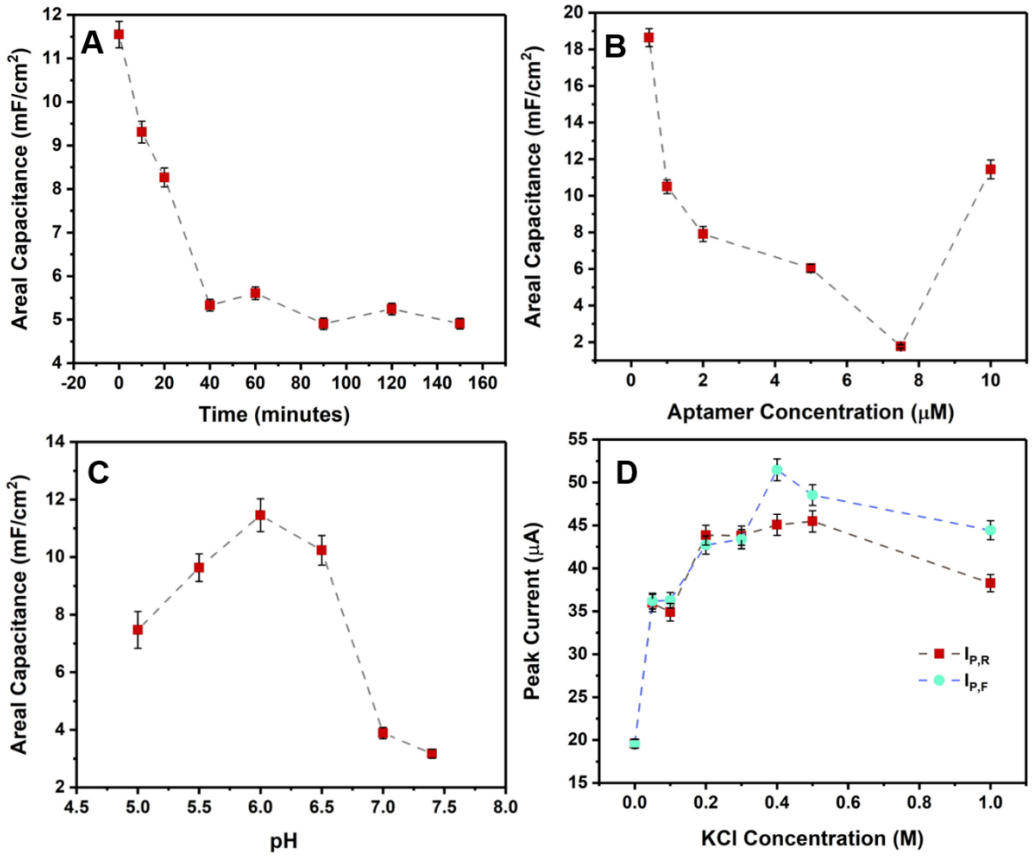

Figure 5.4 A) Areal capacitances calculated from CV curves measured for 500 pM PDGF-BB to study the effect of reaction times. B) Areal capacitances calculated from CV curves measured for 500 pM PDGF-BB to study the effect of aptamer concentration. C) Areal capacitances calculated from CV curves measured for 500 pM PDGF-BB in electrolytes with different pH. D) The oxidation peak currents ($I_{P,F}$) and reduction peak currents ($I_{P,R}$) were measured via CV vs. KCl concentration ranging from 0–1 M.

measurements was studied by conducting CV measurements on $ThL_{RIE+Apt}$ in electrolytes with different KCl concentrations varying from 0-1 M. As the results represented in Figure 5.4D show, the forward (oxidation) peak current (designated as $I_{P,F}$) and reverse (reduction) peak current (designated as $I_{P,R}$) increase proportionally by increasing the KCl concentration up to 0.2 M. Further increasing the KCl concentration did not affect the $I_{P,R}$. At the same time, the $I_{P,F}$ continued its increase up to 0.4 M KCl concentration. The correlation of $I_{P,F}$ and $I_{P,R}$ shows that the oxidation and reduction of $Fe(CN)_6^{-3/-4}$ was reversible up to 0.3 M KCl, and further increasing KCl concentration made the reaction irreversible. By considering the observed saturation point for $I_{P,R}$, the optimum KCl concentration of 0.2 mM was used for sensing performance characterizations.

5.3.4 Sensing Performances of PDGF-BB Aptasensors

The turn-off and turn-on strategies can apply to label-free electrochemical aptasensors in similar manners to optical aptasensors [47, 48]. In this study, the turn-off strategy was designed based on measuring areal capacitances using CV measurements. Likewise, the turn-on strategy was designed based on measuring R_{CT} via EIS measurements in the faradaic mode.

The turn-off responses of C-MEMS aptasensor measured for $ThL_{RIE+Apt}$ in response to 0–50 nM PDGF-BB are presented in Figure 5.5A. The oxidation of peak $Fe(CN)_6^{-3/-4}$ at E= 0.3V (vs. Ag/AgCl) was decreased proportionally to the increase of the PDGF-BB concentration. The observed decrease in the peak current is the result of increased R_{CT} of the sensing probe. The calibration curve for calculated areal capacitances using Eq. 1 is shown in **Figure 5.5B**. The calibration curve was obtained by calculating the average value

of areal capacitances (mF cm^{-2}) from the responses of optimized $ThL_{RIE+Apt}$ aptasensor with the repeated measurements of n=5. The area under the CV curves decreased substantially upon increasing the PDGF-BB concentrations. The decrease in the areal capacitance (charge density) suggests that the PDGF-BB oncoproteins were successfully attached to the $ThL_{RIE+Apt}$ surface and displaced the double-layer [39]. The linear dependence of the output capacitance on the logarithm of PDGF-BB concentration has a slope of -3.33 mF cm^{-2} $Logc^{-1}$ (unit of c, nM) and the R^2 of 0.9751. The correlation of $ThL_{RIE+Apt}$ capacitance to the logarithm of PDGF-BB concentration can be assessed as following (equation 5.5),

$$C=8.93 - 3.33\ Logc^{-1},\ r=0.9688 \qquad (5.5)$$

where *C* is the areal capacitance (mF cm^{-2}), *c* is the PDGF-BB concentration (nano-mol L^{-1}) and *r* is the regression coefficient. Hence, the CV measurement's sensitivity to PDGF-BB can be calculated as 3.33 mF cm^{-2} $Logc^{-1}$ (unit of c, nM) The limit of detection (LoD) for $ThL_{RIE+Apt}$ aptasensors based on CV measurements was calculated as 7 pM based on the linear regression (equation 5.6)[49],

$$LoD = \frac{3S}{b} \qquad (5.6)$$

where *S* is the standard deviation of the blank response (STDEV= 0.0353 mF cm^{-2}, n=9), and *b* is the slope of the calibration curve (*b* = -13.82 mF cm^{-2} c^{-1} (unit of c, nM) of areal capacitances.

The turn-on responses of C-MEMS aptasensors measured for $ThL_{RIE+Apt}$ in response to 0–50 nM PDGF-BB are represented in **Figure 5.5C**. The EIS data were recorded at the $E=E_{oxidation}$ (vs. Ag/AgCl), which was defined by conducting CV measurements intended to measure the R_{CT} in faradaic mode. The radius of semi-circles in Nyquist plots, which represents the *resistivity of solution+*R_{CT}, increased proportionally to

the increase of PDGF-BB. The increase of R_{CT} can be explained by target molecule isolative properties [39]. The aforementioned equivalent circuit (Fig. S1) was used for obtaining the values of R_{CT} in which a good match between the fitting curves and measured

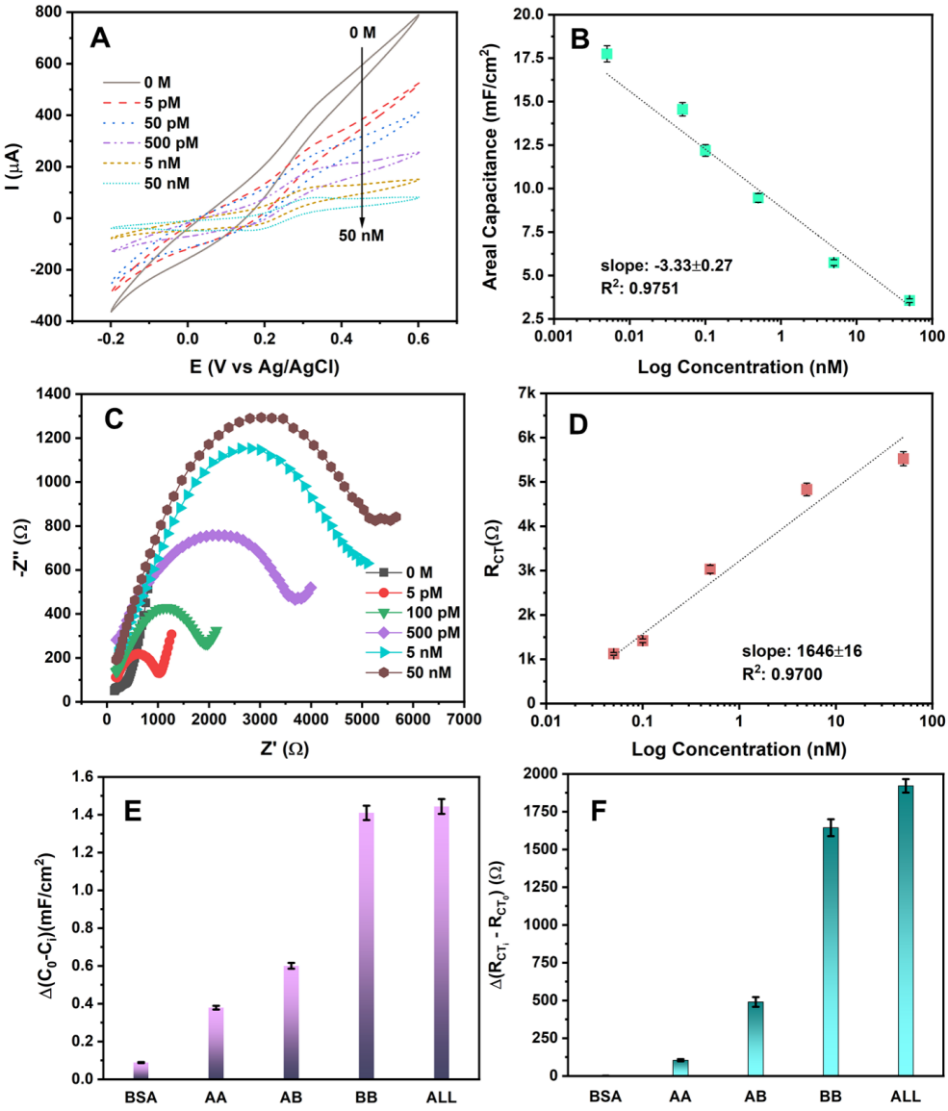

Figure 5.5 A) CV curves of the ThLRIE+Apt electrode's response to PDGF-BB ranging from 0–50 nM. B) Calibration curve for calculated areal capacitances from CV curves with n=5. C) EIS Nyquist plots of the $ThL_{RIE+Apt}$ electrode's response to PDGF-BB ranging from 0–50 nM. D) Calibration curve for R_{CT} extracted from Nyquist plots with n=5. E) Areal capacitances calculated from CV curves and F) R_{CT} calculated from EIS Nyquist plot measured in response of $ThL_{RIE+Apt}$ electrodes to 4 μg mL^{-1} BSA. 50 nM PDGF-AA, 50 nM PDGF-AB, and 500 pM PDGF-BB and all the interference agents added to 500 pM PDGF-BB (designated as ALL).

curves was observed (Table S1). The calibration curve of R_{CT} measured for each concentration of PDGF-BB with repeated measurements of n=5 is presented in Figure 5.5D. The linear dependence of the R_{CT} on the logarithm of PDGF-BB concentration has a slope of 1.65×10^3 Ω $Logc^{-1}$ (unit of c, nM) and R^2 of 0.9700. The correlation of R_{CT} to the logarithm of PDGF-BB concentration can be assessed as following (equation 5.7),

$$R_{CT}=3.22\times10^3 + 1.65\times10^3\ Logc^{-1},\ r=0.9604 \quad (5.7)$$

where R_{CT} is charge transfer resistance (Ω), c is the PDGF-BB concentration (nano-mol L^{-1}), and r is the regression coefficient. The EIS measurement's sensitivity to PDGF-BB is found to be 1.65×10^3 Ω $Logc^{-1}$ (unit of c, nM). The LoD for $ThL_{RIE+Apt}$ aptasensors based on EIS measurements was calculated as 1.9 pM based on linear regression (Eq. 6) in which S (i.e., STDEV) was calculated as 2.39 Ω (n=20), and b was calculated as 4.16×10^3 Ω c^{-1} (unit of c, nM).

Both detection strategies were found to be sensitive toward the PDGF-BB with a wide range and linear response. The result showed that the turn-on strategy established lower LoD compared to the LoD for turn-off strategy measurements. The difference in LoD achieved by turn-on and turn-off strategies could be a result of the difference in the essence of CV and EIS measurements as well as considered assumptions for calculating the areal capacitance and R_{CT}.

5.3.5 Analytical Parameters of PDGF-BB Aptasensors

In this study, four analytical parameters of selectivity, stability, repeatability, and robustness of C-MEMS PDGF-BB aptasensor were evaluated. The selectivity of the $ThL_{RIE+Apt}$ aptasensors was studied by measuring the response of the aptasensors to 4 µg

mL^{-1} BSA, 50 nM PDGF-AB, and 50 nM PDGF-AA along with 500 pM PDGF-BB. The concentrations of interference agents were chosen to be approximately 100 times more than that of the target molecules. The results of selectivity measurements are presented in Figure 5.5E and 5.5F in which the areal capacitances (Figure 5.5E) and R_{CT} (Figure 5.5F) were calculated from the CV curves and EIS Nyquist plots and differentiated from their blank responses, respectively. The capacitive response of $ThL_{RIE+Apt}$ aptasensors to PDGF-BB was 3.72 and 2.34 times higher than that of the aptasensors to PDGF-AA and PDGF-AB, respectively. Likewise, the resistive response of $ThL_{RIE+Apt}$ aptasensors to PDGF-BB was 15.79 and 3.35 times higher than that of the aptasensors to PDGF-AA and PDGF-AB, respectively. Furthermore, the normalized responses of the label-free C-MEMS aptasensor to interference agents shows the superior selectivity response of the resistance detection method over the capacitance detection method. The selectivity studies suggest that the EIS

Table 5.1 Comparison of recent electrochemical PDGF-BB aptasensors

Substrate	**Active Electrode**	**Labeling**	**Measurement Technique/Parameter**	**Linear Range**	**LoD**	**Ref.**
Au	graphene doped with silver nanoclusters	label-free	EIS/R_{CT}	32.3 fM–1.61 pM	26.5 fM	[2]
glassy carbon	graphene/multi walled carbon nanotubes doped with Se	label-free	differential pulse voltammetry/current	0.1 pM-10 nM	27 fM	[4]
glassy carbon	hydroxyapatite nanoparticles	labeled: hydroxyapatite nanoparticles	square wave voltammetry/current	0.1 pg mL^{-1}-10 ng mL^{-1}	50 fg mL^{-1}	[6]
glassy carbon	molybdenum selenide–graphene	labeled: exonuclease III	differential pulse voltammetry/current	0.0001–1 nM	20 fM	[8]
N/A	catalytic-induced DNA hydrogel	labeled: C_3N_4/Au/Fc-NH_2	square wave voltammetry/current	0.01 pM-10 nM	3.5 fM	[10]
glassy carbon	MoS_2/carbon/gold nanoparticles aerogel composites	labeled: 6-ferrocenyl hexanethiol	differential pulse voltammetry/current	0.001-10 nM	0.3 pM	[12]
SiO_2	carboxyl functionalized photoresist derived carbon	label-free	CV/capacitance EIS/R_{CT}	0.0– 50 nM and 0.005–50 nM	7 pM and 1.9 pM	current study

technique offers more accurate results for label-free C-MEMS based PDGF-BB aptasensors.

The storage stability of PDGF-BB aptasensors was evaluated by repeating the electrochemical measurements on $ThL_{RIE+Apt}$ in response to 500 pM PDGF-BB every two days until the recorded response was less than 50% of the initial response. The capacitive response (9.03 mF cm^{-1}) of ThL aptasensor to 500 pM PDGF-BB after 10 days was 90.34 % of the initial capacitive response (9.99 mF cm^{-1}), which indicates that the developed aptasensor has a sufficiently long lifetime and storage stability. The repeatability of the label-free C-MEMS based PDGF-BB aptasensors was investigated by analyzing the CV response of several (n=8) similarly prepared $ThL_{RIE+Apt}$ electrodes to 500 pM PDGF-BB The repeatability CV tests resulted in STDEV of 0.6055 mF cm^{-2} with an average value of 8.1982 mF cm^{-2}, which illustrates the excellent repeatability of developed aptasensors.

The robustness of biosensors is defined as the capability of the biosensor to remain unaffected by small but deliberate deviations in the methodology parameters [50]. In order to study the robustness of the C-MEMS PDGF-BB aptasensor, a $ThL_{RIE+Apt}$ electrode was heated up to 50°C during several (n=8) regeneration steps to study the capability of the biosensor to recover its initial state. The areal capacitance calculated from CV measurements after each heating step showed an average of 10.59 mF $cm^{-2,}$ which was 88.5% of initial response (11.96 mF cm^{-2}) with STDEV of 0.6093. Thus, the oxygen-plasma treated C-MEMS electrodes were proven to be highly robust platforms for label-free electrochemical PDGF-BB aptasensors.

Table 5.1 compares the current PDGF-BB aptasensor with some of the recently developed electrochemical PDGF-BB aptasensors. The linear ranges attained via both CV and EIS

techniques show noticeable improvement in comparison to both labeled and label-free PDGF-BB electrochemical aptasensors. The linear range sufficiently covers the ranges of PDGF-BB in healthy humans as well as most patients with cancer diseases. Moreover, by considering 0.1 ng mL^{-1} (the equivalent of 41 pM) as the minimum cut off point for normal range of PDGF-BB in human serums, $ThL_{RIE+Apt}$ aptasensors exhibited adequate LoD and sensitivity [51].

The label-free PDGF-BB aptasensors, as the first and simple demonstration of C-MEMS based label-free aptasensors, exhibited highly sensitive and selective performances, which is highly promising for further enhancements. The further enhancement can be deployed for C-MEMS based PDGF-BB aptasensors. For instance, the 3D structured C-MEMS devices can be used for sensing platform in which the enhanced resolution can increase the aptamer loading efficiency. Moreover, the integration of carbon-based nanomaterials (e.g., graphene nanosheets) and C-MEMS devices can enhance the performance of the aptasensors by increasing the accessible surface area and specific capacitances[52]. Additionally, the results achieved in this study illustrate the superior performance of the EIS technique (i.e., resistivity measurements) compare to CV technique (i.e., areal capacitance measurements) for the developed label-free electrochemical C-MEMS aptasensor. Hence, the EIS technique is suggested for future POC device development.

5.4 Conclusion

In this chapter, a novel method was used to covalently immobilize the PDGF-BB affinity aptamers on the surface of C-MEMS electrodes. The oxygen-plasma treatment introduces the carboxyl groups to the surface of C-MEMS electrodes. The carboxyl group

covered the surface of C-MEMS enables highly efficient and stable immobilization of the PDGF-BB affinity aptamers. The developed recipe for fabrication of label-free electrochemical cancer aptasensor has high potential to be mass-produced due to the repeatability of synthesizing procedure (i.e., photolithography and high-temperature carbonization) and the oxygen-plasma treatment which it offers a large yield of fabrication and highly stable devices. Both turn-off and turn-on strategies provided sensitive and selective sensing measurements. However, EIS measurement provided more sensitive and selective responses compared to the CV technique. The highly sensitive, selective, and stable label-free electrochemical PDGF-BB aptasensor indicates that the C-MEMS platform is highly promising for developing reliable, precise, and feasible aptasensors for point-of-care and early detection of cancer disease.

5.5 References

[1] WHO. (2020). Cancer. Available: https://www.who.int/health-topics/cancer#tab=tab_1

[2] Z. Zhang, C. Guo, S. Zhang, L. He, M. Wang, D. Peng, et al., "Carbon-based nanocomposites with aptamer-templated silver nanoclusters for the highly sensitive and selective detection of platelet-derived growth factor," Biosensors and Bioelectronics, vol. 89, pp. 735-742, 2017.

[3] S. K. Chatterjee and B. R. Zetter, "Cancer biomarkers: knowing the present and predicting the future,", vol. 114, pp. 1510-1518, 2005.

[4] Y.-H. Wang, Y.-X. Chen, X. Wu, and K.-J. Huang, "Electrochemical biosensor based on Se-doped MWCNTs-graphene and Y-shaped DNA-aided target-triggered amplification strategy," Colloids and Surfaces B: Biointerfaces, vol. 172, pp. 407-413, 2018.

[5] R. Cao, M. A. Björndahl, P. Religa, S. Clasper, S. Garvin, D. Galter, et al., "PDGF-BB induces intratumoral lymphangiogenesis and promotes lymphatic metastasis," Cancer cell, vol. 6, pp. 333-345, 2004.

[6] W. Jiang, D. Tian, L. Zhang, Q. Guo, Y. Cui, and M. Yang, "Dual signal amplification strategy for amperometric aptasensing using hydroxyapatite nanoparticles. Application to the sensitive detection of the cancer biomarker platelet-derived growth factor BB," Microchimica Acta, vol. 184, pp. 4375-4381, 2017.

[7] B. Yi, P. J. Williams, M. Niewolna, Y. Wang, and T. Yoneda, "Tumor-derived platelet-derived growth factor-BB plays a critical role in osteosclerotic bone metastasis in an animal model of human breast cancer," Cancer Research, vol. 62, pp. 917-923, 2002.

[8] K.-J. Huang, H.-L. Shuai, and J.-Z. Zhang, "Ultrasensitive sensing platform for platelet-derived growth factor BB detection based on layered molybdenum selenide–graphene composites and Exonuclease III assisted signal amplification," Biosensors and Bioelectronics, vol. 77, pp. 69-75, 2016.

[9] J. Kawaguchi, S. Adachi, I. Yasuda, T. Yamauchi, T. Yoshioka, M. Itani, et al., "UVC irradiation suppresses platelet-derived growth factor-BB-induced migration in human pancreatic cancer cells," Oncology reports, vol. 27, pp. 935-939, 2012.

[10] Y. Chang, M. Li, Z. Wu, Y. Zhuo, Y. Chai, Q. Xiao, et al., "Homogeneous entropy catalytic-driven DNA hydrogel as strong signal blocker for highly sensitive electrochemical detection of platelet-derived growth factor," Analytical chemistry, vol. 90, pp. 8241-8247, 2018.

[11] J. Cheng, H. Ye, Z. Liu, C. Xu, Z. Zhang, Y. Liu, et al., "Platelet-derived growth factor-BB accelerates prostate cancer growth by promoting the proliferation of mesenchymal stem cells," Journal of cellular biochemistry, vol. 114, pp. 1510-1518, 2013.

[12] L.-X. Fang, K.-J. Huang, and Y. Liu, "Novel electrochemical dual-aptamer-based sandwich biosensor using molybdenum disulfide/carbon aerogel composites and Au nanoparticles for signal amplification," Biosensors and Bioelectronics, vol. 71, pp. 171-178, 2015.

[13] A. M. Cimpean, I. M. Cobec, R. A. CEAUȘU, R. Popescu, A. Tudor, and M. Raica, "Platelet derived growth factor BB: a “Must-have” therapeutic target “redivivus” in ovarian cancer," Cancer Genomics-Proteomics, vol. 13, pp. 511-517, 2016.

[14] C. K. Lau, Z. F. Yang, D. W. Ho, M. N. Ng, G. C. Yeoh, R. T. Poon, et al., "An Akt/hypoxia-inducible factor-1α/platelet-derived growth factor-BB autocrine loop mediates hypoxia-induced chemoresistance in liver cancer cells and tumorigenic hepatic progenitor cells," Clinical Cancer Research, vol. 15, pp. 3462-3471, 2009.

[15] M. Kajizuka, T. Miyachi, H. Matsuzaki, K. Iwata, C. Shinmura, K. Suzuki, et al., "Serum levels of platelet-derived growth factor BB homodimers are increased in male children with autism," Progress in Neuro-Psychopharmacology and Biological Psychiatry, vol. 34, pp. 154-158, 2010.

[16] R. Ma, Q. Yang, S. Cao, S. Liu, H. Cao, H. Xu, et al., "Serum Platelet-Derived Growth Factor Is Significantly Lower in Patients with Lung Cancer and Continued to Decrease After Platinum-Based Chemotherapy," OncoTargets and therapy, vol. 13, p. 1883, 2020.

[17] I. Willner and M. Zayats, "Electronic aptamer-based sensors," Angewandte Chemie International Edition, vol. 46, pp. 6408-6418, 2007.

[18] S. Forouzanfar, F. Alam, N. Pala, and C. Wang, "A Review of Electrochemical Aptasensors for Label-Free Cancer Diagnosis," Journal of The Electrochemical Society, vol. 167, p. 067511, 2020.

[19] A. Prasad, J. Choi, Z. Jia, S. Park, and M. R. Gartia, "Nanohole array plasmonic biosensors: Emerging point-of-care applications," Biosensors and Bioelectronics, vol. 130, pp. 185-203, 2019.

[20] P. Jannetto, "Therapeutic drug monitoring using mass spectrometry," in Mass Spectrometry for the Clinical Laboratory. vol. 1, ed: Elsevier, 2017, pp. 165-179.

[21] C. Pei, C. Liu, Y. Wang, D. Cheng, R. Li, W. Shu, et al., "FeOOH@ Metal–Organic Framework Core–Satellite Nanocomposites for the Serum Metabolic Fingerprinting of Gynecological Cancers," Angewandte Chemie International Edition, vol. 59, pp. 10831-10835, 2020.

[22] A. Syahir, K. Usui, K.-y. Tomizaki, K. Kajikawa, and H. Mihara, "Label and label-free detection techniques for protein microarrays," Microarrays, vol. 4, pp. 228-244, 2015.

[23] R. Zhang, C. Rejeeth, W. Xu, C. Zhu, X. Liu, J. Wan, et al., "Label-free electrochemical sensor for cd44 by ligand-protein interaction," Analytical chemistry, vol. 91, pp. 7078-7085, 2019.

[24] S. Forouzanfar, N. Talebzadeh, S. Zargari, and H. Veladi, "The effect of microchannel width on mixing efficiency of microfluidic electroosmotic mixer," in 2015 3rd RSI International Conference on Robotics and Mechatronics (ICROM), 2015, pp. 629-634.

[25] R. Ranjan, E. N. Esimbekova, and V. A. Kratasyuk, "Rapid biosensing tools for cancer biomarkers," Biosensors and Bioelectronics, vol. 87, pp. 918-930, 2017.

[26] L. Cui, M. Lu, Y. Li, B. Tang, and C.-y. Zhang, "A reusable ratiometric electrochemical biosensor on the basis of the binding of methylene blue to DNA with alternating AT base sequence for sensitive detection of adenosine," Biosensors and Bioelectronics, vol. 102, pp. 87-93, 2018.

[27] F. Ma, S.-h. Wei, and C.-y. Zhang, "Construction of a Robust Entropy-Driven DNA Nanomachine for Single-Molecule Detection of Rare Cancer Cells," Analytical chemistry, vol. 91, pp. 7505-7509, 2019.

[28] C. Wang and M. Madou, "From MEMS to NEMS with carbon," Biosensors and bioelectronics, vol. 20, pp. 2181-2187, 2005.

[29] L. Ferrer-Argemi, E. S. Aliabadi, A. Cisquella-Serra, A. Salazar, M. Madou, and J. Lee, "Size-dependent electrical and thermal conductivities of electro-mechanically-spun glassy carbon wires," Carbon, vol. 130, pp. 87-93, 2018.

[30] M. V. Piñón, B. C. Benítez, B. Pramanick, V. H. Perez-Gonzalez, M. J. Madou, S. O. Martinez-Chapa, et al., "Direct current-induced breakdown to enhance reproducibility and performance of carbon-based interdigitated electrode arrays for AC electroosmotic micropumps," Sensors and Actuators A: Physical, vol. 262, pp. 10-17, 2017.

[31] E. Adelowo, A. R. Baboukani, O. Okpowe, I. Khakpour, M. Safa, C. Chen, et al., "A high-energy aqueous on-chip lithium-ion capacitor based on interdigital 3D carbon microelectrode arrays," Journal of Power Sources, vol. 455, p. 227987, 2020.

[32] V. Penmatsa, H. Kawarada, Y. Song, and C. Wang, "Comparison of different oxidation techniques for biofunctionalization of pyrolyzed carbon," Material Science Research India, vol. 11, pp. 01-08, 2014.

[33] S. Forouzanfar, F. Alam, I. Khakpour, A. R. Baboukani, N. Pala, and C. Wang, "Highly Sensitive Lactic Acid Biosensors Based on Photoresist Derived Carbon," IEEE Sensors Journal, vol. 20, pp. 8965 – 8972, 2020.

[34] C. Wang, G. Jia, L. H. Taherabadi, and M. J. Madou, "A novel method for the fabrication of high-aspect ratio C-MEMS structures," Journal of microelectromechanical systems, vol. 14, pp. 348-358, 2005.

[35] C. Wang, L. Taherabadi, G. Jia, M. Madou, Y. Yeh, and B. Dunn, "C-MEMS for the manufacture of 3D microbatteries," Electrochemical and Solid-State Letters, vol. 7, pp. A435-A438, 2004.

[36] E. Frackowiak, "Carbon materials for supercapacitor application," Physical chemistry chemical physics, vol. 9, pp. 1774-1785, 2007.

[37] E.-Y. Choi, T. H. Han, J. Hong, J. E. Kim, S. H. Lee, H. W. Kim, et al., "Noncovalent functionalization of graphene with end-functional polymers," Journal of Materials Chemistry, vol. 20, pp. 1907-1912, 2010.

[38] J. Coates, "Interpretation of infrared spectra, a practical approach," Encyclopedia of analytical chemistry: applications, theory and instrumentation, 2006.

[39] X. Liu, H.-L. Shuai, and K.-J. Huang, "A label-free electrochemical aptasensor based on leaf-like vanadium disulfide-Au nanoparticles for the sensitive and selective detection of platelet-derived growth factor BB," Analytical Methods, vol. 7, pp. 8277-8284, 2015.

[40] J. B. Allen and R. F. Larry, Electrochemical methods fundamentals and applications: John Wiley & Sons, 2001.

[41] R. Hajian, Z. Tayebi, and N. Shams, "Fabrication of an electrochemical sensor for determination of doxorubicin in human plasma and its interaction with DNA," Journal of pharmaceutical analysis, vol. 7, pp. 27-33, 2017.

[42] R. S. Nicholson and I. Shain, "Theory of stationary electrode polarography. Single scan and cyclic methods applied to reversible, irreversible, and kinetic systems," Analytical chemistry, vol. 36, pp. 706-723, 1964.

[43] N. Aristov and A. Habekost, "Cyclic voltammetry-A versatile electrochemical method investigating electron transfer processes," World J. Chem. Educ, vol. 3, pp. 115-119, 2015.

[44] N. Elgrishi, K. J. Rountree, B. D. McCarthy, E. S. Rountree, T. T. Eisenhart, and J. L. Dempsey, "A practical beginner's guide to cyclic voltammetry," Journal of Chemical Education, vol. 95, pp. 197-206, 2018.

[45] M. Ilgu and M. Nilsen-Hamilton, "Aptamers in analytics," Analyst, vol. 141, pp. 1551-1568, 2016.

[46] G. S. Manning, "The molecular theory of polyelectrolyte solutions with applications to the electrostatic properties of polynucleotides," Quarterly reviews of biophysics, vol. 11, pp. 179-246, 1978.

[47] M. Shamsipur, L. Farzin, M. A. Tabrizi, and F. Molaabasi, "Highly sensitive label free electrochemical detection of VGEF165 tumor marker based on "signal off" and "signal on" strategies using an anti-VEGF165 aptamer immobilized BSA-gold nanoclusters/ionic liquid/glassy carbon electrode," Biosensors and Bioelectronics, vol. 74, pp. 369-375, 2015.

[48] A. Benvidi, M. Banaei, M. D. Tezerjani, H. Molahosseini, and S. Jahanbani, "Impedimetric PSA aptasensor based on the use of a glassy carbon electrode modified with titanium oxide nanoparticles and silk fibroin nanofibers," Microchimica Acta, vol. 185, p. 50, 2018.

[49] A. Shrivastava and V. Gupta, "Methods for the determination of limit of detection and limit of quantitation of the analytical methods," Chronicles of Young Scientists, vol. 2, pp. 21-25, January 1, 2011 2011.

[50] J. Ermer and J. H. M. Miller, Method validation in pharmaceutical analysis: A guide to best practice: John Wiley & Sons, 2006.

[51] K. Leitzel, W. Bryce, J. Tomita, G. Manderino, I. Tribby, A. Thomason, et al., "Elevated plasma platelet-derived growth factor B-chain levels in cancer patients," Cancer research, vol. 51, pp. 4149-4154, 1991.

[52] V. Penmatsa, T. Kim, M. Beidaghi, H. Kawarada, L. Gu, Z. Wang, et al., "Three-dimensional graphene nanosheet encrusted carbon micropillar arrays for electrochemical sensing," Nanoscale, vol. 4, pp. 3673-3678, 2012.

6. PDGF-BB Aptasensors based on BPE-Graphene

6.1 Introduction

Cancer disease is one of the significant causes of death, killing millions of people every year [1]. Most cancer diseases have a high fatality rate because cancer is diagnosed when it has significantly progressed and invaded many vital organs [3]. The main reason for such a late diagnosis is that patients with cancer diseases have no physical symptoms at the early stages of the cancer diseases [5]. Many cancer biomarkers associated with various cancer diseases have been discovered [3]. Among the discovered cancer biomarkers, platelet-derived growth factor-BB (PDGF-BB) is known to have a potent role in the growth and metastasis of several solid malignant tumors, and its levels in the blood increase under the influence of the cancer diseases [8]. Numerous studies have reported the involvement of PDGF-BB in the development and lymphatic metastasis of various cancers, including breast [10], pancreatic [11], prostate [12], ovarian [13], and liver [14]. Several studies have reported the correlation of elevated levels of PDGF-BB in human serum with cancer diseases. For example, a concentration above 1.72 nM (the equivalent of 42 ng mL^{-1}) is confirmed for patients with lung cancer [15], although there is no Food and Drug Administration (FDA) official report for the healthy and cancerous levels of PDGF-BB in human blood. The significant role of PDGF-BB in developing and metastasis of different cancer diseases highlights the importance of developing point-of-care (POC) biosensors to detect PDGF-BB biomarker. The PDGF-BB POC biosensors can be an immense help for the early diagnosis of many cancer associated with solid tumors such as breast, brain, prostate, ovarian, and lung cancers.

The price of sensing units is one of the major concerns in developing feasible POC biosensors. The envisioned sensing unit should be accurate and yet inexpensive enough to rationalize its installment for on-site applications. Combining label-free detection with economically efficient manufacturing techniques can be an auspicious option for developing versatile sensing systems to detect and monitor different bio-targets, including PDGF-BB. Thus far, noticeable attention has been devoted to developing cheap and disposable electrochemical biosensors. Various substrates such as paper, polymers (e.g., polyethylene terephthalate), and screen-printed carbon electrodes have been used for developing disposable biosensors [16-18]. For instance, Wang et al. have demonstrated disposable paper-based label-free cancer biomarker aptasensors in which paper-based electrodes were functionalized with amino-treated graphene, gold nanoparticles, and Prussian blue. The proposed disposable aptasensors showed good sensing performances with linear ranges of 0.01–500 ng mL^{-1} for carcinoembryonic antigen and limit of detection (LoD) of 2 pg mL^{-1} [16]. Yaman et al. have proposed label-free cancer cell aptasensors based on pencil graphite electrodes. The developed aptasensors were functionalized with diphenyl alaninamide-based peptide nanoparticles and DLD-1 cancer cells affinity aptamers. The disposable pencil graphite aptasensor exhibited a good linear range ranging from 2×10^2-2.0×10^5 cells mL^{-1} with a LoD of 100 cells mL^{-1} [19]. The proposed disposable label-free cancer aptasensors illustrate the high potential of this class of aptasensors for PDGF-BB disposable POC aptasensors.

Since the discovery of graphene in the early 2000s, graphene has attracted massive attention in various domains because of its unique features [20]. The large surface area, high thermal conductivity and charge mobility, wide electrochemical window, and

unconventional superconductivity of graphene made this material a potent candidate for the development of biosensors [21, 22]. The conventional application of graphene for biosensors includes synthesis of graphene with wet chemical processes (e.g., Hummers) or electrochemical approaches, reduction of exfoliated graphene oxide (GO) to reduced graphene oxide (rGO), and deposition of it on the desired biosensing electrode [23]. Wet chemical synthesis requires harsh oxidizing agents such as $KMnO_4$, $NaNO_3$, and $KClO_3$ in strong acidic agents such as hydrohalic acid and hydrazine [24-27]. The application of harsh chemicals can be limited using electrochemical approaches; however, there could be non-desired functional groups and basal plane damage during the anodic exfoliation[28-30]. Furthermore, the comparative study by Kauling et al. have demonstrated that the commercially available graphene (from 60 different vendor worldwide) has low graphene content (less than 10% in most products and not more than 50% in the highest quality available product), which illustrates the reason why commercial graphene-based devices are not commonly available yet [31]. Nonetheless, the conventional methods for synthesis and deposition of GO and rGO cannot simultaneously exfoliate, reduce, and deposit GO and rGO in an environmentally friendly fashion. Such a combination can be achieved via bipolar electrochemistry[32]. In addition, Khakpour et al. have demonstrated that the bipolar exfoliated rGO has vertically aligned morphology, which could eliminate the necessity of using spacers such as carbon nanotubes to prevent the aggregation of graphene nano-flakes [33, 34].

Herein, the novel application of bipolar exfoliation of graphene for disposable label-free PDGF-BB aptasensor is presented. There are no reports on applying bipolar exfoliated (BPE) graphene for the biosensor application to the best of our knowledge. The bipolar

exfoliation method presented in this study is a direct single-step of exfoliation, deposition, and reduction of graphene utilizing a graphite rod in deionized water (DIW). The process of bipolar exfoliation includes applying a constant electric field between two conductive feeder electrodes, which aggregates in opposite polarizations of the graphite rods. Consequently, if the apparent electrical field is strong enough, simultaneous faradaic reactions of reduction at the cathodic pole and oxidation at the anodic pole would occur[32]. Thus far, BPE has been demonstrated for various applications due to the simplicity of the setup and lower cost of the process [33, 35-37].

In this study, the BPE-graphene was deposited on stainless steel (SS) electrodes and gold-covered polyethylene terephthalate electrodes (PET/Au) electrodes for comparative study and as the proposed disposable biosensors, respectively. The analysis confirmed that the BPE-rGO deposited on the cathodic (i.e., negative) feeding electrode is highly suitable for aptasensing applications. Thus, PET/Au were used as negative feeding electrodes. The amino-terminated PDGF-BB affinity aptamers were covalently immobilized on BPE-graphene deposited on SS and PET/Au electrodes. The BPE-graphene crystal structure and its morphology were studied via transmission electron microscopy (TEM) and scanning electron microscopy (SEM), respectively. The characteristics of the fabricated BPE-based aptasensors were studied using Fourier-transform infrared spectroscopy (FTIR). Electrochemical and sensing performance analyses were conducted using differential pulse voltammetry (DPV) and cyclic voltammetry (CV). The results revealed that the bipolar exfoliation provides highly quality rGO with promising characteristics suitable for aptasensors. Furthermore, the BPE technique was proven to be both versatile and amenable to mass production, thus making it a promising technique for various biotechnology

applications, including but not limited to disposable cancer aptasensors and POC microdevices.

6.2 Experimental Section

6.2.1 Materials and Reagents

The PDGF-BB binding aptamer (ssDNA, amino linker-5'-C_6-CAG GCT ACG GCA CGT AGA GCA TCA CCA TGA TCC TG-3' [3]) was purchased in HPLC purification from ThermoFisher Scientific, USA. Tris-ethylenediaminetetraacetic acid (TE) buffer, ethanol, acetone, phosphate-buffered saline (1M and pH 8) (PBS), 1-ethyl-3-(3-dimethylaminopropyl) carbodiimide hydrochloride linker (EDC), N-hydroxysuccinimide linker (NHS), hydrochloric acid (HCl), Polyoxyethylene (20) sorbitan monolaurate (Tween-20), KCl, and $K_3Fe(CN)_6$ were purchased from ThermoFisher Scientific, USA. Trehalose, bovine serum albumin (BSA), platelet-derived growth factor-AA, AB, and BB were purchased from Sigma Aldrich, USA. NANO^{TM} SU-8 25 negative photoresist was purchased from Microchem., USA. Graphite rods (3 cm in length and 6.15 mm in diameter, Ultra "F″ Purity 99.9995%) were purchased from Fisher Scientific, USA. The 316 stainless steel (SS) electrodes were purchased from Maudlin Inc., USA. All chemicals were analytical grade. Milli-Q (Sigma Aldrich, USA) deionized water was used in this study.

6.2.2 Apparatus

Bio-Logic versatile multichannel potentiostat (VMP3) was used for the electrochemical analysis. JEOL SEM 6330 and Philips CM-200 FEG TEM were used to

obtain the SEM and TEM images of the deposited materials, respectably. Agilent Technologies N6705A dc Power Analyzer was used for applying a DC voltage of 45 V across the feeding electrodes. An Ag/AgCl (KCl saturated) and Pt wire were used as reference electrode and working electrodes in all electrochemical measurements, respectably. A 713 Metrohm pH meter was used for measuring the pH of electrolytes. JASCO FTIR 4100 was used to conduct FTIR analysis.

6.2.3 Preparing PDGF-BB aptasensors

Prior to aptamer immobilization, the BPE-treated SS and PET/Au electrodes were washed with PBS and DIW. The stock solution of binding aptamers was diluted to the desired concentration in aqueous solution of a 0.1 M TE buffer in the final volume of 20 µL. Next, 20 µL of 20 mg mL^{-1} NHS and 10 µL of 20 mg mL^{-1} EDC were added to the aptamer solution and incubated at 25°C for 30 minutes. This step is recommended in the oligonucleotide datasheet released by ThermoFisher Scientific for activating the amino tags of the aptamers. Next, the BPE-treated electrodes were dipped in a small sealed container and incubated overnight at 25°C. Following the incubation, the electrodes were washed completely in DIW to remove any unattached binding aptamers. Next, the electrodes with immobilized aptamer were dipped in an aqueous solution of 1% (v:v) Tween-20 + 0.1 M PBS to block the blank areas of the aptasensors.

6.2.4 Electrochemical Characterization of PDGF-BB Aptasensors

The CV measurements were recorded at a voltage window of -0.8 V to 0.4 V versus the reference electrode with scan rates of 10–100 $mV.s^{-1}$ and cycle repeating of n=20. DPV

measurements were recorded at a voltage range of 0.2 to 0.9 V (vs Ag/AgCl) for SS based electrodes and -0.05 to 0.5 V (vs Ag/AgCl) for PET/Au based electrodes with pulse height of 200 mV and pulse width of 100 ms with n=10 number of repetitions. The electrolyte pH was attuned using HCl to attain electrolytes with a pH of 8-5.5.

6.3 Results and Discussion

In this study, a bipolar exfoliation cell illustrated in Figure 6.1a has been used for exfoliation, reduction, and deposition of graphene nanosheets on SS and PET/Au electrodes. The bipolar mechanism details have been discussed in previous studies [32, 33, 38]. Briefly, a 45 V direct current (DC) voltage was applied through the 2×2 cm feeding

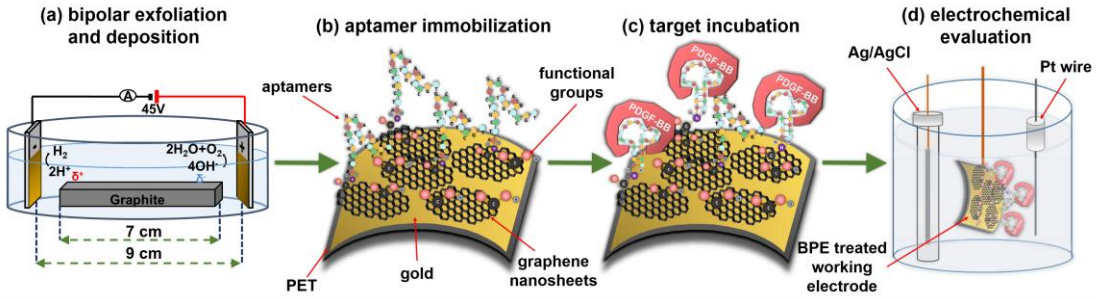

Figure 6.1 Schematic illustration of (a) bipolar exfoliation cell, (b) development of PET/Au/rGO$_{Apt}$ PDGF-BB aptasensors, (c) target incubation, and (d) three-electrode electrochemical cell with Ag/AgCl reference electrode, Pt wire counter electrode, and PET/Au/rGO$_{Apt}$ in 5 mL aqueous electrolytes of 0.1 M PBS/5 mM $K_3Fe(CN)_6$/ 0.05-1 M KCl.

electrodes with a 9 cm distance to induce an electric field of 5 V cm^{-1}. The resistivity of DIW used for bipolar exfoliation was 17 MΩ. During bipolar exfoliation, two half-reactions of water electrolysis happen at the feeding electrodes: (1) reduction of two water molecules to one gaseous hydrogen molecules ($2H^+ + 2e^- \rightarrow H_2$) and hydroxyl ions ($OH^-$) at the cathode and (2) oxidation of hydroxyl ions (OH^-) to oxygen gas and water molecules ($4OH^- \rightarrow 2H_2O + O_2 + 4e^-$) at the anode. Furthermore, assuming that the potential drop is

negligible at electrodes and linear in solution, the electric field induces a sufficient potential difference (*>1.5 V*) between two ends of the graphite rod to stimulate faradic reactions at the side surfaces of the graphite rod. This potential difference yields in the oxidation of graphite into GO at the anodic pole of the graphite rod (indicated as δ^+ in Figure 6.1a). Prior to immobilizing aptamers, each electrode was examined with SEM to confirm the uniform deposition of rGO or GO on the electrodes. Next, the amino-modified PDGF-BB affinity aptamers were immobilized on SS and PET/Au electrodes modified with BPE-graphene (Figure 6.1b). The aptasensors were incubated with the desired PDGF-BB concentration at various temperatures ranging from 20°C to 50°C for between 10 and 150 minutes (Figure 6.1c). The optimum incubation temperature was found to be 30°C, and the optimum reaction time for target molecules to bind with aptamers was found to be 40 minutes. A three-electrode setup illustrated in Figure 6.1d was used for CV and DPV evaluations of the electrodes. The 5 mL aqueous electrolytes of 0.1 M PBS, 5 mM - $K_3Fe(CN)_6$, and different KCl concentrations in the range of 50 mM to 1 M were utilized for electrochemical analysis.

The electrochemical and FTIR characterizations were conducted on four different BPE-treated SS electrodes referred to as SS/GO, SS/rGO, SS/GO_{Apt}, and SS/rGO_{Apt}, which represent the samples of GO deposited on SS electrode (i.e., positive feeding electrode), rGO on deposited SS electrode (i.e., negative feeding electrode), aptamer immobilized on SS/GO electrode, and aptamer immobilized on SS/rGO electrode, respectively. The aptamer concentration of 15 µM was used to fabricate SS/GO_{Apt}, SS/rGO_{Apt}, and PET/Au/rGO_{Apt} electrodes studied in the following subsections except for PET/Au/rGO_{Apt} electrodes prepared for defining the optimum concentration of aptamer. The optimum

aptamer concentration of 10 µM was utilized to fabricate PET/Au/rGO$_{Apt}$ electrodes studied in subsections 2.4. All BPE-treated electrodes had an effective area of 0.5 cm^2 confined via bee's wax to minimize side reactions.

6.3.1 Material Characterization of BPE Treated Electrodes

The SEM image of BPE-rGO deposited on SS electrodes after 24 hours of deposition is presented in Figure 6.2a. The SEM image of rGO deposited on negative feeding electrodes clearly show a porous morphology with vertically aligned structures with a pore size of approximately 100 nm. This porous morphology is highly suitable for various applications, including electrochemical biosensors and energy storage

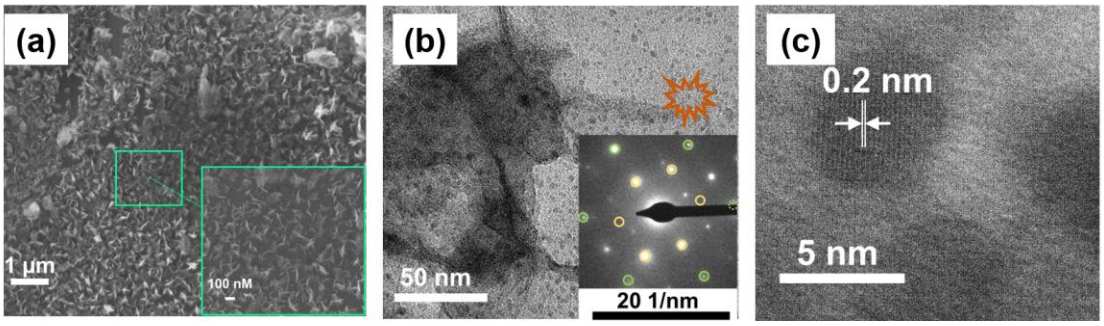

Figure 6.2 SEM images of BPE-rGO deposited on negative feeding electrode. (b) TEM image (SAED patterns in inset, yellow circle are associated to $\langle 1\bar{1}00\rangle$ planes and green circle are associated to $\langle 2\bar{1}10\rangle$ planes). (c) HRTEM image of BPE-rGO

microdevices. On the other hand, the SEM image of GO deposited on positive feeding electrodes **(**Figure S6.1) shows bulky plane structures with cracks implying restacking of GO during the deposition stage.

The TEM and selected area electron diffraction (SAED) images of BPE-rGO deposited on the TEM mesh are given in Figure 6.2b. The TEM image shows that thin sheets of rGO (with overlaps or folds) with a span of approximately 400 nm are formed.

Single crystalline SAED patterns confirm that the low defected graphene sheets are formed during the bipolar exfoliation. Only a few diffraction spots beside the spots related to the crystal are formed, and no superlattice arrays are identified in the deposited graphene. Therefore, it can be concluded that the BPE-rGO is reduced and has high purity [39, 40].

Moreover, it has been reported that when the intensity of spots diffracted from $\langle 2\bar{1}\bar{1}0\rangle$ planes is higher than the intensity of spots diffracted from $\langle 1\bar{1}\bar{0}0\rangle$ planes, there is more than one layer stacked in the graphene material. It can be seen in the SAED pattern of TEM image given in Figure 6.2b that spots diffracted from $\langle 2\bar{1}\bar{1}0\rangle$ planes (marked with

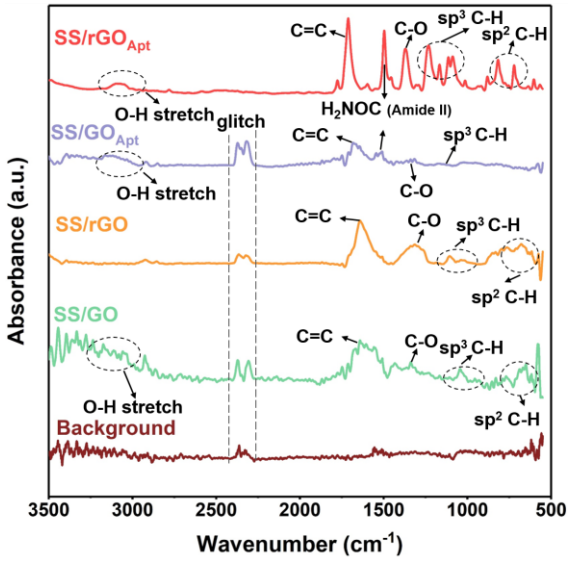

Figure 6.3 FTIR spectra of SS/GO, SS/rGO, SS/GO$_{Apt}$, and SS/rGO$_{Apt}$ electrodes.

green circles) have lower intensity than spots diffracted from $\langle 1\bar{1}\bar{0}0\rangle$ planes (marked with yellow circles). The difference in the intensity of spots diffracted from $\langle 2\bar{1}\bar{1}0\rangle$ planes and $\langle 1\bar{1}\bar{0}0\rangle$ planes suggest the graphene deposited on negative feeding electrode has a few layers[39, 40]. The interplanar spacing (also known as d-spacing) of 0.2 nm is measurable from the high-resolution TEM (HRTEM) image presented in Figure 6.2c**,** in which the measured interplanar spacing is smaller than the typical value of GO [39, 40].

The FTIR characterization was used to analyze the spectral data of the BPE-rGO and BPE-GO samples deposited on SS electrodes, including the formation of amide biding after aptamer immobilization. The FTIR spectra of background, SS/GO, SS/rGO, SS/GO_{Apt}, and SS/rGO_{Apt} are represented in Figure 6.3. Three samples of SS/GO, SS/GO_{Apt}, and SS/rGO_{Apt} showed a broad peak between 2800-3200 cm^{-1}, which is ascribed to O-H stretching [41]. The noteworthy peaks for all samples were identified at 1430 and 1600 cm^{-1}, ascribed to C-O bending and aromatic C≡C stretching, respectively [42]. Furthermore, All the samples showed peaks at 1100-1300 cm^{-1}, which are attributed to sp^3 C-H bending [41].

The FTIR spectrum for SS/GO_{Apt} and SS/rGO_{Apt} confirms a peak at 1571 cm^{-1}, associated with amide II band, representing covalent bonding of PDGF-BB aptamers with BPE-graphene [41]. The FTIR results confirm that the locally formed carboxyl groups on the graphene surfaces can be used directly to immobilize the amino-terminated biorecognizers agents. The immobilization efficiency can also be improved using oxygen-plasma etching to increase the percentages of carboxyl groups on the surface of the BPE-graphene [1, 43].

6.3.2 Electrochemical Analysis of BPE-Graphene Samples

Herein, the electrochemical analysis of BPE-graphene based aptasensors in different stages of development is presented. The analysis intended to compare the different electrochemical properties of BPE-graphene deposited on negative and positive SS electrodes. Two hypotheses for comparative analysis of the BPE-based aptasensors were considered: first, the electrodes based on BPE-rGO exhibit better electrochemical

performance than BPE-GO; second, trapped target molecules (i.e., the formation of target-aptamer complex) elevates the charge-transfer resistance by blocking redox species pass to the aptasensor electrode, which can be traced as decreasing current measured via the DPV method. A sample of 100 pM PDGF-BB (designated as T) was used as a target sample for electrochemical analysis purposes.

In Figure 6.4a, the CV curves measured for bare SS electrodes, four samples BPE treated electrodes, and subsequent aptasensors are presented. The CV curve of BPE-graphene deposited on the negative feeding electrode (i.e., SS/rGO) shows the highest peak currents and the largest CV curve area. The areal capacitances were calculated from CV curves using equation 6.1[44]:

$$C = \frac{1}{2AsΔV} \int IdV \qquad (6.1)$$

where ΔV is the voltage window, s is scan rate, A is the electrode area, V is the voltage, and I is current. The calculated areal capacitances are given in Figure 6.4b. The SS/rGO electrode has the highest capacitance value with the areal capacitance of 2.69 mF $cm^{-2,}$ while the SS/GO electrode has the lowest capacitance with a value of 0.24 mF cm^{-2}. These results are in agreement with former studies on BPE-graphene. For example, the comparative study by Khakpour et al. on BPE-graphene deposited on negative and positive feeding electrodes has proven superior areal capacitance of samples with BPE-rGO [33]. Immobilizing aptamers decreased the areal capacitance of SS/rGO electrodes to a value of 1.86 mF cm^{-2}. This decrease can be explained by partial replacement of double-layer with immobilized aptamers. The areal capacitance of SS/GO_{Apt} is very similar to that of SS/GO with a value of 0.24 mF cm^{-2} which can be explained by the low loading of immobilized aptamers on the surface of GO due to the limited active area of GO.

In order to estimate the electrochemically active area of BPE-rGO and BPE-GO using the Randles-Sevcik equation, the correlation of CV peak currents and the square root of scan rate were studied to confirm the occurrence of diffused-controlled process. The peak currents of CV measurement conducted on SS/rGO and SS/GO proportionally increased with the increase of scan rates at the scan rates of 10-100 mV s^{-1} (CV curves are given in Figure 6.4c and Figure S6.2, respectively). The CV peak currents of SS/rGO linearly increased in respect to the increase of scan rates' square root (Figure 6.4d) with correlation coefficient (R^2) of 0.9819 and 0.9822 for reduction peak currents and oxidation peak currents, respectively. Similarly, the linear dependence of reduction and oxidation

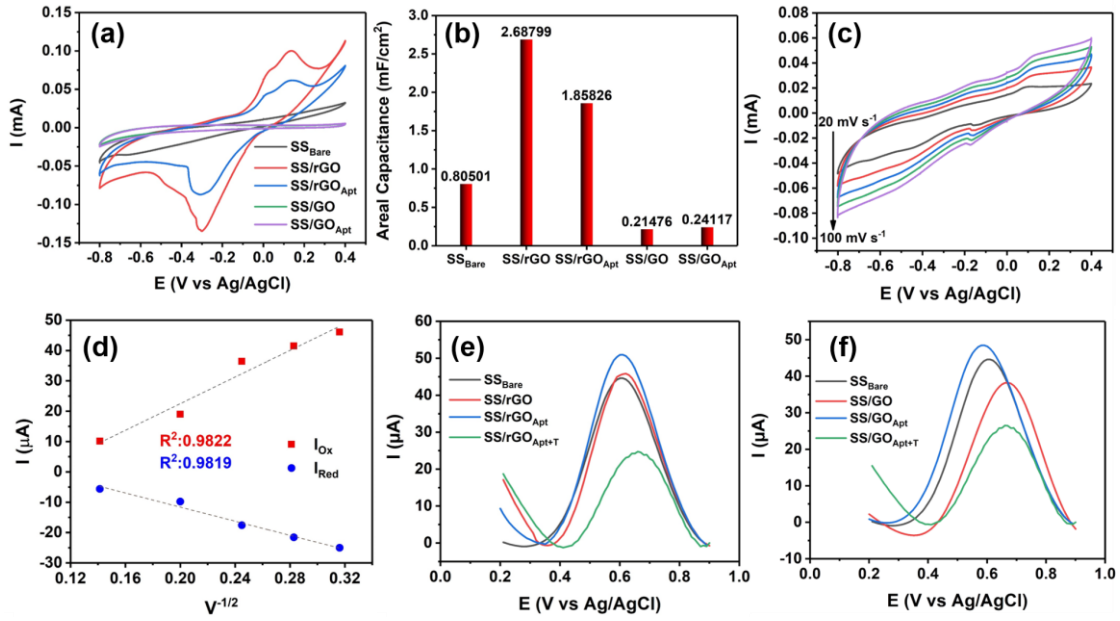

Figure 6.4 (a) CV (40 mV s^{-1}) plots of bare SS and BPE-graphene deposited on SS electrodes before and after aptamer immobilization. (b) The areal capacitance calculated from CV plots. (c) The CV plots of the SS/rGO electrode at different scan rates at range of 10–100 mV s^{-1}. (d) Calibration curves of reduction and oxidation peak current versus the square root of scan rates. (e) The DPV plots of BPE-based aptasensors based on graphene deposited on negative feeding electrode at various development stages and sensing response of the aptasensor to 100 pM PDGF-BB. (f) The DPV plots of BPE-based aptasensors based on graphene deposited on positive feeding electrodes at various development stages and response of aptasensor to 100 pM PDGF-BB

peak currents of SS/GO had R^2 of 0.9723 and 0.9891 for reduction and oxidation peak currents, respectively (the inset calibration plots in Figure S6.2). Having the confirmation of diffused-controlled process occurrence, the active surface area of the BPE-rGO and BPE-GO samples were calculated using the Randles-Sevcik equation at room temperature ($T=295\ K$) (equation 6.2) [45].

$$I_P=(2.69\times10^5)n^{3/2}ACD^{1/2}v^{1/2} \quad (6.2)$$

Where v is the scan rate (V s^{-1}), D is the diffusion coefficient of 5 mM $Fe(CN)_6^{-3/-4}$ (7.6×10^{-6} cm^2 s^{-1}), C is the concentration of $Fe(CN)_6^{-3/-4}$ (5 mol cm^{-3}), n is electron transfer number (n=1), and A is active surface area (cm^{-2}). The active surface area of SS/rGO was calculated as 3.92×10^{-5} cm^2, and the active surface area of SS/GO was calculated as 1.75×10^{-5} cm^2. The calculated active area values show the BPE-rGO has a higher active area than the BPE-GO, which is in agreement with morphological analysis obtained from SEM images. Thus, the CV analysis, including areal capacitance and active area calculations, confirms the first hypothesis regarding better electrochemical properties of BPE-graphene deposited on the negative feeding electrode.

The DPV responses of BPE-rGO and BPE-GO aptasensors at different development stages are given in Figure 6.4e and Figure 6.4f, respectively. The DPV response of SS/rGO shows a similar peak current to SS_{Bare} (i.e., SS electrode without any modifications) with values of 45.8 µA and 44.6 µA for SS/rGO and SS_{Bare}, respectively. These responses suggest a good electrochemical conductivity of deposited rGO on the SS electrode. However, the DPV response of SS/GO shows a decrease in peak current with a value of 37.9 µA, because of the structure of GO and the functional groups covering the

surface of SS/GO. The DPV response of SS/rGO$_{Apt}$ and SS/GO$_{Apt}$ show increased peak currents with a value of 51 μA and 48.4 µA, respectively. The increase in peak currents after aptamer immobilization can be explained by the engagement of negatively charged carboxylate groups in covalent immobilization of aptamers and extinguished remaining functional groups by Tween-20 quencher[6]. The SS/rGO$_{Apt}$ and SS/GO$_{Apt}$ electrodes incubated with target molecules (i.e., SS/rGO$_{Apt+T}$ and SS/GO$_{Apt+T}$) have considerably lower peak currents with values of 24 µA for SS/rGO$_{Apt+T}$ and 26.5 µA for SS/GO$_{Apt+T}$, respectively. The decrease in peak currents is due to the isolative properties of the PDGF-BB oncoproteins, which decreases the pass of the redox species to the SS/rGO$_{Apt}$ and SS/GO$_{Apt}$ electrodes [46]. Therefore, the DPV characterization of BPE-graphene-covered electrodes confirmed successful entrapment of PDGF-BB oncoproteins on the surfaces of the envisioned aptasensors and that seizing the target proteins decreases the peak current.

6.3.3 Parameter Optimization and Comparison of Aptasensors

Several factors are known to affect the performance of electrochemical aptasensors [3]. In this study, the effects of five parameters on responses of BPE-graphene based aptasensors, including reaction-time, the temperature of incubation, pH of the electrolyte, concentration of supporting salt (i.e., KCl), and binding aptamer concentration, have been analyzed. Among the analyzed parameters, the effect of aptamer concentration was studied explicitly for PET/Au-based aptasensors since the other four parameters are predominantly dependent on the aptamers DNA structures, incubation condition, and measurement medium.

Optimum reaction time in aptasensors is referred to as the minimum time required for forming the aptamer-target complex that is both efficient and sufficiently quick. To find the optimum reaction time, the SS/rGO$_{Apt}$ samples were incubated with the 100 pM PDGF-BB for different periods ranging from 10-120 minutes and analyzed by measuring the peak current of the DPV plot. As shown in Figure 6.5a, the peak current decreases by increasing the incubation time up to 40 minutes and saturates afterward. Therefore, the optimum reaction time was found to be 40 minutes.

The effect of pH on DPV measurement was investigated by conducting DPV measurements on SS/rGO$_{Apt}$ incubated with 100 pM PDGF-BB in the electrolyte of 0.2 M

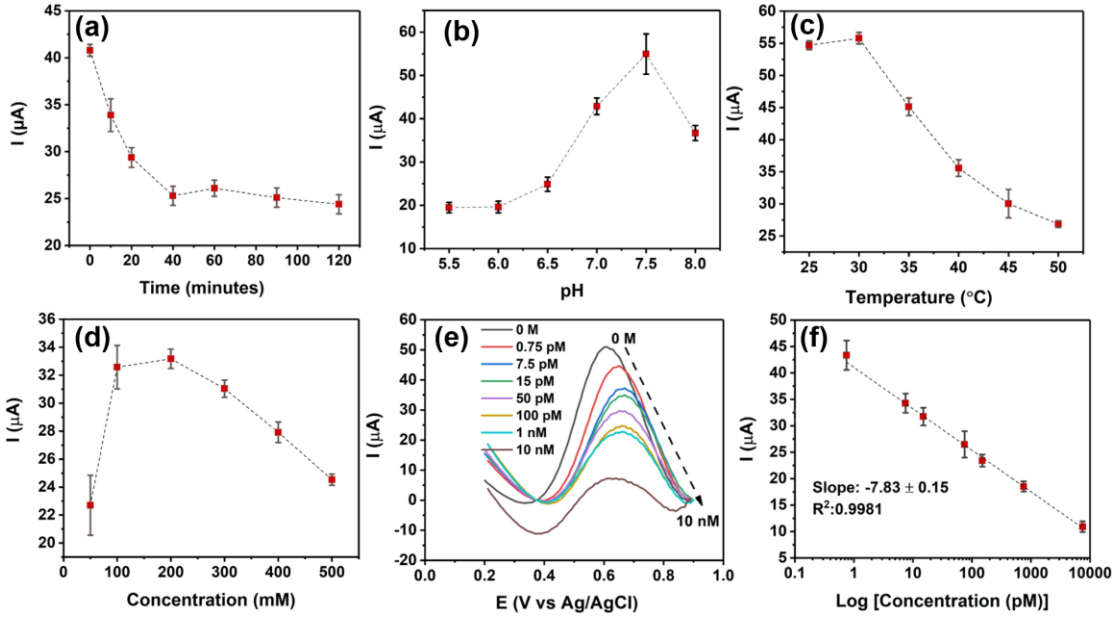

Figure 6.5 (a) Peak currents obtained from DPV curves measured in response to 100 pM PDGF-BB for defining the optimum reaction times. (b) Peak currents obtained from DPV curves in response to 100 pM PDGF-BB for analyzing the effect of pH on peak current. (c) Peak currents obtained from DPV curves measured in response to 100 pM PDGF-BB for studying the effect of incubation temperature. (d) Peak currents obtained from DPV curves measured in response to 100 pM PDGF-BB for studying the effect KCl concentration on peak current. (e) DPV response of the SS/rGO$_{Apt}$ electrode to PDGF-BB ranging from 0–10 nM. (f) Obtained calibration curve of peak currents measured from DPV responses.

KCl/5 mM $K_3Fe(CN)_6$/0.1 M PBS with different pH values in the 5.5-8 range. As given in **Figure 6.5b**, the peak response value was recorded at pH 7.5; thus, the sensing measurements were conducted in the electrolyte with pH 7.5. The incubation temperature effect on peak current was studied by incubating an SS/rGOApt electrode with 100 pM PDGF-BB at different temperatures ranging from 25°C to 50°C. The attained results presented in Figure 6.5c show that the highest peak current was achieved with incubation at 30°C; hence, the 30°C was used as the optimum incubation temperature. The result of optimum supporting salt concentration analysis is presented in Figure 6.5d. The highest peak current was recorded in the electrolyte with 200 mM KCl; therefore, 200 mM was chosen as the optimum KCl concentration.

The responses of SS/rGO_{Apt} to 0-10 nM PDGF-BB measured under optimum conditions are given in Figure 6.5e. The peak current of DPV curves at E≈ 0.6 V (vs. Ag/AgCl) decreases proportionally to the PDGF-BB concentration increase. The observed trend in peak current results from increased charged transfer resistance due to the isolative properties of PDGF-BB oncoproteins [46]. The calibration curve of peak currents measured from DPV curves is presented in Figure 5f. The linear dependence of peak currents to the logarithm of PDGF-BB concentrations has a slop of -7.84 µA $Logc^{-1}$ and the R^2 of 0.9981. The correlation the logarithm of PDGF-BB concentration and SS/rGO_{Apt} peak current can be evaluated as following (equation 6.3),

$$i=41.05 - 7.84\ Logc^{-1},\ r=0.9977 \qquad (6.3)$$

where *c* is the target concentration (pM), *i* is the peak current (µA), and *r* is the regression coefficient. Therefore, the sensitivity of SS/rGO_{Apt} to PDGF-BB can be assessed as 7.84

µA Logc^{-1}. The LoD for SS/rGO$_{Apt}$ aptasensors based on DPV measurements was estimated as 0.53 pM based on the linear regression (equation 6.4) [47],

$$LoD = \frac{3S}{b} \quad (6.4)$$

where *S* is the standard deviation of the blank response *(STDEV*= 0.2360 µA, *n=20*), and *b* is the slope of the calibration curve (*b* = -1.214 µA c^{-1}) of the DPV peak currents.

The responses of SS/GO$_{Apt}$ to 0-10 nM PDGF-BB measured under optimum conditions reached its saturation point at PDGF-BB concentration of 150 pM (see Figure S6.3). The most probable reason for the narrow range of SS/GO$_{Apt}$ is the low amount of immobilized aptamers due to the limited active area. The sensing analysis of SS/rGO$_{Apt}$ and SS/GO$_{Apt}$ demonstrated that the BPE-graphene deposited on negative feeding electrodes because of its highly porous morphology and higher quality provides more suitable material for biosensing application purposes. Hence, the PET/Au based aptasensors were developed using BPE-rGO.

6.3.4 Analysis of PDGF-BB Aptasensor based on PET/Au/rGO Electrodes

The comparative study on BPE-rGO and BPE-GO confirmed that the BPE-rGO provides superior electrode material for envisioned label-free aptasensor. Therefore, the PET/Au electrodes were used as a negative feeding electrode in bipolar exfoliation cell. The SEM analysis, confirmed the successful deposition of BPE-graphene on PET/Au electrodes (Figure 6.6a). Herein, performance analysis of the aptasensors based on BPE-treaded PET/Au electrodes is given.

In Figure 6.6b, DPV plots of aptasensors based on BPE-treaded PET/Au electrodes at different development stages are presented. The DPV results show a similar performance

pattern as DPV analysis of SS based electrodes, in which deposition of BPE-rGO has increased the DPV peak current of BPE-treaded PET/Au electrodes (designated as PET/Au/rGO) with a value of 22.2 µA compared to bare PET/Au electrodes (designated as PET/Au_{Bare}) with peak current value of 12.04 µA. The DPV plot of PET/Au/rGO electrodes after aptamer immobilization (designated as PET/Au/rGO_{Apt}) shows an increase in peak current with a value of 27.45 µA, as discussed in section 2.2.

The optimum aptamer concentration for PET/Au/rGO-based aptasensors was analyzed by measuring the DVP response of PET/Au/rGO based aptasensor prepared with specific aptamer concentration to 100 pM PDGF-BB. A separate PET/Au/rGO_{Apt} electrode was prepared using an aptamer concentration ranging from 0.5-50 µM. As shown in Figure

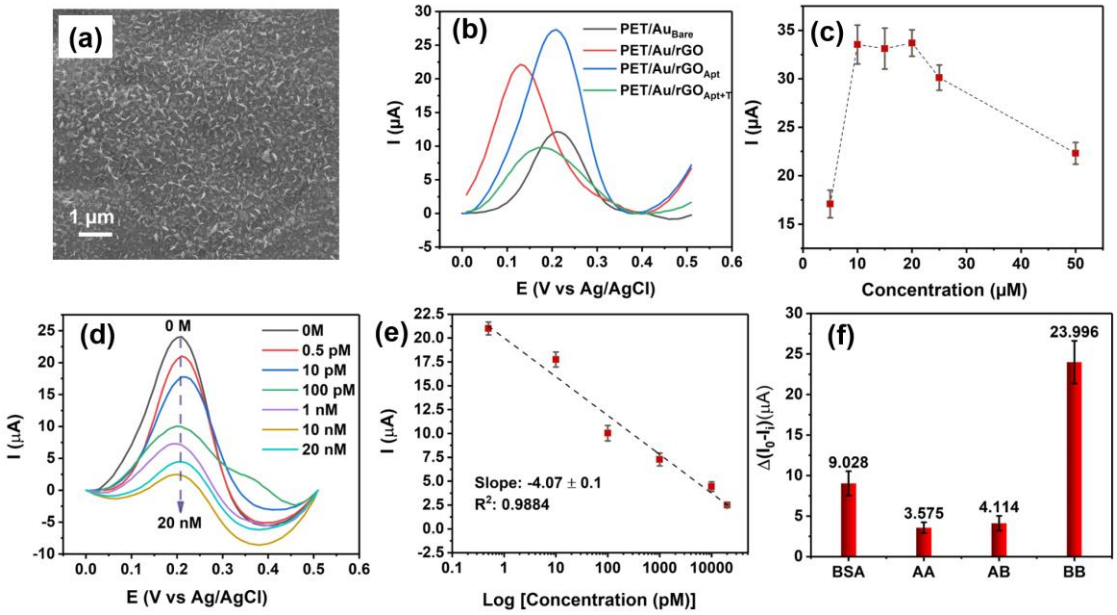

Figure 6.6 (a) SEM image of BPE-graphene deposited on PET/Au negative feeding electrode. (b) The DPV plots of PET/Au-based aptasensors based on graphene deposited on negative feeding electrode at various development stages and response of the aptasensor to 100 pM PDGF-BB. (c) Peak currents obtained from DPV curves measured in response to 100 pM PDGF-BB for studying the effect of aptamer concentration. (d) DPV curves of the PET/Au/rGO_{Apt} electrode's response to PDGF-BB ranging from 0–20 nM. (e) Calibration curve for peak currents measured from DPV curves. (f) DPV peak current measured in response of PET/Au/rGO_{Apt} electrodes to 10 nM PDGF-AA, 1 µg mL^{-1} bovine serum albumin (BSA), 10 nM PDGF-AB, and 100 pM PDGF-B.

6.6c, the PET/Au/rGO$_{Apt}$ aptasensor showed its peak DPV response in a sample prepared with an aptamer concentration of 10 µM, and the peak current saturates afterward. Hence, the 10 µM aptamer concentration was utilized for sensing performance analysis.

The responses of PET/Au/rGO$_{Apt}$ to 0-20 nM PDGF-BB measured under optimum conditions are given in Figure 6.6d. Similar to the sensing performances of aptasensors based on SS electrodes, the peak current of DPV curves decreases proportionally to the increase of PDGF-BB concentration. The calibration curve of peak currents measured from DPV curves is presented in Figure 6.6e. The linear dependence of peak currents to the

Table 6.1 The performance of recent electrochemical PDGF-BB aptasensors

Electrode	**Modification**	**Technique**	**Detection Strategy**	**LoD**	**Linear range**	**Stability**	**Ref.**
GCE	Cu-MOFs/TpBD-COFs	DPV	label-free	0.034 pg mL^{-1}	0.0001-60 ng mL^{-1}	N/A	[2]
	HAP-NPs	SWV	labeled: HAP-NPs	50 fg mL^{-1}	0.1 pg mL^{-1}-10 ng mL^{-1}	N/A	[4]
C-MEMS thin film	oxygen plasma etching	CV	label-free	7 pM	0.01-50 nM	90.34% after 10 days	[6]
		EIS		1.9 pM	0.005-50 nM		
Au	AuNPs[g]	SWV	labeled: α-cyclodextrin	0.52 nM	0.52–1.52 nM	96.4% after 7 days	[7]
	graphene doped with silver nanoclusters	EIS	label-free	26.5 fM	32.3 fM–1.61 pM	96.7% after 10 days	[9]
SS	BPE rGO	DPV	label-free	0.53 pM	0.005-10 nM	91.2% after 6 days	this work
PET/Au				0.65 pM	0.0007-20 nM		

GCE: glassy carbon electrode; Cu-MOFs: Cu-based metal–organic frameworks; TpBD-COFs: 1,3,5-triformylphloroglucinol (Tp), benzidine (BD), covalent organic frameworks (COFs); HAP-NPs: Hydroxyapatite nanoparticles; SWV: square wave voltammetry; C-MEMS: carbon-microelectromechanical systems; EIS: electrochemical impedance spectroscopy; AuNPs: gold nanoparticles;

logarithm of PDGF-BB concentrations has a slop of -4.07 µA $Logc^{-1}$ and the R^2 of 0.9884. The correlation of PET/Au/rGO_{Apt} peak current to the logarithm of PDGF-BB concentration can be assessed as following (equation 6.5),

$$i=20.06 - 4.07\ Logc^{-1},\ r=0.9854 \quad (6.5)$$

where *i* is the peak current (µA), *c* is the PDGF-BB concentration (pico-mol L^{-1}), and *r* is the regression coefficient. Hence, the DPV measurement's sensitivity to PDGF-BB can be calculated as 4.07 µA $Logc^{-1}$. The LoD for PET/Au/rGO_{Apt} aptasensors based on DPV measurements was calculated as 0.65 pM based on the linear regression (equation 4) in which *S* was calculated as 0.174 µA (*n*=10), and *b* was calculated as 0.81 µA c^{-1}.

The selectivity of the PET/Au/rGO_{Apt} electrodes was investigated via recording the response of the aptasensors to 1 µg mL^{-1} bovine serum albumin, 10 nM of PDGF-BB oncoprotein's isomers (i.e., PDGF-AB and PDGF-AA) along with 100 pM PDGF-BB. The concentrations of interference agents were chosen to be approximately 100 times higher than concentrations of the target molecules. The DPV peak currents measured for selectivity are presented in Figure 6.6f**,** in which the peak current was measured from the DPV curves and differentiated from the aptasensor's blank response. The DPV peak current of PET/Au/rGO_{Apt} aptasensor to PDGF-BB was 6.71 and 5.83 times higher than that of PDGF-AA aptasensors and PDGF-AB, respectively. The higher response of the PET/Au/rGO_{Apt} aptasensor to BSA than PDGF-AA and PDGF-AB is attributed to the bigger size of this protein and higher physical adsorption of BSA on the surface of the PET/Au/rGO_{Apt} aptasensor.

The storage stability of the PET/Au/rGO_{Apt} aptasensor was analyzed by conducting continuous electrochemical measurements on PET/Au/rGO_{Apt} in response to 100 pM

PDGF-BB every day. The DPV peak current 25.4 µA of the PET/Au/rGO$_{Apt}$ to 100 pM PDGF-BB after 6 days was 91.02 % of the initial capacitive response (23.12 µA), which implies that the envisioned aptasensor has an adequate storage stability.

Table 6.1 summarizes the recently developed electrochemical aptasensors. The current aptasensor exhibited a wide linear range. In comparison to similar labeled and label-free gold based electrode, noticeable improvement in linear range has been achieved. The linear response range of envisioned aptasensor based BPE-treaded PET/Au covers the healthy levels of PDGF-BB as well as elevated levels in patients with cancer diseases[7, 9]. Furthermore, the proposed aptasensors is sufficiently stable. It is worth noting that the attained LoD of detection of 0.65 pM (the equivalent of 1.29 pg mL^{-1}) is adequately lower than the minimum cut-off point of 0.1 ng mL^{-1} for the healthy levels of PDGF-BB in human serums[48]. In general, the proposed aptasensor provides a wide linear range with efficient accuracy (i.e., limit of detection) suitable for determining PGDF-BB levels in healthy and patients with cancer diseases.

The envisioned disposable biosensor was a suggested concept to study the BPE-graphene compatibility for biotechnology applications. The simplicity of electrochemical bipolar exfoliation of graphene and the process's environmental friendliness has high potential for other various applications, including but not limited to biofuel cells, batteries, and supercapacitors.

6.4 Conclusion

The comparative study on BPE-graphene deposited on negative and positive electrodes confirmed that the BPE-graphene deposited on negative feeding electrode (i.e., rGO) is a more suitable candidate for biosensing applications. The SEM and TEM analysis revealed

that BPE-graphene deposited on the negative feeding electrode was porous graphene with the pore size of 100 nM and consisting of single-layer graphene nanosheets. The electrochemical and biosensing performance analysis confirmed that the BPE-rGO provides a more suitable active material for label-free aptasensing than BPE-GO. The fabricated label-free electrochemical PDGF-BB aptasensor based on BPE-rGO showed a noticeably better sensing performance than the similar BPE-GO based aptasensor. The PET/Au/rGO_{Apt} aptasensor showed a wide linear range of 0.0007-20 nM, high sensitivity of 4.07 µA $Logc^{-1}$ (unit of c, pM), and a low limit of detection of 0.65 pM (S/N=3). This aptasensor demonstrated that electrochemical bipolar exfoliation of graphene is a highly promising technique for developing highly sensitive, reliable and inexpensive biosensors for disposable sensor platforms.

6.5 References

[1] S. Forouzanfar, F. Alam, I. Khakpour, A. R. Baboukani, N. Pala, and C. Wang, "Highly Sensitive Lactic Acid Biosensors Based on Photoresist Derived Carbon," IEEE Sensors Journal, vol. 20, pp. 8965 – 8972, 2020.

[2] Y. Li, Z. Liu, W. Lu, M. Zhao, H. Xiao, T. Hu, et al., "Label-free electrochemical aptasensor based on the core-shell Cu-MOF@ TpBD hybrid nanoarchitecture for the sensitive detection of PDGF-BB," Analyst, vol. 146, pp. 979-988, 2021.

[3] S. Forouzanfar, F. Alam, N. Pala, and C. Wang, "A Review of Electrochemical Aptasensors for Label-Free Cancer Diagnosis," Journal of The Electrochemical Society, vol. 167, p. 067511, 2020.

[4] W. Jiang, D. Tian, L. Zhang, Q. Guo, Y. Cui, and M. Yang, "Dual signal amplification strategy for amperometric aptasensing using hydroxyapatite nanoparticles. Application to the sensitive detection of the cancer biomarker platelet-derived growth factor BB," Microchimica Acta, vol. 184, pp. 4375-4381, 2017.

[5] S. K. Chatterjee and B. R. Zetter, "Cancer biomarkers: knowing the present and predicting the future,", vol. 114, pp. 1510-1518, 2005.

[6] S. Forouzanfar, F. Alam, N. Pala, and C. Wang, "Highly sensitive label-free electrochemical aptasensors based on photoresist derived carbon for cancer biomarker detection," Biosensors and Bioelectronics, vol. 170, p. 112598, 2020.

[7] M. Hasanzadeh, N. Razmi, A. Mokhtarzadeh, N. Shadjou, and S. Mahboob, "Aptamer based assay of plated-derived grow factor in unprocessed human plasma sample and MCF-7 breast cancer cell lysates using gold nanoparticle supported α-cyclodextrin," International journal of biological macromolecules, vol. 108, pp. 69-80, 2018.

[8] V. Penmatsa, A. R. Ruslinda, M. Beidaghi, H. Kawarada, and C. Wang, "Platelet-derived growth factor oncoprotein detection using three-dimensional carbon microarrays," Biosensors and bioelectronics, vol. 39, pp. 118-123, 2013.

[9] Z. Zhang, C. Guo, S. Zhang, L. He, M. Wang, D. Peng, et al., "Carbon-based nanocomposites with aptamer-templated silver nanoclusters for the highly sensitive and selective detection of platelet-derived growth factor," Biosensors and Bioelectronics, vol. 89, pp. 735-742, 2017.

[10] B. Yi, P. J. Williams, M. Niewolna, Y. Wang, and T. Yoneda, "Tumor-derived platelet-derived growth factor-BB plays a critical role in osteosclerotic bone metastasis in an animal model of human breast cancer," Cancer Research, vol. 62, pp. 917-923, 2002.

[11] J. Kawaguchi, S. Adachi, I. Yasuda, T. Yamauchi, T. Yoshioka, M. Itani, et al., "UVC irradiation suppresses platelet-derived growth factor-BB-induced migration in human pancreatic cancer cells," Oncology reports, vol. 27, pp. 935-939, 2012.

[12] J. Cheng, H. Ye, Z. Liu, C. Xu, Z. Zhang, Y. Liu, et al., "Platelet-derived growth factor-BB accelerates prostate cancer growth by promoting the proliferation of mesenchymal stem cells," Journal of cellular biochemistry, vol. 114, pp. 1510-1518, 2013.

[13] A. M. Cimpean, I. M. Cobec, R. A. CEAUȘU, R. Popescu, A. Tudor, and M. Raica, "Platelet derived growth factor BB: a “Must-have” therapeutic target “redivivus” in ovarian cancer," Cancer Genomics-Proteomics, vol. 13, pp. 511-517, 2016.

[14] C. K. Lau, Z. F. Yang, D. W. Ho, M. N. Ng, G. C. Yeoh, R. T. Poon, et al., "An Akt/hypoxia-inducible factor-1α/platelet-derived growth factor-BB autocrine loop mediates hypoxia-induced chemoresistance in liver cancer cells and tumorigenic hepatic progenitor cells," Clinical Cancer Research, vol. 15, pp. 3462-3471, 2009.

[15] R. Ma, Q. Yang, S. Cao, S. Liu, H. Cao, H. Xu, et al., "Serum Platelet-Derived Growth Factor Is Significantly Lower in Patients with Lung Cancer and Continued

to Decrease After Platinum-Based Chemotherapy," OncoTargets and therapy, vol. 13, p. 1883, 2020.

[16] Y. Wang, J. Luo, J. Liu, S. Sun, Y. Xiong, Y. Ma, et al., "Label-free microfluidic paper-based electrochemical aptasensor for ultrasensitive and simultaneous multiplexed detection of cancer biomarkers," Biosensors and Bioelectronics, vol. 136, pp. 84-90, 2019.

[17] F. Alam, A. H. Jalal, S. Forouzanfar, M. Karabiyik, A. R. Baboukani, and N. Pala, "Flexible and linker-free enzymatic sensors based on zinc oxide nanoflakes for noninvasive L-lactate sensing in sweat," IEEE Sensors Journal, vol. 20, pp. 5102-5109, 2020.

[18] S. Carvajal, S. N. Fera, A. L. Jones, T. A. Baldo, I. M. Mosa, J. F. Rusling, et al., "Disposable inkjet-printed electrochemical platform for detection of clinically relevant HER-2 breast cancer biomarker," Biosensors and Bioelectronics, vol. 104, pp. 158-162, 2018.

[19] Y. T. Yaman, Ö. Akbal, G. Bolat, B. Bozdogan, E. B. Denkbas, and S. Abaci, "Peptide nanoparticles (PNPs) modified disposable platform for sensitive electrochemical cytosensing of DLD-1 cancer cells," Biosensors and Bioelectronics, vol. 104, pp. 50-57, 2018.

[20] K. S. Novoselov, D. Jiang, F. Schedin, T. Booth, V. Khotkevich, S. Morozov, et al., "Two-dimensional atomic crystals," Proceedings of the National Academy of Sciences, vol. 102, pp. 10451-10453, 2005.

[21] S. Azzouzi, L. Rotariu, A. M. Benito, W. K. Maser, M. B. Ali, and C. Bala, "A novel amperometric biosensor based on gold nanoparticles anchored on reduced graphene oxide for sensitive detection of l-lactate tumor biomarker," Biosensors and Bioelectronics, vol. 69, pp. 280-286, 2015.

[22] Q. Chen, T. Sun, X. Song, Q. Ran, C. Yu, J. Yang, et al., "Flexible electrochemical biosensors based on graphene nanowalls for the real-time measurement of lactate," Nanotechnology, vol. 28, p. 315501, 2017.

[23] D. C. Marcano, D. V. Kosynkin, J. M. Berlin, A. Sinitskii, Z. Sun, A. Slesarev, et al., "Improved synthesis of graphene oxide," ACS nano, vol. 4, pp. 4806-4814, 2010.

[24] P. Mahanandia, F. Simon, G. Heinrich, and K. K. Nanda, "An electrochemical method for the synthesis of few layer graphene sheets for high temperature applications," Chemical Communications, vol. 50, pp. 4613-4615, 2014.

[25] J. Chen, B. Yao, C. Li, and G. Shi, "An improved Hummers method for eco-friendly synthesis of graphene oxide," Carbon, vol. 64, pp. 225-229, 2013.

[26] S. Park, J. An, J. R. Potts, A. Velamakanni, S. Murali, and R. S. Ruoff, "Hydrazine-reduction of graphite-and graphene oxide," carbon, vol. 49, pp. 3019-3023, 2011.

[27] S. Pei, J. Zhao, J. Du, W. Ren, and H.-M. Cheng, "Direct reduction of graphene oxide films into highly conductive and flexible graphene films by hydrohalic acids," Carbon, vol. 48, pp. 4466-4474, 2010.

[28] K. S. Rao, J. Senthilnathan, Y.-F. Liu, and M. Yoshimura, "Role of peroxide ions in formation of graphene nanosheets by electrochemical exfoliation of graphite," Scientific reports, vol. 4, pp. 1-6, 2014.

[29] P. Yu, S. E. Lowe, G. P. Simon, and Y. L. Zhong, "Electrochemical exfoliation of graphite and production of functional graphene," Current opinion in colloid & interface science, vol. 20, pp. 329-338, 2015.

[30] A. Abdelkader, A. Cooper, R. Dryfe, and I. Kinloch, "How to get between the sheets: a review of recent works on the electrochemical exfoliation of graphene materials from bulk graphite," Nanoscale, vol. 7, pp. 6944-6956, 2015.

[31] A. P. Kauling, A. T. Seefeldt, D. P. Pisoni, R. C. Pradeep, R. Bentini, R. V. Oliveira, et al., "The worldwide graphene flake production," Advanced Materials, vol. 30, p. 1803784, 2018.

[32] A. Allagui, M. A. Abdelkareem, H. Alawadhi, and A. S. Elwakil, "Reduced graphene oxide thin film on conductive substrates by bipolar electrochemistry," Scientific reports, vol. 6, p. 21282, 2016.

[33] I. Khakpour, A. Rabiei Baboukani, A. Allagui, and C. Wang, "Bipolar Exfoliation and in Situ Deposition of High-Quality Graphene for Supercapacitor Application," ACS Applied Energy Materials, vol. 2, pp. 4813-4820, 2019.

[34] J. L. Suter, R. C. Sinclair, and P. V. Coveney, "Principles governing control of aggregation and dispersion of graphene and graphene oxide in polymer melts," Advanced Materials, vol. 32, p. 2003213, 2020.

[35] S. E. Fosdick, K. N. Knust, K. Scida, and R. M. Crooks, "Bipolar electrochemistry," Angewandte Chemie International Edition, vol. 52, pp. 10438-10456, 2013.

[36] L. Koefoed, S. U. Pedersen, and K. Daasbjerg, "Bipolar electrochemistry—A wireless approach for electrode reactions," Current Opinion in Electrochemistry, vol. 2, pp. 13-17, 2017.

[37] A. R. Baboukani, I. Khakpour, V. Drozd, A. Allagui, and C. Wang, "Single-step exfoliation of black phosphorus and deposition of phosphorene via bipolar electrochemistry for capacitive energy storage application," Journal of Materials Chemistry A, vol. 7, pp. 25548-25556, 2019.

[38] A. Allagui, J. M. Ashraf, M. Khalil, M. A. Abdelkareem, A. S. Elwakil, and H. Alawadhi, "All-Solid-State Double-Layer Capacitors Using Binderless Reduced Graphene Oxide Thin Films Prepared by Bipolar Electrochemistry," ChemElectroChem, vol. 4, pp. 2084-2090, 2017.

[39] N. R. Wilson, P. A. Pandey, R. Beanland, R. J. Young, I. A. Kinloch, L. Gong, et al., "Graphene oxide: structural analysis and application as a highly transparent support for electron microscopy," ACS nano, vol. 3, pp. 2547-2556, 2009.

[40] K. Krishnamoorthy, M. Veerapandian, K. Yun, and S.-J. Kim, "The chemical and structural analysis of graphene oxide with different degrees of oxidation," Carbon, vol. 53, pp. 38-49, 2013.

[41] E.-Y. Choi, T. H. Han, J. Hong, J. E. Kim, S. H. Lee, H. W. Kim, et al., "Noncovalent functionalization of graphene with end-functional polymers," Journal of Materials Chemistry, vol. 20, pp. 1907-1912, 2010.

[42] J. Coates, "Interpretation of infrared spectra, a practical approach," Encyclopedia of analytical chemistry: applications, theory and instrumentation, 2006.

[43] V. Penmatsa, H. Kawarada, Y. Song, and C. Wang, "Comparison of different oxidation techniques for biofunctionalization of pyrolyzed carbon," Material Science Research India, vol. 11, pp. 01-08, 2014.

[44] E. Frackowiak, "Carbon materials for supercapacitor application," Physical chemistry chemical physics, vol. 9, pp. 1774-1785, 2007.

[45] J. B. Allen and R. F. Larry, Electrochemical methods fundamentals and applications: John Wiley & Sons, 2001.

[46] X. Liu, H.-L. Shuai, and K.-J. Huang, "A label-free electrochemical aptasensor based on leaf-like vanadium disulfide-Au nanoparticles for the sensitive and selective detection of platelet-derived growth factor BB," Analytical Methods, vol. 7, pp. 8277-8284, 2015.

[47] A. Shrivastava and V. Gupta, "Methods for the determination of limit of detection and limit of quantitation of the analytical methods," Chronicles of Young Scientists, vol. 2, pp. 21-25, January 1, 2011 2011.

[48] K. Leitzel, W. Bryce, J. Tomita, G. Manderino, I. Tribby, A. Thomason, et al., "Elevated plasma platelet-derived growth factor B-chain levels in cancer patients," Cancer research, vol. 51, pp. 4149-4154, 1991.

7. PDGF-BB Aptasensors based on C-MEMS integrated with BPE-rGO

7.1 Introduction

Cancer disease is one of the significant causes of death, killing millions of people every year [1]. Most cancer diseases have a high fatality rate because cancer is diagnosed when it has significantly progressed and invaded many vital organs [2]. The main reason for such a late diagnosis is that patients with cancer diseases have no physical symptoms at the early stages of the cancer diseases [3]. Many cancer biomarkers associated with various cancer diseases have been discovered [2]. Among the discovered cancer biomarkers, platelet-derived growth factor-BB (PDGF-BB) is known to have a potent role in the growth and metastasis of several solid malignant tumors, and its levels in the blood increase under the influence of the cancer diseases [4]. Numerous studies have reported the involvement of PDGF-BB in the development and lymphatic metastasis of various cancers, including breast [5], pancreatic [6], prostate [7], ovarian [8], and liver [9]. Several studies have reported the correlation of elevated levels of PDGF-BB in human serum with cancer diseases. For example, a concentration above 1.72 nM (the equivalent of 42 ng mL^{-1}) is confirmed for patients with lung cancer [10], although there is no Food and Drug Administration (FDA) official report for the healthy and cancerous levels of PDGF-BB in human blood. The significant role of PDGF-BB in developing and metastasis of different cancer diseases highlights the importance of developing point-of-care (POC) biosensors to detect PDGF-BB biomarker. The PDGF-BB POC biosensors can be an immense help for the early diagnosis of many cancer associated with solid tumors such as breast, brain, prostate, ovarian, and lung cancers.

Electrochemical aptasensors are highly suitable for POC applications since they possess several advantages over other types of aptasensors. For instance, the electrochemical parameters can be measured without utilizing labels (i.e., label-free detection), in which label-free detection refers to the process of eliminating foreign molecules (e.g., fluorescents tags, chemiluminescent, and nanoparticle) that are temporarily or chemically attached to the target of interest, in order to detect its presence or activity [11, 12]. Electrochemical aptasensors can also be efficiently miniaturized and integrated with lab-on-chip devices and complementary metal–oxide–semiconductor (i.e., CMOS) circuits. The price of electrochemical sensing units can be considerably reduced (e.g., paper-based electrochemical sensing electrodes) [13]. Moreover, label-free electrochemical detection can reduce the cost of operation and blood sample consumption by requiring relatively simple sample preparation [14-17]. However, the sensing performance of label-free electrochemical aptasensors such as sensitivity, selectivity, and dynamic range requires further enhancements to match the performance of the clinical test.

Carbon-based microelectromechanical devices (C-MEMS) are glassy-carbon devices derived from pyrolyzed epoxy-based photoresists (i.e., SU-8 photoresist) at high temperatures in oxygen-free environments. C-MEMS-based electrodes possess features that make them highly suitable for biosensing applications, such as good conductivity, high physiochemical stability, wide electrochemical windows, high tolerance against biofouling phenomenon, and highly accessible surface functionalization [18-21]. The C-MEMS synthesis technique can produce electrodes with high resolution (i.e., tens of nanometers) and good fabrication yields, which are highly favorable for POC applications [18]. Nano-enabled C-MEMS electrodes enhance aptamer immobilization efficiency (i.e., by

providing a larger accessible surface area), and highly accessible functionalization promotes the stability of the aptasensor by providing covalent immobilization of the aptamers.

Since the discovery of graphene in the early 2000s, graphene has attracted massive attention in various domains because of its unique features [22]. The large surface area, high thermal conductivity and charge mobility, wide electrochemical window, and unconventional superconductivity of graphene made this material a potent candidate for the development of biosensors [23, 24]. The comparative study by Kauling et al. has demonstrated that the commercially available graphene (from 60 different vendors worldwide) has low graphene content (less than 10% in most products and not more than 50% in the highest quality available product), which illustrates the reason why commercial graphene-based devices are not commonly available yet[25]. Nonetheless, the conventional methods for synthesis and deposition of graphene oxide (GO) and reduced graphene oxide (rGO) cannot simultaneously exfoliate, reduce, and deposit GO and rGO in an environmentally friendly fashion. Such a combination can be achieved via bipolar electrochemistry[26]. Besides, Khakpour et al. have demonstrated that the bipolar exfoliated rGO has vertically aligned morphology, eliminating the necessity of using spacers such as carbon nanotubes to prevent the aggregation of graphene nano-flakes [27, 28].

In this study, the integration of bipolar exfoliated rGO (BPE-rGO) on three-dimensional (3D) CMEMS microelectrodes was investigated. The 3D CMEMS microelectrodes were used as negative feeding electrodes in a BPE cell. Amino-terminated ssDNA aptamers were covalently immobilized on the surface of the 3D CMEMS

microelectrodes decorated with BPE-rGO. The morphology of 3D CMEMS microelectrodes decorated with BPE-rGO was studied via scanning electron microscopy (SEM). The characteristics of the fabricated BPE-based aptasensors were studied using Fourier-transform infrared spectroscopy (FTIR). Electrochemical and sensing performance analyses were conducted using cyclic voltammetry (CV). The results revealed that the integration of BPE-rGO with 3D CMEMS enhances the areal capacitance of the microelectrodes and improves the sensitivity of the aptasensors. Furthermore, the BPE technique was proven to be both versatile and amenable to mass production, thus making it a promising technique for various biotechnology applications, including but not limited to POC cancer aptasensors.

7.2 Materials and Methodology

7.2.1 Materials and Reagents

The PDGF-BB binding aptamer (ssDNA, amino linker-5'-C_6-CAG GCT ACG GCA CGT AGA GCA TCA CCA TGA TCC TG-3' [2]) was purchased in HPLC purification from ThermoFisher Scientific, USA. Tris-ethylenediaminetetraacetic acid (TE) buffer, ethanol, acetone, phosphate-buffered saline (1M and pH 7.4) (PBS), 1-ethyl-3-(3-dimethylaminopropyl) carbodiimide hydrochloride linker (EDC), N-hydroxysuccinimide linker (NHS), hydrochloric acid (HCl), Polyoxyethylene (20) sorbitan monolaurate (Tween-20), KCl, and $k_3Fe(CN)_6$ were purchased from ThermoFisher Scientific, USA. Trehalose, bovine serum albumin (BSA), and platelet-derived growth factor-AA, AB, and BB were purchased from Sigma Aldrich, USA. NANO^{TM} SU-8 25 and SU-8 100 negative photoresist were purchased from Microchem., USA. Graphite rods (3

cm in length and 6.15 mm in diameter, Ultra "F″ Purity 99.9995%) were purchased from Fisher Scientific, USA. The 316 stainless steel (SS) electrodes were purchased from Maudlin Inc., USA. All chemicals were analytical grade. Milli-Q (Sigma Aldrich, USA) deionized water (DI water) was used in this study.

7.2.2 Apparatus

Bio-Logic versatile multichannel potentiostat (VMP3) was used for the electrochemical analysis. JEOL SEM 6330 was used to obtain the SEM images of the electrodes. Agilent Technologies N6705A dc Power Analyzer was used for applying a DC voltage of 45 V across the feeding electrodes. An Ag/AgCl (KCl saturated) and Pt wire were used as reference electrode and working electrode in all electrochemical measurements, respectably. A 713 Metrohm pH meter was used for measuring the pH of electrolytes. JASCO FTIR 4100 was used to conduct FTIR analysis.

7.2.3 3D CMEMS Photolithography

The 3D CMEMS microelectrodes were fabricated via the previously reported C-MEMS synthesis process [1, 29-31], which is schematically illustrated in Figure 7.1a. The fabrication process started with cleaning a 4-inch p-doped single-side polished silicon wafer with acetone and methanol. A layer of SU-8 25 photoresist was spin-coated on the wafer at 300 rpm for 10 seconds and then accelerated to 3000 rpm for 30 seconds to provide a uniform photoresist layer with a thickness of approximately 15 µm. Soft bakes at 65°C for 3 minutes and 95°C for 7 minutes were conducted on hotplates, followed by UV light exposure with a dose of 300 mJ cm^{-2}. Post-exposure bakes were conducted at 65°C for 1

minute and 95°C for 5 minutes on hotplates. After developing the first layer, the thick layer of SU-8 100 photoresist was spin-coated on the wafer at 300 rpm for 12 seconds and then accelerated to 2000 rpm for 30 seconds to provide a uniform photoresist layer with a thickness of approximately 150 µm. Soft bakes at 65°C for 20 minutes and 95°C for 60 minutes were conducted on hotplates, followed by UV light exposure with a dose of 700 mJ cm^{-2}. Post-exposure bakes were conducted at 65°C for 2 minutes and 95°C for 15 minutes on hotplates. The developed electrodes were pyrolyzed in a Lindenberg tube furnace with a temperature ramp of 10°C min^{-1} in two steps of 250°C with a dwell time of 30 minutes, and 900°C with a dwell time of 60 minutes, under 500 sccm flow of forming gas (5%H_2 + 95%N_2). The samples were left in the furnace overnight to cool to room

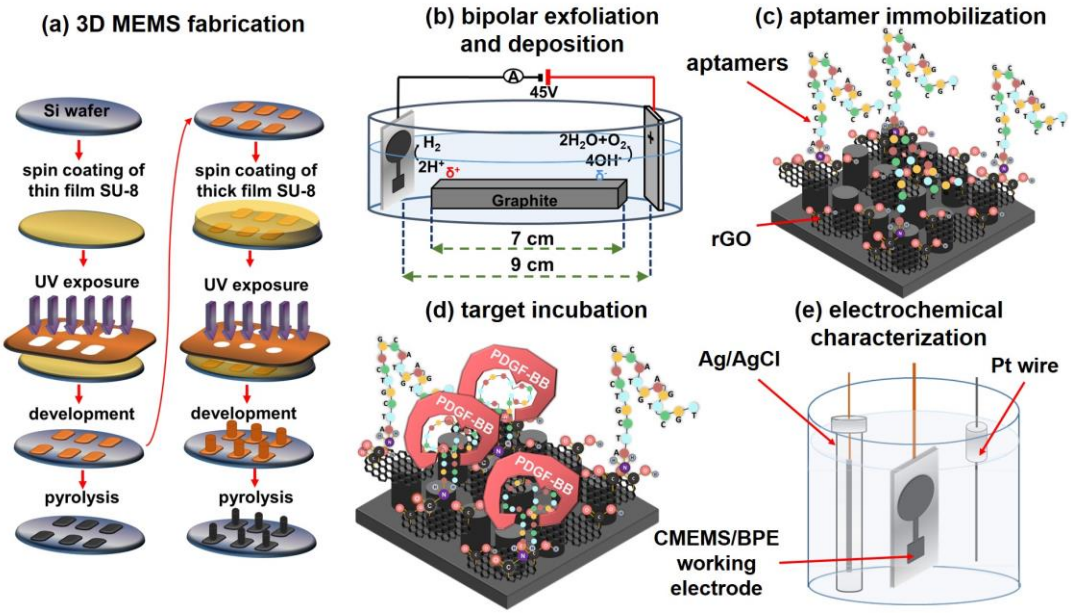

Figure 7.1 Schematic illustration of (a) 3D CMEMS microfabrication process, (b) bipolar exfoliation cell, (c) development of CMEMS/BPE/Apt PDGF-BB aptasensors, (d) target incubation, and (e) three-electrode electrochemical cell with Ag/AgCl reference electrode, Pt wire counter electrode, and CMEMS/BPE/Apt in 5 mL aqueous electrolytes of 0.1 M PBS/5 mM $K_3Fe(CN)_6$/0.2 M KCl.

temperature.

7.2.4 Bipolar Exfoliation/Deposition of rGO

A bipolar exfoliation cell illustrated in Figure 7.2b has been used for exfoliation, reduction, and deposition of graphene nanosheets on 3D CMEMS electrodes. The bipolar mechanism details have been discussed in previous studies [26, 27, 32]. Briefly, a 45 V direct current (DC) voltage was applied through the CMEMS microelectrode as the negative feeding electrode and 2×2 cm stainless steel positive feeding electrodes with a 9 cm distance to induce an electric field of 5 V cm^{-1}. The resistivity of DIW used for bipolar exfoliation was 17 MΩ. After 24h of bipolar treatment, the 3D CMEMS electrodes treated with BPE-rGO (designated as CMEMS/BPE) were thoroughly washed in DIW and dried in an oven at 70°C overnight to evaporate remaining moisture from CMEMS/BPE electrodes.

7.2.5 Aptasensor Development

The aptamer stock solutions were prepared based on the suggested procedure in the datasheet released by ThermoFisher Scientific for oligonucleotide preparation and storage. The diluted stocks were prepared in 0.1 M TE buffer with a final volume of 10 µL. Before immobilizing aptamers, 5 µL of 20 mg mL^{-1} EDC and 10 µL of 20 mg mL^{-1} NHS were added to the aptamer solution with a concentration of 20 µM. The aptamer solution was incubated for 30 minutes at room temperature. This step is recommended for activating the amino linker tags of the aptamers. The prepared aptamer solution was deposited on the CMEMS/BPE electrode surfaces and followed by incubation for 2 hours at room temperature. After incubation, electrodes were washed thoroughly in DI water to wash any

unattached aptamers. In order to quench blank areas of the CMEMS/BPE electrodes, 50 µL of the aqueous solution of 0.1 M PBS + 1% (v:v) Tween-20 was deposited on the electrodes and followed by incubation for 10 minutes. The aptamer immobilized electrodes (designated as CMEMS/BPE/Apt) (Figure 7.1c) were washed with DI water for 5 minutes and stored in 0.1 M TE buffer in the refrigerator (4°C) when not in use.

7.2.6 Electrochemical Characterization of Aptasensors

The stock solutions of PDGF-AA, AB, and BB were prepared based on the suggested procedure in the datasheet released by Sigma Aldrich. The samples were diluted in an aqueous solution of DI water and 5% (v:v) trehalose to a final volume of 15 µL. The desired target was added to the CMEMS/BPE/Apt microelectrodes and followed by incubation at room temperature (25°C) for 40 minutes. Following target immobilization, which is schematically illustrated in Figure 7.1d, the ThL electrodes were washed in DI water before electrochemical measurements were conducted. The electrodes incubated with the target were immediately tested via the three-electrode setup illustrated in Figure 7.1e for CV evaluations. The 5 mL aqueous electrolyte based on a mixture of 5 mM $k_3Fe(CN)_6$, 0.1 M PBS, and 0.2 M KCl was used for electrochemical measurements. In CV measurements, CMEMS electrodes were tested between -0.3 V to 0.6 V versus reference electrode with scan rate 40 $mV.s^{-1}$. All CV data were typically taken after conducting 20 continuous cycles to ensure a reliable data recording. After every electrochemical measurement, the C-MEMS aptasensors were regenerated by immersing the sensing electrodes in 1 M TE buffer with gentle stirring for 30 minutes. All of the target incubations and electrochemical tests were conducted at room temperature (25°C).

7.3 Results and Discussion

7.3.1 Material Characterization

The SEM image of the 3D CMEMS micropillar covered with rGO deposition after 24 hours of deposition is presented in Figure 7.2a. The SEM images of rGO deposited on

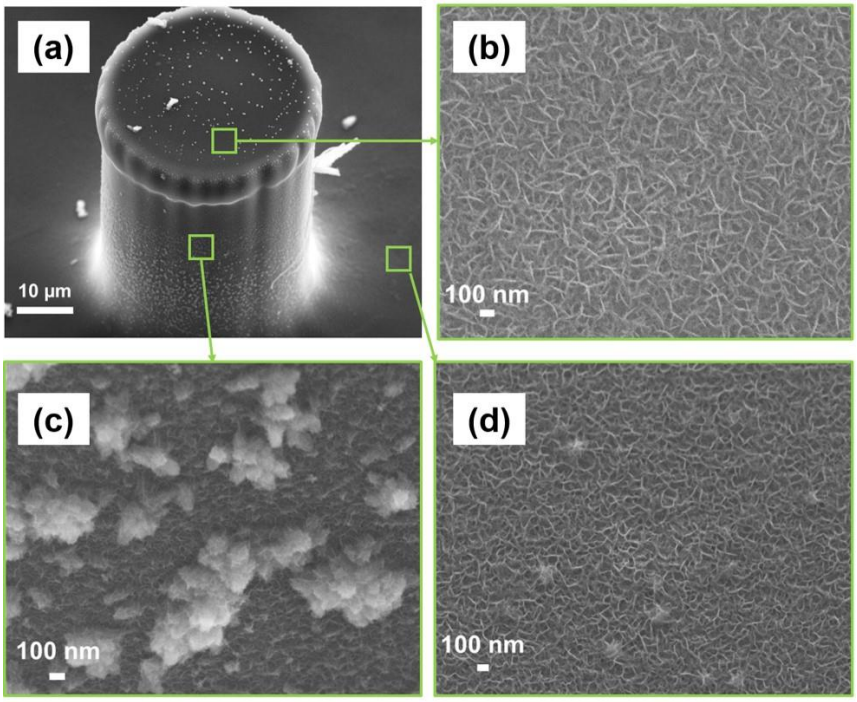

Figure 7.2 SEM images of (a) C-MEMS micro pillars with BPE-rGO, (b) BPE-rGO deposition on top of the micropillar, (c) BPE-rGO deposited on sides of the micropillar, and (d) BPE-rGO deposited on thin-film base electrode.

top of the pillar **(Figure 7.2b**), side of the pillars (Figure 7.2c), and supporting thin-film (Figure 7.2d) show that the deposition of BPE-rGO is uniform with a porous morphology with a pore size of around 100 nm and vertically aligned structures. This porous morphology is highly suitable for various applications, including electrochemical biosensors and energy storage microdevices. The SEM image confirms that the BPE can be used for uniform deposition of BPE-rGO with good efficacy and high coverage without

requiring spacers such as carbon nanotubes (CNTs) to prevent the agglomeration of rGO nanosheets.

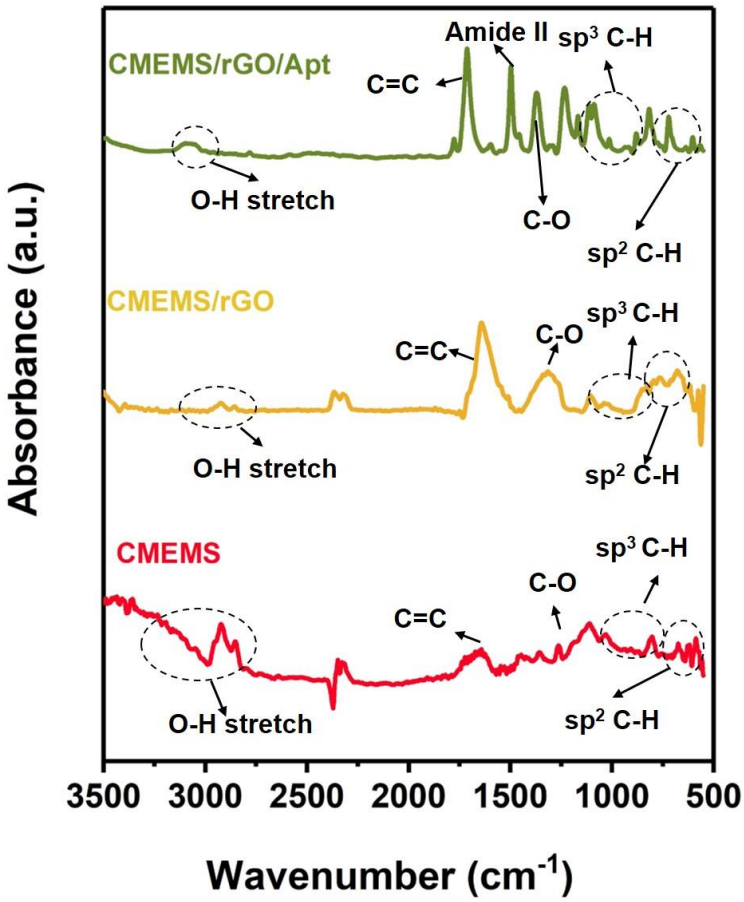

Figure 7.3 FTIR spectra of (a) C-MEMS electrode before any modification, (b) C-MEMS electrode after BPE-rGO deposition (CMEMS/rGO), and (c) C-MEMS/rGO after aptamer immobilization (CMEMS/rGO/Apt)

The FTIR characterization was used to analyze the spectral data of the CMEMS microelectrodes before BPE treatment, after and BPE-rGO deposition, and after aptamer immobilization. The FTIR spectra of CMEMS, CMEMS/BPE, and CMEMS/BPE/Apt microelectrodes are represented in Figure 7.3. Three samples of CMEMS, CMEMS/BPE, and CMEMS/BPE/Apt showed a broad peak between 2800-3200 cm^{-1}, ascribed to O-H stretching [33]. The noteworthy peaks for all samples were identified at 1430 and 1600

cm^{-1}, ascribed to C-O bending and aromatic C≡C stretching, respectively[34]. Furthermore, All the samples showed peaks at 1100-1300 cm^{-1}, attributed to sp^3 C-H bending [33].

The FTIR spectrum for CMEMS/BPE/Apt confirms a peak at 1571 cm^{-1}, associated with amide II band, representing covalent bonding of PDGF-BB aptamers with the surface of CMEMS/BPE/Apt microelectrodes [33]. The FTIR results confirm that the locally formed carboxyl groups on the graphene surfaces can be used directly to immobilize the amino-terminated biorecognizers agents. The immobilization efficiency can also be improved using oxygen-plasma etching to increase the percentages of carboxyl groups on the surface of the BPE-graphene [1, 35].

7.3.2 Electrochemical Characterization

In order to analyze the effect of deploying C-MEMS technology and deposition of BPE-rGO on 3D CMEMS on the capacitance of the electrodes, CV tests were done on stainless steel control sample and 3D CMEMS microelectrodes at each development stage. The CV analysis is given in Figure 7.4a. The area under the CV curve can be used to calculate the areal capacitance using equation 7.1 [36]:

$$C = \frac{1}{2As\Delta V} \int IdV \tag{7.1}$$

where ΔV is the voltage window, s is scan rate, A is the electrode area, V is the voltage, and I is current. The calculated areal capacitances from CV curves are presented in Figure 7.4b. The area under the CV curve of the 3D CMEMS electrode was much larger than the CV curve of the stainless steel electrode, in which the increased area under the CV curve can be interpreted as increased areal capacitance from 0.32 mF cm^{-2} to 7.67 mF cm^{-2} for

stainless steel electrodes and 3D CMEMS microelectrodes, respectively. The increase in the capacitance can be explained by the increase in the surface area of the electrode and better electrochemical properties of CMEMS materials. After deposition of BPE-rGO, the areal capacitance was increased to 19.89 mF cm^{-2}, resulting from the increased active area after BPE-rGO. These results agree with former studies on BPE-graphene. For example, the comparative study by Khakpour et al. on BPE-graphene deposited on negative electrodes has proven increased areal capacitance of samples after deposition of BPE-rGO [27].

After immobilizing the aptamers, the areal capacitance was slightly increased to 21.43 mF $cm^{-2,}$ which could result from the engagement of carboxylate groups of the surface in amide bonding (i.e., covalent immobilization of aptamers) and quenched

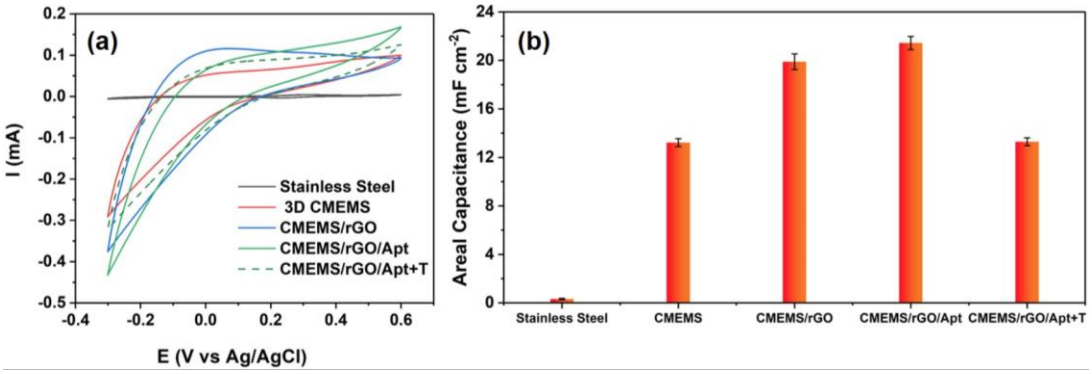

Figure 7.4 (a) CV plot of C-MEMS bare electrode and after each modification with scan rate of 40 mV s-1 and incubation with 100 pM PDGF-BB (b) Areal capacitances calculated from CV plots.

remaining carboxyl groups by Tween-20 quencher. The previous study proved that capturing the target molecules (i.e., PDGF-BB oncoproteins) decreases the areal capacitance [31]. The areal capacitance of the aptasensor was decreased from 21.43 mF

cm^{-2} to 13.29 mF cm^{-2} after incubation with 100 pM of target molecules. Hence, a turn-off response was expected from CMEMS/BPE/Apt aptasensors.

7.3.3 Sensing Characterization

The turn-off strategy can apply to label-free electrochemical aptasensors in similar manners to optical aptasensors [37, 38]. In this study, the turn-off strategy was designed based on measuring areal capacitances using CV measurements.

The turn-off responses of CMEMS/rGO/Apt aptasensor in response to 0–10 nM PDGF-BB are presented in Figure 7.5a. The oxidation of peak $Fe(CN)_6^{-3/-4}$ at E= 0.3V (vs. Ag/AgCl) was decreased proportionally to the increase of the PDGF-BB concentration. The observed decrease in the peak current is the result of the increased R_{CT} of the sensing probe. The calibration curve for calculated areal capacitances using equation 7.1 is shown in Figure 7.5b. The calibration curve was obtained by calculating the average value of areal capacitances (mF cm^{-2}) from the repeated measurements of n=3. The area under the CV curves decreased substantially upon increasing the PDGF-BB concentrations. The decrease in the areal capacitance (charge density) suggests that the PDGF-BB oncoproteins were successfully attached to the CMEMS/rGO/Apt aptasensor's surface and displaced the double-layer [39]. The linear dependence of the output capacitance on the logarithm of PDGF-BB concentration has a slope of -3.09 mF cm^{-2} $Logc^{-1}$ (unit of c, pM) and the R^2 of 0.9854. The correlation of CMEMS/rGO/Apt capacitance to the logarithm of PDGF-BB concentration can be assessed as following (equation 7.2),

$$C=21.47 - 3.09\ Logc^{-1},\ r=0.9887 \qquad (7.2)$$

where C is the areal capacitance (mF cm^{-2}), c is the PDGF-BB concentration (pM) and r is the regression coefficient. Hence, the CV measurement's sensitivity to PDGF-BB can be calculated as 3.09 mF cm^{-2} $Logc^{-1}$. The limit of detection (LoD) for CMEMS/rGO/Apt aptasensors based on CV measurements was calculated as 0.75 pM based on the linear regression (equation 7.3) [40],

$$LoD = \frac{3S}{b} \qquad (7.3)$$

where S is the standard deviation of the blank response (STDEV= 0.0347 mF cm^{-2}, n=9), and b is the slope of the calibration curve (b = -13.88 mF cm^{-2} c^{-1} of areal capacitances).

The selectivity of the CMEMS/rGO/Apt aptasensors was studied by measuring the response of the aptasensors to 4 µg mL^{-1} BSA, 50 nM PDGF-AB, and 50 nM PDGF-AA along with 500 pM PDGF-BB. The concentrations of interference agents were chosen to be approximately 100 times more than that of the target molecules. The selectivity measurements are presented in Figure 7.5c, in which the areal capacitances were calculated from the CV curves. The change in capacitive response of CMEMS/rGO/Apt aptasensors

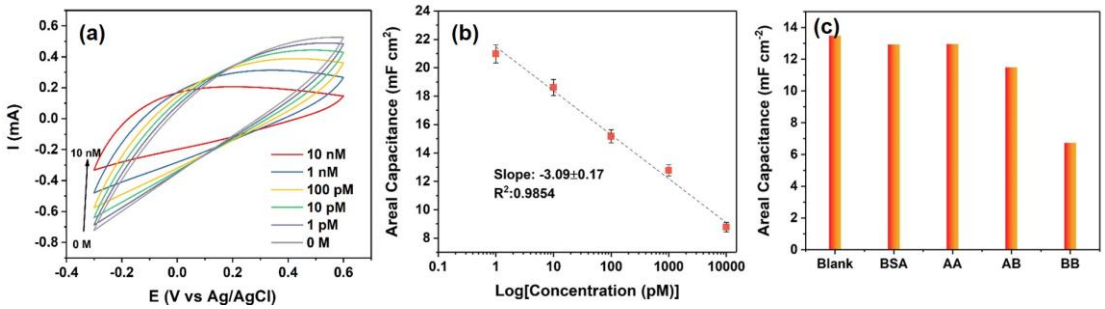

Figure 7.5 (a) CV curves of the CMEMS/rGO/Apt electrode's response to PDGF-BB ranging from 0–10 nM. (b) Calibration curve for calculated areal capacitances from CV curves with n=5. C) (c) Areal capacitances calculated from CV curves measured in response of CMEMS/rGO/Apt electrodes to 4 µg mL^{-1} BSA. 50 nM PDGF-AA, 50 nM PDGF-AB, and 500 pM PDGF-BB

to PDGF-BB was 12.73 and 3.34 times higher than that of the aptasensors to PDGF-AA and PDGF-AB, respectively.

7.4 Conclusion

In this chapter, the integration of bipolar exfoliated graphene and 3D CMEMS microelectrodes was investigated. The SEM analysis confirmed a uniform deposition of rGO on micropillars and the support thin-film electrode. The CV analysis confirmed enhanced areal capacitance after deposition of rGO, resulting from increased surface area and improved conductivity of the 3D CMEMS electrodes after deposition of rGO. The aptasensors based on 3D CMEMS electrodes decorated with BPE-rGO showed high sensitivity and low limit. The achieved results suggest that bipolar electrochemistry can offer a highly efficient and environmentally friendly technology for the deposition of rGO on CMEMS microelectrodes. The integration of bipolar electrochemistry and CMEMS technology is highly promising for feasible lab-on-chip biosensors.

7.5 References

[1] S. Forouzanfar, F. Alam, I. Khakpour, A. R. Baboukani, N. Pala, and C. Wang, "Highly Sensitive Lactic Acid Biosensors Based on Photoresist Derived Carbon," IEEE Sensors Journal, 2020.

[2] S. Forouzanfar, F. Alam, N. Pala, and C. Wang, "A Review of Electrochemical Aptasensors for Label-Free Cancer Diagnosis," Journal of The Electrochemical Society, vol. 167, p. 067511, 2020.

[3] S. K. Chatterjee and B. R. Zetter, "Cancer biomarkers: knowing the present and predicting the future,", vol. 114, pp. 1510-1518, 2005.

[4] V. Penmatsa, A. R. Ruslinda, M. Beidaghi, H. Kawarada, and C. Wang, "Platelet-derived growth factor oncoprotein detection using three-dimensional carbon microarrays," Biosensors and bioelectronics, vol. 39, pp. 118-123, 2013.

[5] B. Yi, P. J. Williams, M. Niewolna, Y. Wang, and T. Yoneda, "Tumor-derived platelet-derived growth factor-BB plays a critical role in osteosclerotic bone

metastasis in an animal model of human breast cancer," Cancer Research, vol. 62, pp. 917-923, 2002.

[6] J. Kawaguchi, S. Adachi, I. Yasuda, T. Yamauchi, T. Yoshioka, M. Itani, et al., "UVC irradiation suppresses platelet-derived growth factor-BB-induced migration in human pancreatic cancer cells," Oncology reports, vol. 27, pp. 935-939, 2012.

[7] J. Cheng, H. Ye, Z. Liu, C. Xu, Z. Zhang, Y. Liu, et al., "Platelet-derived growth factor-BB accelerates prostate cancer growth by promoting the proliferation of mesenchymal stem cells," Journal of cellular biochemistry, vol. 114, pp. 1510-1518, 2013.

[8] A. M. Cimpean, I. M. Cobec, R. A. CEAUȘU, R. Popescu, A. Tudor, and M. Raica, "Platelet derived growth factor BB: a “Must-have” therapeutic target “redivivus” in ovarian cancer," Cancer Genomics-Proteomics, vol. 13, pp. 511-517, 2016.

[9] C. K. Lau, Z. F. Yang, D. W. Ho, M. N. Ng, G. C. Yeoh, R. T. Poon, et al., "An Akt/hypoxia-inducible factor-1α/platelet-derived growth factor-BB autocrine loop mediates hypoxia-induced chemoresistance in liver cancer cells and tumorigenic hepatic progenitor cells," Clinical Cancer Research, vol. 15, pp. 3462-3471, 2009.

[10] R. Ma, Q. Yang, S. Cao, S. Liu, H. Cao, H. Xu, et al., "Serum Platelet-Derived Growth Factor Is Significantly Lower in Patients with Lung Cancer and Continued to Decrease After Platinum-Based Chemotherapy," OncoTargets and therapy, vol. 13, p. 1883, 2020.

[11] A. Syahir, K. Usui, K.-y. Tomizaki, K. Kajikawa, and H. Mihara, "Label and label-free detection techniques for protein microarrays," Microarrays, vol. 4, pp. 228-244, 2015.

[12] R. Zhang, C. Rejeeth, W. Xu, C. Zhu, X. Liu, J. Wan, et al., "Label-free electrochemical sensor for cd44 by ligand-protein interaction," Analytical chemistry, vol. 91, pp. 7078-7085, 2019.

[13] Y. Wang, J. Luo, J. Liu, S. Sun, Y. Xiong, Y. Ma, et al., "Label-free microfluidic paper-based electrochemical aptasensor for ultrasensitive and simultaneous multiplexed detection of cancer biomarkers," Biosensors and Bioelectronics, vol. 136, pp. 84-90, 2019.

[14] S. Forouzanfar, N. Talebzadeh, S. Zargari, and H. Veladi, "The effect of microchannel width on mixing efficiency of microfluidic electroosmotic mixer," in 2015 3rd RSI International Conference on Robotics and Mechatronics (ICROM), 2015, pp. 629-634.

[15] R. Ranjan, E. N. Esimbekova, and V. A. Kratasyuk, "Rapid biosensing tools for cancer biomarkers," Biosensors and Bioelectronics, vol. 87, pp. 918-930, 2017.

[16] L. Cui, M. Lu, Y. Li, B. Tang, and C.-y. Zhang, "A reusable ratiometric electrochemical biosensor on the basis of the binding of methylene blue to DNA with alternating AT base sequence for sensitive detection of adenosine," Biosensors and Bioelectronics, vol. 102, pp. 87-93, 2018.

[17] F. Ma, S.-h. Wei, and C.-y. Zhang, "Construction of a Robust Entropy-Driven DNA Nanomachine for Single-Molecule Detection of Rare Cancer Cells," Analytical chemistry, vol. 91, pp. 7505-7509, 2019.

[18] C. Wang and M. Madou, "From MEMS to NEMS with carbon," Biosensors and bioelectronics, vol. 20, pp. 2181-2187, 2005.

[19] L. Ferrer-Argemi, E. S. Aliabadi, A. Cisquella-Serra, A. Salazar, M. Madou, and J. Lee, "Size-dependent electrical and thermal conductivities of electro-mechanically-spun glassy carbon wires," Carbon, vol. 130, pp. 87-93, 2018.

[20] M. V. Piñón, B. C. Benítez, B. Pramanick, V. H. Perez-Gonzalez, M. J. Madou, S. O. Martinez-Chapa, et al., "Direct current-induced breakdown to enhance reproducibility and performance of carbon-based interdigitated electrode arrays for AC electroosmotic micropumps," Sensors and Actuators A: Physical, vol. 262, pp. 10-17, 2017.

[21] E. Adelowo, A. R. Baboukani, O. Okpowe, I. Khakpour, M. Safa, C. Chen, et al., "A high-energy aqueous on-chip lithium-ion capacitor based on interdigital 3D carbon microelectrode arrays," Journal of Power Sources, vol. 455, p. 227987, 2020.

[22] K. S. Novoselov, D. Jiang, F. Schedin, T. Booth, V. Khotkevich, S. Morozov, et al., "Two-dimensional atomic crystals," Proceedings of the National Academy of Sciences, vol. 102, pp. 10451-10453, 2005.

[23] S. Azzouzi, L. Rotariu, A. M. Benito, W. K. Maser, M. B. Ali, and C. Bala, "A novel amperometric biosensor based on gold nanoparticles anchored on reduced graphene oxide for sensitive detection of l-lactate tumor biomarker," Biosensors and Bioelectronics, vol. 69, pp. 280-286, 2015.

[24] Q. Chen, T. Sun, X. Song, Q. Ran, C. Yu, J. Yang, et al., "Flexible electrochemical biosensors based on graphene nanowalls for the real-time measurement of lactate," Nanotechnology, vol. 28, p. 315501, 2017.

[25] A. P. Kauling, A. T. Seefeldt, D. P. Pisoni, R. C. Pradeep, R. Bentini, R. V. Oliveira, et al., "The worldwide graphene flake production," Advanced Materials, vol. 30, p. 1803784, 2018.

[26] A. Allagui, M. A. Abdelkareem, H. Alawadhi, and A. S. Elwakil, "Reduced graphene oxide thin film on conductive substrates by bipolar electrochemistry," Scientific reports, vol. 6, p. 21282, 2016.

[27] I. Khakpour, A. Rabiei Baboukani, A. Allagui, and C. Wang, "Bipolar Exfoliation and in Situ Deposition of High-Quality Graphene for Supercapacitor Application," ACS Applied Energy Materials, vol. 2, pp. 4813-4820, 2019.

[28] J. L. Suter, R. C. Sinclair, and P. V. Coveney, "Principles governing control of aggregation and dispersion of graphene and graphene oxide in polymer melts," Advanced Materials, vol. 32, p. 2003213, 2020.

[29] C. Wang, G. Jia, L. H. Taherabadi, and M. J. Madou, "A novel method for the fabrication of high-aspect ratio C-MEMS structures," Journal of microelectromechanical systems, vol. 14, pp. 348-358, 2005.

[30] C. Wang, L. Taherabadi, G. Jia, M. Madou, Y. Yeh, and B. Dunn, "C-MEMS for the manufacture of 3D microbatteries," Electrochemical and Solid-State Letters, vol. 7, pp. A435-A438, 2004.

[31] S. Forouzanfar, F. Alam, N. Pala, and C. Wang, "Highly sensitive label-free electrochemical aptasensors based on photoresist derived carbon for cancer biomarker detection," Biosensors and Bioelectronics, vol. 170, p. 112598, 2020.

[32] A. Allagui, J. M. Ashraf, M. Khalil, M. A. Abdelkareem, A. S. Elwakil, and H. Alawadhi, "All-Solid-State Double-Layer Capacitors Using Binderless Reduced Graphene Oxide Thin Films Prepared by Bipolar Electrochemistry," ChemElectroChem, vol. 4, pp. 2084-2090, 2017.

[33] E.-Y. Choi, T. H. Han, J. Hong, J. E. Kim, S. H. Lee, H. W. Kim, et al., "Noncovalent functionalization of graphene with end-functional polymers," Journal of Materials Chemistry, vol. 20, pp. 1907-1912, 2010.

[34] J. Coates, "Interpretation of infrared spectra, a practical approach," Encyclopedia of analytical chemistry: applications, theory and instrumentation, 2006.

[35] V. Penmatsa, H. Kawarada, Y. Song, and C. Wang, "Comparison of different oxidation techniques for biofunctionalization of pyrolyzed carbon," Material Science Research India, vol. 11, pp. 01-08, 2014.

[36] E. Frackowiak, "Carbon materials for supercapacitor application," Physical chemistry chemical physics, vol. 9, pp. 1774-1785, 2007.

[37] M. Shamsipur, L. Farzin, M. A. Tabrizi, and F. Molaabasi, "Highly sensitive label free electrochemical detection of VGEF165 tumor marker based on “signal off” and “signal on” strategies using an anti-VEGF165 aptamer immobilized BSA-gold nanoclusters/ionic liquid/glassy carbon electrode," Biosensors and Bioelectronics, vol. 74, pp. 369-375, 2015.

[38] A. Benvidi, M. Banaei, M. D. Tezerjani, H. Molahosseini, and S. Jahanbani, "Impedimetric PSA aptasensor based on the use of a glassy carbon electrode modified with titanium oxide nanoparticles and silk fibroin nanofibers," Microchimica Acta, vol. 185, p. 50, 2018.

[39] X. Liu, H.-L. Shuai, and K.-J. Huang, "A label-free electrochemical aptasensor based on leaf-like vanadium disulfide-Au nanoparticles for the sensitive and selective detection of platelet-derived growth factor BB," Analytical Methods, vol. 7, pp. 8277-8284, 2015.

[40] A. Shrivastava and V. Gupta, "Methods for the determination of limit of detection and limit of quantitation of the analytical methods," Chronicles of Young Scientists, vol. 2, pp. 21-25, January 1, 2011 2011.

8. Conclusions and Outlook

8.1 Summary

In this dissertation, carbon-based biosensors for cancer biomarker detection were designed, developed, and analyzed. Label-free detection is highly important for developing feasible point-of-care (POC) cancer biomarker biosensors. The lower sensitivity, higher background noise, lower selectivity, and degradation are the main drawbacks of label-free biosensing. Hence, these limitations should be overcome before label-free POC cancer biomarker biosensors become commonly available. Carbon and its derivatives possess unique features that can be used for developing sensitive, selective, and stable label-free cancer biomarker biosensors. The major achievements of this dissertation are as follows:
In the first phase of this dissertation, C-MEMS-based biosensors for detecting lactic acid as a complementary cancer biomarker were designed and developed. The achieved results showed that oxygen-plasma treatment of CMEMS microelectrodes enhances the immobilization of biorecognizers on the surfaces of the electrodes through the covalent bonding of enzymes and -COOH groups. Furthermore, the oxygen-plasma treatment the current generated during the oxidation of lactic acid in the electrolyte. This dissertation phase confirms that the CMEMS platform is very promising for developing precise and feasible biosensors for POC.

In the second phase, the oxygen-plasma treated CMEMS electrodes were used as the sensor platform to detect PDGF-BB cancer biomarkers. The ssDNA aptamers with a high affinity toward PDGF-BB oncoproteins were used biorecognizers and covalently immobilized on the CMEMS surface. The results showed that CMEMS electrodes could provide a sensing medium with low background noise while providing high stability and

selectivity. The results also confirmed that the CMEMS platform provides a robust and stale platform with good fabrication processes.

In the third phase of the dissertation, the suitability of the bipolar exfoliated graphene for biosensing was investigated. The comparative study revealed that the graphene deposited on a negative feeding electrode (i.e., rGO) has better properties for biosensing, including bigger surface area, higher capacitance, and lower deficiency than the graphene deposited on the positive feeding electrode (i.e., GO). As proof of concept, a disposable label-free electrochemical biosensor was developed for the detection of PDGF-BB. The developed biosensor showed high sensitivity and sufficient stability.

In the last phase of this dissertation, the bipolar exfoliated graphene was deposited on 3D CMEMS electrodes to investigate the effect of deposited rGO on the sensing performance of the C-MEMS-based biosensors. The analysis showed that the deposition of rGO enhances the capacitance of the CMEMS based biosensors, which can improve the sensitivity of the biosensors.

8.2 Future Works

The present dissertation has introduced novel carbon-based biosensors for cancer biomarker detection. Based on the current work, the author suggests the following future work to be undertaken:

1. *Optimization of CMEMS/rGO based biosensors:* The initial results showed that the biosensor based on the integration of bipolar exfoliated rGO and CMEMS (CMEMS/rGO) has a high potential for developing highly accurate and stable biosensors. Hence, the author suggests that the parameters such as deposition time,

pH of deposition medium, amount of aptamer, and incubation temperature are optimized.

2. *Integration of microfluidics with carbon-based biosensors:* Automation of detection is vital in developing feasible point-of-care biosensors. Integration of microfluidics to the carbon-based biosensors—especially CMEMS-based biosensors—can be achieved in wafer-level development. The addition of microfluidics to the sensor system can benefit the sensor in various ways, such as separation of big molecules from blood samples before reaching the test chamber, which can noticeably enhance the selectivity and accuracy of the sensor.
3. *Multiplexing the biosensors:* Multiplexing biotechnology devices is an important topic in lab-on-chip and point-of-care biodevices studies since they offer cost reduction and expedited operations while minimizing the possible tissue damages (e.g., fewer penetration numbers). Multiplexed biosensing is referred to a class of biosensors that can simultaneously perform or measure several bio-related phenomena. Multiplexing of electrochemical C-MEMS biosensors can be achieved via fabricating several interconnected sensing units and use microplasma writing to functionalize the surface of C-MEMS selectively.
4. *Integration of Zwitterion-based peptides on the surface of CMEMS electrodes:* Zwitterion-based materials are neutral molecules containing both negative and positive charges and fall under the category of anti-biofouling materials. With steric and electrostatic repulsion characteristics, Zwitterion-based coatings' robust features such as ionic solvation, the ability to attach to different functional groups, and thicker hydration shell compared to PEG give them an advantage over other

anti-biofouling materials. These coatings have been used for aptasensors for several targets such as immunoglobulin E and prostate-specific antigen-based on gold electrodes, and adenosine triphosphate and thrombin based on glassy carbon electrodes. To the best author's knowledge, there are no studies on the integration of anti-biofouling materials and C-MEMS electrodes for cancer aptasensing.

APPENDIX

Supplementary Information for Chapter 6

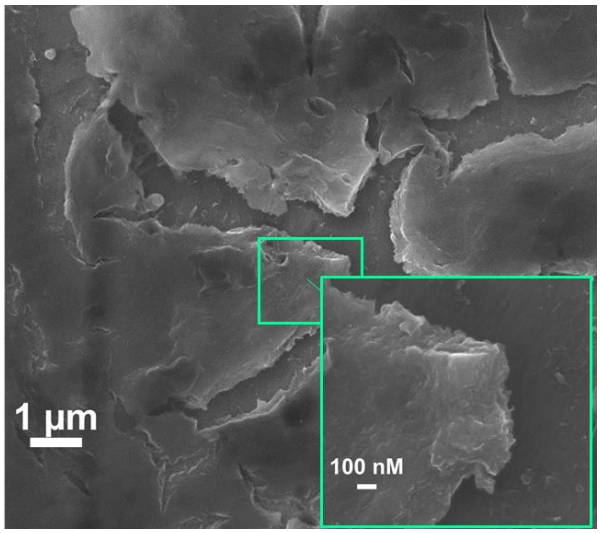

Figure S6.1 SEM images of GO deposited on stainless steel electrode (inset image is a magnified image of designated area)

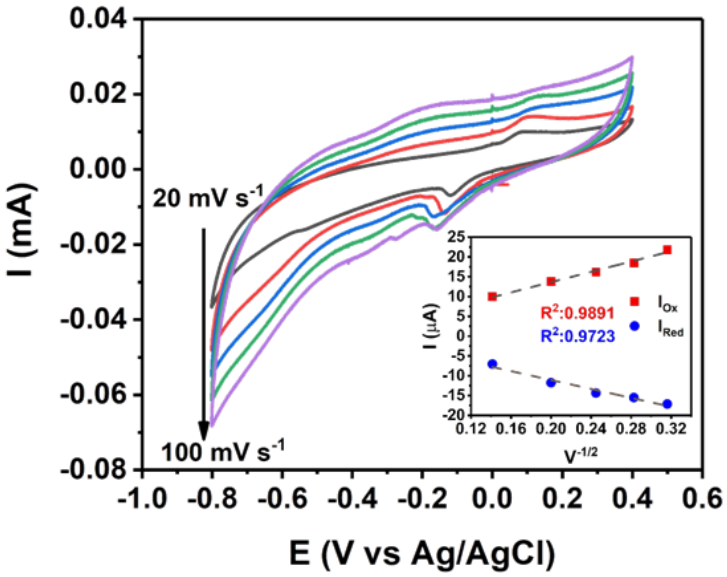

Figure S6.2 The CV plots of the SS/GO electrode at different scan rates at the range of 10–100 mV s^{-1} and the calibration curves of reduction and oxidation peak current versus the square root of scan rates (inset plots).

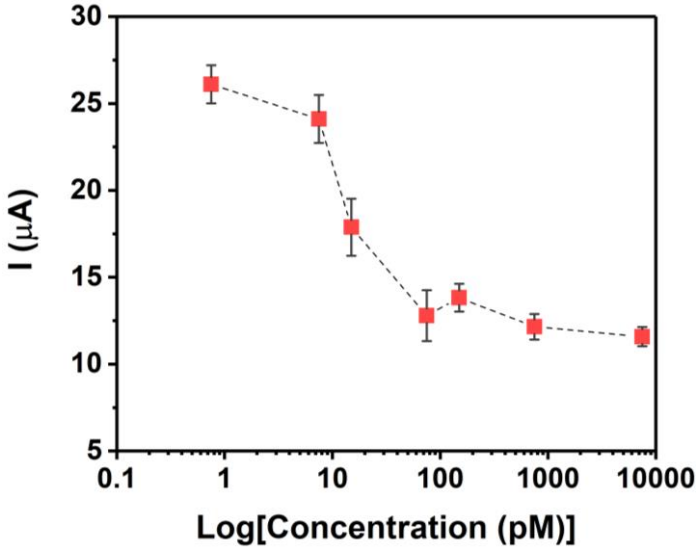

Figure S6.3 DPV peak current for SS/GO_{Apt} electrode response to PDGF-BB ranging from 0–1 nM.

VITA

SHAHRZAD FOROUZANFAR

2011-2015	B.Sc.: Electrical Engineering, (Honors Class) University of Tabriz
2017-2020	M.Sc.: Electrical Engineering Florida International University Miami, FL, USA
2017-2020	Research Assistant Florida International University Miami, FL, USA
2020-2021	Doctoral Candidate: Electrical Engineering Florida International University Miami, FL, USA

PUBLICATIONS AND PRESENTATIONS

Shahrzad Forouzanfar, Iman Khakpour, Fahmida Alam, Nezih Pala, Chunlei Wang, Novel Application of Bipolar Exfoliated Graphene for Highly Sensitive Disposable Label-Free Cancer Biomarker Aptasensors, submitted to Adv. Functional Materials, April 2021

Fahmida Alam, Ahmed Hasnain Jalal, Shahrzad Forouzanfar, Muhammad Mahmudul Hasana Nezih Pala, Thin-film nanostructure-based enzymatic alcohol sensor for wearable sensing and monitoring applications, 2021, SPIE journal, doi: 10.1117/12.2587808

Fahmida Alam, Muhammad Mahmudul Hasan, Masudur Rahman Siddiquee, Shahrzad Forouzanfar Ahmed Hasnain Jalal, Nezih Pala, Miniaturized, wireless multi-channel potentiostat platform for wearable sensing and monitoring applications, 2021, SPIE journal, doi: 10.1117/12.2587955

Shahrzad Forouzanfar, Nezih Pala, Marc Madou, Chunlei Wang, Perspectives on C-MEMS and C-NEMS Biotech Applications, 2021, Biosensors and Bioelectronics, doi:10.1016/j.bios.2021.113119

Shahrzad Forouzanfar, Fahmida Alam, Nezih Pala, Chunlei Wang, Highly Sensitive Label-Free Electrochemical Aptasensors Based on Photoresist Derived Carbon for Cancer Biomarker Detection, 2020, Biosensors and Bioelectronics, doi: 10.1016/j.bios.2020.112598

Shahrzad Forouzanfar, Fahmida Alam, Nezih Pala, Chunlei Wang, A Review of Electrochemical Aptasensors for Label-Free Cancer Diagnosis, 2020, Journal of The Electrochemical Society, doi: orcid.org/0000-0003-4225-276X

Shahrzad Forouzanfar, Fahmida Alam, Iman Khakpour, Amin Rabiei Baboukani, Nezih Pala, and Chunlei Wang, Highly Sensitive Lactic Acid Biosensors Based on Photoresist Derived Carbon, IEEE Sensors Journal, 2020, doi: 10.1109/JSEN.2020.2988383

Fahmida Alam, Ahmed Hasnain Jalal, Shahrzad Forouzanfar, Mustafa Karabiyik, Amin Rabiei Baboukani, Nezih Pala, Flexible and Linker-Free Enzymatic Sensors Based on Zinc Oxide Nanoflakes for Noninvasive L-Lactate Sensing in Sweat, IEEE Sensors Journal, 2020, doi: 10.1109/JSEN.2020.2968278

Fahmida Alam, Sohini Roy Choudhury, Ahmed Hasnain Jalal, Yogeswaran Umasankar, Shahrzad Forouzanfar, Naznin Akter, Shekhar Bhansali, Nezih Pala, Lactate biosensing: The emerging point-of-care and personal health monitoring, 2018, Biosensors and Bioelectronics, doi: 10.1016/j.bios.2018.06.054

Fahmida Alam, Ahmed Hasnain Jalal, Shahrzad Forouzanfar, Chunlei Wang, Nezih Pala, ZnO Nanoflakes based Enzymatic Sensor for the determination of lactic acid in sweat, 2019, 2019 IEEE SENSORS, doi: 10.1109/SENSORS43011.2019.8956843

Shahrzad Forouzanfar, Nima Talebzadeh, Siavash Zargari, Hadi Veladi, The effect of microchannel width on mixing efficiency of microfluidic electroosmotic mixer, 2015, IEEE, doi: 10.1109/ICRoM.2015.7367856

Novel Electrochemical Aptasensors Based on Bipolar Exfoliated Graphene for Label-Free Detectionof Cancer Biomarkers, May 2021, 239th ECS Meeting, Accepted Abstract

C-MEMS Bases Label-Free Electrochemical Aptasensors for Turn-on and Turn-off Detection of Cancer Biomarkers, November 29, 2020 MRS Fall Meeting, Boston, Massachusetts, United State

Label-Free Electrochemical Aptasensors Based on Photoresist Derived Carbon for Cancer Biomarker Detection, October 5, 2020, 238th ECS Meeting, Honolulu, Hawaii, United States

ZnO Thin Film-Based Flexible Biosensor for Continuous Monitoring of Glucose Levels in Sweat, November 29, 2020 MRS Fall Meeting, Boston, Massachusetts, United State

Zinc Oxide Nanostructure Based Noninvasive and Continuous Sweat pH Sensing and Monitoring Platform, October 14, 2019, 236th ECS Meeting, Atlanta, Georgia, United States

Highly Sensitive Lactate Sensors Based on Carbon MEMS (CMEMS), November 27, 2018 MRS Fall Meeting, Boston, Massachusetts, United State